Biosensors for pathogen detection

Juan Leva Bueno

Submitted in accordance with the requirements for the degree of
Doctor of Philosophy

The University of Leeds
School of Biomedical Sciences - Faculty of Biological Sciences

July, 2022

Declaration

The candidate confirms that the work submitted is his own, except where work formed part of jointly authored publications has been included. The contribution of the candidate and the other authors to this work has been explicitly indicated below. The candidate confirms that appropriate credit has been given within the thesis where reference has been made to the work of others.

1) Parts of **Chapter 1** appeared in the following publication: Host-pathogen adhesion as the basis of innovative diagnostics for emerging pathogens, 2021, van Belkum A, Almeida C, Bardiaux B, Barrass SV, Butcher SJ, Çaykara T, Chowdhury S, Datar R, Eastwood I, Goldman A, Goyal M, Happonen L, Izadi-Pruneyre N, Jacobsen T, Johnson PH, Kempf VAJ, Kiessling A, **Leva Bueno J**, Malik A, Malmström J, Meuskens I, Milner PA, Nilges M, Pamme N, Peyman SA, Rodrigues LR, Rodriguez-Mateos P, Sande MG, Silva CJ, Stasiak AC, Stehle T, Thibau A, Vaca DJ, Linke D.; Diagnostics, 11(7):1259.

Leva Bueno J contributed Section "5.1. Biosensor-based pathogen detection".

Van Belkum A and Linke D: conceptualization and original draft preparation. All other authors with validation, review and editing. Goldman A: writing and final review.

2) Parts of **Chapter 1** appeared in the following publication: A review on impedimetric immunosensors for pathogen and biomarker detection, 2020, **Leva-Bueno J,** Peyman SA. & Millner, PA.; Med Microbiol Immunol, 209**,** 343–362.

Leva Bueno J: all of the writing. Peyman S and Millner P: review and editing.

3) Parts of **Chapter 7** appeared in the following publication: The trimeric autotransporter adhesin YadA of *Yersinia enterocolitica* serotype O:9 binds glycan moieties, 2022, Meuskens I, **Leva-Bueno J**, Millner P, Schütz M, Peyman SA and Linke D.; Front. Microbiol, 12:738818.

Leva Bueno J contributed to the heparin-based biosensor for YadA$_{O:9}$-expressing bacteria and did respective data acquisition, methodology, data visualisation, draft writing and review.

I. Meuskens: data acquisition and visualization, methodology, writing of the original draft, and project conceptualization. Millner P, Schütz M and Peyman S: conceptualization, draft review and editing. Linke D: project administration, project conceptualization, draft writing and editing.

4) **Section 5.2.4** in **Chapter 5** appeared in the following publication: Reagentless Affimer- and antibody-based impedimetric biosensors for CEA-detection using a novel non-conducting polymer, 2021, Shamsuddin SH, Gibson TH, Tomlinson DC, David MJ, Jayne G, Millner PA.; Biosensors and Bioelectronics, 178:113013.

Leva Bueno J: electrochemical data acquisition and technical assistance of some non-conducting POc behaviour.

Shamsuddin S: conceptualization, methodology, validation, formal analysis, investigation and original draft. Gibson T: methodology, formal analysis, resources, review and editing. Tomlinson D: resources and supervision. McPherson M: resources, supervision, review and editing. Jayne D: resources, supervision. Millner P: conceptualization, methodology, validation, resources, supervision, review and editing.

5) Parts of **Chapter 6** appeared in the following publication: A novel, proof-of-concept electrochemical impedimetric biosensor based on extracellular matrix protein-adhesin interaction, 2022, **Juan Leva Bueno**, Ina Meuskens, Dirk Linke, Paul A. Millner and Sally A. Peyman; Sens. Diagn., *in the press*. DOI:10.1039/d2sd00075j

Leva Bueno J: investigation, writing original draft and visualisation except for the fluorescence assay.

Meuskens I: validation and visualisation of fluorescence assay. Writing parts of original draft. Linke D: conceptualisation, supervision, review. Millner P: conceptualisation, supervision, project administration, review and editing. Peyman S: conceptualisation, supervision, project administration, review and editing.

"**Don't judge each day by the harvest you reap but by the seeds that you plant."**

-Robert Louis Stevenson

Acknowledgements

First, I would like to express my sincerest gratitude to the European Union’s Horizon 2020 Research and Innovation Programme under the Marie Skłodowska-Curie grant for sponsoring my PhD studentship. Without it, the ViBrANT consortium would have never existed.

I want to give a huge thank you to my supervisors, Prof. Paul A Millner and Dr Sally A Peyman, for their excellent guidance, their continual proximity and for letting creativity be a big part of the research. I would like to especially acknowledge your patience, in particular with the “Spanglish”. I could not have been better supported after all the challenges faced throughout this project. To Prof. Millner for his out-of-work hours at the Bioincubator or from the Lakes, teaching far beyond good science: about life. To Dr Sally A Peyman for her excellent advice and supervision, and for being especially supportive when most needed.

Big thanks to Prof. Dirk Linke and Early-Stage Researcher Ina Meuskens. Especially to Ina Meuskens: thanks for being the best collaborator I could ever have. For understanding that the benefits of science are above all of us. That ego can only be a barrier and that collaboration is always worth it, no matter whether your name is or is not on an author list or which position it has. I hope our philosophical conversations, beers, and friendship will last forever. I am glad to have taken part in the ViBrANT consortium and to have met all ESR colleagues and members of it. A special thanks to project officer Pirjo Johnson for the exceptional management, extraordinary kindness and excellent manners. Big thanks to Dr Timothy Gibson and Mr Duncan Sharp for sharing their expertise on electrochemical biosensors, which were extremely helpful throughout my PhD. Many thanks to Tim, Declan, Emma, Sarah, Arindam, Eiman, Kaniz and Shazana, who made my stay in the Bioincubator a remarkable journey. Sharing lab, office, and some drinks with you made my time more enjoyable.

My journey in Leeds would not have been the same if I hadn’t been recommenced to play tennis with Prof. Christos Pliotas. It was a pleasure to meet you and to spend hours playing our favourite sport.

My secondments in Hull would have been different if I had not met Lisandro, whom I hope to keep in touch with forever.

Despite not participating in my PhD, I would like to thank Prof. Arben Merkoçi and Dr Lorenzo Russo. To Prof. Merkoçi, for allowing me to enter into the biosensing world during my BSc and MSc. To Dr Russo, for his excellent supervision and mentoring during my BSc and MSc, which made me not question enrolling on a PhD journey. You all played an essential role in my life by then, and you still are. Thanks.

It is important for me to acknowledge and thank all school and high school teachers I had that positively contributed to my early formation, especially to Manuel Arce.

Big thanks to all the friends I made during my journey and my friends back in Spain, who have unconditionally supported me.

This journey would not be the same without Joe. I am very proud to have met you as one of my closest friends. You have been the best lockdown partner I could ever have. A big thanks to you and to the Dooley family.

A big thanks to Rita, Lisa and Harry. You have also been important to me during this journey.

Finally, I would like to have the most sincere thanks to the following people.

To Shannon Amy Jenkins. For giving the best support, help and love that I could ever ask for.

To my parents, grandmother and my sister. You are the pillars of my life.

Abstract

Antibiotic resistance is rising and presents an increasing health risk for humans. The selection of effective antibiotic treatment is essential, and rapid diagnostic tools are of the utmost importance. Biosensors have been developed in the past decades and can compete with other current diagnostics. Electrochemical impedance biosensors provide excellent sensitivity, are label-free and rapid, making them ideal for commercialisation. Bioreceptor selection is essential for biosensor fabrication and relies upon the specificity and affinity for the target analyte. The most commonly used bioreceptors are antibodies whilst other common bioreceptors are artificial affinity proteins, oligonucleotides and molecularly imprinted polymers. Extracellular matrix (ECM) proteins could provide detection of groups of pathogens that express adhesins and have not been widely studied in this context. In this project, collagen, an ECM protein, was used to target adhesin-expressing bacteria as bioreceptors within an electrochemical biosensor. Two collagen-based electrochemical biosensors, prepared using different fabrication routes, were studied for their capability to capture whole bacterial cells through a collagen-binding to recombinant *E. coli* expressing the adhesin YadA. Cyclic voltammetry and electrochemical impedance spectroscopy were employed for biosensor characterisation and to assess the bacterial binding, corroborated by fluorescent binding assays. A collagen-polymer matrix-based biosensor was first developed and detected bacteria over the concentration range 8×10^5 cfu to 8×10^7 cfu in a 10 µL sample. Then, a second step-by-step, fully optimised biosensor was studied based on direct collagen attachment to a polymer-coated electrode, shown to detect bacteria over 8×10^4 cfu to 8×10^7cfu in a 10 µL sample. To conclude, this work has shown that ECM proteins can be used as a bioreceptor for pathogenic bacteria capture. Further development is needed for a fully optimised device.

Table of contents

Chapter 3: Pretreatment effects in two different commercial screen-printed gold electrodes over various surface coatings 90

List of Figures

List of Tables

List of Equations

Abbreviations

2-MEA	2-mercaptoethylamine HCl
3 MPA	3-mercaptopropionic acid
Ad5	Adenovirus type 5
AFM	Atomic force microscopy
AMR	Antimicrobial resistance
AuNPs	Gold nanoparticles
CC	Chronocoulometry
C_{dl}	Double layer capacitance
cfu	Colony-forming unit
CPE	Constant phase element
CV	Cyclic Voltammetry
diH_2O	Deionised water
DMSO	Dimethyl sulfoxide
DTSP	3-dithiobis-(sulfosuccinimidylpropionate)
ECL	Enhanced chemiluminescence
ECM	Extracellular matrix
EIA	Enzymes immunoassay
EIS	Electrochemical Impedance Spectroscopy
ePADs	Paper-based analytical devices
ESA	Electrochemical surface area
EUS	Epizootic ulcerative syndrome
GAG	Glycosaminoglycan
GOx	Glucose oxidase
GPMS	(3-glycidoxypropyl) trimethoxysilane
GWE	Gold wire electrodes
HA	Hyaluronic acid
HAU	Hemagglutination units
HER	Hydrogen evolution reaction
HOR	Hydrogen oxidation reaction
HRP	Horseradish peroxidase
IDAM	Interdigitated array microelectrode
ITO	Indium tin oxide

LB	Lysogeny broth
LOC	Lab-on-a-chip
LSV	Linear sweep voltammetry
MACA	Mercaptoacetic acid
MCH	Mercaptohexanol
MDR	Multidrug-resistant
MNAC	Magnetic nanoparticle-antibody conjugate
MPA	Mercaptopropionic acid
MSNTs	Magnetic silica nanotubes
NHS	N-hydroxysuccinimide ester
OM	Octadecyl-mercaptan
PANI	Polyaniline
PBS	Phosphate buffer
PC	Polycarbonate
PDMS	Polydimethylsiloxane
PDX	Powder X-ray diffraction
PEDOT	Poly(3,4-ethylenedioxythiophene)
PEI	Polyethyleneimine
PFGE	Pulse-field electrophoresis
PMMA	Polymethylmethacrylate
POc	Polyoctopamine
POC	Point-of-care
PPy	Polypyrrole
Ptyr	Polytyramine
PPV	Plum pox virus
QCM	Quartz crystal microbalance
R_{ct}	Charge transfer resistance
rGOP	Reduced graphene oxide paper
Rs	Solution resistance
SAM	Self-assembled monolayer
SERS	Surface-enhanced Raman scattering
SPE	Screen-printed electrode
SPCE	Screen-printed carbon electrode

SPGE	Screen-printed gold electrode
SPIMs	Screen-printed interdigitated microelectrodes
TAA	Trimeric autotransporter adhesin
TCEP	Tris (2-carboxyethyl) phosphine
Vn	Vitronectin
YadA	*Yersinia* adhesin A
$\|Z\|$	Impedance *modulus*
Z’	Real impedance
Z’’	Imaginary impedance
W	Warburg impedance
WGA	Wheat germ agglutinin
WE	Working electrode
WGM	Whispering-gallery microgravity

Chapter 1

Introduction

Chapter 1: Introduction

1.1. Overview

Antibiotics, since their discovery in the 20th century, have been the primary approach to treating bacterial infection. Modern medicine, such as organ transplantation, cancer therapy or surgeries, needs adequate antibiotics to control bacterial infections. However, antimicrobial resistance (AMR) has appeared due to multidrug-resistant (MDR) bacteria. The irresponsible prescribing of antibiotics and lack of new antibiotic development have led to their appearance (Laxminarayan et al., 2013; Aslam et al., 2018). The over-prescription leads to a reduction in bacterial strains that would otherwise compete with MDR bacteria and keep their numbers under control, leaving them to become dominant.

Antibiotic resistance has been declared global health emergency by leading healthcare organisations worldwide, such as the Centers for Disease Control and Prevention (CDC), the Infectious Disease Society of America, and the WHO (Aslam et al., 2018). According to O'Neill's report, the AMR problem is estimated to put at risk around 10 million people and will cause costs of 100 trillion USD (O'neill, 2016). Some studies revealed that around 30 % to 50 % of the antibiotic treatments are inadequate in the USA, and about 99,000 annual deaths are caused by antibiotic-resistant hospital-acquired infections (HAIs) (Aslam et al., 2018). For these reasons, microorganism early detection is essential to provide efficient treatment and fight against MDR bacteria.

Colony counting, enzyme-linked immunosorbent assay (ELISA), microscopy, polymerase chain reaction (PCT), multiple-tube fermentation (MTF), surface-enhanced Raman scattering (SERS), and others are currently employed techniques in bacterial diagnostics. ELISA and other immunoassays methods can specifically detect epitopes found on the bacteria's surface. Still, these methods can be expensive and time-consuming, showing cross-reactivity and narrow detection ranges. Microscopy can be convenient to assess morphological features but can also be time-consuming and less sensitive than other techniques. MTF filters a sample of water, concentrates the bacterial cells and incubates them prior to detection. The MTF test depends on bacterial growth and can take up to 96 h. PCR shows highly specific detection and is adequate for small samples but lacks reliability due to false positives. Finally, SERS typically requires expensive and sophisticated laser equipment (Sakamoto et al., 2018; Zhao, Li & Xu, 2018; Joung et al., 2012; Croxen et al., 2013; Douterelo et al., 2014; Zhao, Li & Xu, 2018). These mentioned techniques provide excellent sensitivity and selectivity. However, as previously said, 30 % to 50 % of antibiotic treatments are inadequate in the USA (O'neill, 2016). Moreover, critically ill patients from infections would need an accurate fast antibiotic response, a delay of which could result in increased mortality, longer stays and a rise in morbidity (Dellinger et al., 2013).

Therefore, the need for a rapid diagnostic test to start treatment before a more time-consuming technique to test the exact species is of the utmost importance.

Early-stage fast diagnostics technologies such as lab-on-a-chip (LOC) devices and biosensors have arisen in the past two decades to solve these complications. Biosensing technology offers highly sensitive analyte detection and quantification with cheaper ease-of-use devices, allowing rapid testing. For instance, impedimetric biosensors apply electrochemical impedance spectroscopy (EIS) to monitor the binding between the bioreceptor and the analyte, providing excellent selectivity and sensitivity. In the impedimetric biosensors case, pre-enrichment steps are not required, thus affording low-cost and miniaturisation.

Commonly, antibodies, proteins, oligonucleotides, and others have been employed for pathogen detection in impedimetric biosensors. In this project, another alternative for a bioreceptor has been studied: using extracellular matrix (ECM) proteins as a bioreceptor to capture whole bacteria based on the ECM protein-adhesin interaction.The biosensors developed in this study employed EIS as the primary detection technique of the whole pathogen over commercial screen-printed gold electrodes (SPGEs). SPGE was chosen as the ideal transduction platform as a model for medical and user-friendly easy handling.

Initially, a step-by-step optimisation of an immunosensor against *E. coli* was investigated, which corresponded to the first stages of the PhD project. This research can be found in **Chapter 4** and it aimed to gain experience employing characterisation and analytical techniques such as CV, EIS and microbiological methods. In addition, the fabricated immunosensor would be later compared to the novel ECM protein-adhesin-based biosensor, which was the main objective of the PhD project.

Then, two biosensors were investigated to determine bacterial adhesion using collagen binding to adhesins recombinantly expressed in *E. coli*. First, a biosensor was developed to prove collagen-adhesin binding through EIS. The electrode surface was coated with a collagen-polymer matrix, employed as a bioreceptor to capture whole bacteria. The second biosensor was fully optimised in which the collagen was directly attached to the polymer-coated electrode. This research can be found in **Chapter 6** and published in (Leva-Bueno et al., 2022). Miniaturisation, portability and compatibility of the biosensor were attempted by the biosensor integration into a microfluidic device and can be found in **Chapter 7**.

Despite the ECM protein-adhesin-based biosensor being the main objective of the PhD project, other relevant studies were carried out. For example, another impedimetric biosensor was developed to demonstrate that the YadA$_{O:9}$-expressing bacteria direct binds to heparin. This research belongs to a collaboration with Early-Stage Researcher (PhD student) Ina Meuskens and

Prof. Dirk Linke, both part of ITN ViBrANT based at the University of Oslo. Part of this collaborative research can be found in **Chapter 7** and published in (Meuskens et al., 2022).

Finally, **Chapter 3** evaluated the electrochemical stability and reproducibility of two commercial SPGEs after different electrode pretreatments for different surface coatings.

1.2. Biosensors

1.2.1. Overview

Several biosensor definitions can be found in the literature. A biosensor is typically defined as a compact analytical device that uses a biological recognition agent that detects and quantifies biological target analytes. Biosensors are usually composed of three main elements: a biological receptor, usually antibodies, DNA or enzymes, that specifically targets the biological analyte; a transducer, which converts the biological recognition into a quantifiable signal and a signal processing display (Yoo & Lee, 2010; Rushworth et al., 2013) (**Figure 1.1**).

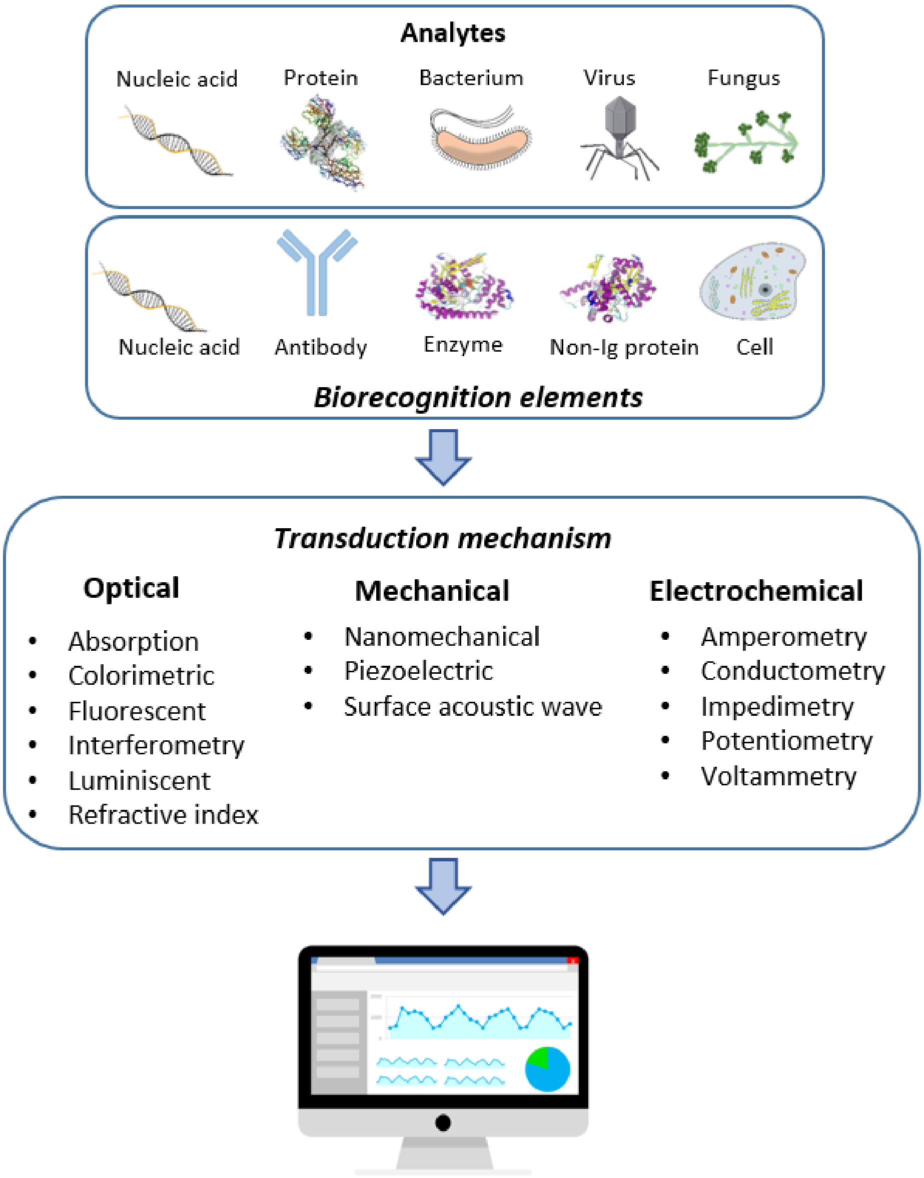

Figure 1.1: Types of biosensor platforms scheme. A general biosensor types overview. Different biorecognition elements and transduction mechanisms are possible. Some images are reproduced from CSIRO ScienceImage.

The first biosensor was developed in 1962 (Clark & Lyons, 1962) that electrochemically detected glucose levels in the blood. Glucose oxidase catalyses glucose oxidation, and the resulting H_2O_2 was monitored by the biosensor through the current change at the working electrode. Since then, electrochemical biosensors have drawn different research areas' attention given their high sensitivity, possible miniaturisation and easy manipulation. Medical applications have been one of the most common applications for the development of biosensors. Biosensors can detect and quantify pathogens in fluids such as blood, urine and saliva (Oblath et al., 2013; Chowdhury et al., 2018). Implantable biosensors for different monitoring uses, such as glucose, are already used nowadays (Wilson & Gifford, 2005).

Biosensors are classified according to their transduction mechanism or bioreceptor. Biosensors employing antibodies as bioreceptors are called immunosensors. Antibodies are the most employed bioreceptor type; specific analytes are targeted given their highly specific non-covalent interaction between antibodies and antigens (van Oss *et* al., 2002). Three main categories classifying biosensors according to their transduction mechanism are mechanical, optical and electrochemical (Monošík et al., 2012). Electrochemical biosensors are generally subdivided into potentiometric, amperometric and impedimetric (Yan et al., 2011).

1.2.2. Mechanical

Mechanical biosensors, also known as gravimetric biosensors, detect alterations in the surface properties upon bioreceptor-analyte binding. Gravimetric biosensors commonly use thin piezoelectric quartz crystals that vibrate at a specific frequency depending on the material detected mass and the applied current. The most widely employed types of gravimetric biosensors for biological sample detection and identification are quartz crystal microbalance (QCM), piezoelectric-based biosensors and magnetoelastic-based (MES) biosensors. Gravimetric biosensors mainly offer a sensitive, fast, label-free, real-time diagnostics, specifically for macro-biomolecule and whole cell detection compared to less sensitive small biomolecule detection (Naresh & Lee, 2021).

The piezoelectric-based biosensors are used with a crystal coated with the bioreceptor element that is elastically deformed after the potential or current application. A wave in the crystal is created by the application of an alternating electric field at a specific frequency. This frequency changes upon analyte binging and provides information on the analyte-bioreceptor recognition. The piezoelectric principle is applied to QCM biosensors. The differentiative QMC component is a quartz disc placed between two electrodes. The application of an external electrical field generates mechanical stresses in the crystal. Applying a voltage to the disk makes it oscillate perpendicular to the surface of the plate. The crystal oscillation takes place at a specific resonant frequency at series resonance. A change in the resonance frequency occurs upon the analyte-bioreceptor interaction and allows detection and quantification (Jean et al., 2020; Naresh & Lee, 2021). These biosensors are popular for their label-free detection of pathogens. That is the case of the *Mycobacterium tuberculosis* (*Mtb*), responsible for causing the disease of tuberculosis. Different QCM biosensors have been developed for tuberculosis diagnostics: for the whole *Mtb* cell detection (He et al., 2002) and for the bacterial antigens (Hiatt & Cliffel, 2012). (Hiatt & Cliffel, 2012) developed a QCM immunosensor for *Mtb* whole cell detection. They reached the detection of 8.7×10^5 cfu/mL. Other pathogenic QCM biosensors detected malaria (Wangmaung et al., 2014), dengue (Chen et al., 2009), and Hepatitis B (Yao et al., 2013). Several examples of QCM biosensors for pathogen detection can be found in the literature (Jean et al., 2020).

The MES biosensor's working principle is magnetostriction, in which the application of a magnetic field causes a mechanical deformation. The variation of the magnetic field generates magnetoelastic vibrations that make the field-generated strain change with time. As a result, longitudinal elastic waves are created, and they produce perceptible magnetic flux. MES biosensors are convenient for biomedical applications as they present a long lifetime, are wireless, small in size, and have lower costs than other mechanical techniques (Naresh & Lee, 2021). An example of a magnetoelastic biosensor detected *Salmonella typhimurium* in food samples. The bacterial binding to the polyclonal antibodies generated a change in the resonance parameters, which created a shift in the resonance frequency that allowed the bacteria detection and quantification. The bacteria could be detected at $5x10^3$ cfu/mL in water samples (Guntupalli et al., 2007).

1.2.3. Optical

Optical biosensors are excellent tools for diagnostics in biomedical research. Different variables need to be considered for their fabrication, such as the transduction signal generation, the fluidics designs, the surface immobilisation chemistry, the detection format and the data analysis. Based on their optical properties, there are mainly two types of visual biosensing detections: labelled and label-free. Labelled detection includes fluorescence. Fluorescence-based detection employs fluorescence-tagged biorecognition molecules or target molecules. The fluorescence intensity provides information about the analyte presence in the sample and the interaction strength between the analyte and the bioreceptor. Fluorescence-based detection is susceptible and can reach a single molecule's detection limits. However, the number of fluorophores on the tagged molecules cannot be controlled with detailed accuracy, making quantitative detection challenging. In addition, the labelling process can be time-consuming, arduous and expensive and require sophisticated instrumentation and space. Labelled detection is widely used in structural biology (Raghuraman et al., 2019; Naresh & Lee, 2021), biochemical assays (Nishi et al., 2015) and diagnostic imaging (Detante et al., 2012).

In the case of label-free detection, no labelling is required for target molecules. As a result, faster and cheaper optical biosensors can be developed. Label-free biosensors present excellent quantitative detection and measurement of molecular interaction kinetics. Surface plasmon resonance (SPR), SERS and interferometer-based biosensors are among the most employed label-free biosensors. The SPR occurs when photons reach a metallic surface at an angle of incidence. Some of the energy coming from the photons couples with the electrons at the metallic exterior and causes movement due to the excitation. The electron movements are called plasmon (Nguyen et al., 2015). SPR has been extensively studied to assess the change of refractive index (RI) upon target molecule binding: a modification in the reflected light and the SPR angle indicates a difference in the RI. The change in RI is associated with the sample concentration rather than the total sample mass. This phenomenon is especially advantageous for small detection volumes in the order of nanoliter to femtoliter (Shrivastav, Cvelbar & Abdulhalim, 2021). Pathogenic detection through SPR has been studied for a wide range of pathogens: *E. coli* was detected upon monoclonal antibodies attached to alkanethiol self-assembled monolayers (SAMs) over gold surface, reaching an LOD of 10^4 cfu/mL (Taylor et al., 2005); *Salmonella typhimurium* was detected up to a concentration of 10^6 cfu/mL in chicken carcass samples (Lan et al., 2008); *Listeria monocytogenes* was detected down to 2×10^6 cfu/mL through SPR employing a phage-display antibody (Nanduri et al., 2007) and many other pathogen detections that can be found in the literature (Fan et al., 2008; Park et al., 2022).

1.2.4. Electrochemical

Several definitions of electrochemistry can be found in the literature. Electrochemistry is typically defined as the chemistry branch which interrelates chemical and electrical reactivity (Bard & Faulkner, 2001). Nowadays, electrochemical transduction appears to be one of the most abundant because of ease-of-use, fast analysis, low-cost and the possibility of system miniaturisation. An electrochemical biosensor monitors the electrode surface, where electrons flow between the surface and the electrolytes in the solution. The alterations occurring at the electrode's surface are monitored through mass transfer from the bulk solution to the electrode's surface, electrolyte resistance, capacitance change or charge transfer resistance. Electrochemical biosensors typically have three main transduction mechanisms: potentiometric, amperometric and impedimetric (M. Barreiros dos Santos et al., 2013).

1.2.4.1. Potentiometric sensors

The potentiometric transduction mechanism determines, at zero current, the potential at the working electrode with respect to the reference electrode. Under equilibrium, the measurement occurs when no current flows through the electrochemical cell. These biosensors are employed to measure ion concentrations over the electrode surface. Different biorecognition elements, mostly enzymes, along with the transduction element, can monitor the uptake or release of ions while enzymes act on their target. The most common measured ions are H^+ or NH_4^+ although others such as Na^+, K^+ and Ca^{+2} are also widely assessed (Chaubey & Malhotra, 2002; Grieshaber et al., 2008; Pisoschi, 2016). The free ion concentration and the potential relationship are calculated through the Nernst equation (**Equation 1.1**).

$$\boldsymbol{E_{cell} = E^0_{cell} - \frac{RT}{nF}\ln Q} \qquad \textbf{Equation 1.1}$$

Where,

E_{cell} is the cell potential,

E^0_{cell}, the standard cell potential,

R, the universal gas constant,

T, the temperature,

n, the charge number of electrode reaction,

F, the Faraday constant and

Q, the ratio of ion concentrations between cathode and anode.

In the case of voltammetric biosensors, the current is measured after applying a varied potential. The three most common voltammetry techniques are potential step, linear sweep, and cyclic voltammetry (CV). CV and EIS are the most employed techniques in this project. CV results are helpful for biosensor fabrication by polymer electrodeposition and for biosensor characterisation (Barlett & Cooper, 1993; Chaubey & Malhotra, 2002)

1.2.4.2. Amperometric sensors

Typically, amperometric biosensors monitor the current at a constant potential. The glucose biosensor was the first practical amperometric biosensor. The depletion of oxygen and the change in current was measured by the enzyme-catalysed reaction of glucose oxidase (GOx) (**Scheme 1.1**) (Clark & Lyons, 1962; Weltin, Kieninger & Urban, 2016). These biosensors are called first-generation glucose biosensors and use oxygen as a cosubstrate and generate hydrogen peroxide, which is then detected by oxidation (**Scheme 1.2**) (Yoo & Lee, 2010). The disadvantage is the high potential (+0.7 V) needed to oxidise H_2O_2 since this will non-specifically oxidise other metabolites in the blood, such as ascorbate and urea (Sanzò et al., 2017).

Second-generation glucose biosensors use electron mediators to re-oxidise the Flavin cofactor within GOx, instead of oxygen. Electron mediators commonly used are ferrocene and potassium ferricyanide. Then, the reduced mediator is subsequently re-oxidised at the electrode surface in **Schemes 1.3 to 1.5** (Wang, 2001).

Third-generation glucose biosensors do not depend on an electron mediator, instead relying on direct electron exchange between the enzyme and the electrode. This allows for continuous readout and modern implantable sensors work this way (Yoo & Lee, 2010). This has allowed the development of an “artificial pancreas” where such sensors are linked to an insulin pump, allowing very close control over blood glucose (Breton et al., 2020). Recent advances enable glucose monitoring without enzymatic activity. They usually employ catalytic electrodes for glucose detection. Those electrodes are typically modified by etching, electrodeposition or electrochemical anodisation. These are the fourth-generation glucose biosensor (Metkar & Girigoswami, 2019).

$$\text{Glucose} + \text{Oxygen} \xleftrightarrow{\text{GOx}} \text{Gluconic acid} + \text{Hydrogen peroxide} \qquad \textbf{Scheme 1.1}$$

$$H_2O_2 \rightarrow O_2 + 2H^+ + 2e^- \qquad \textbf{Scheme 1.2}$$

$$\text{Glucose} + \text{GOx}_{(ox)} \rightarrow \text{Gluconic acid} + \text{GOx}_{(red)} \qquad \textbf{Scheme 1.3}$$

$$\text{GOx}_{(red)} + 2M_{(ox)} \rightarrow \text{GOx}_{(ox)} + 2M_{(red)} + 2H^+ \qquad \textbf{Scheme 1.4}$$

$$2M_{(red)} \rightarrow 2M_{(ox)} + 2\,e^- \qquad \textbf{Scheme 1.5}$$

In general, label-free amperometric biosensors are not possible. Usually, the biochemical reaction is catalysed by an oxidoreductase enzyme, which produces a change in current over the electrode surface proportional to the analyte concentration. Amperometric biosensors permit fast test response with high sensitivity, better than potentiometric biosensors (Nguyen et al., 2019). However, specific enzymes are required for amperometric biosensors (Vakurov et al., 2009) and these need to be robust and have rapid turnover to function efficiently. Commercial amperometric biosensors can detect and quantify the presence of glucose in animals and microbial cultures (Tothill et al., 1997), lactose, other metabolites (Hirst et al., 2013) and lipid molecules such as cholesterol (Chiang et al., 2011).

Faraday's Law (**Equation 1.2**) determine the relationship between analyte concentration and current produced:

$$\boldsymbol{I = n \cdot F \cdot A \cdot J} \qquad \textbf{Equation 1.2}$$

Where,

I is the current,

n the number of electrons transferred to the electrode,

F the Faraday constant,

A the area of the electrode and

J is the Flux coefficient.

1.2.4.3. Impedimetric sensors

Impedance is defined as the opposition to current flow in an electrical circuit. The difference between impedance and common resistance is that resistance appears in direct current (DC) circuits and obeys Ohm's law. In DC, there is no lag between the applied voltage and the generated current. However, impedance appears in alternating current (AC) circuits. There, capacitive and inductive effects are present, causing a lag in the voltage-current phase angle. In an impedimetric biosensor, the impedance consists of capacitive and resistive components that are a result of an interaction with a small amplitude voltage as a function of the frequency (J. Lin et al., 2015; Randviir & Banks, 2013).

Impedance biosensors are label-free and do not depend on any specific enzyme for analyte detection. Instead, they rely on a bioreceptor that specifically binds the analyte, such as antibodies (Conroy et al., 2009; Ahmed et al., 2013), DNA (Dinçkaya et al., 2011), aptamers (Song et al., 2008) and some synthetic affinity proteins such as Affimers (Tiede et al., 2014; Tiede et al., 2017).

1.3. Electrochemical impedance spectroscopy

1.3.1. Electrochemistry at the electrode surface

Different parameters are obtained after EIS application on biosensors. Bulk impedance (|Z|) can be divided into real and imaginary components, which are the resistive (Z') and the capacitive parts (-Z"), respectively (**Figure 1.2**). The origin of the resistive element is at the electrode surface as a result of the current flow opposition. The capacitive part measures the system's charge storage after a voltage application. There are two ways in which electricity can flow through the electrode at the electrode-solution interface: when electrons are transferred to the electrodes through redox reactions is called a faradaic process and behaves the Faraday's law; when no charge is transferred to the electrode's surface, and still, electricity can flow given the capacitor behaviour, it is called a non-faradaic process (Hou et al., 2013; Kokkinos et al., 2016).

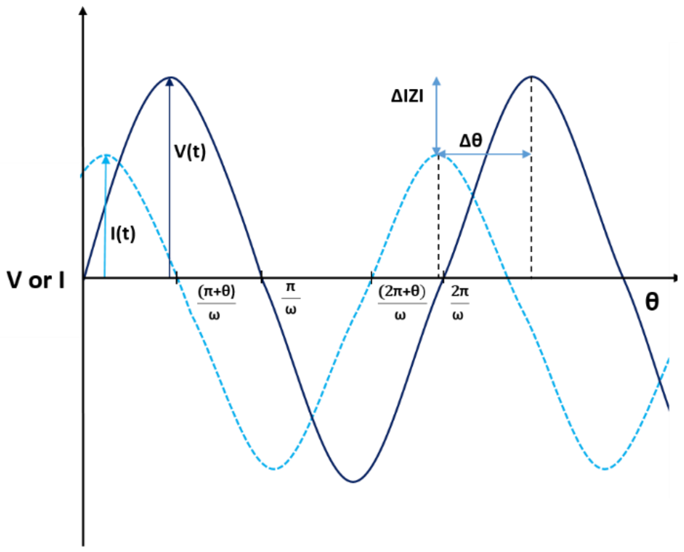

Figure 1.2: Phasor diagram scheme. A phasor diagram represented in the X and Y axes. A scheme about the change in phase angle (Δθ) and magnitude (|ΔZ|) when analyte binding occurs can be observed. In a pure resistor system, (I) and (V) are in-phase whereas they are separated by 90º phase shift in a pure capacitor. However, in a real biosensor, a change in (Δθ) between 0º to 90º with a variation in magnitude (|ΔZ|) occurs upon binding, which alters the AC voltage applied.

EIS consists of applying a low amplitude voltage sine wave to an electrochemical system over various frequencies. As a result, a phased current is obtained. Impedance is defined by the ratio between the applied voltage and the current (**Equation 1.3**). This ratio expresses the electron flow opposition by an electrical AC circuit. Impedimetric biosensors typically conclude with a bioreceptor-analyte interaction. This interaction modifies the electric field due to an alteration in the capacitance and the electron transfer resistance at the working electrode surface (Randviir & Banks, 2013).

$$\boldsymbol{Z(jw) = \frac{V(jw)}{I(jw)}} \qquad \textbf{Equation 1.3}$$

Where,
Z is the impedance,
V is the voltage,
I is the current,
j is the imaginary component and
ω is the frequency.

When the phase angle between current and voltage is zero, the impedance and resistance become the same, as in a purely metallic surface. However, the phase angle is different from zero in most real electrical circuits due to the capacitive and/or inductive effects. Faradaic impedimetric biosensors require immersing the electrode in an electron mediator solution. Common redox pairs are $[Fe(CN_6)]^{3-/4-}$ (ferricyanide/ferrocyanide), $[Ru(NH_3)_6]^{3+/2+}$ hexaammineruthenium (II/III) and ferrocene (Fc^+/Fc). Impedimetric non-faradaic biosensors measure impedance without a redox mediator (Rushworth et al., 2013).

Generally, the electrode’s surface is coated with a SAM or a polymeric layer. These coatings allow bioreceptor immobilisation, increase bio-stability, and develop a dielectric between the electrode surface and the media. SAM formation requires a molecularly flat surface, not usually provided in SPGE, which is fairly rough. Alternatively, conducting and non-conducting polymers are commonly electrodeposited onto metal surfaces. Polyaniline (PANI) or polypyrrole (PPy) are conducting polymers showing conductive or semi-conductive properties, and polytyramine (Ptyr) and polyoctopamine (POc) are non-conducting polymers offering high resistivity (Kokkinos et al., 2016; Bahadir & Sezgintürk, 2016).

As previously mentioned, two types of processes can take place at the electrode-electrolyte interface: faradaic or non-faradaic. A faradaic process allows the charge transfer across the electrode surface and manifests a reversible redox reaction under electrolytes in solution. This process behaves following Faraday’s law. In non-faradaic processes, a transient current flows through the electrode interface due to charge accumulation.

The diffusion phenomena usually takes place in electroanalytical processes when redox reaction kinetics are rapid at the electrode's surface. As a result, a gradient concentration of the analyte and other molecules between the bulk solution is created. Contrarily, the electrochemistry is kinetically controlled when the redox species diffusion is rapid (Kokkinos et al., 2016).

Electrostatically, the electrode will attract oppositely charged ions and concentrate them at the electrode interface. As a result, a double layer acting as a parallel-plate capacitor is created. The electrode surfaces' close region is the inner Helmholtz planes (IHP) which mainly consists of adsorbed ions and solvent molecules. The next layer, the outer Helmholtz plane (OHP), is repleted with non-specifically adsorbed ions (Thakur & Singh, 2008; Gschwend & Girault, 2020). The OHP is followed by diffuse layers, followed by bulk electrolyte, where the mass transport takes place (**Figure 1.3**).

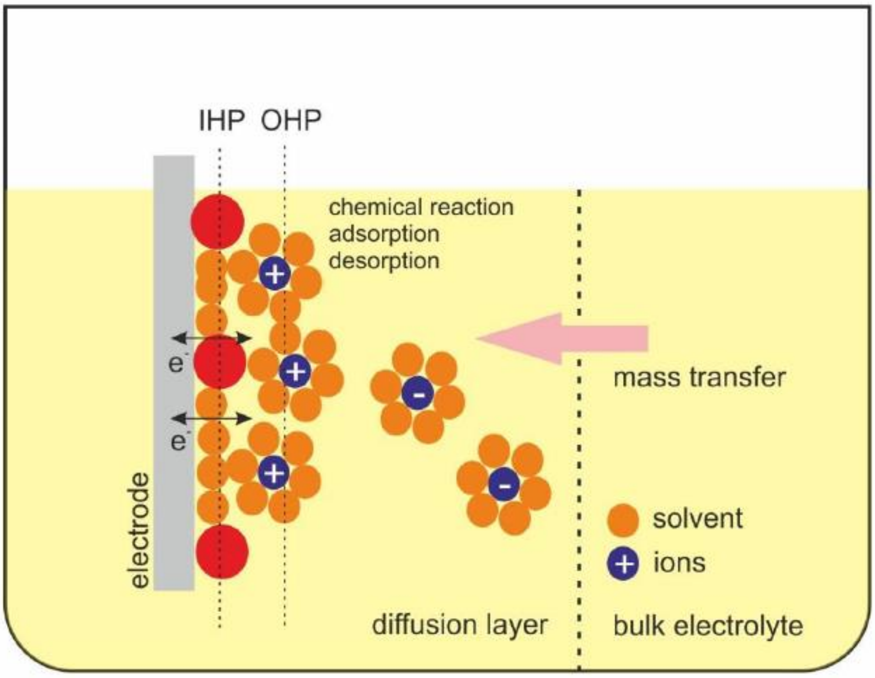

Figure 1.3: Schematic of electrical double layer and bulk electrolyte schematic of the electrode in the solution. The charged electrode surface electrostatically attracts oppositely charged ions and solvent molecules. As a result of the charge adsorption accumulation at the electrode-electrolyte interface, an electrical double layer is formed and composed of the compact layer, created by the IHP and OHP, and the diffuse layer. Reproduced from (Ahmed, 2015).

1.3.2. Equivalent circuit and data presentations

Nyquist and Bode’s plots are typical impedance formats presentation. **Figure 1.4A** shows a schematic of a Nyquist plot and its different components. The Nyquist plot shows an imaginary part of impedance (- Z”), out of phase, plotted against the real component of impedance, (Z’), in-phase and at each excitation frequency. It shows the relationship between the real and the imaginary components for a range of frequencies and is usually used to assess the resistive part of the biosensor. The Bode plot presents a variety of parameters such as the absolute impedance logarithm and shift (Θ) versus the log of excitation frequency and is usually used to determine the capacitive part (Guan et al., 2004; Alshaaer et al., 2017).

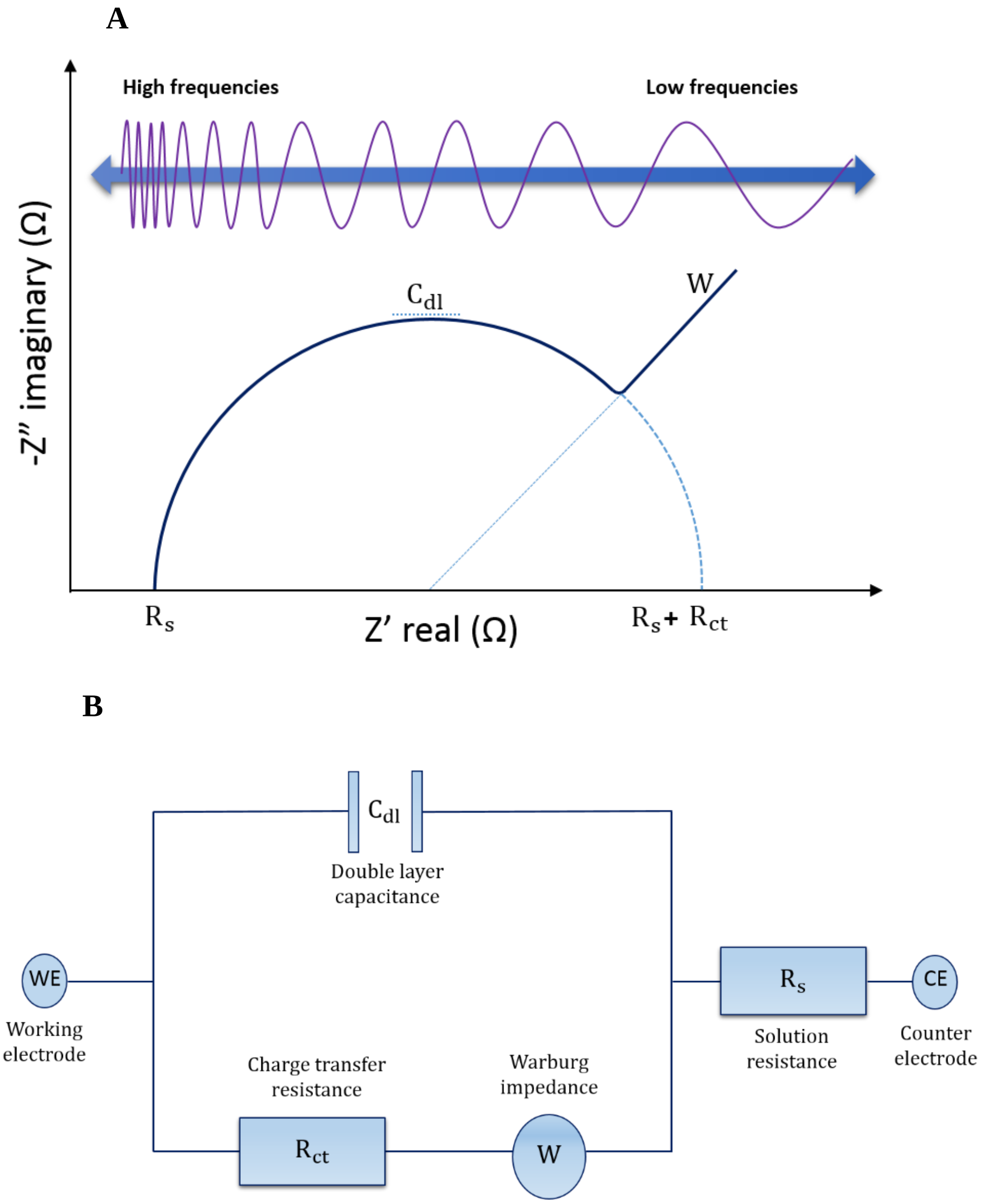

Figure 1.4: Nyquist plot and its Randles' equivalent circuit. A, The Nyquist plot arises after plotting the imaginary (capacitive) against real (resistive) components of impedance. Relevant parameters are charge transfer resistance R_{ct}; the resistance of the solution R_s; the maximum double-layer capacitance $C_{dl;}$ and the Warburg impedance W, only observed in faradaic sensors and represented mass transfer diffusion effects. **B**, Randles' equivalent circuit represents an electrical circuit modelling a faradaic sensor.

The system’s behaviour is different at high and low frequencies. At high frequencies, the signal is controlled by kinetic processes. The electron mediator molecules shift direction before the redox reaction occurs at the electrode surface. This event appears to be a limiting factor as it delays the charge transfer across the electrode, known as solution resistance (R_s). At medium frequencies, minimal resistance is found in the system. As a result, the changes occurring in the system are due to capacitance, mainly due to the double-layer capacitance (C_{dl}) formed at the electrode surface. The charge transfer is only produced from the biosensor construct at low frequencies. The resistance encountered by the electron mediators is due to the electrode surface components and is calculated through the charge transfer resistance (R_{ct}) (Lvovich, 2012).

Sometimes, impedance is manifested as a linear tail at the end of the Nyquist arc at low frequencies. This impedance is known as Warburg impedance (W) and appears due to diffusional limitations of the system when it runs out of charge carriers. A Randles’ equivalent circuit represents all these components and models the behaviour of a typical faradaic biosensor and a schematic of a Randles’ equivalent circuit is shown in **Figure 1.4B**. The main aim of faradaic measurements is to calculate the R_{ct} and the current flowing through the electrode surface. In non-faradaic measurements, a voltage at low frequencies is applied, generating current flow after capacitive component accumulation over the electrode surface (Kokkinos et al., 2016).

In most cases, the impedance value tends to increase with the complexity of the electrode functionalisation: electrons in solution find more impedance upon reaching the electrode surface. **Figure 1.5** illustrates a schematic about the impedimetric evolution after the deposition of material. However, a decrease in impedance can occur upon analyte binding, stretching the polymeric layer and facilitating the electron mediator access.

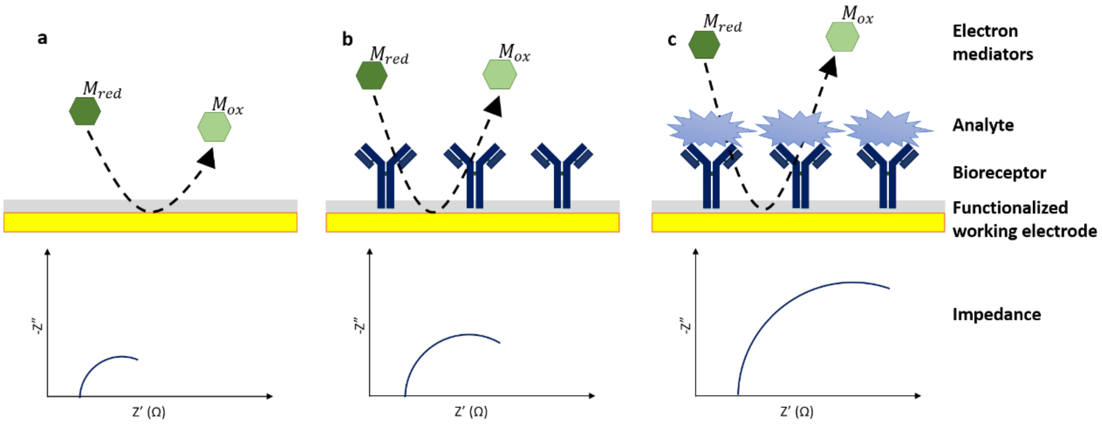

Figure 1.5: Scheme of impedance represented by Nyquist plot for each step of biosensor construction. The impedance magnitude of the systems increases with material deposition over the electrode surface. Material deposition onto the biosensor surface usually causes an increase in both resistance and capacitance, which obstruct the electron transfer between the solution-based mediators and the electrode surface. Therefore, impedance increases from (**a**) bare electrode when (**b**) bioreceptors are tethered and (**c**) increases upon analyte binding.

1.4. Cyclic voltammetry

Cyclic voltammetry (CV) measures the current obtained following a reversible voltage scan from which oxidation and reduction peaks can be derived. CV under $[Fe(CN)_6]^{3-/4-}$ redox pair, when the anodic potential becomes more positive, $[Fe(CN)_6]^{4-}$ starts to oxidise and accomplish a maximum current peak, which indicates completed oxidation. Next, a cathodic reversible scan is applied, and the reduction of the previous oxidation product $[Fe(CN)_6]^{3-}$ begins until the current reduction peak is accomplished (**Figure 1.6**).

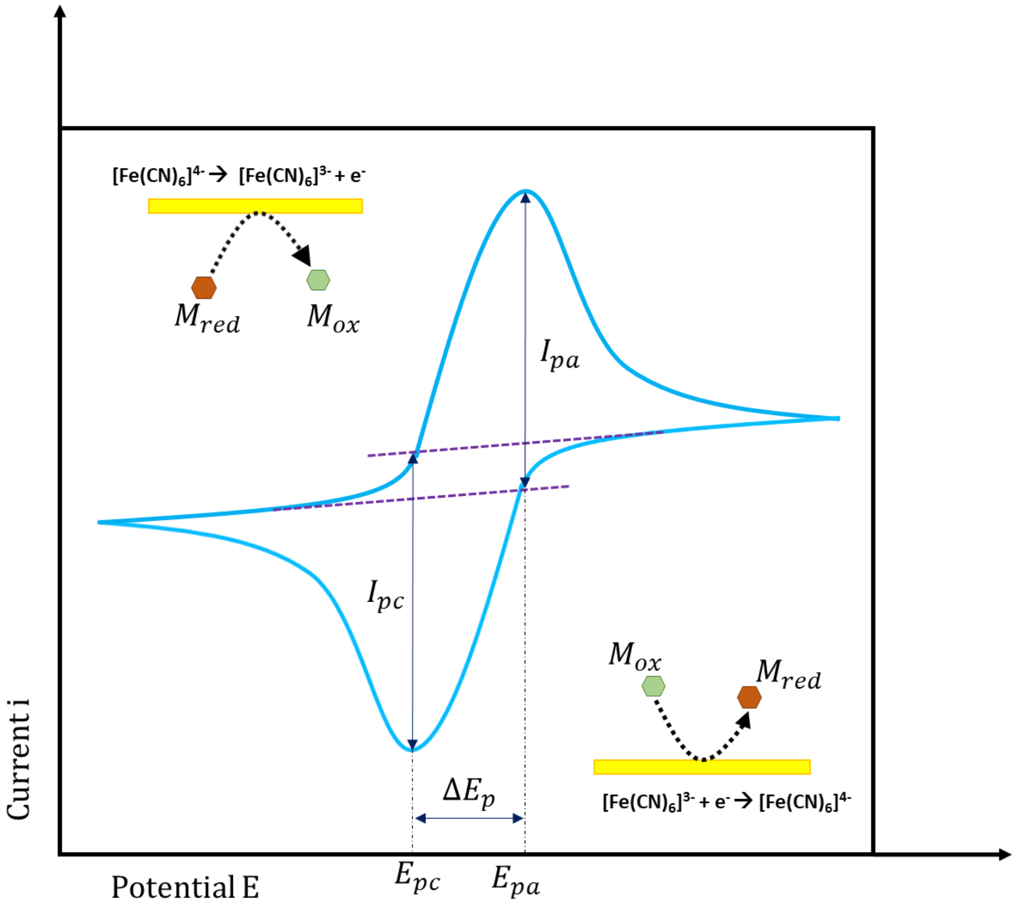

Figure 1.6: Reversible reaction cyclic voltammogram scheme $[Fe(CN)_6]^{3-/4-}$ redox pair. A typical redox reversible voltammogram scan is depicted under $[Fe(CN)_6]^{3-/4-}$ redox pair. I_{pa} represents the anodic peak current, and I_{pc} represents the cathodic peak current. The potential difference between the peak anodic (E_{pa}) and cathodic (E_{pc}) current is named as Δ_{Ep}.

1.5. Biosensors construction

1.5.1. Electrodes

The biosensor is regularly constructed onto a screen-printed electrode (SPE) consisting of a three-electrode system as the one shown in **Figure 1.7**, with a working counter and a reference electrode. The working electrodes act as a transduction element and are commonly made of conductive materials such as gold or carbon, where the bioreceptor will be tethered. Carbon is widely employed as it is cheap to mass-scale produce. Gold is chemically more stable than carbon and has well-studied chemical properties.

The counter electrode is usually made of the same composition as the working electrode. The counter electrode maintains a current flow between the counter and the working electrodes. The reference electrode sets the potential at the working electrode, and it is commonly made of Ag/AgCl, although other compositions such as $Hg/HgCl_2$ are also available. A three-electrode system can be printed on a single chip. Sometimes, more than one working electrode is incorporated to allow different bioreceptors (Bard & Faulkner, 2001).

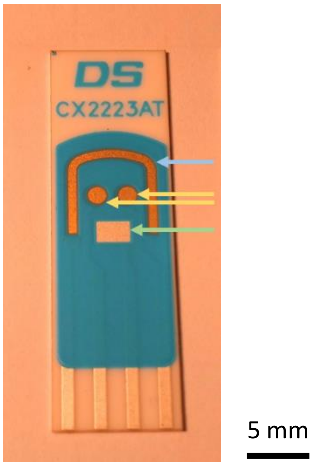

Figure 1.7: Metrohm DropSens CX2223AT screen-printed gold electrode. The chip contains two circular gold working electrodes, a gold counter electrode and a rectangular Ag/AgCl reference electrode, which are screen-printed onto a ceramic base. The blue material insulating the electrodes corresponds to the dielectric, preventing cross-connections. Four silver connectors at the bottom of the chip connect the chip to the potentiostat. Working (🟦), counter (🟨) and reference electrode (🟩).

1.5.2. Polymeric base layers

SAM or polymers are typically used to coat the surfaces of the electrodes. They provide an interface to allow a certain degree of bio-stability to immobilise bioreceptor molecules such as antibodies. These layers also create a dielectric between the surface and the media. Polymers are an alternative to SAM coatings which are incompatible with rough surfaces presented by SPGEs. Conducting and non-conducting polymers are both excellent base layers and are typically electrodeposited onto metallic surfaces, the thickness of which can be controlled. Some conducting polymers are polyaniline (PANi) or polypyrrole (PPy). They present conductive and semi-conductive properties. Non-conducting polymers such as Ptyr and POc (**Figure 1.8**) are employed in this project and offer high sensitivity and selectivity detection (Kokkinos et al., 2016; Bahadir & Sezgintürk, 2016).

Tyramine and octopamine are monomers from Ptyr and POc respectively and have similar structures. Ptyr has shown satisfactory performance as SPGE coating for bacterial-detecting biosensors. However, little has been found about POc-based biosensors for whole bacterial cell detection.

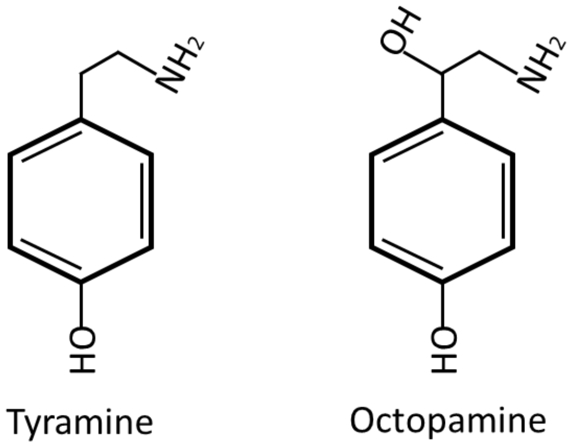

Figure 1.8: **Chemical structures of tyramine and octopamine**. Both monomeric structures are phenolamines, products of the decarboxylated amino acid tyrosine. Their monomers consist of a phenol ring and an amine moiety on the side chain, where octopamine has an extra hydroxyl group.

1.5.3. Bioreceptors

Typically, a bioreceptor molecule is attached to the biosensor's transducer surface. Upon bioreceptor-analyte binding, a change in the transducer surface can be electrochemically, optically or mechanically monitored. The bioreceptor selection is crucial for the biosensors fabrication route and strongly relies on the specificity and affinity of the target analyte. Different analytes can be detected, from small biomolecules to entire viruses or bacterial cells. The use of antibodies as bioreceptor is built upon the antibody-antigen interaction and is the gold standard bioreceptor for pathogen determination (Birch & Racher, 2006). Abundant reports of immunosensors for pathogen detection can be found in the literature. This is the case in recent reviews for either general biosensors (Chen et al., 2018) or electrochemical sensors (Cesewski & Johnson, 2020).

Different bioreceptors used for pathogen detection than antibodies are oligonucleotides, DNA or RNA, which are extensively employed. Some examples can be found in the review by (Wu et al., 2019). Other bioreceptors types include proteins such as lectins (Xi et al., 2011); phage as those used for bacterial determination employing T4 bacteriophages (Shabani et al., 2008) and sol-gel bacterial imprinted films employed for *E. coli* impedimetric detection (Jafari et al., 2019). Adopting ECM proteins for pathogenic detection offers a cheaper option than other bioreceptors such as antibodies. Pathogen detection is based on the ECM protein-adhesin interactions. These adhesins are expressed and present on the bacterial surface. Although some studies have reported their use for toxin detection (Xia et al., 2017), pathogen detection through ECM proteins has not been extensively studied.

1.6. Gold electrode pretreatment

1.6.1. Overview

For decades, gold as a substrate has been widely employed in many techniques including molecule or ion recognition, electron transfer, catalysis, and surface investigation requiring stability such as SPR, voltammetry, EIS and molecular self-assembly (Carvalhal et al., 2005). Gold presents noble metal properties, high electrical and thermal conductivity, and exceptional corrosion resistance. Gold surfaces are an appropriate scaffold for SAMs and polymeric coatings. These coatings can then be employed for coupling molecules, antibodies and nanoparticles (Hoogvliet et al., 2000). Pathogen detection can also directly take place over the gold substrate by tethering enzymes, antibodies or other molecules onto the gold surface. Before SAM formation, pretreatment of the gold surface has to be performed, which determines the surface state and properties, including the contaminant removal, topographical characteristics such as roughness and the system's reproducibility. Thiol-DNA modified SAMs and oligopeptide-SAMs are all gold surface interface types. Generally, different gold surface pretreatments are used, although general patterns can be observed. Usually, a starting alumina or diamond mechanical polishing is carried out. Then, the pretreatment is followed by oxidising chemical methods such as applying *aqua regia* (HNO_3 + 3 HCl) or "piranha solution" (H_2SO_4 + H_2O_2) to remove organic contaminants. Finally, chemical or electrochemical pretreatments eliminate the gold oxide layer previously formed by oxidising techniques. Other techniques are also employed and combined: annealing, ethanol, UV/O_3 and oxygen plasma (Dutta et al., 2012).

Reproducibility is one of the most relevant parameters when developing a biosensor. This is especially valuable in producing biosensors on a large scale. The topographical and chemical properties of the electrodes are directly connected to the pretreatment, which may affect the sensor's stability and quality (St et al., 2019). Another important consideration is the exposure to non-clean room conditions, where electrodes are exposed to contamination. Electrode contamination can alter thiols' binding kinetics, for instance, and other electrochemical events (Kang & Rowntree, 2007).

Some electrochemical techniques, particularly EIS and CV, appear suitable to assess the state of the gold surface after undergoing different pretreatments. CV can be beneficial as other features can be obtained from the CV voltammogram. These are the hydrogen evolution reaction/hydrogen oxidation reaction (HER/HOR) region, the gold oxide formation and reduction, and the electrochemical double layer (EDL) charging region (Xu et al., 2019).

Voltammograms derived from CV measurements can be established as fingerprints for many materials and different states. Particularly in the case of gold, its CV voltammogram can be employed to point crystal faces out (Hamelin, 1996). In addition, CV and other voltammetry techniques are used to perform reductive desorption of alkanethiolates from a gold electrode surface under an alkaline solution **(Equation 1.4)**.

$$RS - Au_{(s)} + e^- \rightarrow RS^- + Au_{(s)}$$ **Equation 1.4**

EIS provides physical impedance and capacitive components information whilst microscopy techniques such as SEM, AFM and STM are also commonly employed and provide information about the gold surface's topographical state, such as roughness. SEM is used to study the macroscopic roughness, whereas AFM is more employed to assess the microscopic roughness (Bernalte et al., 2013). Furthermore, SEM and STM can determine the appearance of gold crystal boundaries and microscopic roughness (Creager et al., 1992). X-ray photoelectron spectroscopy (XPS) provides information about the surface composition. The electronic and chemical state and elemental composition can be determined. Gold oxide or hydrous layers have been detected over the gold surface through XPS (Izumi et al., 1991). Other employed techniques, although less common, are powder X-ray diffraction (PDX) and contact angle (Enomoto et al., 2018) measurement.

SAM research was mainly started in the 1980s when relevant investigations from Nuzzo & Allara, (1983) were reported. They achieved self-assembled organic-oriented molecules in monolayers and it was thought that SAMs could be employed for diverse applications. This is the case for alkanethiol SAMs which are commonly formed over a gold surface (Widrig et al., 1991). The kinetics of the monolayer self-assembly depends on temperature, alkane length, alkanethiol concentration, gold electrode’s structure and state, the adsorption reversibility and the reaction rate with the surface (Bain et al., 1989). Therefore, it is of great relevance to perform preliminary research on the gold surface pretreatment before any further surface functionalisation. An inappropriate pretreatment could damage the surface or create undesirable modifications such as oxide layers (Yang et al., 1995).

1.6.2. Bare gold electrode pretreatment

General research on gold surface pretreatment for electrochemical purposes was carried out by (Fischer et al., 2009). Nine pretreatments were performed over the gold electrode and subsequently characterised through CV, EIS, XPS and AFM. These pretreatments were CV in H_2SO_4; UV/O_3 photoreactor; KOH–H_2O_2; KOH potential sweep; CV in HCl; H_2SO_4 + H_2O_2; dimethylamine borane reducing agent solutions at 25 and 65 °C; and a dilute form of *aqua regia*. The study indicated that the cleanest surfaces were pretreated with KOH + H_2O_2 and KOH sweep method. Standard CVs in H_2SO_4 left an acceptable surface, although less clean than other methods. Gold surface pretreated with CV in HCl and *aqua regia* yielded higher gold removal than expected. KOH + H_2O_2 for gold pretreatment was later used in other studies: KOH and 25 % (v/v) H_2O_2 pretreatment for nanoporous gold electrodes fabrication for electrochemical purposes (Quan et al., 2011); for gold microwire pretreatment for paper-based analytical devices (ePADs) (Adkins & Henry, 2015), or with a joint pretreatment process followed by linear sweep voltammetry in KOH (Garcia-Mutio et al., 2016). The most common pretreatment for metallic surfaces is still CV in H_2SO_4, employed for rhodium (Custidiano et al., 1987), platinum (Sun et al., 1988) and gold electrodes. A variety of examples can be observed in **Table 1.1**. Despite the widespread use of CV in H_2SO_4 for gold electrode pretreatment, topological alterations have been observed. Some techniques such as XPS have shown gold oxide or hydrous oxide formation after CV in H_2SO_4 for gold electrode pretreatment (Izumi et al., 1991; Burke & Hopkins, 1984).

Gold oxide formation has been widely researched. An investigation developed a method to create hydrous oxide layers through a triangular potential sweep application under an alkaline solution. To decrease the oxide film thickness, cathodic sweeps under alkaline solutions were applied, and the appearance of six different peaks was observed. This suggested different gold oxide types (Burke & Hopkins, 1984). Hydrous oxide formation has also been described over cobalt (Burke et al., 1982) and nickel (L.D. Burke & T.A M. Twomey, 1984). However, oxides over gold surfaces have been favourably used for surface activation. This was the case of gold surface pretreated with HCl to detect ascorbic acid (Izumi et al., 1991).

(Tunuli, 1988) and (Tunuli & Armendariz, 1987) reported that creating an AuCl surface could activate the gold electrode surface after electrochemical pretreatment with HCl. (Izumi et al., 1991) corroborated the gold surface activation after HCl electrochemical pretreatment. However, that was due to gold crystal growth, verified through SEM and PXD. More recently, gold wire electrodes (GWE) were assessed for: $GWE_{polished}$ with alumina; $GWE_{oxi\text{-}red}$ where CV in H_2SO_4 created and reduced hydrous oxide layer; and GWE_{red} where a low potential was applied under $HClO_4$ solution to reduce water and subsequently form hydrogen gas. GWE_{red} appeared to be the best pretreatment as it showed barely any roughness over the electrode's surface. R_{ct} decreased for the different redox systems. **Figure 1.9** shows SEM images between pretreated GWE_{red} and

GWE $_{\text{oxi-red}}$. Differences between pretreated GWE $_{\text{red}}$ and GWE $_{\text{oxi-red}}$ were observed; GWE $_{\text{oxi-red}}$ presented more evident elevated roughness levels than GWE $_{\text{red}}$. (Lamas-ardisana et al., 2015)

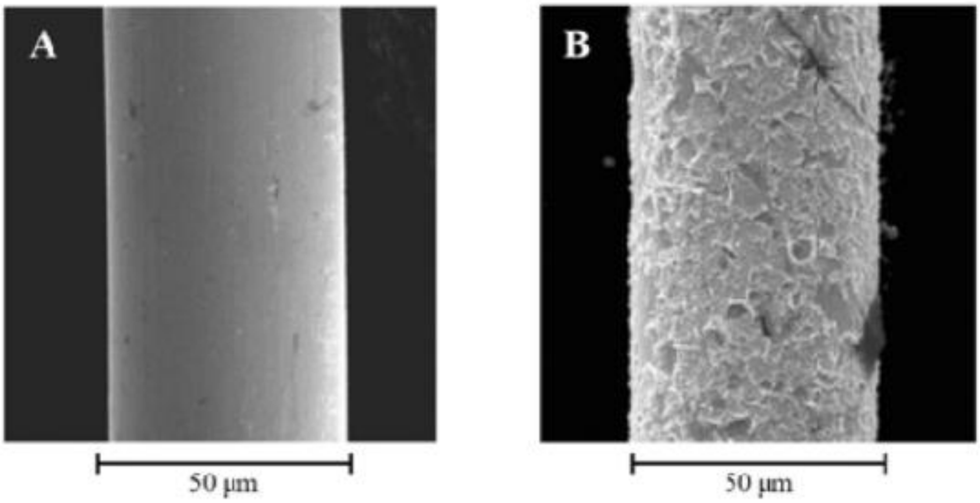

Figure 1.9: SEM images of A, GWE$_{\text{red}}$ and B, GWE$_{\text{oxi-red}}$. SEM images of **A**, GWE$_{\text{red}}$, pretreated with a low potential under $HClO_4$. **B**, GWE$_{\text{oxi-red}}$ where CV in H_2SO_4 created and reduced hydrous oxide layer. A clear increase in the roughness were observed. Reproduced from (Lamas-Ardisana et al., 2015).

The adaptability of the hydrogen evolution as electrode pretreatment was assessed for five redox systems. An improvement in the system's electrochemical behaviour was observed. Recently, the hydrogen evolution of gold electrodes has been favourable under alumina contamination. Alumina contamination appeared to improve the hydrogen evolution activity (Monteiro & Koper, 2019). A relevant study analysed the CV in H_2SO_4 effect over a system composed of a polycrystalline gold working, Ag/AgCl reference and Pt counter electrode (Xu et al., 2019). Both working and counter electrodes suffered from etching, resulting in chloride leaked and some Pt dissolved. All this had a negative impact on the electrode's reproducibility. Other parameters such as the effect of the electrolyte volume or the influence of Cl^- and $SO_4^{(2-)}$ anion were also investigated.

1.6.3. Gold pretreatment for alkanethiol SAM formation

Gold substrate for electrochemical usage is partly due to inertness to oxidise, and Au can bond with thiol through a covalent bond (Tkac & Davis, 2008). SAMs ease chemical or biological reactive surface layer production with different applications such as biomolecular adsorption, operating as thin dielectric, or impacting the mobility of the charge in semiconducting materials in field-effect transistors (Huck, 2007).

An adequate gold electrode pretreatment is essential to form a dense uniform SAM. The earliest pretreatments consisted of mechanical polishing and are still used nowadays. Emery paper, diamond or alumina are some of the most common materials to polish the electrode surface. This mechanical step is usually followed by an oxidative step, mainly used for organic contaminant removal. Examples of oxidising techniques are oxygen plasma, UV radiation, piranha or *aqua regia* solutions.

Oxidising pretreatments are mainly employed to remove organic contaminants. These oxidative methods can cause gold oxide formation, thus affecting SAM's formation. The creation of gold oxide has been corroborated through XPS (Ishida et al., 1997), CV (Guo et al., 1994) and contact angle (Ron et al., 1998). A reducing agent is then required to remove the gold oxide layer. Reducing methods such as cathodic potential (Tkac & Davis, 2008) are employed to remove the gold oxide layer. Finally, thermal or electrochemical pretreatments are frequently used to achieve activated surface and signal stabilisation (G. Feng et al., 2011).

(Yang et al., 1995) reported the chemical and mechanical polycrystalline gold disc electrode pretreatments for octadecyl-mercaptan (OM) SAM. Bare and SAM-coated electrodes were electrochemically assessed for different pretreatments. It was concluded that the formed SAM structure and bare electrodes were affected by the type of pretreatment. The electrochemical results were corroborated by Auger spectroscopy (Ilyin, 2017). The effect of mechanical polishing was studied through redox pair analysis. The SAM surface coverage was assessed through electrochemical desorption in alkaline media, a common technique to assess the surface coverage of alkanethiols (Widrig et al., 1991). It was concluded that diamond slurry polished gold electrodes presented denser SAM formation than alumina polished ones. Before (Yang et al., 1995) study, some studies had already reported that different compositions in polishing cloths could create some hydrophobic areas (Fagan et al., 1985; J.C.Hoogvliet, et al., 1986). Mechanical polishing was one of the earliest gold electrode surface pretreatment and nowadays is used alone or in joint pretreatments (Kelley et al., 1997; Yang & Lai, 2011; Tercero et al., 2009; Gebala & Schuhmann, 2010; Cui et al., 2017; Pagliarini et al., 2019; Alshehri et al., 2017).

UV/O_3 as a pretreatment has shown notable success in removing surface contaminants suitable for later surface patterning, depositing film or adhesive bonding. UV/O_3 can be used under atmospheric pressure and has shown to be less aggressive and milder than other techniques such as oxygen plasma. The application of UV/O_3 relies upon several variables: UV source, previous sample pretreatment, distance from the source to the sample, and the nature of the substrate and contaminant. Typically, UV light is absorbed by the contaminant at short wavelengths which then, along with free radicals react with atomic oxygen creating volatile molecules such as CO_2, N_2 and H_2O. Nevertheless, UV/O_3 application should last enough, so ozone does not create undesirable oxides (Kohli, 2019; Vig, 1990). A study for alkanethiol SAM formation over gold electrode involved a previous UV/O_3 step followed by ethanol pretreatment to overcome the gold oxides formation issues (Ron et al., 1998). Generally, organic contaminants can be removed with the UV/O_3 application, creating parallel gold oxide, which could be reduced in metallic Au after ethanol immersion. UV/O_3 pretreatment has been used for gold surface pretreatment alone or in joint pretreatments: formation of ss-DNA or ss-DNA/oligo(ethylene glycol) (OEG) SAMs (Boozer et al., 2006); gold substrate recycling after alkyl SAMs formation (Fealy et al., 2011); thiolated DNA SAMs formation and removal for XPS analysis (Mirsaleh-Kohan, et al., 2010).

In most studies, oxidative pretreatments are effective removing surface contamination. However, some of them are prone to create oxide over the gold surface. Ethanol showed to remove gold oxide layers. An alternative to ethanol was CV in H_2SO_4 (Tkac & Davis, 2008). These two pretreatments were compared after the independent pretreatment of polycrystalline gold surfaces for two different SAM formations. The results showed that CV in H_2SO_4 was at least as efficient as ethanol treatments. It was suggested that CV in H_2SO_4 and ethanol joint pretreatment might be advantageous and was later employed to pretreat gold surfaces before thiol self-assembly for a glycan biosensor (Kveton et al., 2017).

The quality and reproducibility of a thioctic acid SAM formation over polycrystalline gold electrode was investigated (Hoogvliet et al., 2000). They obtained smother surfaces by potential pulse regime application for PB at pH 7.4 and observed a roughness decrease over the surface by a factor of 2 compared to mechanically polished surfaces. This pretreatment has been, for instance, employed for 1,6 hexanethiol SAM formation in reusable capacitive sensor (Li et al., 2005).

Aqua regia and oxygen plasma were compared as pretreatments for gold. The stress formation of hexanethiol SAM on gold pretreated with *aqua regia* or oxygen plasma was studied using micromachined cantilevers (A. G. Hansen et al., 2001). *Aqua regia* provided greater adsorption rates and more significant stress change than oxygen plasma. This was supposedly caused by the greater roughness created by the *aqua regia* etching, which allowed higher adsorption sites density, as observed by AFM. Nevertheless, oxygen plasma gold pretreated surfaces showed better adsorption reproducibility.

Many studies report gold electrode pretreatments for alkanethiol SAM formation, but most only assess one or a few methods under the same working conditions. An extensive research assessed different pretreatments and combinations to pretreat polycrystalline gold electrode surfaces for 3-mercaptopropionic acid (3 MPA) thiol self-assembly (Carvalhal et al., 2005). Mechanical polishing with alumina slurry, M; piranha solution, C; CV in 0.5 M H_2SO_4, E. Pretreatment with ethanol, and a combination of some of them were also tested: M + E, M + C, C + E, M + C + E. C showed to be relevant towards gold surface activation. C and E presented more reproducible surfaces as they significantly minimise the roughness of the surface. **Figure 1.10** shows the electrochemical surface area (ESA) for different pretreatment combinations. On the one hand, M pretreatment gave the maximum ESA despite clear lowest reproducibility. This was explained by the terrace and hole formation, which created a greater surface area than the theoretical geometric one. On the other hand, C and E presented lower ESA values, although they were more reproducible than M. Gold pretreated surfaces showed small microscopic roughness due to the dissolution of the gold oxide particles. Given the importance of a reproducible ESA in real applications, M + C and M + C + E pretreatments showed to be the most suitable. The surface activation was investigated through CV too. It was determined that surface activation could not be related to the ESA increase but to the gold oxide amount and class formed in the pretreatment steps. **Figure 1.11** shows the CV voltammograms of bare electrode and 3 MPA modified electrode under different pretreatments. Mechanically polished SAM-coated electrodes CV voltammogram did not differ from the bare electrode under the same conditions. This could be related to many imperfections during SAM formation as it conceives elevated diffusion of the redox mediators. The best SAM packing was obtained for gold pretreated with M + C + E.

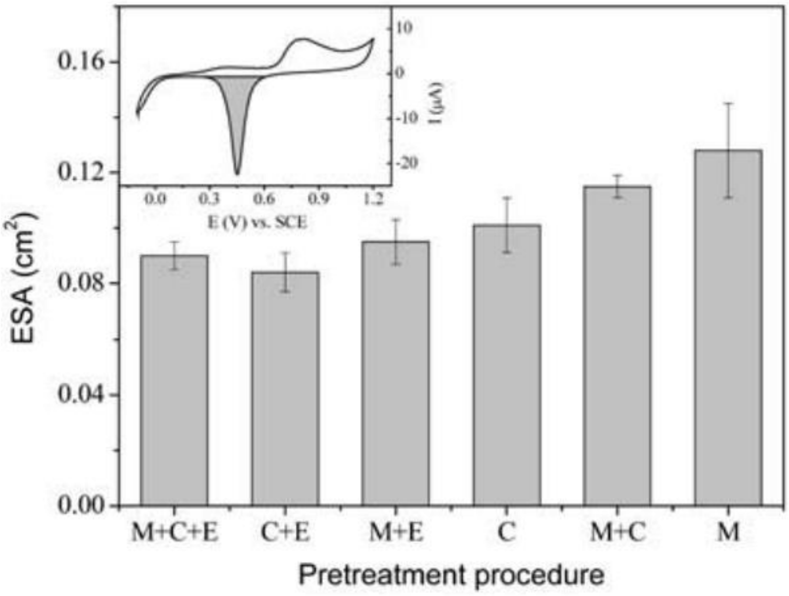

Figure 1.10: The electrochemical surface area (ESA) for different pretreatment combinations. ESA for different individual or combined pretreatment were presented. The ESA was determined by the integration of gold reduction peak from the voltammogram curves from -0.1 V and +1.1 V. Reproduced from (Carvalhal et al., 2005).

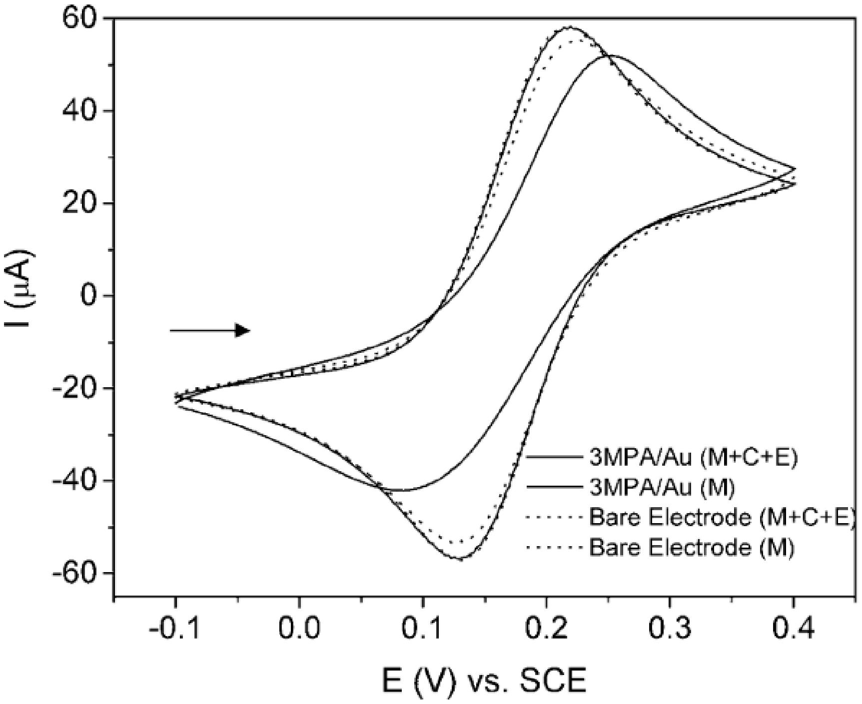

Figure 1.11: Bare electrode and 3 MPA modified electrode CV under different pretreatments. CV profiles of bare gold surface and 3 MPA functionalised gold electrode in 5 mM hexacyanoferrate (II/III) in 0.1 M KCl pH 8, 100 mV/s for different individual or combined pretreatment were presented. Reproduced from (Carvalhal et al., 2005).

Pretreating gold electrode surfaces with a combination of M and/or C and/or E or similar variations have been widely used: C and E prior to PEDOT deposition for implantable neural applications (Seymour et al., 2011); M + C + E prior SAM formation for electrochemical biosensor for celiac disease-related anti-tissue transglutaminase antibodies (Dulay et al., 2011) and prior SAM formation for electrochemical immunosensor for the anti-gliadin antibodies detection (Rosales-Rivera et al., 2011); (Bandyopadhyay et al., 2013) employed the C + E combination prior SAM formation for an azide terminated amine-containing SAMs research. C + E was also used for SAM formation for uranyl cations impedimetric biosensor (Motaghedifard et al., 2014) and in another study prior SAM and mixed SAM formation for hydroquinone biosensor (Mossanha et al., 2015).

Another study investigated different gold surface pretreatments for the dodecanethiol SAM formation (G. Feng, et al., 2011). Electrodes were mechanically polished, sonicated, followed with pretreatments: *aqua regia*, reductive annealing, UV/O3, piranha and mechanical polishing. Then, they were electrochemically treated with H_2SO_4 until reproducible profiles were obtained. Electrochemical reductive desorption in 0.5 M NaOH was used to evaluate the SAM surface coverage: *aqua regia* ~ reductive annealed > UV/O_3 ~ piranha ~ mechanical polishing. Mechanical polishing, UV/O_3 and piranha pretreated surfaces showed less surface coverage due to oxidation at the gold surface. *Aqua regia* showed minor roughness, followed by reductive annealing. These results concluded that *aqua regia* and reductive annealing were the best gold pretreatments to achieve better SAM surface coverage and surface roughness. Therefore, combining a first mechanical and sonication pretreatment with *aqua regia* followed by electrochemical treatment resulted in the best pretreatment for dodecanethiol SAM formation. This is another similar combination to the M + C + E from (Carvalhal, et al., 2005), but where the C pretreatment corresponds to *aqua regia* and a sonication step is included before the chemical pretreatment.

Similar pretreatment was employed in (Links, 2011; Links, 2012). However, some variations were carried out, such as replacing *aqua regia* for piranha solution and in (Boubour & Lennox, 2000), where the electrochemical pretreatment step used $HClO_4$ rather than H_2SO_4. Even though oxidising techniques for gold pretreatment surfaces appear to be the most prevalent methods, some of them can cause damage to the surface despite any subsequent reductive methods: piranha may create sulphur close to the surface region, limiting the gold surface binding sites (Thomas et al., 2012).

A recent study assessed the mercaptohexanol SAM reproducibility on pretreated and non-pretreated polycrystalline gold electrodes (Makaraviciute et al., 2017). CV in H_2SO_4, piranha followed by linear sweep voltammetry in KOH and oxygen plasma followed by incubation in ethanol were the gold surfaces pretreatments before SAM formation. The ESA analysis concluded there was no difference between pretreated and non-pretreated electrodes. All pretreatments reduced the contamination and increased the SAM coverage. In the case of SAM coverage density, it was up to 2.75 times higher for oxygen plasma and ethanol pretreatment. However, better reproducibility was obtained for non-pretreated electrodes and appeared not to differ much from the pretreated ones.

Oxygen plasma followed by ethanol was included in gold pretreatment for a potentiometric DNA sensor study (Xu et al., 2020). In another study, oxygen plasma could cause Au_2O_3 contamination with oxidised sulphur components (Raiber et al., 2005). The combination of an oxidising technique followed by a chemical reduction for gold pretreatment for alkanethiol SAM formation has been observed in (Ron et al., 1998, Tkac & Davis, 2008; Carvalhal *et* al., 2005).

1.6.4. Thiol-modified DNA oligopeptide SAMs

The assembly of thiol-modified oligonucleotides SAMs over the gold substrate is mainly found in biosensor applications. Gold pretreated with 10-30 s of piranha was optimal for thiol-oligonucleotide SAM formation for thrombin binging. Oxidises sulphur was observed over the gold surface after 60 s or longer of piranha exposure (Thomas et al., 2012). A very extensive study (Li et al., 2014) assessed the effect of six different gold electrode pretreatment for thiol-modified ss-DNA and thiol-modified ds-DNA: M + E, M + C (piranha), M+ C (dilute *aqua regia*), M+ C + E (piranha), M + C + E (dilute *aqua regia*) and RM + C + E (piranha), in which M is mechanical polishing with alumina slurries, E is CV in 0.5 M H_2SO_4, C either piranha or dilute *aqua regia* and RM roughly M. These pretreatments' effects were assessed through CV, EIS, CC (chronocoulometry) and SEM. Each pretreatment yielded different roughness, obtained from the integral charge reduction peak after CV in H_2SO_4 (**Figure 1.12**). The roughness of gold pretreated surfaces followed the decreasing order: RM + C + E (piranha) > M + E ≈ M+ C (piranha) ≈ M + C + E (piranha) > M + C (dilute *aqua regia*) ≈ M+ C + E (dilute *aqua regia*). **Figure 1.13** shows low magnification SEM of gold electrodes under different pretreatments and confirmed that RM + C + E (piranha) left rougher surface than the rest of the pretreatments. At the same time, M + E, M + C and M + C + E presented similar roughness in high magnification SEM (**Figure 1.14**) except for some small marks from the dilute *aqua regia* procedure. This was explained by HNO_3 oxidising Au to Au^{3+}, which interacts with Cl^- from HCl to form $[AuCl_4]^-$. However, surface coverage, ion penetration and charge transfer were similar for all pretreatments except for M + C (dilute *aqua regia*). These results differ from those reported in the literature, where the pretreatments substantially impacted those parameters for alkanethiol SAM formation over the gold substrate. The structural difference between an alkanethiol and a thiol-DNA molecule could explain those results.

Recently, several gold pretreatments for impedimetric thrombin-specific aptasensors (Song et al., 2008) were tested to obtain the best biosensor performance (L. S. J. Ho et al., 2019). The biosensors consisted of a Mercaptopropionic acid (MPA) SAM over which an aptamer was tethered via biotin-streptavidin. Amongst all pretreatments, the mechanical polishing and exposure in 50 mM KOH/H_2O_2 (3:1) was shown to be the best pretreatment compared to the rest, which included mechanical polishing and mechanical polishing followed by either chemical (piranha), electrochemical by cycling potential in H_2SO_4 and combined acidic pretreatments. The same gold pretreatment protocol was recently followed to fabricate impedimetric aptasensors for histamine detection (L. S. J. Ho et al., 2020).

In another study, different gold surface pretreatments were assessed for a dense oligopeptide SAM formation (Enomoto et al., 2018). Ozone, dilute *aqua regia*, plasma, and UV irradiated gold surfaces were all tested. Techniques such as AFM, contact angle and optical microscopy were employed to assess the surface cleanliness. After all pretreatments, the contact angle significantly decreased. This could be due to organic surface contaminant removal, making the surface more hydrophobic. No notable differences were observed with optical microscopy except for *aqua regia* pretreatment, of which roughness increased as confirmed through AFM.

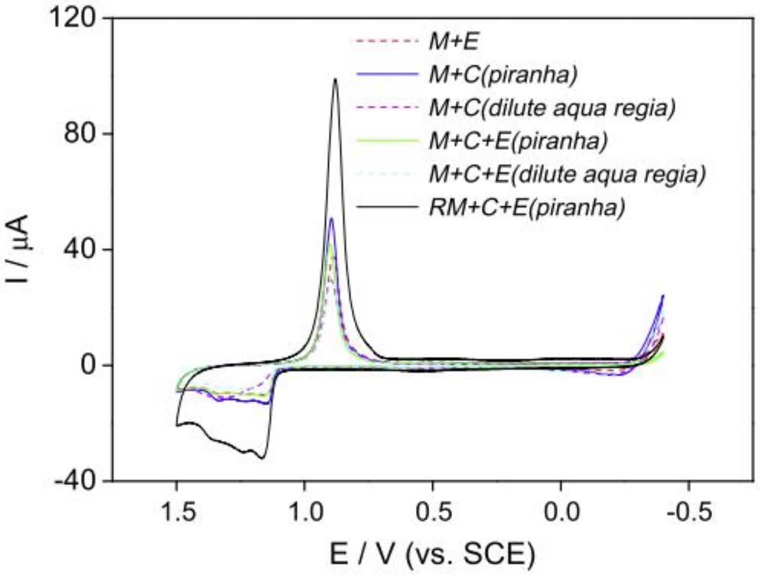

Figure 1.12: Cyclic voltammograms for different pretreated gold electrodes to obtain the integral charge reduction. CV for gold electrodes pretreated with the following combinations: M + E, M + C (piranha), M + C (dilute *aqua regia*), M + C + E (piranha), M+ C + E (dilute *aqua regia*) and RM + C + E (piranha). The CVs were conducted in 0.5 M H_2SO_4 to obtain the integral charge reduction. Reproduced from (Li et al., 2014).

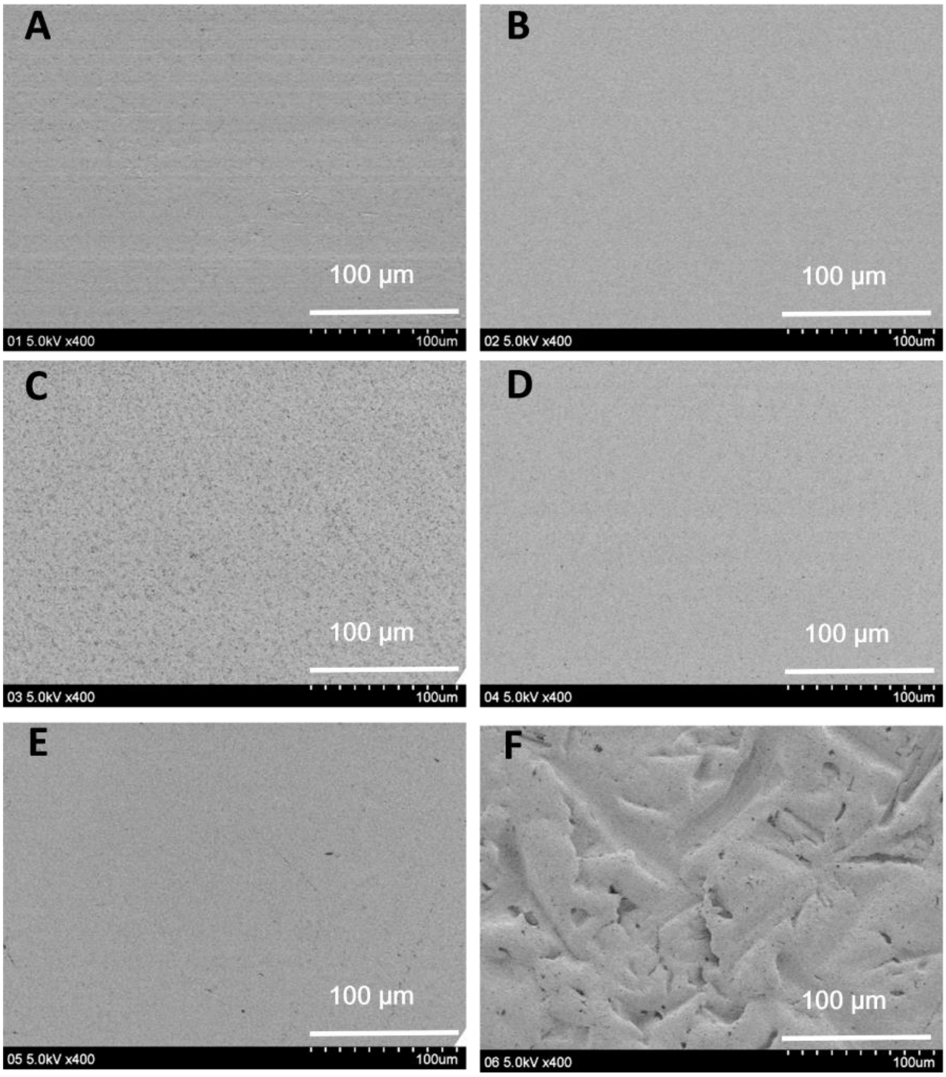

Figure 1.13: Low magnification SEM of gold electrodes under different pretreatments. Gold electrode surface roughness was assessed through low magnification SEM images after the following pretreatments (from **A** to **F**): M+E, M+C (piranha), M + C (dilute *aqua regia*), M + C + E (piranha), M + C + E (dilute *aqua regia*) and RM + C + E (piranha). Reproduced from (Li et al., 2014).

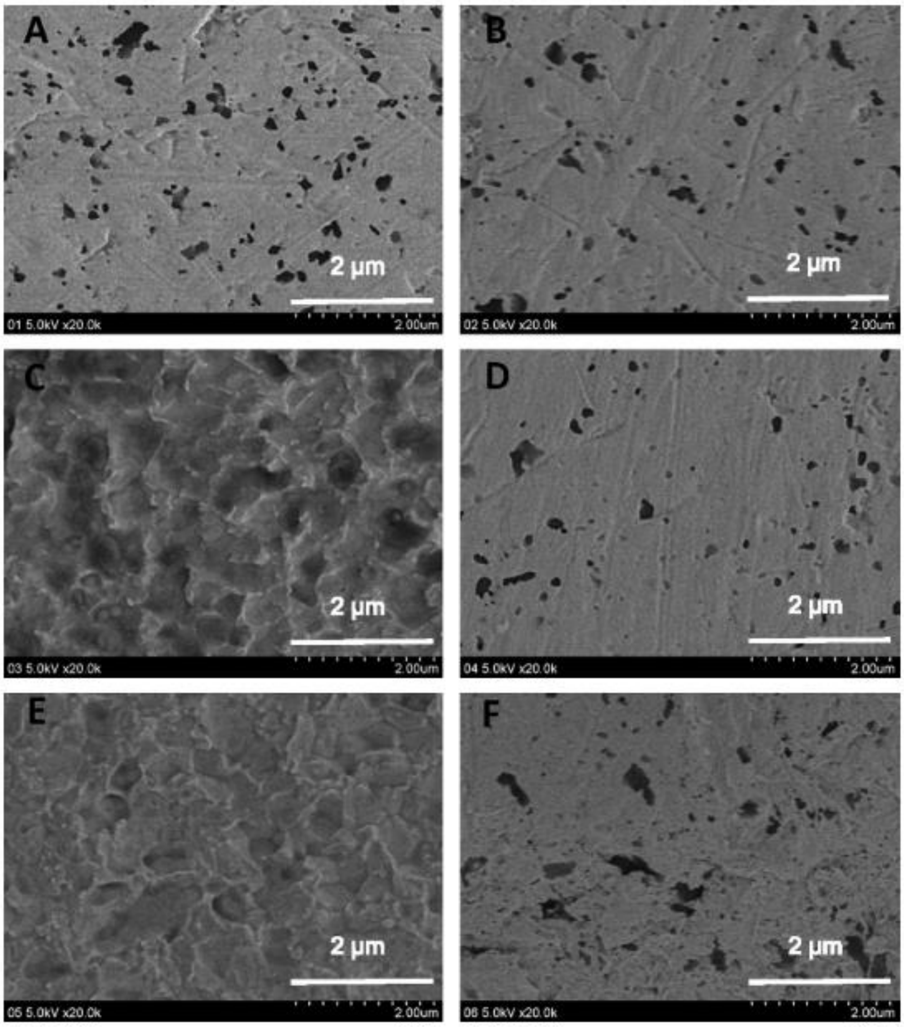

Figure 1.14: High magnification SEM of gold electrodes under different pretreatments. Gold electrode surface roughness was assessed through high magnification SEM images after the following pretreatments (from **A** to **F**): M+E, M+C (piranha), M + C (dilute *aqua regia*), M + C + E (piranha), M + C + E (dilute *aqua regia*) and RM + C + E (piranha). Reproduced from (Li et al., 2014).

1.6.5. Screen-printed gold electrodes

Low-cost commercial screen-printed electrode availability has increased in the last few decades. They are available for a wide range of electrochemical applications. Despite their extended application, little is known about the SPGE behaviour at their close surface level. Different conditions can alter the electrochemical SPGE performance. These are printing ink composition, variable temperature conditions during curing and printing processes, and several pretreatment procedures (Garc, Fern & Pern, 2008; Bernalte et al., 2013). Some research has dealt with the SPE characterisation, mainly electrochemical and electron microscopy (Bernalte et al., 2013). As reported in previous sections, common gold electrode pretreatments include electrochemical, chemical, sonication or ethanol pretreatment. Some studies do not indicate any pretreatment procedure. Up to date, there are no in-depth studies about the SPGE pretreatments.

The investigations of an impedimetric biosensor for *Streptococcus pyogenes* (Ahmed et al., 2013) detection lead to a brief study on the best SPGE pretreatment before polymer electrodeposition. CV in H_2SO_4 appeared to be better pretreatment than chemical with piranha or sonication in ethanol. It yielded lower R_{ct} values and smoother surfaces than the other methods. Dielectric material deposition and erosion were found in SPEG pretreated with piranha. Despite the favourable results for CV in H_2SO_4, the biosensor construction was ultimately performed with sonication in ethanol pretreatment. Very recently, a more sophisticated study about the most adequate pretreatment for SPGEs was carried out by (Stan et al., 2022). They recommend pretreating the SPGE surface with CV in 5 mM $K_4[Fe\ (CN)_6]/K_3[Fe(CN)_6]$ although the most efficient pretreatment was a solution of H_2O_2 with the application of multiple CV.

Despite differing opinions about the optimal pretreatment for SPGE, the literature suggests CV in H_2SO_4 as one of the best options, confirmed by several studies using it before biosensor construction (Radi et al., 2009; Escamilla-Gómez et al., 2008; Sakamoto et al., 2018; Loaiza et al., 2008; Aghaei et al., 2017; Ndiaye et al., 2016; Pagliarini et al., 2019; Cardoso et al., 2016; Kuralay et al., 2011; Escamilla-Gómez et al., 2009). SPGE manufacturers such as Metrohm DropSens (Metrohm Dropsens), Micrux (Micrux Technologies) and Pine (PINE Research, 2016) accept CV in H_2SO_4 as a pretreatment for their commercial SPGEs. Other companies such as Zimmer and Peacock (Zimmer & Peacock AS, 2020) suggest applying acidic potential and Basi[33], using large cathodic or anodic potentials.

(Stan et al., 2022) evaluated the SPGE surfaces with CV and EIS and performed SEM and energy dispersive X-ray analysis (EDX) for bare SPGE surfaces. However, no literature has been found about the effect of pretreatment for different surface coatings. In this project, **Chapter 3** shows a comparative study of two commercial SPGE where different pretreatments were studied for bare, polymer-coated, SAM-coated, and polymer-antibody matrix-coated SPGEs. The systems were assessed by CV and EIS to assess electrodes' quality, stability, and reproducibility. AFM and XPS respectively studied the surface topology and electrode composition.

Table 1.1: A summary of gold pretreatments reported in the literature. Different types of electrodes, interfaces and pretreatments are considered.

Year	Research group	Type of electrode	Interface	Pretreatments	Conclusions
2009	(Fischer et al., 2009)	Gold electrode chips were fabricated on 100 mm (100) silicon wafers		**KOH-H_2O_2 and KOH potential sweep; CV in H_2SO_4**.	The cleanest surfaces were obtained with KOH + H_2O_2 and KOH sweep method. CV in H_2SO_4 were not as clean as expected, although acceptable.
1991	(Izumi et al., 1991)	Gold disk and gold rectangular	Ascorbic acid oxidation	Alumina, ultrasound, and **CV in 0.37 M HCl** for 5 min (25 scans), (-0.04 to +1.41 V). Similar process but using H_2SO_4 and $HClO_4$.	CV in HCl activated the gold electrode surface by rearranging gold atoms for ascorbic acid oxidation.
2015	(Lamas-ardisana, et al., 2015)	Gold wire electrodes		Hydrogen evolution (GWE red): -3 V in 1 M $HClO_4$ for 60 s.	GWE_{red} was the best pretreatment: the gold surface hardly presented roughness and showed favourable EIS parameters such as R_{ct} and C_{dl}.
2012	(Dutta et al., 2012)	Gold plate electrodes	Reduction of p-benzoquinone and the oxidation of the glucose	**Piranha** at 80 °C for 10 min; Tris buffer with 10 mM **NaBH4** for 15 min; **mechanical polishing** with alumina slurry for 1 min.	All pretreatments improved the electrocatalytic activity, being piranha the most notable although had the roughest surface. $NaBH_4$ had similar roughness to non-pretreated.
1995	(Yang et al., 1995)	Gold disc electrode	Octadecyl mercaptan (OM) SAM	**Mechanical polishing** with either diamond or alumina slurry. Then, sonicated in different solvents for 1 min each in the following sequences: H_2O-ethanol- H_2O or H_2O-dichloromethane-H_2O.	Diamond polished electrodes had a denser packed SAM than the ones polished with alumina. Sonication in different solvents was not as relevant as mechanical polishing.
1992	(Creager et al., 1992)	Gold thin film electrodes (prepared from polycrystalline gold bulk)	$C_{12}H_{26}SH$, 0.020 M $C_{16}H_{33}SH$, and 0.020M $C_{18}H_{37}SH$ SAMs	Electrodes were polished with alumina slurry and sonicated in water. Then, etched in either diluted or concentrated ***aqua regia***.	Bulk gold electrodes etched with *aqua regia* provided with better SAM formation than surfaces created by evaporation onto silicon substrates.

1995	(Worley & Linton, 1995)	Gold substrates prepared by thermal evaporation on glass microscope slides	Cystamine SAM	**UV/O_3**: exposed to UV radiation for 5 min while oxygen was continuously flushed through the UV chamber	UV/ O_3 pretreatment removed adhered sulphur contaminants.
1997	(Ron et al., 1998)	{111} textured gold films	Octadecanethiol SAM	**UV/ O_3** for 10 min + pure **ethanol** for 20 min with stirring	The organic contaminants were removed with UV/ O_3. The gold oxide formed because of UV/ O_3 was converted into Au metallic by a reduction in ethanol.
2008	(Tkac & Davis, 2008)	Polycrystalline gold electrodes	OEG thiol ((1-mercapto-11-undecyl)tri(ethylene glycol) and 1-dodecanethiol SAMs	Piranha, CV in H_2SO_4, **electrochemical stripping** and ethanol. Electrochemical stripping consisted of 10 CV scans in 0.1 M H_2SO_4	Electrochemical stripping was at least as efficient as the ethanol pretreatment. The surface coverage of both SAMs increased after the electrochemical stripping.
2000	(Hoogvliet et al., 2000)	Polycrystalline gold electrodes	Thioctic SAM	**A triple-potential pulse**. Pulse regimes of +1.6/0.0/-0.8 V. The best conditions were achieved with a cathodic pulse to -0.8 V in a flow cell under 2000-5000 s of prolonged pulsing	Triple-potential pulse substantially decreased the roughness of the surface compared to mechanically polished surfaces. Without flow, no polishing effect was observed.
2001	(A. G. Hansen et al., 2001)	Gold substrate	Hexanethiol SAM	***Aqua regia*** or **oxygen plasma**	*Aqua regia* generated greater thiol adsorption rates. Oxygen plasma provided a better reproducibility of adsorption.
2005	(Carvalhal et al., 2005)	Polycrystalline gold electrodes	3-mercaptopropionic acid (3 MPA) thiol SAM	**M+C+E+ethanol**: M, mechanical polishing; C, piranha for 10 min; E, CV in 0.5 M H_2SO_4 and ethanol	C was relevant for surface activation. C and E provided more reproducible and less rough surfaces. M+C+E+ethanol allowed a better SAM packing.

2011	(G. Feng, et al., 2011)	Polycrystalline gold electrodes	1-dodecanethiol	**M+C+E**: M, mechanically polished and sonicated; C, *aqua regia* or reductive annealing; E, CV in N_2-purged 0.5 M H_2SO_4.	*Aqua regia* and reductive annealing were recommended for SAM formation.
2017	(Makaraviciute et al., 2017)	Polycrystalline gold electrodes	Mercaptohexanol (MCH) (or 6-Mercapto-1-hexanol)	**Oxygen plasma + ethanol**: Electrodes were pretreated in N_2 and O_2 plasma. Then, incubated in ethanol for 30 min	The best pretreatment was oxygen plasma + ethanol. Other pretreatments were H_2O_2 + KOH and LSV and finally CV in H_2SO_4. All reduced surface contamination and increased SAM coverage.
2012	(Thomas et al., 2012)	Polycrystalline gold electrodes	Single stranded-thrombin binding aptamer (TBA) SAM	10-30 s of **piranha solution**	Ten to 30 s of piranha allowed successful SAM formation. Oxidised sulphur appeared after pretreatments longer than 60 s.
2014	(Li et al., 2014)	Polycrystalline gold electrodes	Thiol-modified ss-DNA and thiol-modified ds-DNA	**M+ C (dilute *aqua regia*) and M + C + E (dilute *aqua regia*):** M, mechanical polishing; C, *aqua regia* for 5 min; E, CV in 0.5 M H_2SO_4 from -0.4 V to +1.5 V	The surface coverage, ion penetration and charge transfer were similar for all the pretreatments except for M+C.
2019	(L. S. J. Ho et al., 2019)	Gold stalk electrodes	Mercaptopropionic acid (MPA)	**M + combined alkaline**: KOH/H_2O_2 for 10 min + single linear potential sweep -0.2 V and -1.2 V in KOH	The combined alkaline method gave the most uniform surface compared to the rest of the tested pretreatments.
2018	(Enomoto et al., 2018)	Gold substrate electrode	The cell-repulsive oligopeptide (CGGGKEKEKEK) SAM	**UV exposure**	UV irradiation appeared to be the most effective pretreatment.
2013	(Ahmed et al., 2013)	Metrohm DropSens SPGE	Ptyr	5 min **sonication of electrodes in 100 % ethanol** or pretreatment through **CV in 0.1 M H_2SO_4** for 15 scans from 0.0 V to +1.4 V	CV in H_2SO_4 yielded better results although the biosensor construction was made with sonication in ethanol.

1.7. Impedimetric immunosensors for pathogen and biomarker detection

1.7.1. Immunosensors for pathogen detection

1.7.1.1. *Escherichia coli*

E. coli have been an analyte for many immunosensor platforms as it is easy to manipulate and commonly assessed for sensing faecal pollution of water (Wang et al., 2013). A relevant impedimetric biosensor for *E. coli* used gold interdigitated array microelectrodes (IDAMs) as the biosensor substrate and inserted them into a microfluidic device. One-hundred µL samples of 1.2 x 10^3 cfu/mL from ground beef and 1.6 x 10^2 cfu/mL from a pure culture were determined in 35 min (Varshney et al., 2007). Antibodies were conjugated to magnetic nanoparticles through biotin-streptavidin coupling, creating a magnetic nanoparticle-antibody conjugate (MNAC) that captured and concentrated bacteria after a magnetic field application. The IDAMs employment presents several advantages compared to macro-sized electrodes, commonly immersed in a solution. IDAMs' architecture consists of a parallel microband array of electrodes meshing into each other, constituting a set of interdigitated electrode fingers. IDAMs have been shown to lower the detection limit, provide faster detection and higher signal/noise ratio. IDAMs are typically made of gold, although indium tin oxide (ITO), Ti, Pt, Pd or Rh were also reported (Yan *et* al., 2011). Common IDAMs dimensions are 0.1 - 0.2 µm high for each electrode finger, 1 - 20 mm length with inter-electrode space of 1 - 20 µm. *E. coli* O157:H7 determination in river water samples was accomplished by forming a mercaptoacetic acid (MACA) SAM over gold electrodes (Kim et al., 2008). The SAM interface was treated with EDC plus NHS to catalyse the formation of a peptide bond with antibodies. A small sample of 20 µL could detect an LOD of 1 x 10^3 cfu/mL in 1 h. Compared to the 100 µL sample (Yan *et* al., 2011), these results decrease the sample volume despite a long time of analysis.

Using microfluidics, a biosensor was investigated for *E. coli* and *S. aureus* detection (Tan et al., 2011). Alumina nanoporous membranes were modified with self-assembled (3-glycidoxypropyl) trimethoxysilane (GPMS) SAM, onto which antibodies were tethered. Alumina nanoporous increases electron transfer through the electrode-solution interface due to its significant pore density, biocompatibility and increased surface area. In addition, alumina nanoporous membranes are remarkably long-lasting, and the pore size can be relatively easily controlled (La Flamme et al., 2007). The bacterial analytes were detected in 2 h at an LOD of 10^2 cfu/mL.

Another alumina nanoporous-based biosensor was also reported. **Figure 1.15** shows a scheme of HA-coated nanoporous immunosensor for *E. coli* detection in food samples. In this case, hyaluronic acid (HA) modification was added (Joung et al., 2013). HA is a hydrophilic nonsulphated glycosaminoglycan (GAG) used in biosensor fabrication to enhance the signal/noise ratio and improve the antibody immobilisation given from carboxyl groups. The biosensor could detect *E. coli* as low as 83.7 cfu/mL in milk samples. Therefore, the use of HA enhanced the previous sensitivity obtained by (Tan et al., 2011). Other cases where biosensors have employed HA (Joung et al., 2012) or conducting polyaniline (PANI) film surface before antibody immobilisation reaching an LOD of 2 cfu/mL (Chowdhury et al., 2012) were reported.

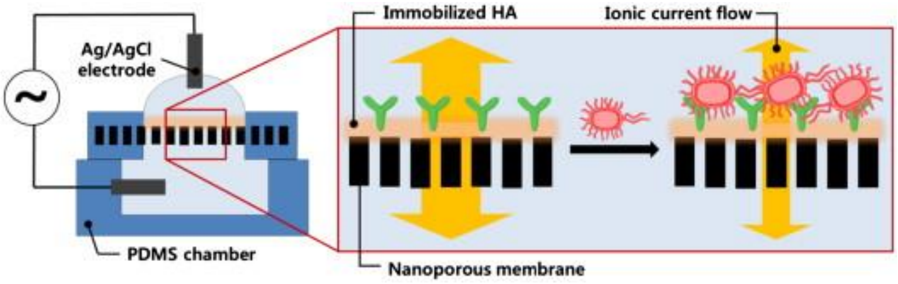

Figure 1.15: Impedimetric immunosensor fabrication scheme using HA-coated alumina nanoporous for *E. coli* detection inserted into a microfluidic device. Scheme of HA-coated nanoporous immunosensor for *E. coli* detection in food samples. The immunosensor is composed of PDMS chambers, HA-antibody functionalised alumina nanoporous membrane and the electrode. The bacteria binding is achieved at the HA-antibody functionalised membrane from the scheme, which affects the ionic current flow depending on the bacterial concentration. Reproduced from (Joung et al., 2013).

A biosensor was developed with reduced graphene oxide paper (rGOP) electrodes, which was altered with gold nanoparticles (AuNPs) to determine *E. coli* in food samples (Wang et al., 2013). Graphene appears advantageous in impedimetric immunosensors as it presents several advantages such as flexibility, rapid electron transfer, biocompatibility and a high specific surface area. AuNPs can provide an adequate microenvironment for the immobilisation of biomolecules and facilitate the electron between the bulk material on the electrode and the electrode itself (Chen et al., 2012).

Amplification steps with AuNPs (Wan et al., 2016) or lectin wheat germ agglutinin (WGA) (Li et al., 2015) to improve sensitivity were employed after analyte addition in impedimetric immunosensors (**Figure 1.16**). Screen-printed interdigitated microelectrodes (SPIMs) were coated with 3-dithiobis-(sulfosuccinimidylpropionate) (DTSP) and subsequently functionalised with antibodies. After the bacteria were tested, WGA was used to amplify the signal (Li et al., 2015). The biosensor construction scheme can be followed in (**Figure 1.16A**), step-by-step monitored through EIS (**Figure 1.16B**) and tested for different bacterial concentrations signal in (**Figure 1.16C**).

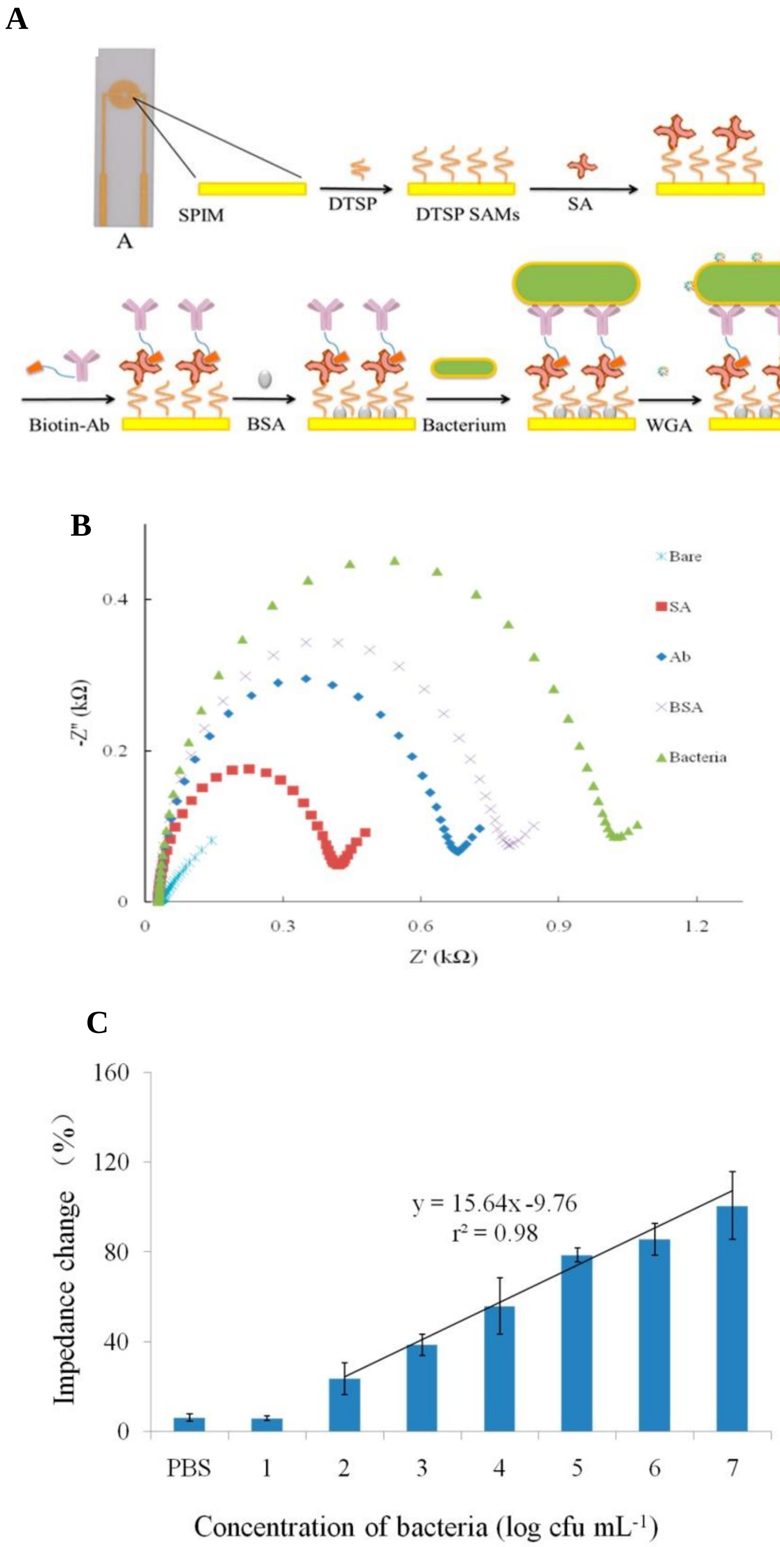

Figure 1.16: Scheme of impedimetric immunosensor for bacteria detection with amplification step with WGA, Nyquist plot of step-by-step functionalisation and bacterial detection. A, layer-by-layer construction scheme of the impedimetric immunosensor. The photo A corresponds to a SPIM. The width of a finger and the gap between two fingers were 200 µm. **B**, Nyquist plot of each step electrode functionalisation. **C**, Impedance change (%) plotted against increasing concentration of *E. coli* in log (cfu/mL). Reproduced from (Li et al., 2015).

Antibody-coated magnetic nanobeads were employed to segregate and manipulate bacteria from the initial culture to another platform. The pathogen was concentrated onto a biosensor electrode and electrochemically assessed (Wang et al., 2015). Au, Ag and Pt are common working electrode materials, although biosensors over ITO electrodes were reported (Barreiros dos Santos et al., 2015). A concentration as low as 1 cfu/mL in a 400 µL PBS sample was detected in 45 min.

1.7.1.2. *Salmonella*

Salmonella is a Gram-negative bacteria from the *Enterobacteriaceae* family. The most common *Salmonella* types that infect humans are *Salmonella typhimurium* (*S. typhimurium*) and *Salmonella typhi* (*S. typhi*). *S. typhimurium* symptoms appear from 12 to 72 h after the infection and are less virulent. This pathogen can cause diarrhoea, fever, abdominal colic and headache. *S. tiphi* causes typhoid fever, responsible for approximately 200,000 deaths per year and morbidity of around 20 million new cases per year (Dougan & Baker, 2014).

An immunosensor was constructed to determine the presence of *S. typhimurium* in milk samples (Pournaras et al., 2008). A thiol-based SAM-coated gold working electrode was functionalised with antibodies against *Salmonella* through glutaraldehyde cross-linking. An LOD of 10^2 cfu/mL in a 2 mL PBS after 2 h and in 2 mL milk after 10 h was achieved. Similarly, antibodies were tethered to the SAM via glutaraldehyde (Farka et al., 2016) and could detect $1x10^3$ cfu/mL in a 1 mL sample in 20 min, thus enhancing previous results from (Pournaras et al., 2008). Magnetic silica nanotubes (MSNTs) were employed to functionalise IDAM-based immunosensor (Nguyen et al., 2014). The MSNTs present a multifunctional structure and are less susceptible to self-aggregation under abundant salt levels in the media. Other IDAM-based immunosensor detected an LOD of 10^2 cfu/mL in only 50 µL volume after 1 h (Wen et al., 2017), improving the previous sample volumes from (Pournaras et al., 2008; Farka et al., 2016). Little has been reported about *S. typhi* impedimetric immunosensor detection.

1.7.1.3. Sulphate reducing bacteria

Bacterium *Desulforibrio caledoiensis,* an SRB, uses sulphate as a terminal electron acceptor in its electron transport chain. This sulphate gives rise to sulphide which is a complication for industries and the environment (Muyzer & Stams, 2008). An early SRB impedimetric immunosensor immobilised the lectin concanavalin A (ConA) for an agglutination assay (Wan et al., 2009) over a SAM. A molecule of lectin possesses four carbohydrate-combining sites. Then, lectins react with cells, thus creating cross-linking and precipitation (Lis & Sharon, 1998). To entrap bacteria, a different SRP immunosensor employed Ni foam coated with 11-mercaptoundecanoic acid (11-MUA) (Wan et al., 2010). This system is shown in **Figure 1.17.** The inclusion of reduced graphene sheets (RGS) for SRB biosensors was also reported (Wan et al., 2011). RGS are 2D biocompatible structures with low manufacturing costs (Yang et al., 2011). A biosensor functionalised with RGS-doped chitosan nanocomposite film determined bacteria from 1.8×10^2 to 1.8×10^7 cfu/mL. This biosensor used a smaller sample volume, 10 µL, and faster analysis than the SRB detection on (Wan et al., 2009; Wan et al., 2010), although the sensitivity was not improved.

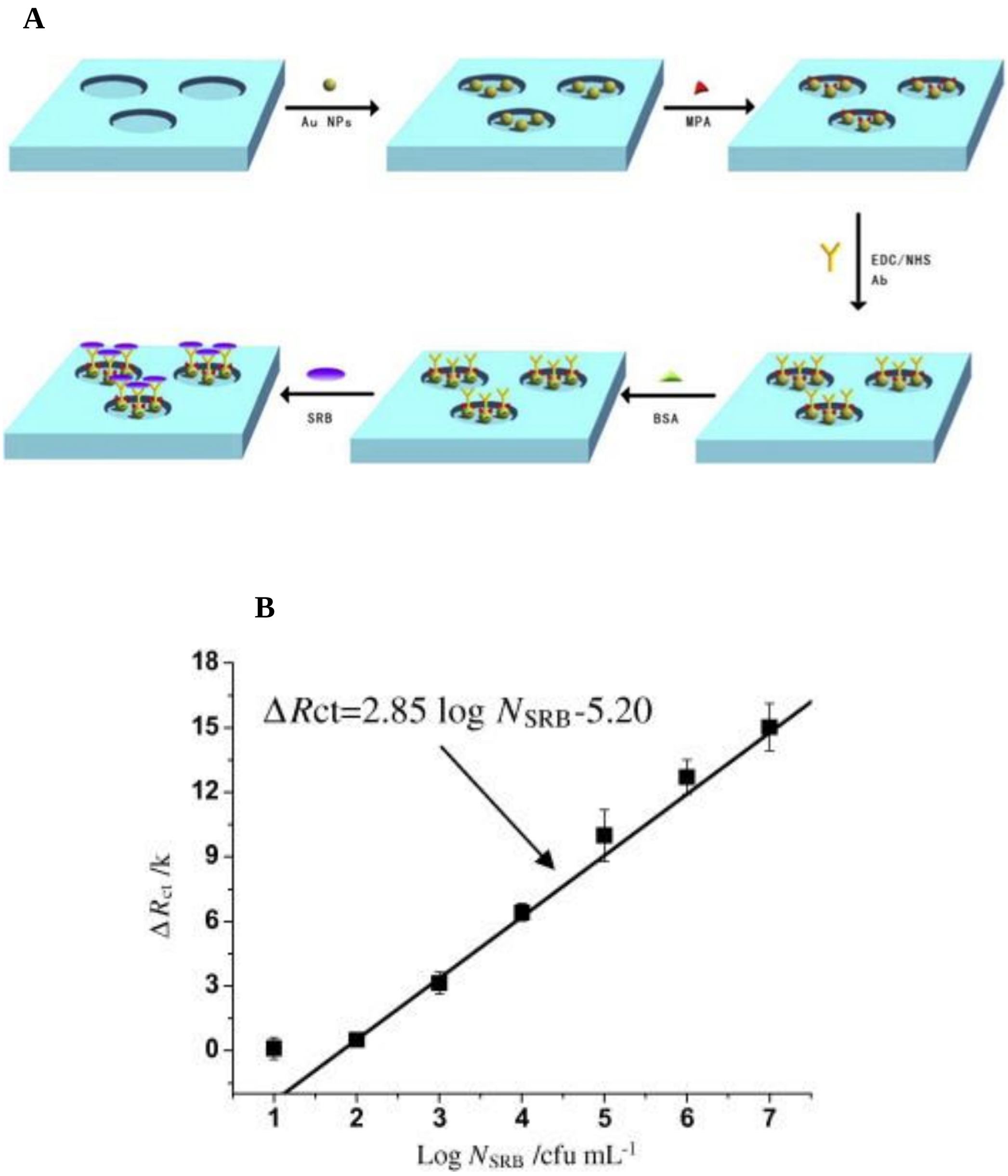

Figure 1.17: Scheme of the impedimetric biosensor construction for SRB detection over 3D-foam Ni and bacterial detection. A, the gold NPs were assembled over the foam Ni electrode surface. Then, the surface was immersed in an ethanol solution containing the MPA for 8 h to achieve the functionalisation of the SAM. Then, the antibodies were immobilised onto the surface through EDC/NHS. The non-specific sites were blocked with BSA. **B**, R_{ct} change plot shows a calibration curve for different bacterial concentrations. Reproduced from (Wan et al., 2010).

1.7.1.4. *Listeria monocytogenes*

Listeria monocytogenes (*L. monocytogenes*) is a Gram-positive bacterium usually infecting contaminated food through ingestion. Typically, *L. monocytogenes* derived diseases include febrile gastroenteritis, perinatal infection, and systemic infections, infecting the central nervous system (Drevets & Bronze, 2008). An immunosensor was able to determine *L. monocytogenes* at an LOD of 4.7 x 10^2 cfu/mL employing a TiO_2 nanowire bundle microelectrode. This detection technique surpassed Dot blot assay with 2.2 x 10^5 cfu/mL LOD. TiO_2 nanowire presents exclusive semi-conductive bandgap, biocompatibility, chemical and photochemical stability, and relatively simple fabrication (Wang et al., 2008). Another immunosensor for *L. monocytogenes* was investigated by (Kanayeva et al., 2012) in which antibody-coated magnetic nanoparticles determined bacteria as low as 10^4 cfu/mL for food samples in only 20 nL. Low sample volumes were achieved by inserting the biosensor into a microfluidic device.

1.7.1.5. *Pseudomonas aeruginosa, Streptococcus pyogenes* and *Staphylococcus aureus*

Pseudomonas aeruginosa (*P. aeruginosa*) is a Gram-negative bacterium usually located in contaminated water. Human infections include the respiratory system, urinary tract and systemic diseases (Wu & Li, 2015). An impedimetric immunosensor for *P. aeruginosa* (Bekir et al., 2015) was constructed through polyclonal antibody immobilisation over a screen-printed carbon electrode (SPCE). *Streptococcus pyogenes* (*S. pyogenes*)*, a* Gram-positive bacterium, is accountable for chronic inflamation, cellulitis, meningitis and other diseases. An immunosensor in which commercial SPGE were modified by Ptyr electrodeposition for *S. pyogenes* determination was reported (Ahmed et al., 2013). Bacteria could be detected as low as 10^2 cells in 10 µL after 30 min incubation. A scheme of the biosensor construction is shown in **Figure 1.18**. *Staphylococcus aureus* (*S. aureus*), a Gram-positive bacterium could be detected through immunosensor over SAM gold-coated electrodes. Specific antibodies against *S. aureus* were attached to the SAM-coated electrode (Bekir et al., 2015).

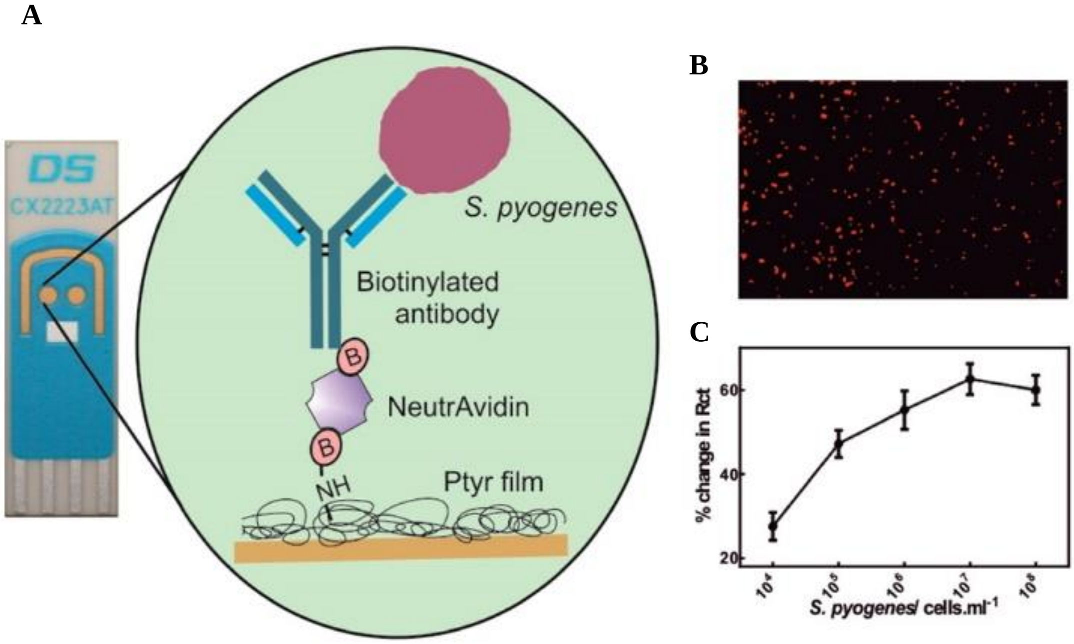

Figure 1.18: Scheme of the biosensor construction for *S. pyogenes* and bacterial detection. **A**, a general immunosensor scheme against Streptococcus pyogenes construction over Metrohm DropSens SPGE (CX2223AT). **B**, a bound S. pyogenes fluorescence imaging. **C**, a % change in R_{ct} plot upon the addition of bacteria, from 10^4 to 10^8 cells/mL. Reproduced from (Ahmed et al., 2013).

1.7.1.6. Viral and fungal detection

Avian Virus Influenza (IV) H5N1 is profoundly pathogenic and is mainly seen in birds. Nevertheless, human infection by IV H5N1 is commonly related to various diseases and death (Kayali et al., 2016) . A biosensor was developed for IV H5N1 determination (Wang et al., 2009). Polyclonal antibodies were immobilised over gold IDAM against IV H5N1 surface antigen HA (hemagglutinin) via protein A. Similarly, IV H5N1 determination in chicken swabs was accomplished (J. Lin et al., 2015). A gold IDAM electrode was employed and functionalised via protein A with monoclonal antibodies against IV H5N1. Impedimetric immunosensors were also developed for a regenerable biosensor for adenovirus type 5 (Ad5) detection (D. Lin et al., 2015), plum pox virus (PPV) determination (Jarocka et al., 2011), and for oomycete fungus *Aphanomucenes invadans* (Qi et al., 2017).

1.7.2. Other bioreceptors

Antibody-derived proteins such as nanobiodies have been employed in impedimetric immunosensors. Nanobodies comprise a single-domain antibody fragment in camelids (Steeland et al., 2016). Nanobodies were used over glassy carbon electrodes to detect testosterone concentration in 1 h, accomplishing an LOD of 0.045 ng/mL (Li et al., 2016). Another nanobody-based biosensor was fabricated to determine rabbit IgG (Goode et al., 2016). Affimers are non-antibody proteins that have shown binding properties (Tiede et al., 2014; Tiede et al., 2017). An Affimer-based impedimetric biosensor determined Her4 protein tumour as low as 1 pM (Zhurauski et al., 2018). A summary of different types of impedimetric immunosensors has been included in **Table 1.2**. The table provides information regarding the analyte, immobilisation step, LOD, sample volume and detection time.

Table 1.2: A summary of impedimetric immunosensors reported in the literature. Different biosensor components, construction steps, and features are shown, namely: immunosensor electrode, analyte, immobilisation step, LOD and sample volume.

Immunosensor electrode	Analyte	Immobilisation step	LOD	Sample volume	Detection time	Reference
Au IDAM	*E.coli O157:H7*	MNAC/SA/BT/Ab	-1.2 x 10^3 cfu/mL from ground beef samples -1.6 x 10^2 cfu/mL from pure culture	100 µL	35 min	(Varshney et al., 2007)
Au	*E.coli O157:H7*	MACA/EDC+NHS/Ab	1 x 10^3 cfu/mL in culture	20 µL	1 h	(Kim et al., 2008)
Au	*E.coli O157:H7*	MHDA/(EDC+PFP+DIEA)/Ab/AEE	2 cfu/mL	_	45 min	(M. Barreiros dos Santos et al., 2013)
Pt wire	*E.coli O157:H7 /Staphilococcus aureus*	NAM/GPMS/Ab	10^2 cfu/mL	_	2h	(Tan et al., 2011)
Ag/AgCl	*E.coli O157:H7*	NAM/HA/EDC+NHS/Ab	83.7 cfu/mL in milk	_	_	(Joung et al., 2013)
Au microelectrode	*E.coli O157:H7*	PANI/GLU/Ab	10^2 cfu/mL	_	_	(Chowdhury et al., 2012)
Au	*E.coli O157:H7*	11M1UD/ECD/HA/EDC+NHS/Ab	7 cfu/mL	1 mL	_	(Joung et al., 2012)
rGOP	*E.coli O157:H7*	Au-NPs/SA/BT/Ab/BSA	-1.5 x 10^3 cfu/mL cucumber -1.5 x 10^4 cfu/mL ground beef samples	_	_	(Wang et al., 2013)
Au	*E.coli O157:H7*	MUA/EDC+NHS/Ab/AuNPs	10^2 cfu/mL	_	2h	(Wan et al., 2016)
Au SPIM	*E.coli O157:H7*	DTSP/EDC+NHS/SA/BT/Ab/BSA/ WGA	10^2 cfu/mL	_	< 1 h	(Li et al., 2015)
Au SPIM	*E.coli O157:H7*	MgNbs/SA/Biotin/Ab	1.4 x 10^3 cfu/mL	25 µL	_	(Wang et al., 2015)

ITO	*E.coli O157:H7*	GPMS/Ab	1 cfu/mL	400 μL	45 min	(Barreiros dos Santos et al., 2015)
Au-W microwire	*E.coli K12*	PEI/SA/BT/Ab	10^3 cfu/mL	5 μL	_	(Lu et al., 2013)
Au	*E.coli O157:H7*	(Au-MBA-Ab), (Au-MBA-ProteinA/G-Ab), (Au-Cys-Ab), (Au-Cys-Ferrocene-Ab), (Au-Cys-PAMAM-Ferrocene-Ab)	3 cfu/mL	1 mL	90 min	(Malvano, et al., 2018)
Au	*S. typhimurium*	Ptyr/GLU/Ab/BSA	-10 cfu/mL in culture -10^2 in milk	2 mL	3 h, 10 h respectively	(Pournaras et al., 2008)
Au SPE	*S. typhimurium*	Cys/Glu/Ab/BSA	-10^3 cfu/mL in PBS -9 x 10^3 in milk	1 mL	20 min	(Farka et al., 2016)
Ti-Au IDAM	*S. typhimurium*	MUA/EDC+NHS/Ab/BSA	10^3 cfu/mL	_	30 min	(Nguyen et al., 2014)
Au IDAM	*S. typhimurium*	16-MHDA/SA/BT/Ab	10^2 cfu	50 μL	1 h	(Wen et al., 2017)
Pt interdigitated microelectrodes	*S. typhi*	Au-NPs/AbPEG-thiol	10^2 cfu/mL	10 μL	1 h	(Pal, Sharma & Gupta, 2016)
Au	SRB	MUA/EDC+NHS/lectin-ConA	1.8 cfu/mL	_	2 h	(Wan, Zhang & Hou, 2009)
Foam Ni	SRB	AuNPs/11-MUA/EDC+NHS/Ab/BSA	2.1 x 10^1 cfu/mL	_	2 h	(Wan et al., 2010)
Glassy carbon disc	SRB	CS+RGS/Glu/Ab/BSA	1.8 x 10^1 cfu/mL	10 μL	1 h	(Wan et al., 2011)
Au microelectrode	*L. monocytogenes*	TiO2 nanowire/(SH-(CH2)3-CH3)/Ab	4.7 x 10^2 cfu/mL	15 μL	50 min	(Wang et al., 2008)
IDAM	*L. monocytogenes*	MNPs/SA/BT/Ab	10^4 cfu/mL in milk, beef and lettuce.	20 nL	3 h	(Kanayeva et al., 2012)
SPCE	*P. aeruginosa*	PP3CA/EDC+NHS/Ab	10 cfu/mL		_	(Bekir et al., 2015)
Au SPE	*S. pyogenes*	Ptyr/BT/NA/BT/Ab/BSA	10^2 cfu/mL	10 μL	30 min	(Ahmed et al., 2013)

Au	*S. aureus*	MHDA/EDC+NHS/Ab	10 cfu/mL	5 mL	_	(Bekir et al., 2015)
Au IDAM	AI virus H5N1	Protein A/Ab/BSA	Titer higher than 10^3 EID$_{50}$/mL	50 µL	2h	(Wang et al., 2009)
Au IDAM	AI virus H5N1	Protein A/ Ab /BSA	2^{-1} HAU/50µl	30 µL	45 min	(J. Lin et al., 2015)
Au	Ad5	1,6-HDT/AuNPs/MUA/EDC+NHS/Ab	30 virus particles/mL	200 µL	_	(D. Lin et al., 2015)
Au	PPV	1,6-HDT/AuNPs/Ab/BSA	10 pg/mL	_	30 min	(Jarocka et al., 2011)
Pt wire	*Aphanomyces invadans*	G-AuNPs/SAM-Ab-BSA/GCE	309 ng/mL	_	10 min	(Qi et al., 2017)
Au SPE	TREM-1/MMP-9/HSL	Thiolated Ab	-3.3 pM for TREM-1 -1.1 nM for MMP-9 from mock wound fluid -1.4 nM for HSL	10 µL	< 1 h	(Ciani et al., 2012)
Au	cTnI/sLOX-1	16-MHDA/BT-caproyl-DPPE species/NA/BT/Ab	10^{-13} M for each analyte in PBS and serum	_	30 min	(Billah et al., 2012)
IDAM	hTB antigen	Ab/blocking buffer	10 ng/mL	10 µL	10 min	(Cui et al., 2013)
Au	CD14/CD16 monocytes	MUA-MH/Protein G/BSA/Ab	10^3 cfu/mL	1 mL	2h	(Montrose et al., 2013)
Flat Au wire	Mb	MUA-MPA/EDC-NHS/Ab-Mb/BSA	5.2 ng/	_	_	(Rajesh et al., 2010)
Screen-printed MWCNTs	Mb	Ab-Mb/BSA	0.08 ng/mL	5 µL	_	(Khan et al., 2016)
ITO-coated glass plates	Mb	APTES/ EDC-NHS/Pt(MPA)/Ab-cMb/BSA	1.70 ng/mL		12 min	(Mishra et al., 2014)
Au	cTnI	(MHA)/EDC-NHS/TMB/EDCH-NHS-/Dendrimer/Ab/BSA	11.7 ± 0.62 fM (0.28 ± 0.015 pg/mL)	_	1 h	(Akter et al., 2017)
Au microelectrode	D-dimer	SWCN-COOH/Ab/casein	0.1 pg/mL (0.53fM)	_	10 min	(Bourigua et al., 2010)

SWCNT SPE	EGFR	CNT/EDC/NHS/Ab/BSA	2 fg/mL	_	_	(Asav & Sezgintürk, 2014)
Au	EGFR	AuNPS/ Cys/PDITC/Protein G/Ab	-0.34 pg/mL in PBS -0.88 pg/mL in human plasma	_	1 h	(Elshafey et al., 2013)
Au microelectrode	PSA	16MHDA/EG3SH/EDC-NHS/Amine-PEG-BT/Avidin-(BT Ab-Ag Psa-HRP Ab)	- 0.51 ng/mL for t-PSA -0.07 ng/mL for f-PSA	_	_	(Gutiérrez-Zúñiga et al., 2016)
Au	CA-125	MPA/EDC-NHS/AuNP-SiO2/QDs/mAb	0.0016 U/mL in serum of ovarian cancer patients	_	< 1 h	(Johari-Ahar et al., 2015)
Polycrystalline Au	MDM2	Cysteamine (CA) SAM/1,4-phenylene diisothiocyanate (PDITC)/Ab/EA	0.29 pg/mL	_	_	(Elshafey et al., 2013)
Oxidised GCE	DHEAS	ox-GCE/AuNPs-ARG/Ab/EDC/NHS/BSA	7.4 µg/dL in blood plasma samples	_	_	(Lima et al., 2019)
GCE	Testosterone	EDC-NHS/SA/BSA/Nanobody	0.045 ng/mL	20 µL	1 h	(Li et al., 2016)
Au	Rabbit IgG	Ptyr/sulfo-SMCC/Nanobody	666 fM	10 µL	30 min	(Goode et al., 2016)
Au IDµE	Her4 tumour protein	Cys-Her4 affimer/PBS-tween 20 based starting block (SB)/Her4	< 1 pM in buffer and serum	_	30 min	(Zhurauski et al., 2018)

*Table legend: 1,6HDT: 1,6-hexanedithiol; 11M1UD: 11-Mercapto-1-undecanol; 16MHDA: 16-Mercaptohexadecanoic; 2M2P: 2-methyl-2-propanethiol; Ab: antibody; AEE: 2-(2-aminoethoxy) ethanol; APTES: 3-aminopropyltriethoxy silane; AuNP@SiO2: silica-coated gold nanoparticles; bTB: bovine tuberculosis; BCNT-IL: bamboo-like multiwall carbon nanotubes-ionic liquid; BSA: bovine serum albumina; BT: biotin; CA-125: cancer antigen 125; ConA: concanavalin A; CS: chitosan; cTnI: Cardiac troponin I; DHEAS: dehydroepiandrosterone sulfate; DIEA: N,N-diisopropylethylamine; DTSP: 3-dithiobis-(sulfosuccinimidyl-propionate); EA: ethanolamine ; ECD: Epichlorohydrin; EG3SH; tri(ethylene glycol); EGFR: epidermal growth factor; G-AuNPs: Graphene gold nanoparticles; GCD: glassy carbon disc; GLU: glutaraldehyde; GPMS: (3-glycidoxypropyl)trimethoxysilane; Cys: cysteamine; HA: hyaluronic acid; hTB: Human tuberculosis; IDμE: interdigitated micro-electrode; MACA: mercaptoacetic acid; Mb: myoglobin; MBA: 4-mercaptobenzoic acid; MDM2: Murine double min 2; MH: 6-mercapto-1-hexanol; MHDA: Mercaptohexadecanoic; MgNbs: Magnetic nanobeads; MgNPs: magnetic nanoparticles; MNAC: magnetic nanoparticle-antibody conjugates; MPA: 3-mercapto propionic acid; MUA: mercaptoundecanoic acid; MWCNT: multi-walled carbon nanotube; NAM: nanoporous alumina membrane; NA: neutravidin; PAMAM: polyamidoamine; PANI: polyaniline; PDITC; 1,4- phenylene diisothiocyanate; PEG-thiol: carboxy-thiolpolyethyleneglycol; PEI: Polyethyleneimine; PFP: 2,3,4,5,6-pentafluorophenol; PoPD: poly (ortho-phenylenediamine; PP3CA: poly(pyrrole-3-carboxylic acid); PSA: prostate-specific antigen; PSSA: polystyrene sulphonic acid; Ptyr: Polytyramine; QDs: quantum dots; rGO: reduced graphene oxide; rGOP: Reduced graphene oxide paper; RGS: reduced graphene sheets; SA: streptadivin; sLOX-1: Soluble lectin-like oxidised low-density lipoprotein receptor-1; SPCE: screen-printed carbon electrode; SPE; screen-printed electrode; SPIE: screen-printed interdigitated electrode; sulfo-SMCC: sulfosuccinimidyl 4-[N-maleimidomethyl] cyclohexane-1-carboxylate; SWCN: single-walled carbon nanotube; TMB: 3, 3′,5, 5′-tetramethyl benzidine; VACNT: vertically aligned carbon nanotube; WGA: wheat germ agglutinin. Table reproduced from (Leva-Bueno, Peyman & Millner, 2020).

1.8. *Escherichia coli* (employed for antibody-based biosensor)

E. coli is a rod-shaped Gram-negative anaerobic bacterium. It is typically found in birds' and mammals' gastrointestinal tracts (Lim et al., 2010; Leung & Gallant, 2014). Common *E. coli* strains are not pathogenic even at elevated concentrations. However, some *E. coli* strains are pathogenic and can be virulent towards host organisms (Lim et al., 2010). *E. coli's* main pathologies can be divided into three main clinical syndromes: diarrhoeal disease, urinary tract infections and sepsis/meningitis (Kaper et al., 2004). Some of the following *E. coli* pathotypes cause these syndromes or pathologies: enteroinvasive (EIEC), enteropathogenic (EPEC), enteroaggregative (EAEC), enterohaemorrhagic (EHEC), enterotoxigenic (ETEC), diffusively adherent (DAEC) and uropathogenic *E. coli* (UPEC) (Clements et al., 2012; Kaper et al., 2004; Kudinha, 2017).

1.8.1. *Escherichia coli* pathogenesis

Urinary tract infections (UTIs) are caused by *E-coli* in 80-90% of the cases, mainly caused by pathotype UPEC. UTIs are more frequent in women, and it is primarily attributed to host focal flora extending the infection to the lower genitourinary tract via the perineal, vaginal and periurethral regions where these bacteria endure. Contaminated water could also be an origin of infection. Several virulence factors are related to the UTIs' pathologies: toxins, adhesins, siderophores, invasins and protective polysaccharide coatings. *E. coli* colonises the bladder through the use of adhesins. There, *E. coli* compete with the host for iron and release toxins such as alpha-hemolysin and CNF-1. These toxins can inflame the urinary tract and cause tissue damage and cellular disorder. The infection's persistence and specific protein (Usp) develop the infection extension to the bloodstream. This event can result in conceivably fatal sepsis from bacteremia (Kudinha, 2017).

These events reflect the concern of an early *E. coli*-derived UTI diagnosis. *E. coli* is the leading cause of bacteraemia in under 3 years old infants and is among the most common isolated organisms in sepsis (Mahjoub-Mes*sai* et al., 2011; Lefort et al., 2011). In addition, 10-15% of children with UTI will suffer permanent kidney damage, causing eventually chronic hypertension and renal insufficiency. Moreover, UTIs can also be responsible for bacterial meningitis and pneumonia, causing maternal and neonatal deaths during pregnancy (Kudinha, 2017). In addition, a common *E. coli* gut infection is manifested by diarrhoeal disease, attributed to pathotypes EAEC, ETEC, EHEC and EPEC (Schultsz et al., 2000).

1.8.2. Current detection methods for *Escherichia coli*

Current techniques for *E. coli* diagnosis commonly involve urine or stool sample analysis through mass spectrometry, especially matrix-assisted laser desorption ionisation time-of-flight mass spectrometry (MALDI-TOF MS). This technique has substantially improved microorganism identification (Croxatto et al., 2012). Other frequent *E. coli* diagnosis techniques are enzyme immunoassays (EIA), real-time PCR and pulse-field electrophoresis (PFGE) (Everley et al., 2008). However, these techniques present several issues as they are expensive and labour intensive, require trained personnel, and do not yield instant data (Everley et al., 2008). In the case of MALDI-TOF MS, hours of bacteria culture from urine and stool samples are required for the analysis. The presented techniques show the need for new diagnostic technologies which can be user-friendly, cheap and rapid. This will be beneficial for individuals and will be translated into a reduction in healthcare costs.

1.9. Collagen

Collagen is the most present protein in animals, with at least 28 types described and at least made of 46 different polypeptide chains. Collagen is a fibrous, structural protein in a right-handed triple helical structure composed of three parallel left-handed polyproline II-type (PPII) helices. Each of the PPII helices results from a repeating X-Y-Gly sequence, where X and Y are other amino acids (Shoulders & Raines, 2009).

Collagen type I (Col-I) can be found either as a homotrimer or heterotrimer, and it is made of more than 1000 amino acids, yielding a length up to 300 nm and a width of 1 to 5 nm with a molecular mass of around 300,000 Dalton. Three domains compose the Col-I structure: central domain, C telopeptide, and the N telopeptide. Most of the molecule structure is located in the central domain, up to 95 %. The structure of Col-I is the same as for general collagen, which consists of a repeating α-β-Gly sequence, where α and β are aminoacids other than Gly. The glycine position is fundamental for establishing the formation of the helical structure (Naomi, Ridzuan & Bahari, 2021). The collagen composition varies among types and variants. The composition of Bovine-skin type I collagen (BAT) is glycine (33.40 %), proline (12.90 %), hydroxyproline (9.20 %), alanine (10.5 %), glutamic acid (8.01 %), aspartic acid and arginine (both 4.80%), and others (Zhao & Chi, 2009).

This research uses Col-I from calfskin as a bioreceptor for whole pathogen capture. The carboxylic acid presented by glutamic acid and aspartic acid are covalently bond to NH_2 from polyoctopamine (POc) via EDC/sulfo-NHS as detailed in **Section 2.2.5.3** and studied in **Chapter 6**. Col-I from bovines are easily available, presents low immunogenicity and is biocompatible (Naomi et al., 2021).

1.10. Adhesins - *Yersinia* adhesin A (YadA) of *Yersinia enterocolitica*

To affect the colonisation of different tissues or the infection of a host cell, a bacterial cell requires adhesion to its surface. The molecules that bacteria employ to adhere in the first instance are called adhesins and are predominantly monomeric (Pizarro-Cerdá & Cossart, 2006). Some of the expressed adhesins specifically adhere to one host cell factor and others can bind to several of them (Pizarro-Cerdá & Cossart, 2006; Meuskens et al., 2019). Gram-negative bacteria such as *E. coli* and a few Gram-positive have fimbria or pili, filamentous structures anchored to the bacterial outer membrane whose function is to attach bacteria to a surface. Fimbria and pili are described as scaffold-like rod that contains an adhesin at the tip. Type I pili are examples of pili or fimbria encoded in *E. coli*, uropathogenic *E. coli* (UPEC) and diffusely adhesive *E. coli* (DAEC), which contains a region, FimH, that targets monomannose and trimannose-containing glycoprotein receptors. The different types of pili are expressed according to the bacterial species or strain and the targeted surface. Apart from fimbria and pili, many different adhesins attach to other components of host-cell surfaces or ECM proteins, such as collagen, laminin, elastin, and proteoglycans. One of these adhesins is the adhesin *Yersinia* adhesin A (YadA) and it is expressed by enteropathogenic *Yersinia enterocolitica* and *Yersinia pseudotuberculosis* (**Figure 1.19A**). YadA is part of the autotransporter adhesins group (type V secretion systems) (Nummelin et al., 2002; Leo et al., 2008; Mühlenkamp et al., 2015). These molecules are trimeric autotransporter adhesins (TAAs) and are present on the bacterial surface (Linke et al., 2006).

Autotransporter molecules are proteins located on the bacterial surface and are in charge of protein secretion. This secretion system is known as Type V secretion (Leo et al., 2012). Many autotransporters have been identified to play a role in the adhesion of *E. coli*. For instance, BabA, an autotransporter adhesin found in *Helicobacter pylori* (Ilver et al., 2012) attach to the Le^b group antigen, which is a blood group antigen of the red blood cells in the gastric mucosa. In the advanced infection process, another autotransporter, SabA, was also identified (Mahdavi et al., 2007).

The TAA’s molecular organisation comprises a head-stalk-anchor structure. Both the N-terminal head and stalk exhibit a small set of domains that appear repetitively, and it is theorised to be directly involved in the adhesion to the host (Linke et al., 2006). These adhesins are presented by several Gram-negative bacteria and allow them to interact with ECM proteins. ECM is composed of different proteins such as collagen, laminin, fibronectin, and glycoproteins like vitronectin (Vn) or glycosaminoglycans (GAGs) and others. Vn is glycosylated, showing three N-linked glycans, and its conformation depends on the interaction with other molecules such as heparin. YadA has been shown to bind several proteins of the ECM, including collagen, fibronectin and laminin (El Tahir & Skurnik, 2001; Meuskens et al., 2022).

In this project, YadA from different *Y. enterocolitica* serotypes have been expressed in *E. coli. Y. enterocolitica* is extensively found in nature, from intestinal tract in mammals to aquatic niches. The strains found in humans are usually located in the intestinal tract and cause enteritis. *Y. enterocolitica* is classified into 6 biogroups according to phenotypic features, 5 of them considered pathogenic. The most common isolated strains in humans are O:3, O:5,27, O:8 and O:9 (Fàbrega & Vila, 2012). There are different *Yersinia* serotypes, O:X, based on the O-antigen, the terminal glycan part of the Lipopolysaccharide (LPS). To avoid mentioning YadA and which *Y. enterocolitica* comes from, the following nomenclature is used $\text{YadA}_{\text{O:X}}$.

The structure of the head domain for $\text{YadA}_{\text{O:3}}$ was solved in (Nummelin et al., 2004). The major difference between YadA head domains from different serotypes is that $\text{YadA}_{\text{O:9}}$ presents a loop insertion that has recently been described to bind glycans (Meuskens et al., 2022). $\text{YadA}_{\text{O:9}}$ binding to glycans finding was carried out in collaboration with Ina Meuskens and detailed in **Chapter 7** of this thesis. $\text{YadA}_{\text{O:3}}$ and $\text{YadA}_{\text{O:8}}$ present shorter loops (**Figure 1.19B**). The loop insertion in $\text{YadA}_{\text{O:9}}$ had initially been described as important for cell binding (Heise & Dersch, 2006) and was later described to rely on vitronectin binding (Mühlenkamp et al., 2017). Later, it was shown that it is not vitronectin directly that is bound. Instead, $\text{YadA}_{\text{O:9}}$ binds the glycan moieties found as a post-translational modification on the vitronectin. YadA from all *Y. enterocolitica* serotypes interacts with different ECM molecules (Meuskens et al., 2019). Many of these interactions with other ECM proteins occur independently of which *Y. enterocolitica* serotype the YadA comes from. Some of the significant interaction targets are collagen (Leo et al., 2008; Leo et al., 2010), fibronectin and laminin (Meuskens et al., 2019). This project focuses on the YadA-collagen interaction, using collagen as a novel receptor for detecting YadA-expressing bacteria.

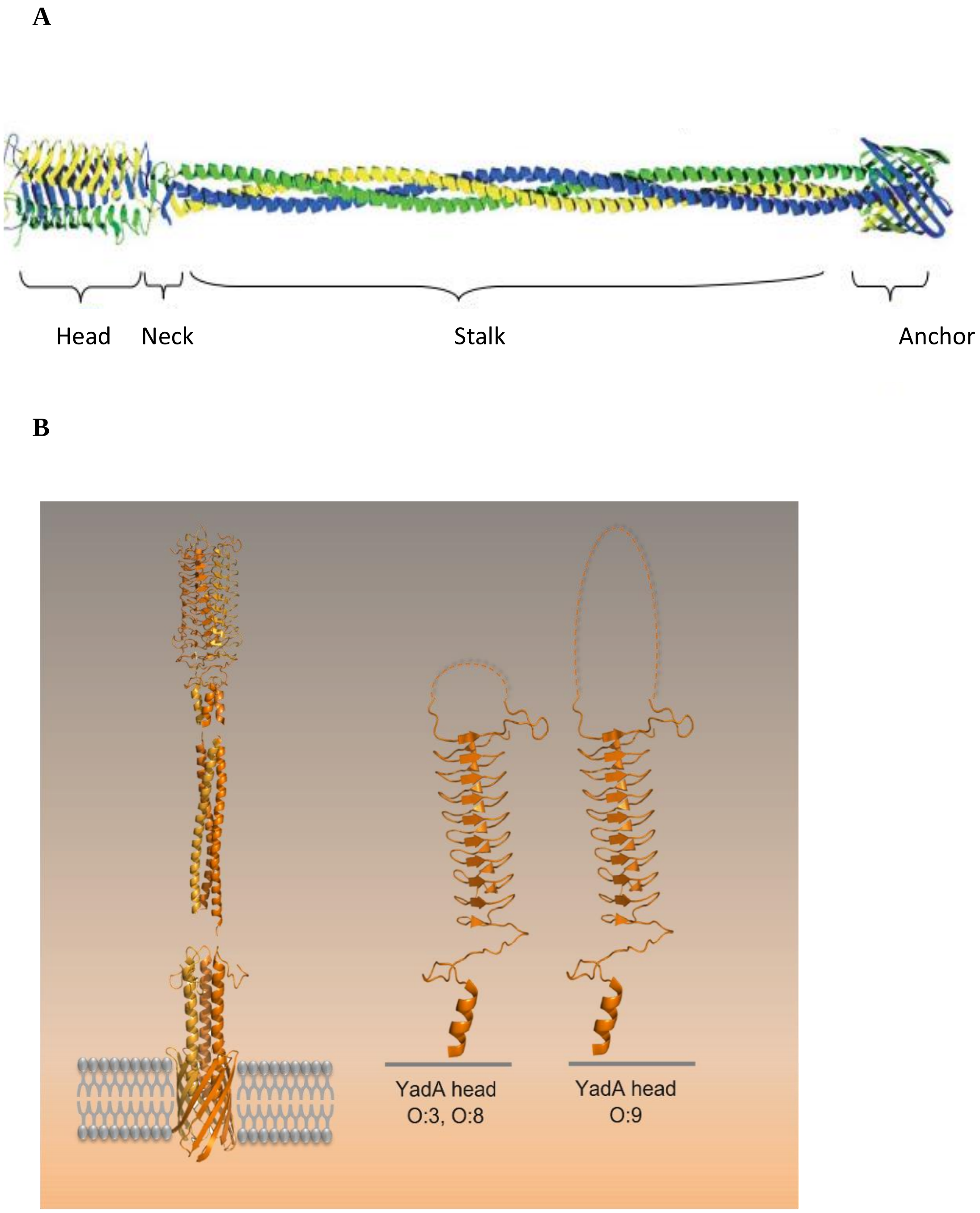

Figure 1.19: Scheme of a YadA complete structure and different YadA from different *Y. enterocolitica* serotypes. A, the membrane anchor domain is found at the C terminus of the TAAs structure and it is homologous to all different TAAs. The stalk domains consist of highly repetitive structures and are variable in length. The head domain corresponds to the N terminus of the TAA and typically possesses the motifs that bind to ECM proteins. Reproduced from (Linke et al., 2006). **B**, different YadA head domain structures can be observed. YadA$_{O:3}$ and YadA$_{O:8}$ present shorter head domains compared to YadA$_{O:9}$, in which the inserted loop responsible for glycan binding can be observed. Figure **B** provided by Ina Meuskens (University of Oslo).

1.11. Introduction to microfluidics

Microfluidic devices are a network of micron-sized channels fabricated into a solid substrate through which fluid can be pumped. Microfluidics or lab-on-a-chip (LOC) is a relatively new scientific field that appeared in the 1980s and emerged in the 1990s. The field combines different sciences such as chemistry, biology, physics, fluid dynamics, etc. Given the different purposes and applications, microfluidic devices are also referred to as microreactors, LOC, or organ-on-chip. The miniaturisation reduces the reagent consumption, the price per analysis due to the ability of multiplex on a single device, the risk of contamination and improves sensitivity and specificity (Niculescu et al., 2021). These features and portability make microfluidic devices excellent platforms for POC diagnostic devices (Lei, 2012). Microfluidic devices are used to make new constructs for drug delivery, cell targeting and analysis, clinical and environmental diagnosis, cell culture, etc. These devices can be a powerful analytical tool as they can integrate an analytical procedure onto a single device, such as sample pretreatment, manipulation, separation and detection of the sample or reagent.

Microfluidics aims to take advantage of these micro-engineered devices to manipulate small amounts of fluids. These fluids can be manipulated by external pumps such as syringe pumps, pressure pumps or by integrated on-chip pumping mechanisms. The device’s material determines other properties such as the fluid’s contact angle, the durability of the material, the biological and chemical compatibility with the reagents, and to match certain pressure and temperature conditions. Thus, different materials can be employed for microfluidic device fabrication: silicon, polymers, ceramic and glass are just some examples found in the literature (Lei, 2012; Niculescu et al., 2021).

Polymers are usually cheaper than other materials such as silicon substrate and can be used to develop devices for different biological analytical purposes such as immunoassays, nucleic acid and cell detection. Some polymeric materials can yield transparent or semi-transparent devices that allow optical interrogation. The most common polymeric material employed for microfluidic device fabrication is polydimethylsiloxane (PDMS), polymethylmethacrylate (PMMA) and polycarbonate (PC) (Lei, 2012; Niculescu et al., 2021).

PDMS is widely used given its cheap fabrication cost and properties: biocompatibility (Nielsen et al., 2020), hydrophobicity (Pan et al., 2018), transparency (Nielsen et al., 2020), easy to prototype (Nielsen et al., 2020), etc. These properties make PDMS microfluidic devices good candidates for many applications in the bio-research field, including cell culture, pathogen detection, cell screening, etc (Rivet et al., 2011). However, many organic solvents cannot be employed due to the PDMS porosity. Their molecules can diffuse into and be incorporated into the channel walls (Liao et al., 2019). Water evaporation has proven to be a drawback on some occasions, leading to a more concentrated sample. PMMA shows no small-molecule absorption, thus widening the solvent possibilities (Campbell et al., 2021). In addition, it provides good mechanical properties and permits surface modification. The device employed in this project was made of PC: a durable material (Nge et al., 2013) that offers low moisture absorption, high glass transition temperature and great machining properties. However, PC presents low resistance to various organic solvents and UV absorbance. These properties make PC more suitable for use in biomedical research and bioanalyses (Ogończyk et al., 2010).

Nowadays, the fabrication methods are extensive and can be classified into: chemical, such as inkjet 3D printing, employed for the fabrication of PDMS masters or etching masks (Niculescu et al., 2021); mechanical, such as hot embossing, typically used for the fabrication of PMMA and PC devices (Deshmukh & Goswami, 2020); laser-based, such as stereolithography, used to create 3D polymeric devices with special features; and others such as soft lithography, typically used to fabricate PDMS devices (Niculescu et al., 2021).

The employment of microfluidic devices in diagnostics is extensive. Various studies have reported them, such as detection of creatinine levels (Narimani et al., 2020), detection of hormones (for instance for pregnancy test using paper microfluidics) (Walgama et al., 2020), as a diagnostic technique for COVID-19 (in which SERS coupled with the microfluidic device was employed as a detection platform) (Jadhav et al., 2021), using microfluidic digital PCR for the chromosomal aneuploidy detection (Fan et al., 2009), and other applications. Microfluidic devices have also been employed for whole bacteria detection via electrochemical impedance. Bacteria from ground beef samples were electrochemically detected using a microfluidic device. The microfluidic chip inserted gold IDAM functionalised with magnetic nanoparticle-antibody conjugates, which allowed the bacteria to be targeted from 10^4 to 10^7 cfu/mL (Varshney et al., 2007); *Listeria* cells were detected through the combination of EIS technique and a microfluidic device and allowed detection of 1.6×10^2 cfu/mL after the immunoreaction (Chen et al., 2016); *E. coli* was electrochemically detected through impedance by employing a microfluidic chip with interdigitated microelectrodes inserted and a micro-mixing zone. The bacteria was detected at an LOD of 500 cfu/mL (Wang et al., 2018).

The Reynold number (Re) controls the microfluidic fluid flow, representing the relative ratio between inertial and viscous effects (**Equation 1.5**).

$$Re_c = \frac{\rho U D_h}{\mu} \qquad \textbf{Equation 1.5}$$

where ρ corresponds to the fluid density, and it is expressed in kg/m^3; U to the flow velocity average of the flowing liquid, expressed in m/s; D_h to the hydraulic diameter of the channel, expressed in m and calculated as $D_h = 2wd/(w + d)$ for a rectangular section, where w and d are width and depth of the channel; and μ to the fluid viscosity, expressed in Ns/m^2. Laminar flow typically works $\sim 1 < Re_c < \sim 100$ and turbulent flow typically $Re_c > \sim 2000$ (Rodriguez-Mateos et al., 2021). It is interesting to work at lower Re_c as the fluid behaviour can be easily predicted, making the liquid flow controllable and avoiding turbulent mixing, which increases with time (Peyman *et* al., 2009).

1.12. Project aims

The project's main aim was to develop and optimise a label-free impedimetric ECM protein-based biosensor employing commercial SPGEs to detect whole bacteria based on the ECM protein-adhesin interaction. The YadA-collagen binding will be used to develop biosensors, given the well-known interaction reported in the literature. The employment of collagen as ECM protein to bind $YadA_{O:8}$-expressing bacteria for a low-cost, rapid test analysis had to be investigated. The fabrication and step-by-step optimisation of the biosensor could lead to the development of a novel impedimetric biosensor which could present alternatives to the current ones employing antibodies or related molecules such as nanobodies and Affimers. The main advantage of the antibody-based biosensor is the high specificity for a pathogen. However, being too specific to a particular pathogen could miss other species detection. ECM proteins could present a competitive alternative to classic immunosensors since ECM proteins as bioreceptors could offer pan-specificity: the biosensor could detect a group of organisms rather than a specific organism. By detecting a group of organisms, clinicians could perform a rapid diagnostic test to start treatment. A balance in specificity could provide more accurate diagnostics results for clinicians. In addition, the cost of ECM proteins production could be more competitive than antibodies or other methodologies in the market as bioreceptor.

The biosensor construction will consist of two parts. First, a non-optimised collagen-based biosensor for $YadA_{O:8}$-expressing bacteria will be developed. With the use of a proprietary protocol from ELISHA Ltd., the collagen will be the entrapped in a non-conducting polymer over the SPGEs, allowing a rapid biosensor fabrication for bacterial screening. Secondly, a biosensor will be optimised step-by-step to achieve the best sensitivity and selectivity in the fastest analysis time. For that, the ECM protein will be covalently attached to the non-conducting polymer via cross-linkers. This biosensor will be later compared to classic immunosensor performance reported in the literature.

Another main objective of this PhD was to assess the stability, reproducibility and variability of different commercial SPGEs. Different parameters such as ink composition, room conditions such as humidity, temperature and curing process could affect the performance from one SPGE to another. Therefore, it was of great interest to establish a pretreatment protocol for SPGE to allow the best reproducibility and stability of the biosensor construction and analyte testing. Different pretreatments methods for gold electrodes have been reported in the literature. Some of the most commonly employed pretreatment techniques, such as CV in H_2SO_4, have contradicting advice on their use. No literature has been found about the effect of pretreatment for different coatings over SPGE.

Chapter 2

Materials & methods

Chapter 2: Materials and methods

2.1. Materials

2.1.1. Chemicals

Yeast extract, tryptone, agar, H_2SO_4, Na_2HPO_4, NaH_2PO_4, KH_2PO_4, Na_3PO_4, NaOH, KCl, octopamine hydrochloride, 11-mercaptoundecanoic acid (11-MUA), (+)-biotin N-hydroxysuccinimide ester (NHS-biotin), acetic acid and ethanol were purchased from Sigma Aldrich (UK). NaCl, tyramine hydrochloride and DMSO was purchased from Fisher Chemical (UK). $K_3[Fe(CN)_6]$, $K_4[Fe(CN)_6] \cdot 3H_2O$ and ethanol were purchased from VWR International (UK). NeutrAvidin was purchased from Invitrogen (UK). Sodium *meta*-periodate, HCl, sulfo-NHS (N-hydroxysulfosuccinimide), 1-ethyl-3-(3-dimethylaminopropyl) carbodiimide (EDC) and 1 M MES buffer pH 7 were purchased from Thermo Fisher Scientific (UK). Anhydrotetracycline hydrochloride (AHTC) was purchased from Abcam (UK). Heparin-biotin sodium salt was purchased from Merck (UK).

The 10 mM PBS was made with 137 mM NaCl, 2.7 mM KCl, 10 mM Na_2HPO_4 and 1.8 mM KH_2PO_4. Ten times PBS was made using the same ratio multiplied by 10.

2.1.2. Proteins

Polyclonal antibodies were raised in rabbits against a mixture of *E. coli* strains (*E. coli* BL21, 35218, DH5a, HGB101, and NCTC10418) performed by GenScript (USA). Anti-protein A antibodies were from GenScript (USA). Goat HRP-conjugated anti-rabbit, calf skin collagen, BSA and casein powder from bovine milk were all purchased from Sigma Aldrich (UK). Collagen was resuspended to a 1 mg/mL final stock concentration in 0.01 M acetic acid. Rabbit anti-collagen type I from bovine and human was purchased from 2BScientific (UK).

2.1.3. Bacteria

E. coli 35218, HB101, NCTC10418, DH5a, and BL21 were obtained from John Wright, Faculty of Biological Sciences, University of Leeds. *E. coli* Top10 pARA sfGFP was donated from the University of Oslo, which was used for the expression of YadA of *Yersinia enterocolitica* serotype O:8 and O:9 from *pASK-Iba4c*.

2.1.4. Electrodes

Gold screen-printed Metrohm DropSens CX2223AT and CX2220AT electrodes from Metrohm DropSens Ltd contained two gold working, a counter and an Ag/AgCl reference electrode forming a 4-electrode chip (**Figures 2.1A-B**). The working electrodes are defined as WE1 and WE2 for working electrode 1 and working electrode 2 respectively. BVT-AC1.W1.RS.Dw2 from BVT Technologies contained one gold working, one counter, and a 98 % Ag/ 2 % Pd reference electrode, forming a 3-electrode chip (**Figure 2.1C**). For clarity, Metrohm DropSens CX2223AT is defined as Electrode 1, Metrohm DropSens CX2220AT as Electrode 2 and BVT-AC1.W1.RS.Dw2 as Electrode 3.

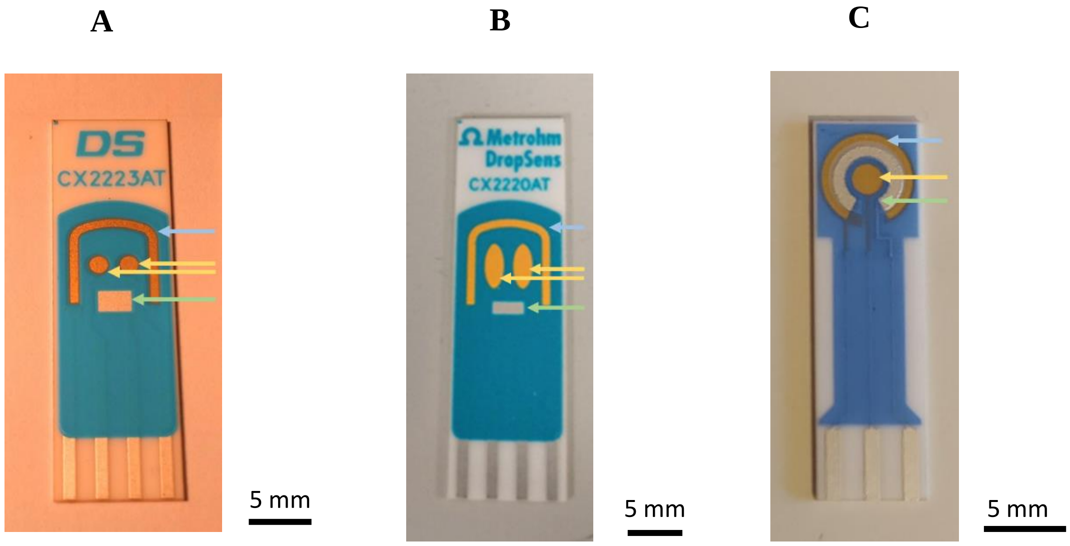

Figure 2.1: Metrohm DropSens CX2223AT (Electrode 1), Metrohm DropSens CX2220AT (Electrode 2) and BVT-AC1.W1.RS.Dw2 (Electrode 3) from BVT Technologies. A, replicate from **Figure 1.7**. Metrohm DropSens SPGE CX2223AT consists of a 4 electrode-chip made of 2 round gold working electrodes, a U-shaped gold counter electrode and a rectangular Ag/AgCl reference electrode. **B**, Metrohm DropSens SPGE CX2220AT consists of a 4 electrode-chip made of 2 oval gold electrodes, a U-shaped gold counter electrode and a rectangular Ag/AgCl reference electrode. **C**, BVT-AC1.W1.RS.Dw2 SPGE from BVT Technologies consists of a 3 electrode-chip made of 1 round gold working electrode, an O-shaped gold counter electrode and an O-shaped 98 % Ag/ 2 % Pd reference electrode. Working (▬), counter (▬) and reference electrode (▬).

2.1.5. Electrochemical equipment

Autolab workstation consisted of Autolab type III Fra II potentiostat and NOVA (2.1.4) software were from Metrohm Autolab B.V. (The Netherlands) (**Figure 2.2**). Palmsens workstation consisted of Palmsens4 potentiostat, galvanostat and frequency response analyser (FRA), PSTrace (5.8) software, a channel multiplexer (MUX8-R2) and an electrode adapter were from Palmsens B.V. (The Netherlands) (**Figure 2.3**).

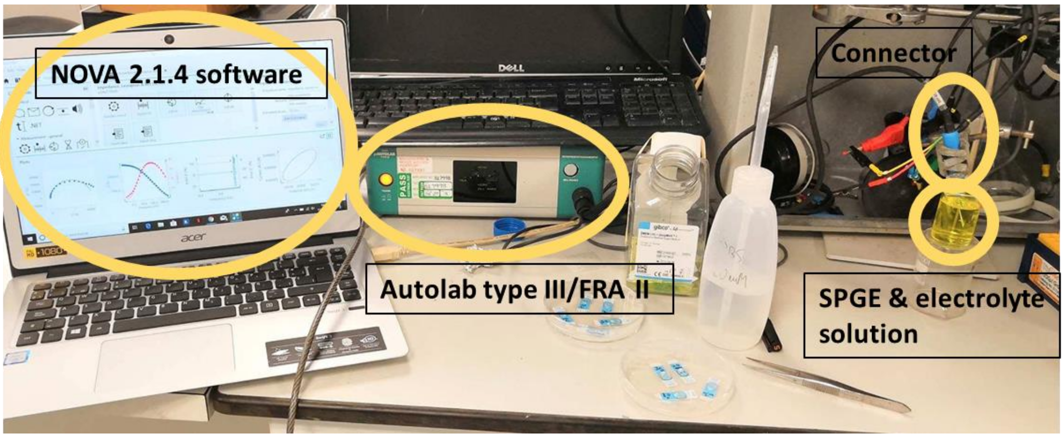

Figure 2.2: Autolab workstation setup. The Autolab type III Fra II potentiostat connected to a single Electrode 2 through a connector and immersed in an electrolyte solution. The potentiostat is controlled by NOVA 2.1.4 software.

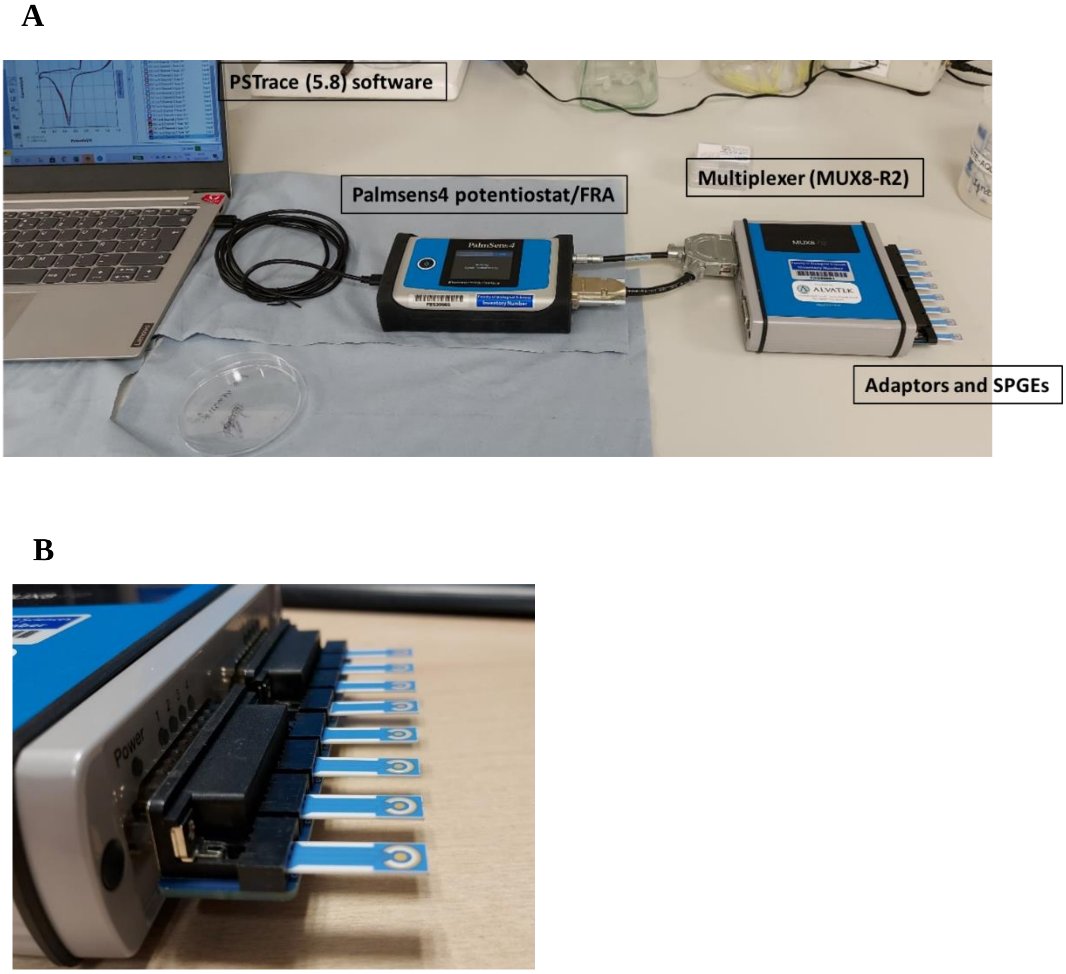

Figure 2.3: Palmsens workstation setup. A, Palmsens4 potentiostat, galvanostat and frequency response analyser (FRA) coupled to a multiplexer (MUX8-R2) with adaptors connected to 8 different Electrodes 3. The potentiostat was controlled through PSTrace 5.8 software. **B**, a closer image corresponding to the adapter and the set of 8 SPGEs.

2.2. Methods

2.2.1. Electrode pretreatment

The CV in H_2SO_4 pretreatment was conducted by spreading 100 µL of 0.1 M H_2SO_4 across the Electrodes 2 and Electrodes 3' surface. Next, 15 CV cycles were applied at a scan rate of 50 mV/s and potential applied of 0.0 V to +1.4 V using Autolab workstation. The electrodes were rinsed with diH_2O and air-dried using an Ar or N_2 gas stream. Next, ethanol pretreatment was carried out by immersing the electrode in 97 % ethanol solution for 30 min. After that, the electrodes were rinsed with diH_2O and air-dried using an Ar or N_2 gas stream.

2.2.2. Polymer electrodeposition

2.2.2.1. POc electrodeposition in Chapter 3

A final concentration of 5 mM octopamine in 10 mM phosphate buffer pH 7.2 was created. Then, the solution was spread over the Electrodes 2 and Electrodes 3 surface using a pipette and electropolymerised. Two CV cycles were applied at a scan rate of 100 mV/s from 0.0 V to +1.6 V using Autolab workstation.

2.2.2.2. POc electrodeposition in Chapter 7 for microfluidics experiments

Octopamine was dissolved at a concentration of 2.5 mM in 10 mM PB at a pH 7.2 and electropolymerised over Electrodes 2 by applying a two-cycle CV at a scan rate of 100 mV/s and an applied potential from 0.0 V to +1.6 V using Autolab workstation.

2.2.2.3. POc-antibody-complex electrodeposition

The mixed POc-Ab bioreceptor complex was created following a protocol provided by ELISHA Systems Ltd. Twenty-five µL of 5 mM octopamine in 10 mM PB pH 7.2 was mixed with a solution of 200 µg/mL antibody at a ratio of 1:1 and then kept in ice. The resulting solution consisted of 2.5 mM octopamine and 100 µg/mL antibodies. After that, the solution was spread over the Electrodes 2 and Electrodes 3 and electropolymerised applying two CV cycles at a scan rate of 100 mV/s from 0.0 V to +1.6 V using Autolab workstation.

2.2.3. SAM formation

A solution of 10 mM of 11-MUA in ethanol was created. Next, the Electrodes 2 and Electrodes 3 were submerged in the solution for 24 h to allow SAM formation. The SPGEs were subsequently washed with 10 mM PBS pH 7.2 to remove the excess of unbound 11-MUA.

2.2.4. Bacterial culture

2.2.4.1. *E. coli* (DH5a) - growth and culture

LB broth was made by mixing: 5 g NaCl, 5 g yeast and 10 g tryptone (1:1:2) (w/w) dissolved in 1 L diH_2O. LB agar plates were also made in the lab from NaCl, yeast, tryptone and agar at a ratio of 1:1:2:2.4 (w/w) dissolved in diH_2O. Both solutions were shaken until complete dissolution and subsequently autoclaved at 120 ℃. Next, a single colony of *E. coli* DH5a was added to 5 mL of LB broth and left shaking in an incubator at 37 ℃ at 180 rpm for 16-18h. The subculture was prepared in LB medium and left at 37 ℃ at 180 rpm until the desired OD_{600}. Then, the sample was centrifuged and resuspended in 10 mM PBS pH 7.2. Different bacterial concentrations were made through serial dilutions.

2.2.4.2. *E. coli* Top 10 pARA_sfGFP preparation

2.2.4.2.1. Cloning O:8 FL

This methodology was performed by Ina Meuskens, another ESR on ITN ViBrANT at University of Oslo. For the pASK-Iba4c based YadA full-length constructs, Gibson cloning was performed. In short: YadA O:8 was PCR-amplified using Q5 polymerase from the plasmid used in (Saragliadis & Linke, 2019) using the following primers: 5’-CGACAAAAATCTAGATAACGAGGGCAAAAAatgactaaagattttaagatcagtgt-3’ and 5’-GCCATTTTTCACTTCACAGGTCAAGCTTAGttaccactcgatattaaatgatgca-3’. These primers have overlaps to pASK-Iba4c for later Gibson annealing. pASK-Iba4c was linearised in a PCR reaction using Q5 polymerase (New England Biolabs) and the following primers: 5’-CTAAGCTTGACCTGTGAAGT-3’ and 5’- TTTTTGCCCTCGTTATCTAGATT-3’. The plasmid and the insert were PCR purified, and DpnI (New England Biolabs) digested for 30 min at 37°C in Cutsmart buffer (New England Biolabs). DpnI was then inactivated by incubation at 80°C for 10 min. The Gibson assembly was carried out with a self-made Gibson mix for 20 min at 50°C with a 1:5 concentration ratio of the plasmid to insert. The assembly mix was transformed into TSS competent *E. coli* Top10 and incubated in SOC medium for 1 h at 37°C. The transformed *E. coli* were plated on LB agar plates with 12.5 µg/mL. From this plate, two colonies were chosen, and 5 mL overnight cultures were prepared with plasmids isolated the next day. After Sanger sequencing, the correct plasmid was transformed into fluorescent *E. coli* Top10 and used for further experiments.

2.2.4.2.2. Growth and induction of YadA expression

E. coli Top 10 pARA_sfGFP (El Tahir & Skurnik, 2001) were transformed with vector pIBA4c_YadA_FL and then were streaked out on a plate. The plate was supplemented with 25 µg/mL chloramphenicol, and just a single colony was picked for further experiments. The overnight cultures were grown in a 5 mL LB medium supplemented with 25 µg/mL chloramphenicol. The next day a subculture was prepared in LB medium, supplemented with 25 μg/mL chloramphenicol. The medium was grown at 37 °C and shacked in an incubator to an OD_{600} of 0.5, in which YadA expression was induced by the addition of 1:10.000 anhydrotetracycline (AHTC, 2 mg/mL stock). The YadA expression was left for another 2 h at 37°C in the shaking incubator. The negative controls were made by not adding AHTC. YadA expression could be checked by visual inspection of the bacterial aggregation behaviour, which was indicative of YadA surface presence (Leo et al., 2010). After expression, the OD_{600} was again calculated to determine the cfu. The bacteria were diluted to the required cfu in PBS and used for measurements.

2.2.4.3. *E. coli* Top10 glmS:sfGFP (AS75) and *E. coli* BL21 (DE3) Gold preparation

This methodology was performed by Ina Meuskens, another ESR on ITN ViBrANT at University of Oslo. *E. coli* Top10 glmS:sfGFP (AS75) was used for whole-cell fluorescence assay and in *E. coli* BL21 (DE3) Gold for protein purification. The growth conditions are described in (Meuskens et al., 2022).

2.2.5. Biosensor construction and optimisation

2.2.5.1. Impedimetric immunosensor optimisation

Electrodes 1 were pretreated by conducting CV for 5 cycles in 100 µL of 1 M H_2SO_4 spread across the surface. The voltammetric conditions were a scan rate of 100 mV/s, and the potential was applied from 0.0 V to +1.6 V using Autolab workstation. Once pretreated, electrodes were rinsed with diH_2O and dried using N_2 gas.

Then, both tyramine and octopamine were dissolved at a concentration of 0.025 M in different buffers, namely: 10 mM PBS pH 7.0, methanol, 1 M HCl, methanol + 0.3 M NaOH and 100 mM PB pH 7.5 + DMSO at 20 % (v/v). Once the best solvent was decided (100 mM PB pH 7.5 + DMSO at 20% (v/v)), the polymer concentration was optimised. Tyramine and octopamine were dissolved at 0.01, 0.025, 0.05 and 0.1 M in 100 mM PB pH 7.5 plus DMSO at 20% (v/v). Next, Electrodes 1 were polymer-coated through electrodeposition by applying a two-cycle CV at a scan rate of 100 mV/s and an applied potential from 0.0 V to +1.6 V using Autolab workstation. For the rest of the immunosensor optimisation and final biosensor construction, 0.1 M of tyramine was dissolved in 100 mM PB pH 7.5 + 20% (v/v) DMSO and electropolymerised as previously mentioned.

Both antibodies used, anti-*E. coli* for specific analyte detection and anti-protein A as control were oxidised to create reactive aldehyde groups to achieve a covalent bond with the polymer amine groups as employed in (Shamsuddin, 2018). This was carried out by first diluting antibodies in 10 mM PBS pH 7.2 to a final concentration of 3 mg/mL. Next, both antibodies were added to an equal volume of 20 mM sodium *meta*-periodate dissolved in Glycolink coupling buffer, then covered with aluminium foil and rotated for 30 min. After that, antibodies were put on ice and protein desalting was conducted to remove excess sodium *meta*-periodate by Zeba spin columns following the manufacturer's guide. Next, the concentration of antibody solutions was measured using a DeNovix nanodrop spectrophotometer and subsequently diluted using Glycolink coupling buffer accordingly to the desired antibody concentration. Three-antibody concentrations were tried: 0.1, 0.5 and 1 mg/mL. Twenty µL of oxidised anti-*E. coli* IgG was spread across the WE1 and anti-Protein A over WE2 and incubated for 1 h in a moist chamber. The moist chamber consisted of a petri dish, the base of which contained a tissue wet with diH_2O. This avoided the evaporation of the samples. The antibodies bound the polymer coating during the incubation. Once completed, all electrodes were washed thoroughly with PBS to remove the unbound antibodies. A schematic figure of the biosensor can be observed in (**Figure 2.4A**).

Then, 5 µL of *E. coli* suspension was applied to both working electrodes, which were incubated in a moist chamber for 15 min. Once completed, electrodes were rinsed thoroughly dried, and EIS analysis was undertaken on each working electrode. This process was carried out for n=4 for

$1\text{x}10^3$ cfu/mL concentrations to $1\text{x}10^8$ cfu/mL *E. coli*, using a new electrode for each measurement.

The affinity of bacterial strains was tested in **Section 4.2.3** and employed a different biosensor construction. A biosensor was fabricated following the same model described in (Ahmed et al., 2013). Generally, the 0.025 M tyramine was dissolved in methanol with 0.3 M NaOH and electropolymerised. Next, the polymerised working electrodes were incubated biotin-NHS and with Neutravidin after that. Finally, the biotinylated antibodies were attached to the biosensors and ready for bacterial testing. An overview schematic picture of the biosensor showing the electrode, polymer SAM and antibody linker chemistry is depicted in **Figure 2.4B**.

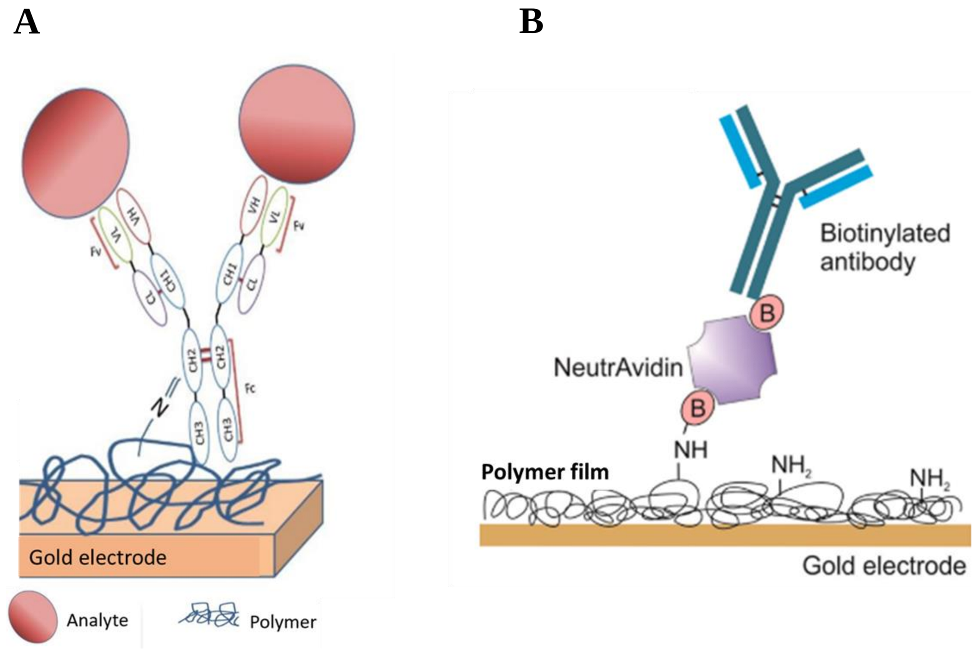

Figure 2.4: Schematic of different biosensors architecture. A, immobilisation of antibodies to the polymer through reactive aldehyde of oxidised oligosaccharide on the Fc region reacting to polymer amine groups to form a covalent bond. Adapted and reproduced from (Shamsuddin, 2018). **B**, immobilisation of antibodies using biotin-NeutrAvidin interaction to bind biotinylated antibodies. This model was employed to test the different bacterial strain specificity. Adapted and reproduced from (Ahmed et al., 2013).

2.2.5.2. Collagen-polymer matrix biosensor optimisation

The ethanol pretreatment was carried out by immersing the Electrodes 3 in ethanol solution for 30 min. After that, the electrodes were rinsed in diH$_2$O and air-dried using a N$_2$ gas stream. Then, bovine collagen Type I was attached to the electrode surface as a bioreceptor using a protocol provided by ELISHA Systems Ltd: Twenty-five µL of octopamine in 10 mM PB pH 7.2 was mixed with 25 µL of 200 µg/mL collagen (1:1) and kept in ice, yielding a final concentration of 2.5 mM octopamine and 100 µg/mL of collagen. The final solution was spread across the working electrode and electropolymerised for 2 cycles at a scan rate of 100 mV/s from 0.0 V to +1.6 V.

Finally, EIS scans of fully constructed biosensors were recorded at 0.0 V over a frequency range from +5 kHz to +0.1 Hz, with a modulation voltage of +10 mV recording three measurements for signal stabilisation. Next, 10 µL of *E. coli* from stock solutions containing $8x10^2$ cfu to $8x10^7$ cfu was applied to the working electrodes, which were incubated for 30 min. The electrodes were then washed with PBS and then analysed by EIS. This procedure was also carried out for the non-induced YadA *E. coli* control. The blank was conducted with the same procedure as the analyte and the control but substituting PBS buffer for the bacterial sample.

2.2.5.3. Collagen direct attachment biosensor optimisation

Ethanol pretreatment was carried out by immersing the Electrodes 3 in ethanol solution for 30 min. Electrodes were then rinsed in diH$_2$O and air-dried using a N$_2$ gas stream. Next, a range of different octopamine concentrations between 1 mM and 250 mM were dissolved in 10 mM PB pH 7.2, spread across the working electrode and electropolymerised for 2 cycles at a scan rate of 100 mV/s from 0.0 V to +1.6 V.

Once the electrodes were POc-coated, three different protocols adapted from (Greg T. Hermanson, 1996) were tested to find the best way to bind collagen to POc. These protocols aimed to create a covalent bond between the carboxylic acid presented by both glutamic and aspartic acid present in collagen, and the NH$_2$ from POc via EDC/sulfo-NHS.

Protocol 1: A final solution of 100 µg/mL collagen with 2 mM EDC and 6 mM sulfo-NHS in 50 mM MES pH 5.5 was created. First, a solution of 1 mg/mL collagen in 0.01 M acetic acid was made. Second, a separate solution of EDC and sulfo-NHS were dissolved in 50 mM MES pH 5.5. Then, the collagen solution was added to the EDC and sulfo-NHS solution yielding 100 µg/mL collagen with 2 mM EDC and 6 mM sulfo-NHS in 50 mM MES pH 5.5 and left 30 min for incubation.

Protocol 2: A final solution of 100 µg/mL collagen with 2 mM EDC and 6 mM sulfo-NHS in 50 mM MES pH 5.5 was created. First, a solution of 1 mg/mL collagen in 0.01 M acetic acid was made. Second, a separate solution of EDC and sulfo-NHS were dissolved in 50 mM MES pH 5.5. Next, the collagen solution was added to the EDC and sulfo-NHS solution yielding 100 µg/mL collagen with 2 mM EDC and 6 mM sulfo-NHS in 50 mM MES pH 5.5 and immediately placed over the 5 mM POc-coated electrodes and left for 2 h incubation. After that, the electrode surface was washed for three times with 50 mM MES pH 5.5. A final wash with 100 mM Tris buffer was performed.

Protocol 3: A final solution of 100 µg/mL collagen with 2 mM EDC and 6 mM sulfo-NHS in 50 mM MES pH 5.5 was created. First, a solution of 1 mg/mL collagen in 50 mM MES pH 5.5 was made, unlike Protocol 2 in which collagen was dissolved in acetic acid. Second, a separate solution of EDC and sulfo-NHS in 50 mM MES pH 5.5 was made. Then, the collagen solution was added to the EDC and sulfo-NHS solution yielding 100 µg/mL collagen with 2 mM EDC and 6 mM sulfo-NHS in 50 mM MES pH 5.5 and immediately placed over the 5 mM POc-coated electrodes and for 2 h incubation. After that, the electrode surface was washed for three times with 50 mM MES pH 5.5. A final wash with 100 mM Tris buffer was performed.

After experiments (**Chapter 6**), protocol 3 appeared to be the best protocol to continue with the biosensor optimisation. Following Protocol 3, different collagen concentrations between 5 µg/mL and 1000 µg/mL were assessed.

For the best resulting collagen concentration (100 µg/mL), induced YadA *E. coli* samples of $8\text{x}10^6$ cfu in 10 µL sample were tested for different incubation times between 5 min and 60 min at RT.

Then, a blocking agent to avoid non-specific binding was assessed for the best-optimised biosensor. BSA at 1.5 mg/mL or 1.5 mg/mL casein in 10 mM PBS were incubated for 1 h over the electrodes at RT to block non-specific binding sites on the biosensor. After that, the electrodes were washed with PBS buffer with 0.05 % (v/v) Tween-20. Next, fully constructed biosensors blocked with either 1.5 mg/mL BSA and 1.5 mg/mL casein were tested with $8\text{x}10^6$ cfu in 10 µL for both induced and non-induced *E. coli* and compared to non-blocked systems.

Finally, once the biosensor was fully optimised, EIS were recorded at 0.0 V over a frequency range of +5 kHz to +0.1 Hz, with a modulation voltage of +10 mV recording three measurements for signal stabilisation. After that, 10 µL of *E. coli* from stock solutions containing $8\text{x}10^2$ cfu to $8\text{x}10^7$ cfu was applied to the working electrodes and incubated for 15 min. The electrodes were then washed with PBS and then analysed by EIS. This procedure was also carried out for the non-induced YadA *E. coli* control. The blank was conducted with the same procedure as the analyte and the control but substituting PBS buffer.

2.2.5.4. Heparin-immobilised-bioreceptor based biosensor construction

Electrodes 3 were used for biosensor construction. Before electrochemical measurements, the electrodes were pretreated in ethanol for 30 min, rinsed with diH_2O and dried with N_2 gas. Twenty-five µL of a final concentration of 2.5 mM of octopamine in 10 mM PB pH 7.2 was spread across the working electrode and electropolymerised for two cycles at a scan rate of 100 mV/s from 0.0 V to +1.6 V. After that, the electrodes were rinsed thoroughly with 10 mM PBS, dried with Ar. After that, the surface was biotinylated and NeutrAvidin was added following the procedure described in (Ahmed et al., 2013). Once the surface was functionalised with NeutrAvidin, 10 µL of 1 mg/mL heparin-biotin was incubated over the surface for 1 h. Finally, 10 mM PBS was used to wash the surface which was dried with Ar. Bacterial samples were added to the fully constructed impedimetric biosensor. Ten µL samples containing either induced or non-induced $YadA_{O:8}$ or $YadA_{O:9}$ were applied to the working electrodes at 10^6 and 10^7 cfu and incubated for 30 min. The EIS analysis was carried out before and after analyte addition to assess the R_{ct} (%). A schematic of this biosensor is shown in **Figure 2.5**.

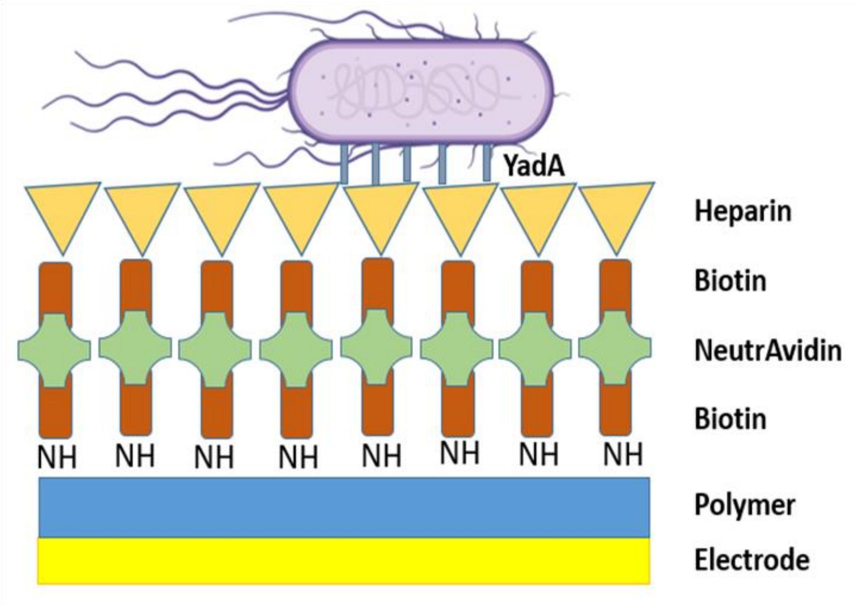

Figure 2.5: Schematic of heparin bioreceptor-based biosensor architecture. The biosensor layer-by-layer construction comprises an electrode, POc film, biotin, NeutrAvidin, and biotinylated heparin.

2.2.6. Cyclic voltammetry analysis

In **Chapter 3**, CV analysis was conducted using an Autolab workstation by immersing Electrodes 2 and Electrodes 3 in a solution of 10 mM $[Fe(CN)_6]^{3-/4-}$ in 10 mM PBS pH 7.2. Next, the potential was swept from -0.4 V to +0.6 V following the reversible redox couple reaction for 10 scans at a scan rate of 100 mV/s.

In **Chapters 5-7,** the CV analysis was conducted by spreading 50 µL of 10 mM $[Fe(CN)_6]^{3-/4-}$ in 10 mM PBS pH 7.2 over Electrodes 3. Then, the potential was swept between -0.6 V to +0.6 V for CV analysis following the reversible redox couple reaction for a different number of scans at a scan rate of 100 mv/s using Palmsens workstation.

In **Chapter 7,** for microfluidics experiments, essentially the same approach as for **Chapter 3** was used on Electrodes 2 but sweeping between -0.6 V to +0.6 V in 10 mM $[Fe(CN)_6]^{3-/4-}$ in 100 mM PBS for 10 scans at 100 mv/s.

2.2.7. Electrochemical impedance spectroscopy measurements

In **Chapter 3**, each EIS measurement was conducted by submerging Electrodes 2 and Electrodes 3 in 10 mM $[Fe(CN)_6]^{3-/4-}$ in 10 mM PBS pH 7.2 and assessed with Autolab workstation. EIS measurements were collected at 0.0 V over a frequency range of +2.5 kHz to +0.25 Hz, with a modulation voltage of +10 mV. Five EIS measurements were taken for signal stabilisation. Nova 2.1.4 software was employed for EIS recording. All analyses were performed in a three-cell system for n=4.

Essentially, the same approach was used on Electrodes 1 in 10 mM $Fe(CN_6)^{3-/4-}$ in 100 mM PBS pH 7.2 in **Chapter 4** and using Electrodes 2 in **Chapter 7** for microfluidics experiments.

In **Chapters 5-7**, each EIS measurement was conducted by spreading 50 µL of 10 mM $[Fe(CN)_6]^{3-/4-}$ in 10 mM PBS pH 7.2 over the Electrodes 3. EIS was recorded at 0.0 V over a frequency range of +5 kHz to +0.1 Hz, with a modulation voltage of +10 mV. Typically, two (**Chapters 5 & 6**) and three (**Chapter 7**) EIS measurements were taken for signal stabilization. All EIS analyses were performed in a three-cell system for $n \geq 6$ using Palmsens workstation.

2.2.8. EIS data analysis

The R_{ct} and C_{dl} values were obtained from fitting the EIS derived Nyquist plots into Randles' equivalent circuits. Metrohm Autolab Nova 2.1.4 was employed to fit Nyquist plots into Randles' equivalent circuit, from which R_{ct} and C_{dl} were obtained. For analyte testing, the R_{ct} was normalized by expressing it in ΔR_{ct} (%). The biosensor was assessed before and after the analyte addition, and ΔR_{ct} (%) was used to evaluate bacterial binding according to **Equation 2.1**:

$$\Delta R_{ct}\,(\%) = ((R_{ct\ analyte} - R_{ct\ zero}) / R_{ct\ zero}) \cdot 100 \qquad \textbf{Equation 2.1}$$

The data plotting and statistical analysis were carried out with OriginPro (2019b).

2.2.9. Microfluidic chip design, fabrication and interfacing

The microfluidic chip design and fabrication were carried out by Dr Alex Iles, experimental officer at University of Hull. Two microfluidic chip designs were employed for the research. First, Chip 1 (**Figure 2.6A**) was designed and fabricated as described in (Patinglag et al., 2020). Chip 2 is shown in **Figure 2.6B** and was made of polycarbonate. AutoCAD was used to do the 2D design, then SolidWorks to extrude it into 3D and SolidCAM to make the toolpaths for creating the G-code to operate the CNC machine milling (Datron M7, Milton Keynes, UK). The sample chamber (7.5 mm wide, 9 mm long, and 0.2 mm depth) is connected to the inlet channels (7.5 mm wide, 22.5 mm long and 0.2 mm depth). An O-ring made of nitrile rubber with 10.1 mm bore and 13.3 mm outer was purchased at RS Components. PTFE Teflon tubing (1.58 mm od x 0.5 mm id, Supelco) were inserted to inlets and outlet through a 2.5 mL syringe luer adaptor and glued with Araldite. Two different pumping systems were employed: pressure pump MFCS-FLEX, Flow Rate Platform Flowboard and Flowunit, and MAESLO Software from Fluigent; and a 5 mL syringe and pumped with a syringe pump (11 Elite, Harvard Apparatus).

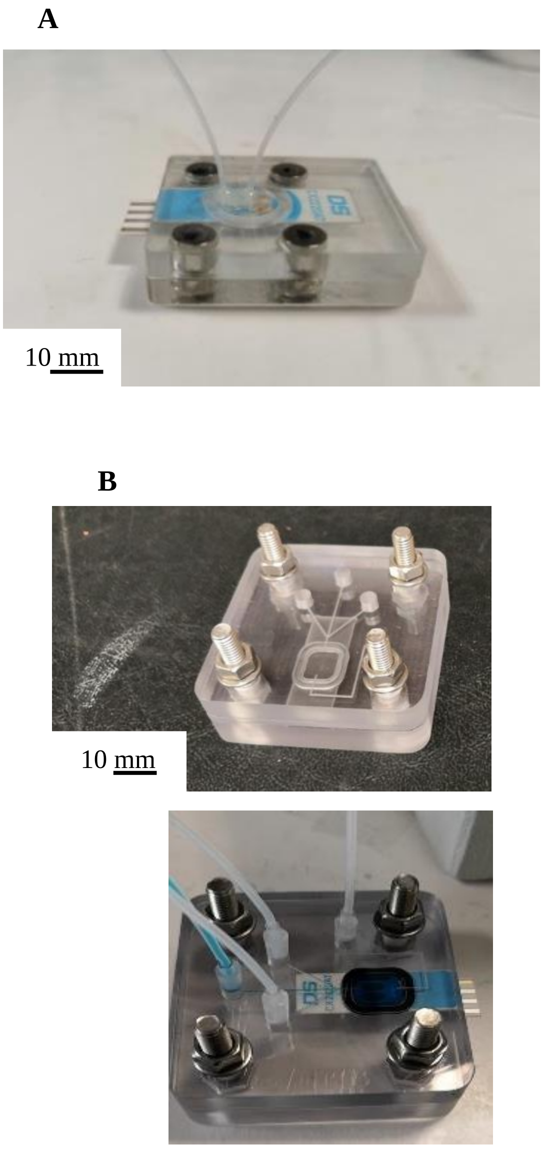

Figure 2.6: Photograph of microfluidic Chip 1 and design and photographs of microfluidic Chip 2. A, the chip was designed and fabricated as described in (Patinglag et al., 2020). **B**, the chip was made of PC fabricated using CNC machine milling. The sample chamber (7.5 mm wide, 9 mm long, and 0.2 mm depth) is connected with the inlet channels (7.5 mm wide, 22.5 mm long, 0.2 mm depth). An O-ring made of nitrile rubber with a 10.1 mm bore and 13.3 mm outer was employed. PTFE Teflon tubing (1.58mm od x 0.5mm id) were inserted into inlets and outlet through a 2.5 mL syringe luer adaptor and glued with Araldite.

2.2.10. Midland blotting

Midland blotting technique (Jo V Rushworth et al., 2013) was performed to validate the collagen coating in **Chapter 6** using on-sensor chemiluminescence. First, the electrode surface was incubated with 1 mg/mL rabbit anti-bovine/human collagen type I (dual-species cross-reactivity). After 1h incubating at RT, a washing step with PBS for 5 min was performed. Next, the electrodes were incubated with (1:1000 in PBS) goat anti-rabbit HRP secondary antibodies for 1 h at RT. The electrodes were then washed 3 times with PBS, 5 min each time. The second wash with PBS included 0.1 % (v/v) Tween-20 to remove the non-specific binding. The final wash was performed with PBS. Finally, ECL reagent was added over the electrodes for the chemiluminescence detection after 1 min using a Syngene G: BOX Gel Imaging System.

2.2.11. X-ray photoelectron spectroscopy

The XPS measurements were carried out by Dr Ben Jonhson, experimental officer at the University of Leeds. XPS spectra were collected with a Thermo Escalab 250 XPS instrument equipped with a monochromatic Al Kα X-ray source. Survey scans were gathered between 0 and 1250 eV, pass energy of 150 eV. The spot size and the power were 500 µm and 150 W respectively. High-resolution spectra were taken with a pass energy of 20 eV and a step size of 0.1 eV. The resultant data was processed with CasaXPS software, within which energy calibration (C1s = 285eV), relative sensitivity factor (C1s = 1) and background subtraction were carried out.

2.2.12. Atomic force microscopy

Lekshmi Kailas, experimental officer in AFM at the University of Leeds, performed the AFM imaging. AFM samples observations were carried out in the air using a Bruker Dimension FastScan AFM operating in tapping mode. Measurements were done employing Bruker FastScan A cantilevers with a nominal spring constant of 18 N/m and a resonant frequency of 1400 kHz. NanoScope (ver 9.4) software was utilised to simultaneously collect height, amplitude error and phase data. Three scan sizes were imaged in two different areas on each sample: 10 µm, 5 µm and 1 µm square. Post-processing of the data was carried out using NanoScope Analysis (ver 1.9) software.

The electrode’s roughness was assessed in two ways. First, 10 µm side images were analysed to obtain a general overview of the surface topography and to observe larger structures such as pollutants or grains. Next, a section analysis was performed. Second, flatter parts of the matrix avoiding pollutants or grains were assessed.

2.2.13. Other methodology

The methodologies included in this section were employed by Early-Stage Researcher (PhD student) Ina Meuskens at the University of Oslo. These techniques are included as a result of the collaborations carried out and detailed in **Chapters 6 and 7**.

2.2.13.1. Fluorescence-based detection of YadA-expressing *E. coli*

The bacteria were grown as described in **Section 2.2.4.2.2**. To also induce sfGFP expression from the genome, 0.02% (w/v) arabinose was added at every step of the growth process. Wells of a 96-well clear plate were coated with 100 µL of a 10 µg/mL collagen solution. As negative controls, PBS was added to the wells. The plates were incubated at RT for 1 h. After that, the solutions were discarded, and the wells were washed three times with 200 µL PBS and afterward blocked with 3% (w/v) BSA in PBS for 1h at RT. After YadA expression was allowed for 3 h, the OD_{600} was set to 1.0 for both the non-induced and the induced culture, and serial 1:10 dilutions were performed in 3% (w/v) BSA in PBS. 100 µL of each dilution was loaded into the plate. The binding of bacteria was allowed for 1 h at RT under static conditions. After that, the wells were washed 3 times with PBS and fluorescence was measured. The measurements were performed in a Synergy H1 plate reader with excitation at 455 nm and an emission of 533 nm at a gain setting of 100.

2.2.13.2. A Heparin-binding assay using bacteria

Materials and methodology were as described in the Section “Heparin Binding Assay Using Bacteria” from (Meuskens et al., 2022).

2.2.13.3. Dot blots for Heparin binding to YadA head domains

Materials and methodology as described in the Section “Dot Blots for Heparin Binding to YadA Head Domains” from (Meuskens et al., 2022).

2.2.13.4. A binding assay employing purified YadA head domains

Materials and methodology were as described in the Section “Binding Assay Using Purified YadA Head Domains” from (Meuskens et al., 2022).

2.2.13.5. Plasmids and constructs of *E. coli* Top10 glmS:sfGFP (AS75) and *E. coli* BL21 (DE3) Gold

The plasmids and constructs that were employed for this research are listed in Table 1 from (Meuskens et al., 2022) and the sequences can be found in the supplements of the same article (Meuskens et al., 2022). The constructs were cloned by Gibson assembly (Gibson et al., 2009).

2.2.13.6. YadA head domain purification

Materials and methodology were as described in the Section “YadA Head Domain Purification” from (Meuskens et al., 2022).

2.2.13.7. Statistical analysis

The statistical analysis applied is indicated within the legend of each graph. Typically, the averaged curves from CV or Nyquist plots are shown for different number of replicates, indicated as $n=x$ in the legend. The errors were indicated as standard deviation (± SD) or as relative standard deviation (± RSD). Analysis of variance (ANOVA) was performed where appropriate, with statistical significance between analyte and control described as $p < 0.001$.

Chapter 3

Pretreatment effects in two different commercial screen-printed gold electrodes over various surface coatings

Chapter 3: Pretreatment effects in two different commercial screen-printed gold electrodes over various surface coatings

3.1. Overview

The surface of the electrodes used in biosensing needs to be clean and their surface chemistry consistent between electrodes to avoid variability in electrochemical measurements. This chapter assesses the electrochemical stability and reproducibility of two different commercial SPGEs. In addition, AFM and XPS analyses were carried out to obtain electrode topography surface information and composition, respectively. Bare, POc-coated, POc-Ab-coated, and alkanethiol SAM-coated electrode surfaces were evaluated for non-pretreated electrodes and for the following pretreatments: H_2SO_4 cycling potential; H_2SO_4 cycling potential followed by immersion in ethanol; and only immersion in ethanol. CV in H_2SO_4 is a redox technique commonly used to remove organic contaminants from the gold surface. Gold oxides can be present on the electrode surface as a consequence of the manufacturing process or after applying an oxidative technique. Therefore, ethanol immersion is employed to remove gold oxides and produce metallic Au and to remove any weakly bound contaminant from the surface (Ron et al., 1998). These conditions were assessed for two different commercial SPGEs: Metrohm DropSens CX2220AT (Electrodes 2) and BVT-AC1.W1.RS.Dw2 (Electrodes 3).

In the following work, bare electrodes, 5 mM POc, 2.5 mM POc + 100 µg/mL non-oriented antibodies, and 11-mercaptoundecanoic acid (11-MUA) SAM-coated electrodes were assessed for surfaces previously pretreated with either 15 CV cycles under 0.1 M H_2SO_4 at a scan rate of 50 mv/s; 15 CV cycles under 0.1 M H_2SO_4 at a scan rate of 50 mv/s followed by immersion in ethanol for 30 min; a 30 min of only immersion in ethanol; or with non-pretreated control SPGEs for comparison.

Different gold electrode surface pretreatments have been reported for SAM formations. Some electrochemical techniques for gold electrode pretreatment have resulted in better SAM formation. Nonetheless, there is currently little research about methods for SAM formation on SPGEs. SAM formation requires a molecularly flat surface, incompatible with the roughness found on the SPGE surface. To bypass this issue, both conducting and non-conducting polymers are electrodeposited onto gold electrode surfaces, including SPGE. Some examples in the literature include POc (Shamsuddin et al., 2021), Ptyr (Pournaras et al., 2008; Ahmed et al., 2013; Goode et al., 2016), polyaniline (Caygill et al., 2012; Chowdhury et al., 2012) and copolymers formed from tyramine and 3-(4-hydroxyphenyl) propionic acid (POPA) (Rushworth et al., 2014). These polymers have been shown to be effective scaffolds, the thickness of which can be controlled by electrodeposition onto rough surfaces.

Little has been studied about suitable gold electrode surface pretreatments for polymeric electrodeposition. However, a brief study researched the suitability of SPGE pretreatments for Ptyr electrodeposition for biosensing analysis purposes (Ahmed et al., 2013). There, CV in H_2SO_4 was shown to be the optimum pretreatment compared to sonication in ethanol and chemical pretreatment in piranha solution. It was found that CV in H_2SO_4 provided better EIS analysis and yielded smoother SPGE surfaces compared to chemical pretreatment employing piranha, where possible erosion signs and dielectric material deposition were found on the gold working electrodes. Nevertheless, sonication in 100 % ethanol was used as a pretreatment: despite less favourable EIS results, it provided better surface conditions towards polymeric coating.

Despite the little research on SPGE pretreatment, CV in H_2SO_4 appeared to be the most common employed methodology for gold electrode pretreatment, as corroborated in many biosensors studies (Radi et al., 2009; Escamilla-Gómez et al., 2008; Sakamoto et al., 2018; Loaiza et al., 2008; Aghaei et al., 2017; Ndiaye et al., 2016; Pagliarini et al., 2019; Cardoso et al., 2016; Kuralay et al., 2011; Escamilla-Gómez et al., 2009). In addition, many SPGE manufacturers or suppliers suggest CV in H_2SO_4 as a pretreatment for their SPGE, such as Metrohm DropSens (Metrohm Dropsens), Micrux (Micrux Technologies) and Pine (PINE Research, 2016). Other companies do not directly suggest H_2SO_4 CV pretreatment but acidic cycling potentials, such as Zimmer and Peacock (Zimmer & Peacock AS, 2020) or the application of large anodic and cathodic potentials such as Basi (BASi). However, there are opposing studies regarding the benefits of this method. Different types of gold surface modifications were observed after the CV in H_2SO_4. Electrochemical techniques and XPS analysis determined the creation of hydrous oxide and gold oxide (Izumi, Watanabe & Yokoyama, 1991; Burke & Hopkins, 1984), which could negatively affect the gold surface reproducibility and quality, thus compromising the subsequent system characterisation or functionalisation. (Burke & Nugent, 1998) showed that multilayer hydrous oxide deposits appeared on gold under acidic solutions through repeated potential cycling and may contain three different hydrous oxide components. This was also corroborated by more recent studies (Lamas-ardisana et al., 2015).

In this study, CV in H_2SO_4, CV in H_2SO_4 combined with immersion in ethanol, and ethanol immersion alone were chosen as pretreatments for commercial Electrodes 2 and Electrodes 3 compared to non-pretreated electrodes. The pretreated and non-pretreated electrodes were assessed for POc, POc-antibody and alkanethiol SAM-coated electrodes. The bare electrode surface was also evaluated for comparison. The systems were analysed through CV and EIS to assess electrodes' quality, stability, and reproducibility. AFM and XPS respectively studied the surface topology and electrode composition. The results indicated that each pretreatment had different effects over each different surface coating and different types of commercial SPGE.

3.2. Results

3.2.1. CV characterisation of bare electrode surface after pretreatment

Bare gold electrode surfaces for Electrodes 2 and Electrodes 3 were assessed for different pretreatments compared to non-pretreated. First, Electrodes 2 were pretreated with the corresponding pretreatment, namely, CV in H_2SO_4, CV in H_2SO_4 + ethanol, and ethanol only, and subsequently washed as described in **Section 2.2.1**. Another set of non-pretreated electrodes was assessed for comparison. The electrodes were immersed in an electrolyte solution to undergo CV analysis as detailed in **Section 2.2.6**. through Autolab workstation. Then, Electrodes 3 were pretreated using the same pretreatment mentioned above (**Section 2.2.1**) and underwent the same CV analysis as Electrodes 2.

Figures 3.1A-B shows the CV profiles of pretreated and non-pretreated Electrodes 2 and Electrodes 3, respectively. No significant changes for CV in H_2SO_4 compared to non-pretreated electrodes were observed for Electrode 2 (**Figure 3.1A**) or for Electrode 3 (**Figure 3.1B**) voltammograms. When both Electrodes 2 and Electrodes 3 were pretreated with CV in H_2SO_4 + ethanol and ethanol alone, a substantial difference compared to non-pretreated could be observed. These differences could be explained by topographic effects such as roughness or surface chemistry modification after pretreatment.

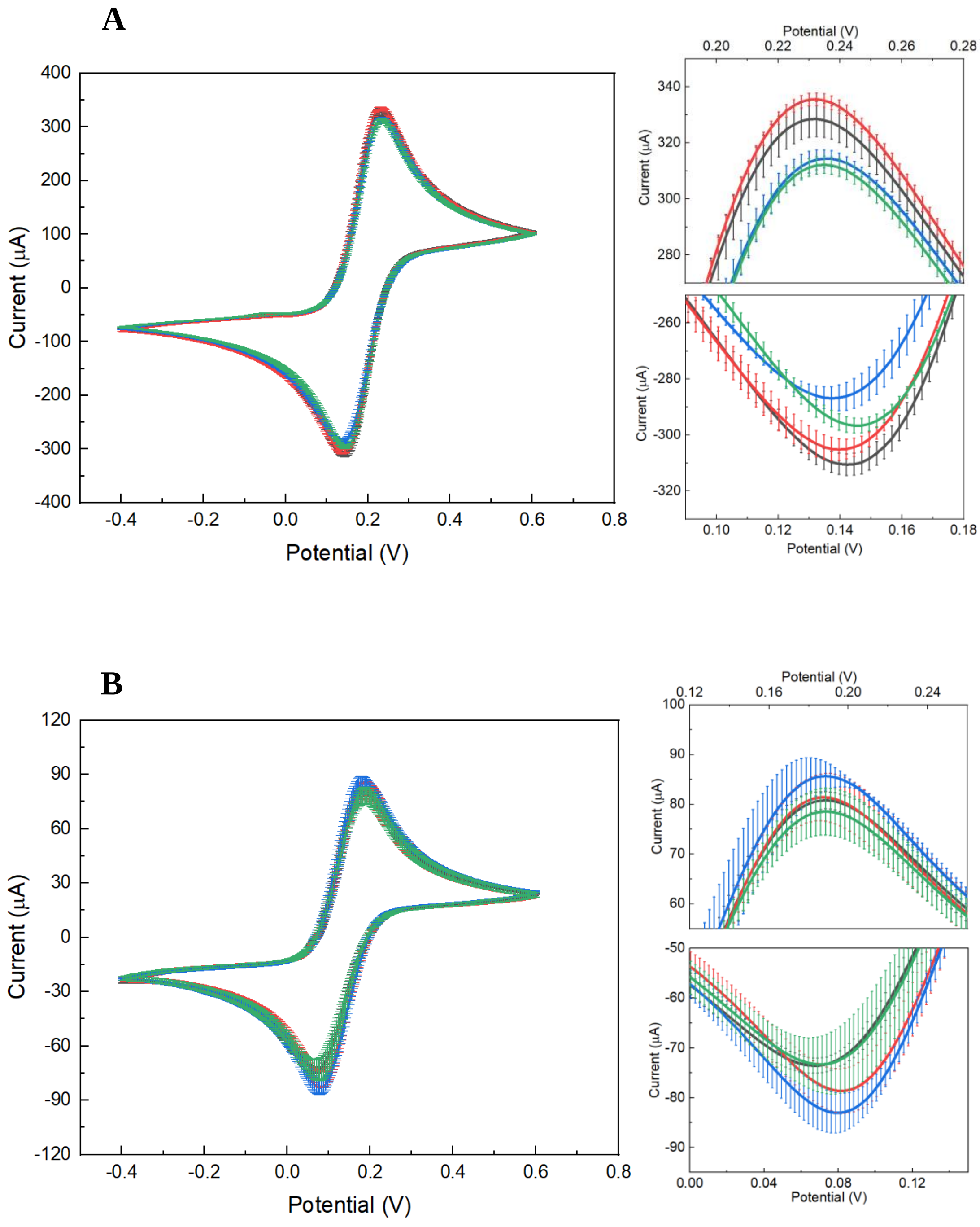

Figure 3.1: Mean (± SD) CV of pretreated and non-pretreated electrodes for bare electrodes. Both Electrodes 2 and Electrodes 3 were pretreated (**Section 2.2.1**) and subsequently subjected to 10 CV cycles of sweeping potential from -0.4 V to +0.6 V in 10 mM $[Fe(CN)_6]^{3-/4-}$ in 10 mM PBS pH 7.2 as detailed in **Section 2.2.6**. **A**, showed Electrodes 2 voltammograms and **B**, showed Electrodes 3 voltammograms. In this figure, only the 2nd scan is represented for each electrode for non-pretreated (━━), CV in H_2SO_4 (━━), CV in H_2SO_4 + ethanol (━━) and ethanol (━━). The zoomed-in inserts show the current peaks at their redox potentials. The CVs show averaged readings from n=4; errors bars indicate standard deviation (± SD).

3.2.2. CV characterisation of functionalised electrode surface after pretreatment

Bare gold electrode surface, POc, POc + Ab, and SAM-coated Electrodes 2 and Electrodes 3 were assessed for different pretreatments compared to non-pretreated. First, Electrodes 2 were pretreated with their corresponding pretreatment, namely, CV in H_2SO_4, CV in H_2SO_4 + ethanol, and ethanol alone, and subsequently washed as described in **Section 2.2.1**. Another set of non-pretreated electrodes was assessed for comparison. Next, 5 mM octopamine was electropolymerised onto the SPGEs surface as detailed in **Section 2.2.2.1**. **Figure 3.2** shows the electropolymerisation CV profiles of 5 mM octopamine over Electrodes 2 pretreated through different pretreatments. A final solution of 2.5 mM POc with 100 µg/mL antibodies was also electrodeposited as described in **Section 2.2.2.3**. **Figure 3.3** shows the electropolymerisation CV profiles of octopamine-Ab and over Electrodes 2 through different pretreatments. Finally, SAM was formed over Electrodes 2 as detailed in **Section 2.2.3**. Then, the POc, POc-Ab and SAM-coated electrodes were immersed in an electrolyte solution to undergo CV analysis as described in **Section 2.2.6**. using an Autolab workstation. A set of bare electrodes were assessed for comparison. Then, Electrodes 3 underwent the same process and octopamine and octopamine-Ab electropolymerisation CV are shown in **Figures 3.4-3.5** respectively.

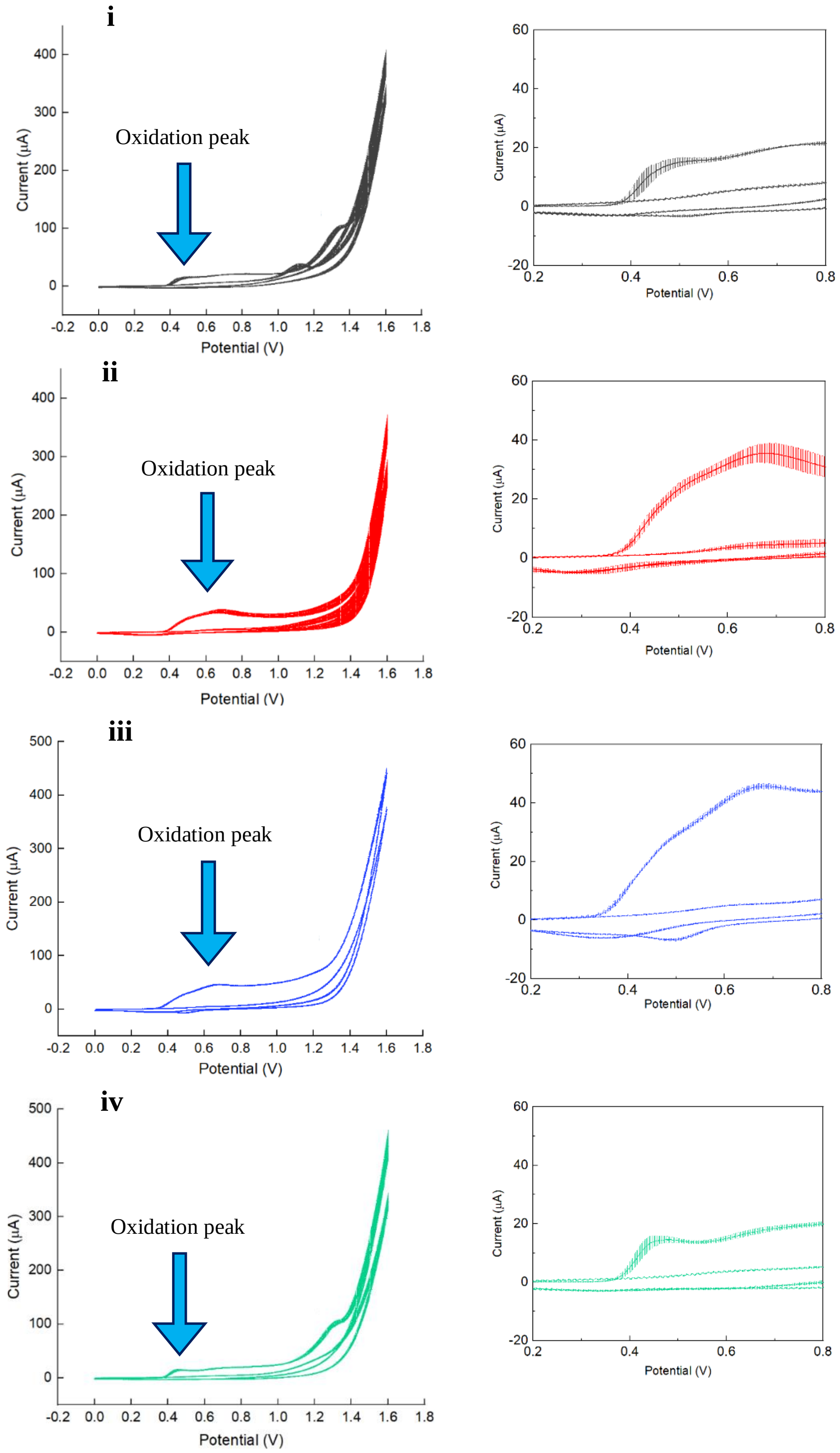

Figure 3.2: Electropolymerisation profile of 5 mM octopamine over Electrodes 2. Electropolymerisation of 5 mM octopamine in 10 mM PB pH 7.2 was performed over different pretreated Electrodes 2 surfaces: non-pretreated (**i**), CV in H_2SO_4 (**ii**), CV in H_2SO_4 + ethanol (**iii**) and ethanol (**iv**). The electrode was cycled from 0.0 V to +1.6 V for 2 cycles as detailed in **Section 2.2.2.1**. The zoomed-in inserts are placed at the right side of each electropolymerisation plot. It aims to show better detail of the oxidation peak by showing the current from +0.2 V to +0.8V. CVs shown were performed with Autolab workstation. CVs show mean from n=4 ± SD.

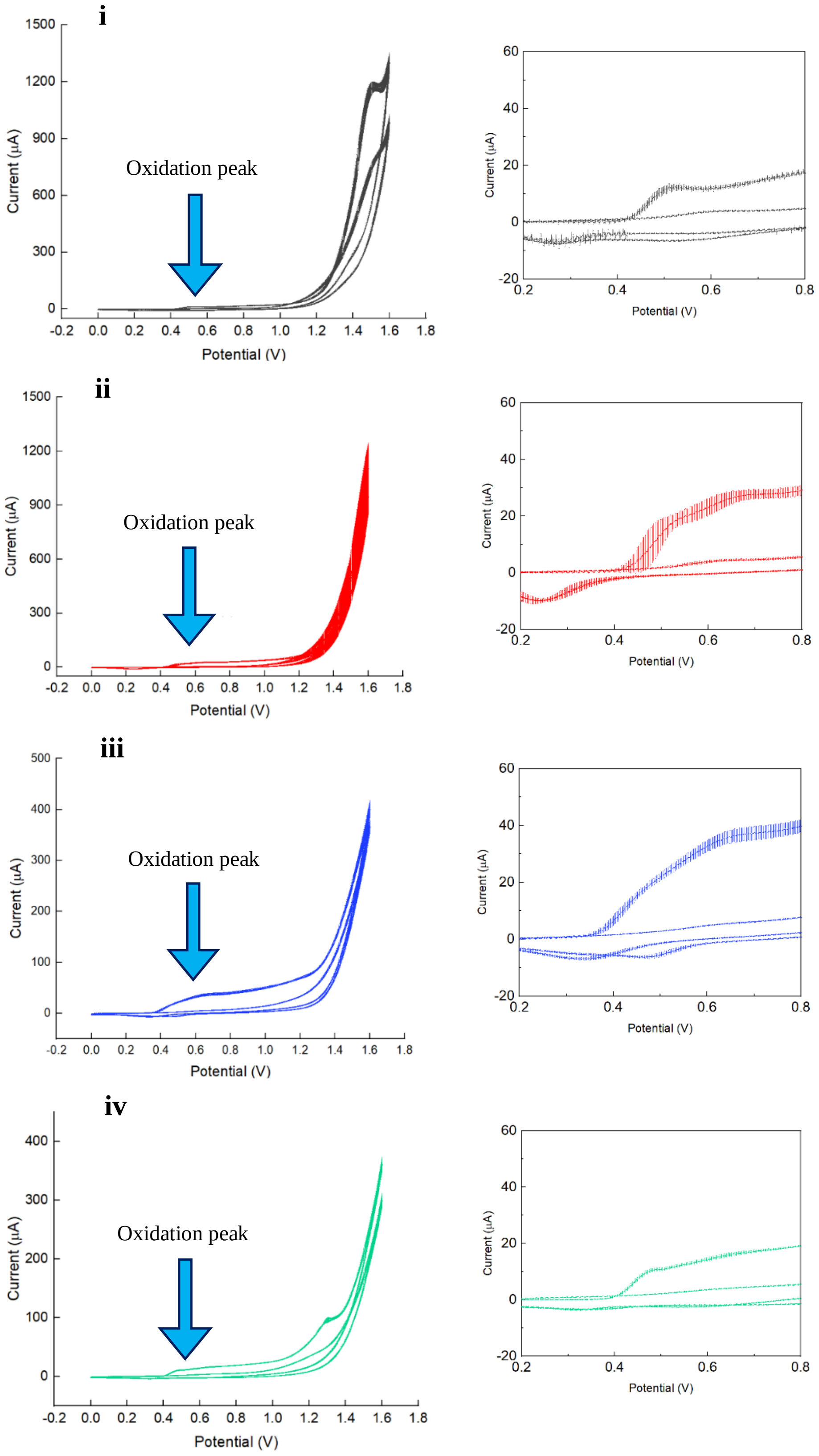

Figure 3.3: Electropolymerisation profile of octopamine-Ab and over Electrodes 2. Electropolymerisation of 2.5 mM octopamine and 100 µg/mL antibodies over different pretreated Electrodes 2 surfaces: non-pretreated (**i**), CV in H_2SO_4 (**ii**), CV in H_2SO_4 + ethanol (**iii**) and ethanol (**iv**). The electrode was cycled from 0.0 V to +1.6 V for 2 cycles as detailed in **Section 2.2.2.1**. The zoomed-in inserts are placed at the right side of each electrodeposition plot. It aims to show better detail of the oxidation peak by showing the current from +0.2 V to +0.8 V. CV were performed with Autolab workstation. CVs show mean from n=4 ± SD.

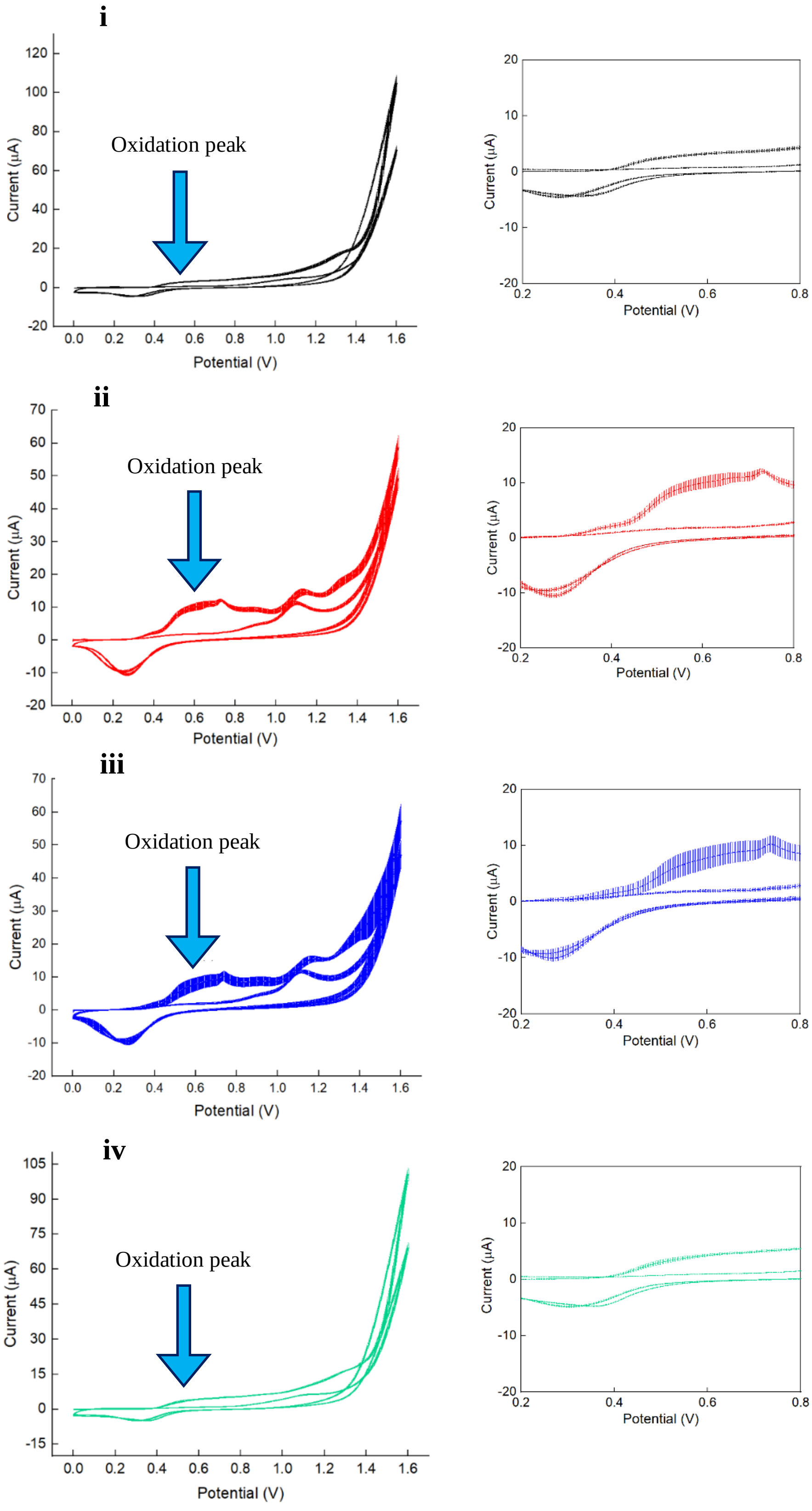

Figure 3.4: Electropolymerisation profile of 5 mM octopamine over Electrodes 3. Electropolymerisation of 5 mM octopamine in 10 mM PB pH 7.2 over different Electrodes 3: non-pretreated (**i**), CV in H_2SO_4 (**ii**), CV in H_2SO_4 + ethanol (**iii**) and ethanol (**iv**). The electrode was cycled from 0.0 V to +1.6 V for 2 cycles as detailed in **Section 2.2.2.1**. The zoomed-in inserts are placed at the right side of each electrodeposition plot. It aims to show better detail of the oxidation peak by showing the current from +0.2 V to +0.8 V. CV were performed with Autolab workstation. CVs show mean from n=4 ± SD.

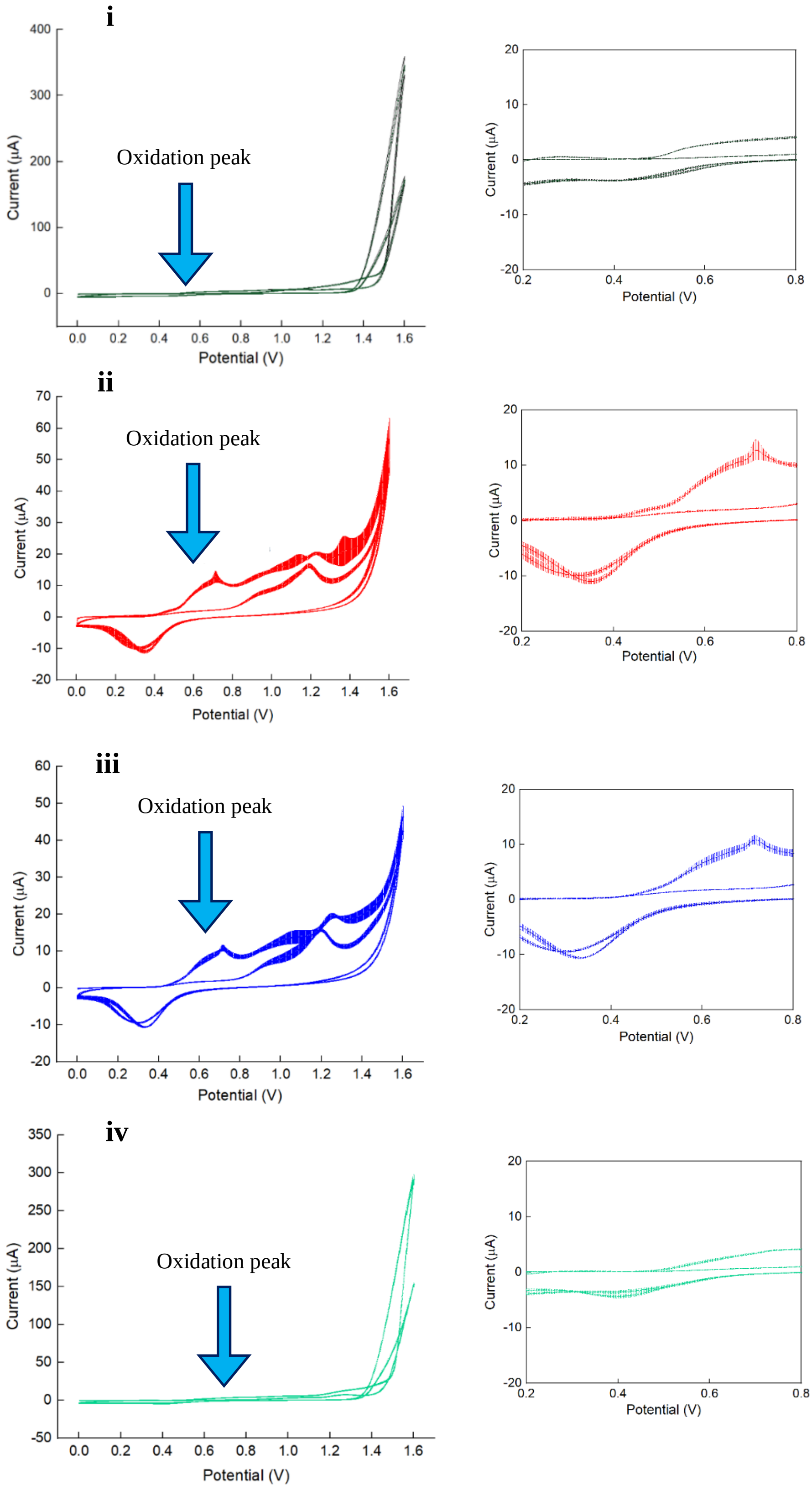

Figure 3.5: Electropolymerisation profile of octopamine-Ab and over Electrodes 3. Electropolymerisation of 2.5 mM octopamine and 100 µg/mL antibodies over different pretreated Electrodes 3 surfaces: non-pretreated (**i**), CV in H_2SO_4 (**ii**), CV in H_2SO_4 + ethanol (**iii**) and ethanol (**iv**). The electrode was cycled from 0.0 V to +1.6 V for 2 cycles as detailed in **Section 2.2.2.1**. The zoomed-in inserts are placed at the right side of each electrodeposition plot. It aims to show better detail of the oxidation peak by showing the current from +0.2 V to +0.8 V. CV were performed with Autolab workstation. CVs show mean from n=4 ± SD.

The voltammograms derived from the CV analysis are shown in **Figure 3.6A** for Electrode 2 and **Figure 3.6B** for Electrode 3. A sharp reversible oxidation and reduction peaks could be observed from the pretreated and non-pretreated bare (black) electrode surface for Electrodes 2 and Electrodes 3 (**Figures 3.6A & B**). Firm insulating layers were achieved for POc (blue) and POc-Ab (red) for both Electrodes 2 and Electrodes 3 which are manifested by a flat CV profile, indicating insulating surfaces (**Figures 3.6A & B**). This was corroborated by previous successful electrodeposition in **Figures 3.2-3.5**: octopamine electropolymerisation profiles from non-pretreated Electrodes 2 and Electrodes 3 (**Figure 3.2i & 3.4i**) showed a clear octopamine oxidation peak, comparable to those obtained with ethanol pretreated SPGEs (**Figure 3.2iv & 3.4iv**), although smaller than those employing CV in H_2SO_4 (**Figure 3.2ii & 3.4ii**). Generally, non-pretreated and ethanol pretreated electrodes presented similar POc and POc + Ab electrodeposition profiles for both Electrode 2 (**Figures 3.2i, iv & 3.3i, iv**) and Electrode 3 (**Figures 3.4i, iv & 3.5i, iv**) SPGEs. Likewise, similar electrodeposition profiles were also obtained for CV in H_2SO_4 or CV in H_2SO_4 + ethanol for both Electrode 2 (**Figures 3.2ii, iii 3.3ii, iii**) and Electrode 3 (**Figures 3.4ii, iii 3.5ii, iii**) SPGEs.

A valuable observation was that the SAM interfaces (green) presented a very different voltammogram mainly depending on the electrode type, although differences were also found according to the pretreatment. SAM voltammograms from Electrodes 2 (**Figure 3.6A**) (green) appeared similar under any pretreatment compared to any bare CV profile from Electrodes 2 (**Figure 3.6A**) (black). However, SAM CV profiles from Electrodes 3 (**Figure 3.6B**) (green) differed according to the pretreatment: non-pretreated **Figure 3.6Bi** and ethanol **Figure 3.6Biv** pretreated SPGEs presented more conducting surfaces than those pretreated with CV in H_2SO_4 (**Figure 3.6Biii**) or CV in H_2SO_4 + ethanol (**Figure 3.6Biv**), that exhibited very insulating properties similar to the POc profile (blue). These results suggested that the SAM formation in Electrodes 2 could have been compromised since voltammograms from Electrodes 3 suggest clear insulating behaviour under any CV in H_2SO_4 methods. Overall, the electrode composition and topographical effects could be involved in the SAM formation process. Therefore, a study of the composition and topography of each Electrode 2 and 3 is crucial to comprehend the undergoing changes in surfaces before and after any pretreatment.

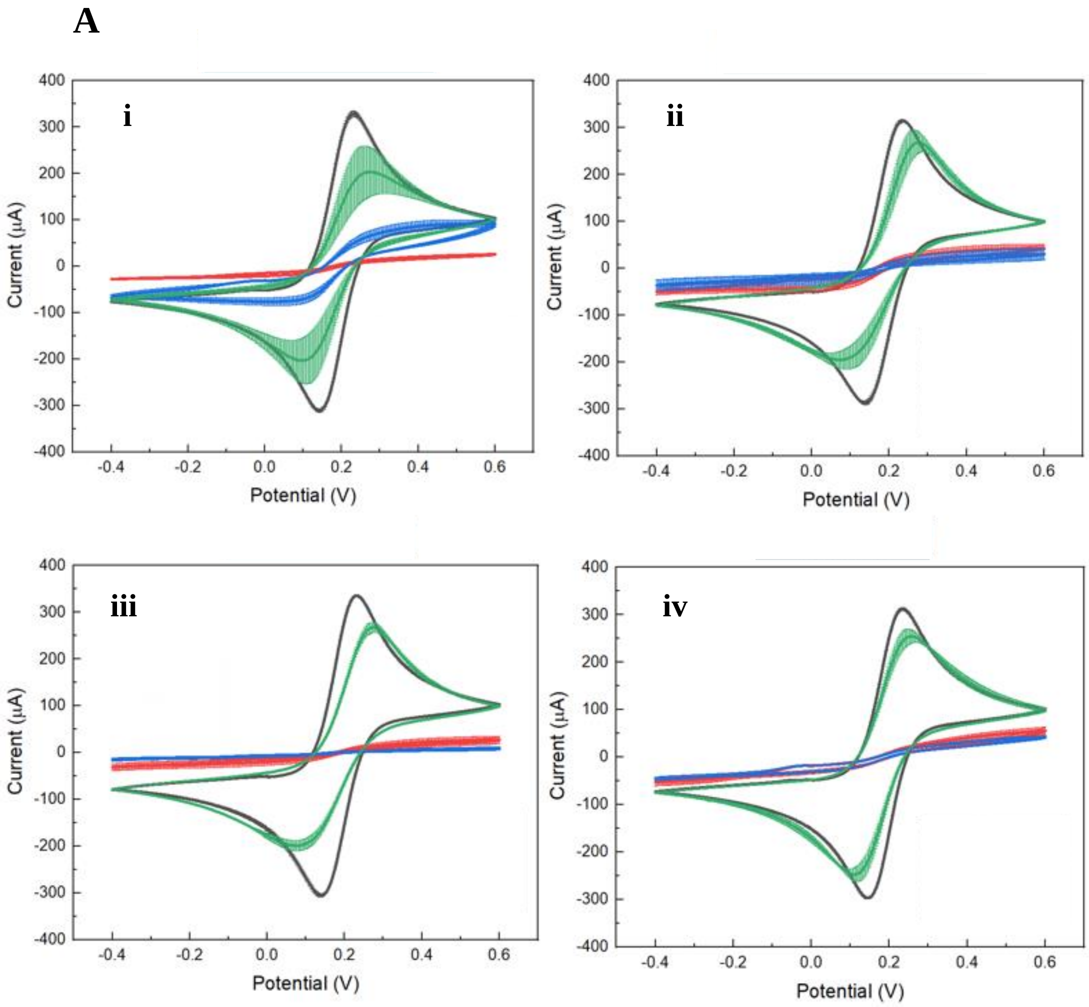
A
i
ii
iii
iv
Current (μA)
Potential (V)
400
300
200
100
0
-100
-200
-300
-400
-0.4
-0.2
0.0
0.2
0.4
0.6

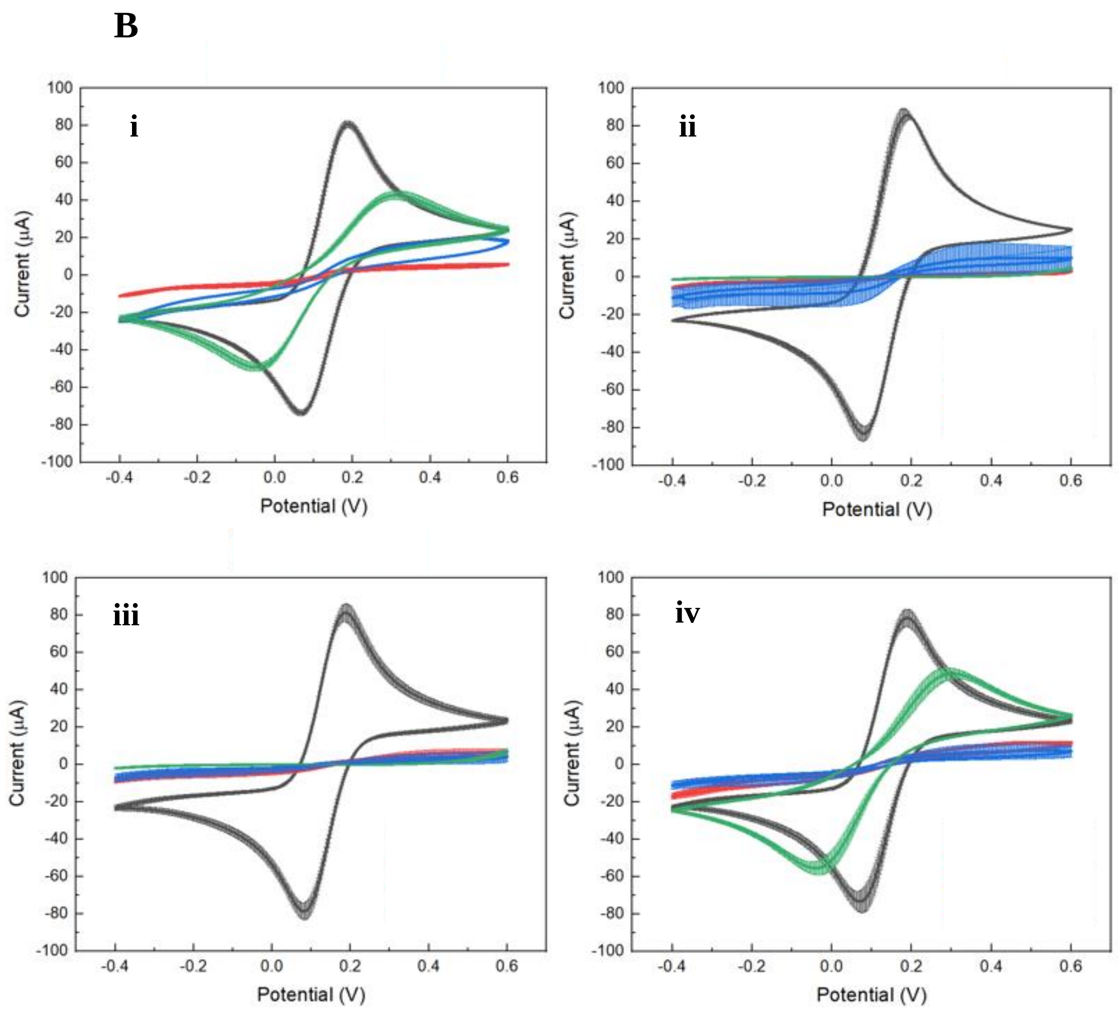

Figure 3.6: Pretreated and non-pretreated CV voltammogram for different surface coatings. The POc (—), POc + Ab (—), SAM (—) coated electrodes, and the bare (—) surface was subjected to 10 cycles of sweeping potential from -0.4 V to +0.6 V in 10 mM $[Fe(CN)_6]^{3-/4-}$ in 10 mM PBS pH 7.2 as detailed in **Section 2.2.6**. Non-pretreated (**i**), CV in H_2SO_4 + ethanol (**ii**), CV in H_2SO_4 (**iii**) and ethanol (**iv**). **A**, shows commercial Electrodes 2, CX2220AT, and **B**, shows commercial Electrodes 3, BVT-AC1.W1.RS.Dw2. In these figures, mean ± SD, of the 2nd scan is represented from n=4.

3.2.3. Degeneration of the surface coating: analysis through CV

CV characterisation was carried out for POc, POc-Ab, SAM and bare electrode surface, previously pretreated to understand the effect of the pretreatment. Ten CV cycles were considered sufficient for reproducibility and stability assessment. The reproducibility was assessed through the standard deviation for each cycle, as each electrode was assessed for n=4. Theoretically, a more conductive CV profile was expected after each cycle due to the coating loss over the same functionalised electrode. This would be manifested by a decrease and increase in their anodic and cathodic peaks, respectively. The difference between each consecutive CV cycle was directly related to the surface's conductivity and, therefore, the surface coating stability. Among the 10 cycles, only the 1st, 2nd and 10th were plotted for clarity.

First, Electrodes 2 were pretreated with the corresponding pretreatment, namely, CV in H_2SO_4, CV in H_2SO_4 + ethanol, and ethanol alone, and subsequently washed as described in **Section 2.2.1**. Another set of non-pretreated electrodes was assessed for comparison. Next, 5 mM octopamine was electropolymerised onto the SPGEs surface as detailed in **Section 2.2.2.1**; a final solution of 2.5 mM POc with 100 µg/mL antibodies was also electrodeposited as described in **Section 2.2.2.3**; and SAM formation as detailed in **Section 2.2.3**. A set of bare electrodes were assessed for comparison. Next, the electrodes were immersed in an electrolyte solution to undergo 10 CV cycle-analysis as detailed in **Section 2.2.6** through Autolab workstation and shown in **Figure 3.7A**. Then, Electrodes 3 (**Figure 3.7B**) were pretreated, coated, and underwent the same CV analysis than Electrodes 2.

Figure 3.7A shows the CV analysis of different surface coatings upon different pretreatments for Electrodes 2**.** Electrodes 2 presented different stability levels depending on the surface coating and pretreatment. POc-coated sensors prepared on CV in H_2SO_4 showed apparent degeneration by the 10th cycle (blue), and an atypical voltammogram compared to POc-coated non-pretreated electrode voltammogram. While POc-coated sensors on non-pretreated electrodes showed a typical reversible CV profile, POc-coated sensors prepared on CV in H_2SO_4 showed a braid-shaped CV profile towards negative potentials at the 10th cycle. POc-coated CV in H_2SO_4 + ethanol pretreated electrodes presented a less degenerated pattern, although the 10th cycle's reproducibility appeared compromised. Generally, POc-Ab-coated non-pretreated electrodes did not show considerable degeneration. Nonetheless, CV in H_2SO_4 pretreated, then POc-Ab-coated electrodes presented large SD values by the 10th cycle, particularly at negative potentials where some current values RSD was around ± 30 %. According to their CV voltammograms, POc and POc-Ab-coated electrode surfaces showed more insulating systems when they had previously been pretreated with CV in H_2SO_4 or CV in H_2SO_4 + ethanol. These results were in line with their electrodeposition profiles previously observed in **Figures 3.2ii-iii & Figures 3.3ii-iii**. However, even though more substantial polymer coating for CV in H_2SO_4 or CV in H_2SO_4 + ethanol pretreated electrodes was observed, the voltammograms showed a higher degree of degeneration or worst reproducibility than non-pretreated or only ethanol pretreated surfaces. As indicated in the previous section, SAM formation over Electrodes 2 seemed to be compromised, and voltammograms similar to bare electrodes were obtained.

Figure 3.7B shows the CV analysis of different surface coatings upon different pretreatments for Electrodes 3**.** POc-coated CV in H_2SO_4 and CV in H_2SO_4 + ethanol pretreated electrode surface presented less degeneration than when pretreated with ethanol or non-pretreated. More degeneration could be explained by both POc-coated non-pretreated and ethanol pretreated electrodes having less polymer coating as deduced from lower oxidative peaks shown at their electrodeposition profiles (**Figure 3.4i & iv**) compared to POc-coated electrodes with CV in H_2SO_4 and CV in H_2SO_4 + ethanol (**Figure 3.4ii-iii**), showing higher oxidative current. Despite the significant degeneration shown by non-pretreated and ethanol pretreated, then POc-coated electrodes, both systems showed reproducible CV voltammograms for all cycles. Generally, CV in H_2SO_4 or CV in H_2SO_4 + ethanol pretreated Electrodes 3 gave more stability for all surface coatings compared to CV in H_2SO_4 or CV in H_2SO_4 + ethanol pretreated Electrode 2. POc-Ab-coated Electrodes 3 showed best reproducibility and stability when pretreated with CV in H_2SO_4 or CV in H_2SO_4 + ethanol. POc-Ab-coated ethanol pretreated Electrodes 3 showed not to be a desirable pretreatment candidate given the degenerative CV cycles and compromised reproducibility. SAM-coated Electrodes 3 presented relevant information. SAM formation over CV in H_2SO_4 or CV in H_2SO_4 + ethanol pretreated surfaces appeared successful, as shown by the non-conductive CV voltammograms. SAM-coated non-pretreated and ethanol pretreated electrodes presented similar conductive voltammogram profiles, although substantial more formation was observed than in any case of Electrodes 2.

SAMs could only be adequately formed over Electrodes 3 under specific CV in H_2SO_4 or CV in H_2SO_4 + ethanol pretreatments. These results concluded that the SAM formation success depended on the electrode and pretreatment types. Therefore, each commercial electrode's composition and topography had to be studied. Rough surfaces present a significant barrier towards SAM formation and other factors such as contamination will also compromise the SAM formation.

POc and POc-Ab presented different CV profiles depending on the Electrode 2 pretreatment. Therefore, a clear conclusion about which pretreatment was best could not be made. The reproducibility, stability, and amount of polymer varied according to the pretreatment, surface coating, and electrode type.

A	**Non-pretreated**	**CV in H_2SO_4**	**CV in H_2SO_4 + ethanol**	**Ethanol**
POc	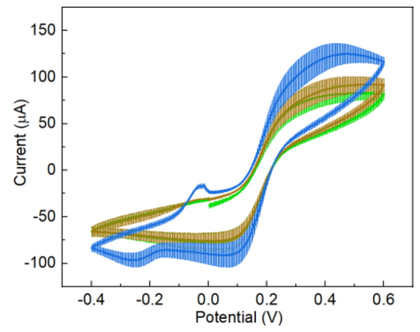	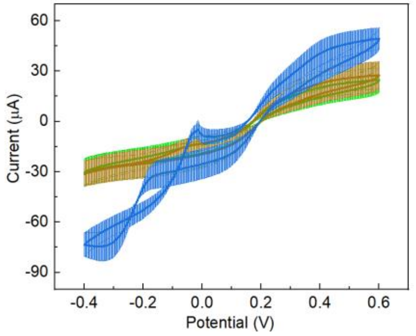	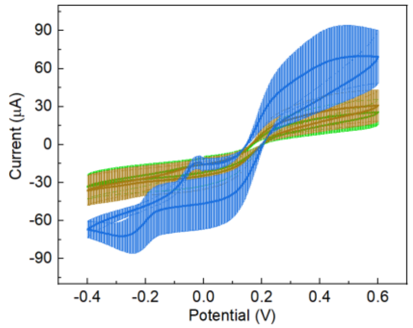	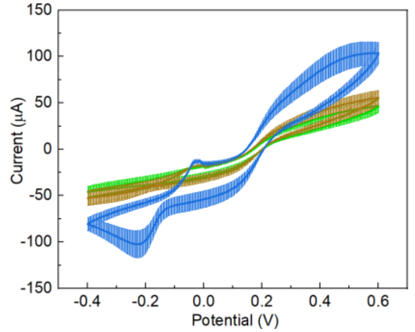
POc-Ab	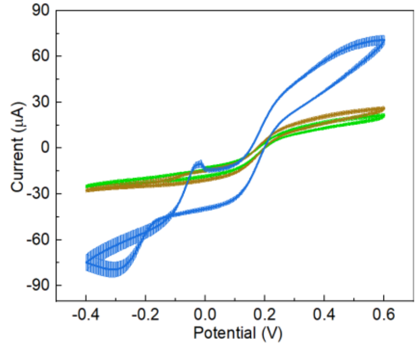	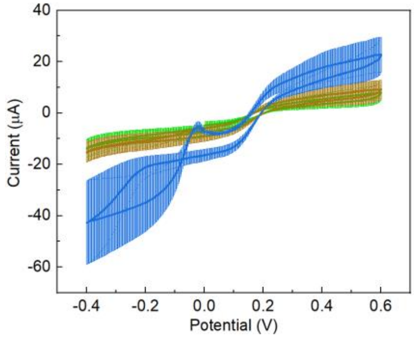	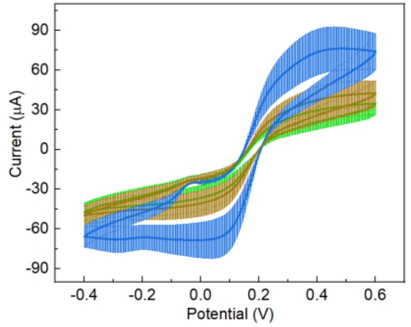	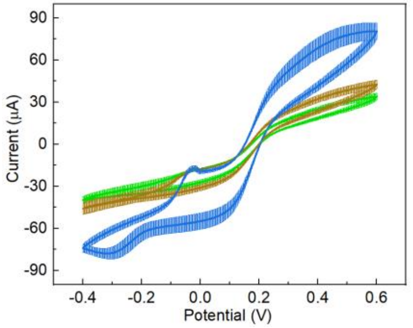
SAM	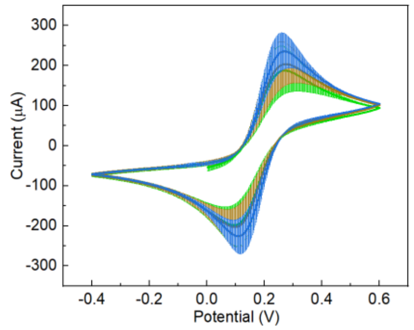	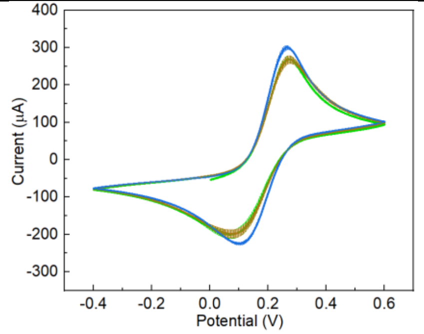	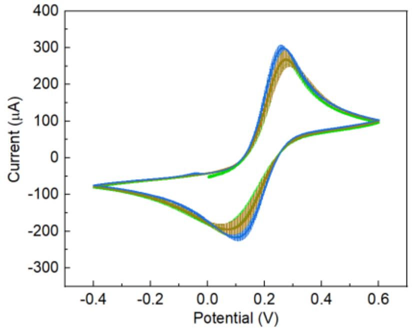	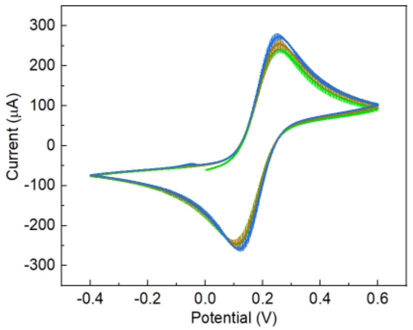

B	**Non-pretreated**	**CV in H_2SO_4**	**CV in H_2SO_4 + ethanol**	**Ethanol**
POc	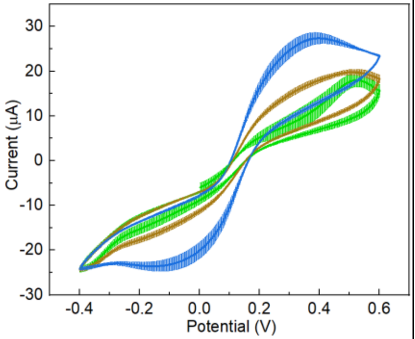	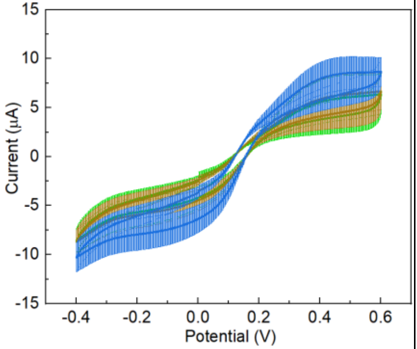	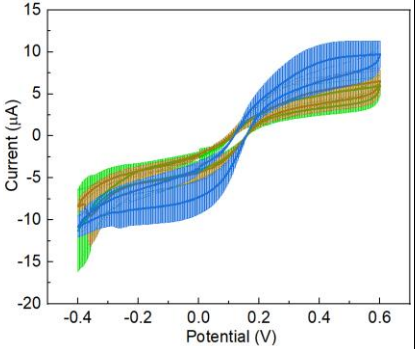	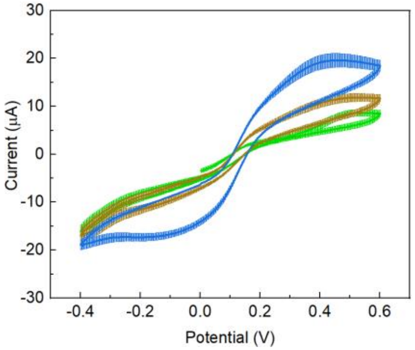
POc-Ab	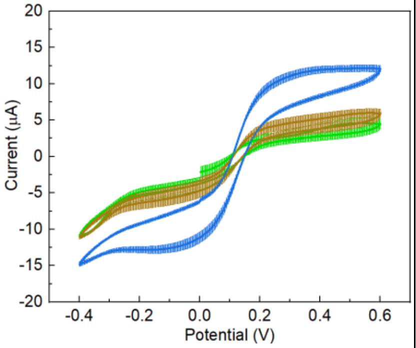	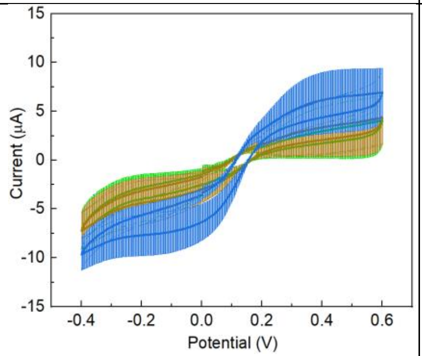	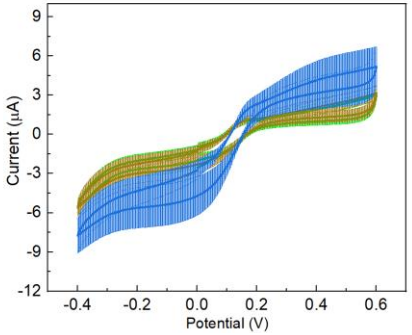	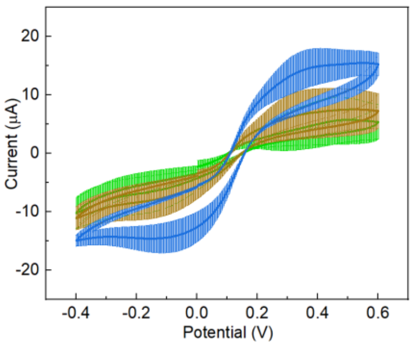
SAM	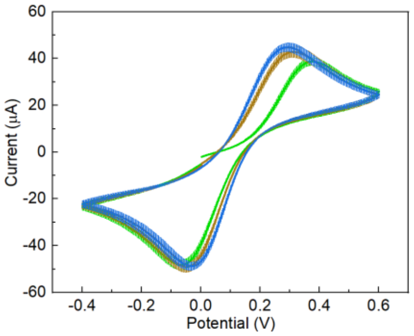	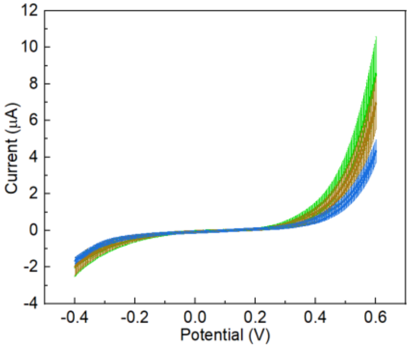	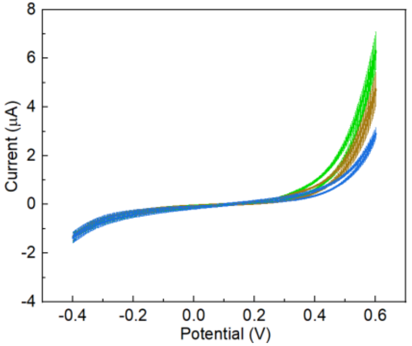	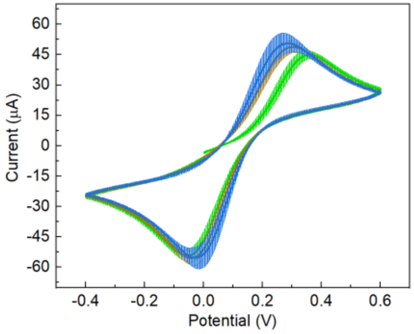

Figure 3.7: CV voltammograms (cycles 1, 2 and 10) of different surface coatings upon different pretreatments for Electrodes 2 and Electrodes 3. The POc, POc + Ab, SAM-coated electrodes, and the bare surface was subjected to 10 cycles of sweeping potential from -0.4 V to +0.6 V in 10 mM $[Fe(CN)_6]^{3-/4-}$ in 10 mM PBS pH 7.2 as detailed in **Section 2.2.6**. First cycle (1st) (▬), 2nd cycle (▬) and 10th cycle (▬). **A**, for commercial Electrodes 2, and **B**, for Electrodes 3. The CVs show averaged readings from n=4; errors bars indicate standard deviation (± SD).

3.2.4. EIS Characterisation

After the previous CV analysis in **Section 3.2.3**, the different surface coatings over SPGE pretreated surfaces were also assessed through EIS, from which R_{ct} and C_{dl} were obtained and shown in **Table 3.1**.

First, Electrodes 2 were pretreated with the corresponding pretreatment, namely, CV in H_2SO_4, CV in H_2SO_4 + ethanol, and ethanol alone, and subsequently washed as described in **Section 2.2.1**. Another set of non-pretreated electrodes was assessed for comparison. Next, 5 mM octopamine was electropolymerised onto the SPGEs surface as detailed in **Section 2.2.2.1**; a final solution of 2.5 mM POc with 100 µg/mL antibodies was also electrodeposited as described in **Section 2.2.2.3**; and SAM formation as detailed in **Section 2.2.3**. Then, the electrodes were immersed in an electrolyte solution to undergo EIS analysis as described in **Section 2.2.7**. through Autolab workstation. Then, Electrodes 3 were pretreated, coated, and underwent the exact EIS analysis than Electrodes 2.

Bare electrodes opposed minimal resistance to the flow of electrons. The Nyquist plots obtained from bare electrode surface presented very conductive profiles that led to complications fitting it into Randle's equivalent circuit to get the R_{ct} and C_{dl}. EIS analysis was performed for POc, POc-Ab, and SAM-coated pretreated surfaces. Then, R_{ct} and C_{dl} were derived from the Nyquist plots and indicated by mean ± RSD.

Table 3.1: R_{ct} and C_{dl} derived from EIS analysis of different surface coatings according to the pretreatment. R_{ct} ± RSD and C_{dl} ± RSD of POc, POc-Ab and SAM-coated Electrodes 2 and Electrodes 3 pretreated with CV in H_2SO_4, CV in H_2SO_4 + ethanol, ethanol and non-pretreated. EIS was conducted by submerging electrodes in 10 mM $[Fe(CN)_6]^{3-/4-}$ in 100 mM PBS pH 7.2. EIS was recorded at 0.0 V over a frequency range of +2.5 kHz to +0.25 Hz, with a modulation voltage of +10 mV as detailed in **Section 2.2.7**. Data shown for all protocols as mean from n=4 ± RSD.

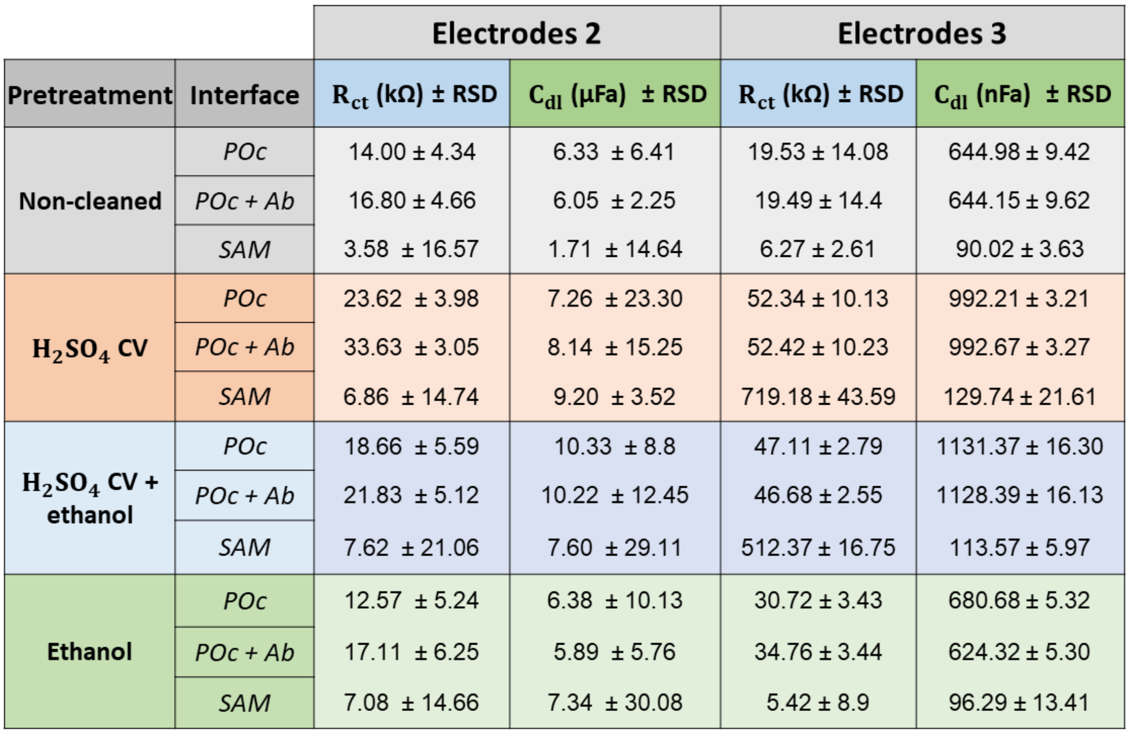

		Electrodes 2		Electrodes 3	
Pretreatment	**Interface**	**R_{ct} (kΩ) ± RSD**	**C_{dl} (μFa) ± RSD**	**R_{ct} (kΩ) ± RSD**	**C_{dl} (nFa) ± RSD**
Non-cleaned	*POc*	14.00 ± 4.34	6.33 ± 6.41	19.53 ± 14.08	644.98 ± 9.42
	POc + Ab	16.80 ± 4.66	6.05 ± 2.25	19.49 ± 14.4	644.15 ± 9.62
	SAM	3.58 ± 16.57	1.71 ± 14.64	6.27 ± 2.61	90.02 ± 3.63
H_2SO_4 CV	*POc*	23.62 ± 3.98	7.26 ± 23.30	52.34 ± 10.13	992.21 ± 3.21
	POc + Ab	33.63 ± 3.05	8.14 ± 15.25	52.42 ± 10.23	992.67 ± 3.27
	SAM	6.86 ± 14.74	9.20 ± 3.52	719.18 ± 43.59	129.74 ± 21.61
H_2SO_4 CV + ethanol	*POc*	18.66 ± 5.59	10.33 ± 8.8	47.11 ± 2.79	1131.37 ± 16.30
	POc + Ab	21.83 ± 5.12	10.22 ± 12.45	46.68 ± 2.55	1128.39 ± 16.13
	SAM	7.62 ± 21.06	7.60 ± 29.11	512.37 ± 16.75	113.57 ± 5.97
Ethanol	*POc*	12.57 ± 5.24	6.38 ± 10.13	30.72 ± 3.43	680.68 ± 5.32
	POc + Ab	17.11 ± 6.25	5.89 ± 5.76	34.76 ± 3.44	624.32 ± 5.30
	SAM	7.08 ± 14.66	7.34 ± 30.08	5.42 ± 8.9	96.29 ± 13.41

POc-coated Electrode 2's surface gave different R_{ct} values depending on the pretreatment, although the reproducibility for any pretreatment and non-pretreatment were similar. POc-coated CV in H_2SO_4 and CV in H_2SO_4 + ethanol Electrode 2 presented relatively high R_{ct} values, 23.62 kΩ ± 3.98 % and 18.66 kΩ ± 5.59 %, respectively. These results suggested that more POc coating for CV in H_2SO_4 and CV in H_2SO_4 + ethanol systems was present compared to non-pretreated or ethanol pretreated Electrodes 2, whose R_{ct} values were 14 kΩ ± 4.34 % and 12.57 kΩ ± 5.24 % respectively. In the POc-Ab functionalised Electrodes 2, a similar R_{ct} pattern than for POc-coated systems was observed: higher R_{ct} values for CV in H_2SO_4 and CV in H_2SO_4 + ethanol, 33.63 kΩ ± 3.05 % and 21.83 kΩ ± 5.12 %, respectively, compared to non-pretreated or ethanol pretreated Electrodes 2, whose R_{ct} values were 16.8 kΩ ± 4.66 % and 17.11 kΩ ± 6.25 % respectively. Both POc and POc-Ab-coated Electrodes 2 showed R_{ct} values in line with their respective oxidative current at electrodeposition profiles (**Figure 3.2 & 3.3**) and CV analysis (**Figure 3.7A**).

As previously explained, SAM formation over Electrodes 2 was minimal. Generally, low R_{ct} values were obtained for all SAM-coated pretreated and non-pretreated systems, with additional large RSD values. Capacitance was also assessed. Only POc and POc-Ab systems showed to be reproducible for ethanol pretreated or non-pretreated systems.

Electrode 3 showed different outcomes depending on the pretreatment and coating. POc-coated pretreated Electrodes 3 EIS analysis appeared similar to Electrodes 2: CV in H_2SO_4 and CV in H_2SO_4 + ethanol pretreated electrodes showed relatively large R_{ct} values, 52.34 kΩ ± 10.13 % and 47.11 kΩ ± 2.79 % respectively, supported by their also large oxidative current at their electropolymerisation profiles (**Figures 3.4ii-iii**). Ethanol pretreated, then POc-coated Electrodes 3 presented larger R_{ct} values, 30.72 kΩ ± 3.43 %, than non-pretreated, 19.53 kΩ ± 14.08 %. POc-coated Electrodes 3 only gave lower RSD values when they had been pretreated with ethanol, either alone or after acidic voltammetry. This was supported by the excellent reproducibility obtained in previous CV analysis **(Figure 3.7B)**. Capacitance was also assessed. POc-Ab-coated Electrodes 3 showed the same reproducibility tendency for R_{ct} and C_{dl} than Electrodes 2. Electrodes 3 successfully achieved SAM formation, particularly CV in H_2SO_4 and CV in H_2SO_4 + ethanol pretreated Electrodes 3 for CV in H_2SO_4 and CV in H_2SO_4 + ethanol pretreated systems with R_{ct} of 719.18 kΩ ± 43.59 % and 512.37 kΩ ± 16.75 % respectively. These values were in accordance with **Figure 3.7B** voltammograms. Despite presenting SAM formation, the SAM-coated CV in H_2SO_4 and CV in H_2SO_4 + ethanol pretreated systems showed compromised reproducibility according to their RSD.

POc-coated CV in H_2SO_4 and CV in H_2SO_4 + ethanol pretreated Electrodes 3 showed the most significant C_{dl} values, although only CV in H_2SO_4 pretreated, then POc-coated electrodes showed reproducible systems with C_{dl} of 992.21 nFa ± 3.21 %. POc-coated ethanol pretreated and non-pretreated electrodes showed C_{dl} of 644.98 nFa ± 9.42 % and 680.68 nFa ± 5.32 %, respectively.

The unsuccessful Electrode 2 SAM formation could be explained by the SPGE composition. SPGE manufacturers use their ink and techniques to create their electrodes. The composition of the ink could vary. SAM coating was only achieved onto Electrodes 3 under specific pretreatments, CV in H_2SO_4 or CV in H_2SO_4 + ethanol. This evidence may be explained by the chemical or topographical change of the Electrode 3 surface under CV in H_2SO_4 pretreatment. However, SAM coating of CV in H_2SO_4 or CV in H_2SO_4 + ethanol pretreated system's R_{ct} values presented large RSD. This could be explained by the SPGEs surface's topography, typically rough. This was investigated using AFM and will be discussed further in **Section 3.2.6**.

3.2.5. X-ray photoelectron spectroscopy

The XPS analysis provided elemental composition (%) on the Electrode 2 and Electrode 3 gold working electrodes (**Table 3.2**). The XPS measurements were carried out by Dr Ben Jonhson, experimental officer at the University of Leeds, as described in **Section 2.2.11**.

Table 3.2: **Elemental composition (%) of Electrodes 2 and Electrodes 3 after XPS analysis.** XPS spectra were collected using a Thermo Escalab 250 XPS equipped with a monochromatic Al Kα X-ray source. Data were processed with CasaXPS software.

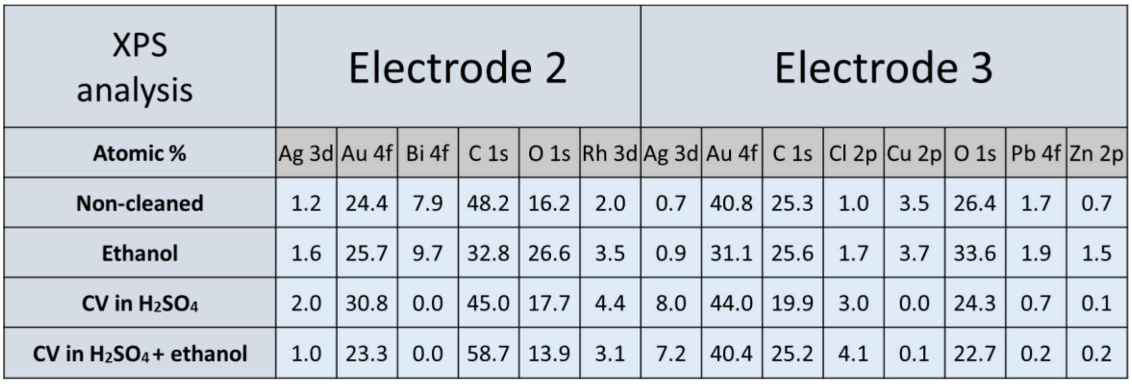

XPS analysis	Electrode 2						Electrode 3							
Atomic %	Ag 3d	Au 4f	Bi 4f	C 1s	O 1s	Rh 3d	Ag 3d	Au 4f	C 1s	Cl 2p	Cu 2p	O 1s	Pb 4f	Zn 2p
Non-cleaned	1.2	24.4	7.9	48.2	16.2	2.0	0.7	40.8	25.3	1.0	3.5	26.4	1.7	0.7
Ethanol	1.6	25.7	9.7	32.8	26.6	3.5	0.9	31.1	25.6	1.7	3.7	33.6	1.9	1.5
CV in H_2SO_4	2.0	30.8	0.0	45.0	17.7	4.4	8.0	44.0	19.9	3.0	0.0	24.3	0.7	0.1
CV in H_2SO_4 + ethanol	1.0	23.3	0.0	58.7	13.9	3.1	7.2	40.4	25.2	4.1	0.1	22.7	0.2	0.2

Electrode 2 showed substantial Bi contamination. The Bi presence in non-pretreated and ethanol pretreated was 7.9 % and 9.7 %, respectively, which could be removed with the CV in H_2SO_4 pretreatment. Bi presence went down to 0.0 % after the CV in H_2SO_4 application and appeared to reveal Au and Rh. Some research on the Electrode 2 manufacturer website was carried out. It was found that they offered bismuth oxide screen-printed carbon electrodes commercialisation, which led us to suspect that some cross-contamination occurred during the manufacturing process. Ethanol pretreatment removed organic contaminants manifested by a decrease in C levels, from 48.2 % in non-pretreated to 32.8 %.

The Bi presence on Electrode 2 could determine the pretreatment employed as only CV in H_2SO_4 could remove it. This could positively impact the polymer amount electrodeposited over the Electrode 2 surface and its reproducibility. In addition, Bi could be the cause of SAM failing to form. However, other factors must have determined the SAM formation as it was not fully formed over Electrode 3 unless pretreated with CV in H_2SO_4 or CV in H_2SO_4 + ethanol. The CV in H_2SO_4 application on Electrode 3 revealed Ag and Cl and reduced the amount of Cu, Pt and Zn. Ethanol pretreatment reduced the Au and increased the Zn amounts on the surface. However, ethanol pretreatment did not lessen the organic contaminant levels as much as it did over Electrode 2.

Electrode 3 presented higher Au composition than Electrode 2. Non-pretreated Electrodes 3 showed 40.8 % of Au. In contrast, only 24.4 % in non-pretreated Electrode 2. Non-pretreated Electrodes 3 presented a 25.3 % C composition, significantly smaller than Electrodes 2, 48.2 %, indicating less presence of an organic contaminant. The presence of O appeared larger on non-pretreated Electrodes 3, 26.4 %, compared to non-pretreated Electrodes 2, 16.2 %, which could indicate oxidising compounds over the surface.

The XPS analysis found the presence of Bi over Electrodes 2 and could be removed after CV in H_2SO_4. Ethanol pretreatment was expected to reduce the O levels after reducing gold oxides to metallic Au. However, the presence of O increased after ethanol pretreatment compared to non-pretreated electrodes for both types of electrodes. In addition, ethanol pretreatment reduced the C levels, which could be explained by removing weakly bound organic components adsorbed over the Electrode 2 surface. The use of SPGE does not guarantee that the electrode composition will be 100 % gold. Different manufacturers' inks and fabrication methodologies could lead to other Au % and the presence of various contaminants or materials.

3.2.6. Atomic force microscopy

AFM images were taken to analyse the topography of each Electrode after pretreatments. Lekshmi Kailas, Experimental Officer in AFM at the University of Leeds, performed the AFM imaging. I assessed the electrodes employing NanoScope (ver 9.4) as detailed in **Section 2.2.12**. The electrode's roughness was evaluated in two different ways. First, 10 µm square images were analysed to obtain a general overview of the surface topography and to observe larger structures such as pollutants or grains. Then, a section analysis was carried out. Secondly, flatter parts of the matrix avoiding pollutants or grains were assessed. **Table 3.3** showed the roughness mean, Ra, of 10 µm, 5 µm and 1 µm square images over approximately 1 µm^2 surface.

Table 3.3: Roughness mean (Ra) ± SD for different pretreatments for each electrode type. The table shows Ra as the mean from n=3 ± SD of 1 µm^2 surface within the 10 µm, 5 µm and 1 µm square field.

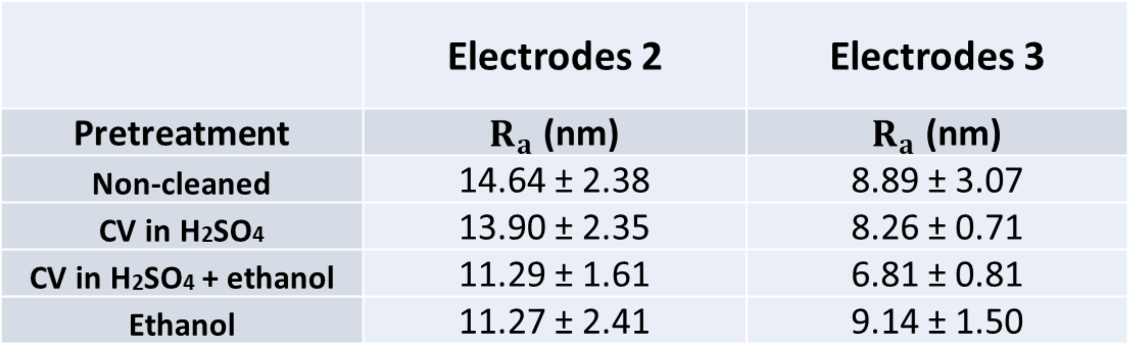

	Electrodes 2	Electrodes 3
Pretreatment	R_a (nm)	R_a (nm)
Non-cleaned	14.64 ± 2.38	8.89 ± 3.07
CV in H_2SO_4	13.90 ± 2.35	8.26 ± 0.71
CV in H_2SO_4 + ethanol	11.29 ± 1.61	6.81 ± 0.81
Ethanol	11.27 ± 2.41	9.14 ± 1.50

Figure 3.8A shows phase mode AFM images of Electrodes 2**.** Electrodes 2 had contaminant removal after CV in H_2SO_4 or CV in H_2SO_4 + ethanol pretreatment (**Figure 3.8Aii & iv**). The electrode surface seemed to be revealed after CV in H_2SO_4 or CV in H_2SO_4 + ethanol pretreatments, showing the appearance of terraces over the topography of the surface. AFM images along with previous XPS analysis concluded that the contaminant was Bi as observed from **Table 3.2**, where only after CV in H_2SO_4 or CV in H_2SO_4 + ethanol pretreatment did Bi disappeared from electrode composition. This indicated that only CV in H_2SO_4, amongst the treatments tested, could remove the Bi.

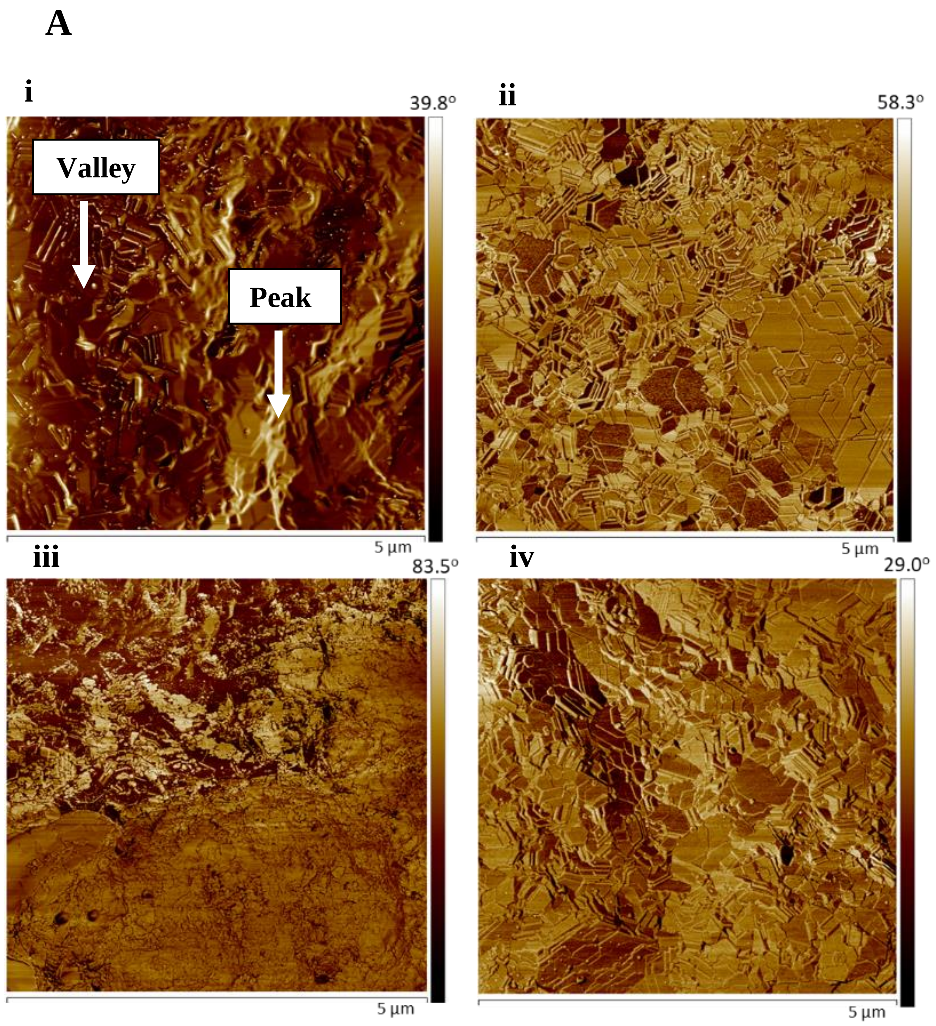
A
i
39.8°
Valley
Peak
5 µm
ii
58.3°
5 µm
iii
83.5°
5 µm
iv
29.0°
5 µm

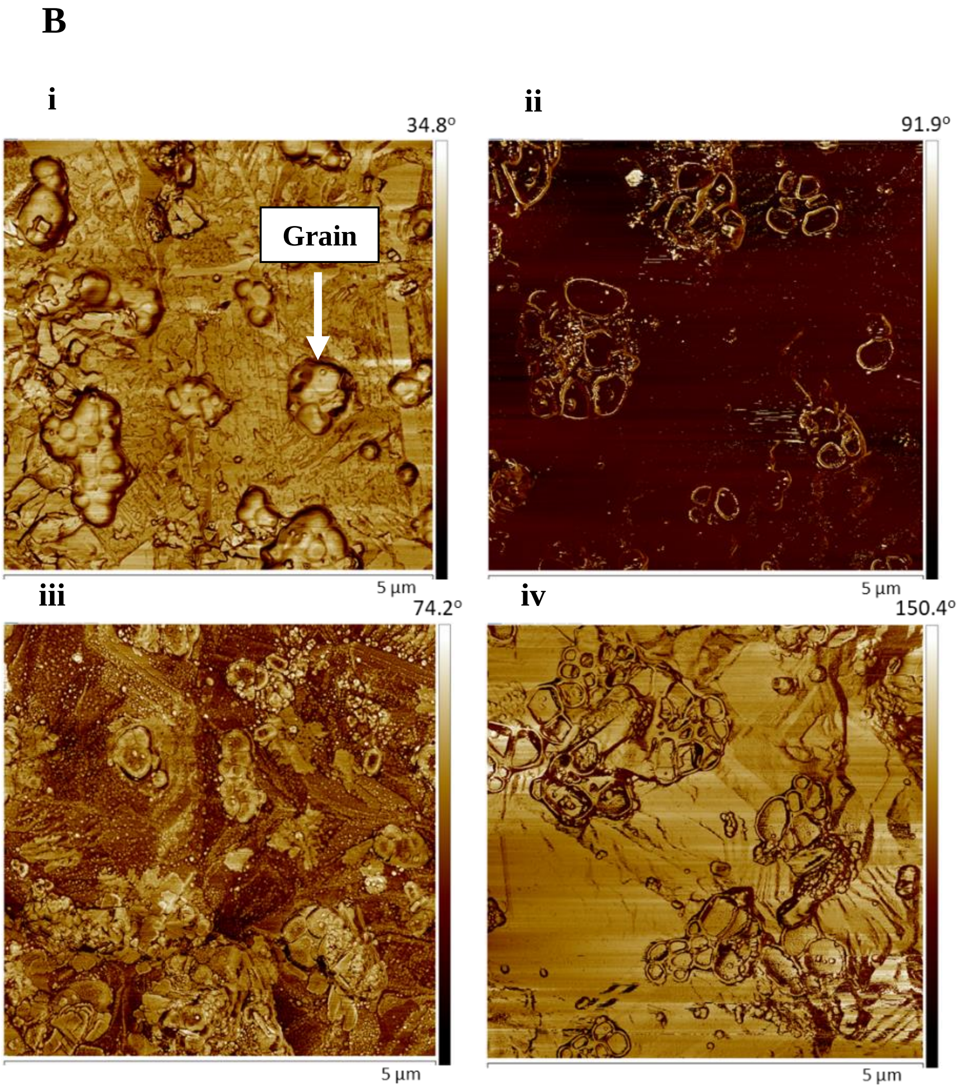

Figure 3.8: Phase mode AFM images of Electrode 2 and Electrode 3. The 5 µm scan-sized images were taken as detailed in **Section 2.2.12** assessed with NanoScope (ver 9.4) for non-pretreated (**i**), CV in H_2SO_4 (**ii**), ethanol (**iii**) and CV in H_2SO_4 + ethanol (**iv**). Figure A shows commercial Electrodes 2, CX2220AT, and B shows commercial Electrodes 3, BVT-AC1.W1.RS.Dw2.

Section analysis for non-pretreated Electrodes 2 and Electrodes 3 showed roughness differences in **Figure 3.9.** Electrode 2 roughness was manifested as peaks and valleys (**Figure 3.9A**). Some of the artefacts present on the surface appeared to be a lack of coating by the gold ink. A similar pattern could be observed for the rest of pretreated Electrodes 2. Electrodes 3 showed grains which caused sudden height levels over the surface (**Figure 3.9B**). No pretreatment removed the grains from the surface. However, CV in H_2SO_4 and CV in H_2SO_4 + ethanol pretreatment kept their elevated grain edges, followed by a depression inside the grain. This could indicate that CV in H_2SO_4 pretreatment etched some surface ink composition. XPS analysis confirmed that those removed elements were Cu and Pb and a bit of Zn (**Table 3.2**).

Table 3.3 shows the electrodes' surface roughness for the mean Ra of 1 μm^2 surface for both Electrode 2 and Electrode 3. This was indicative of the microscale roughness of tiny surfaces independent of bigger surface artefacts such as contaminants, grains and incomplete coverage by the gold ink. Electrodes 3 showed slightly flatter surfaces than Electrodes 2. Usually, flat gold surfaces yield better reversible CV voltammograms than rougher gold surfaces typically found in SPGEs. In this study, Electrodes 2 had more reproducible CV profiles of bare electrodes pretreated with different pretreatments than Electrodes 3 (**Figure 3.1**). However, pretreated Electrodes 3 provided more reproducible CV profiles than Electrode 2 trying different coatings (**Figure 3.6**). An electrochemical study employing carbon electrodes (Kadara et al., 2009) showed that the best reversible CV voltammogram was obtained from the roughest surface due to the more number of exposed edges. The employed graphite and deposition technique may have also affected the CV voltammogram. It was highlighted that a reversible CV voltammogram was not necessarily indicative of the reproducibility level of the electrode. This behaviour was also replicated in Metrohm DropSens SPGEs (Garc et al., 2008). All of this concluded that although SPGEs showed good reversibility from the CV profile, the roughness of the surface could limit their reproducibility.

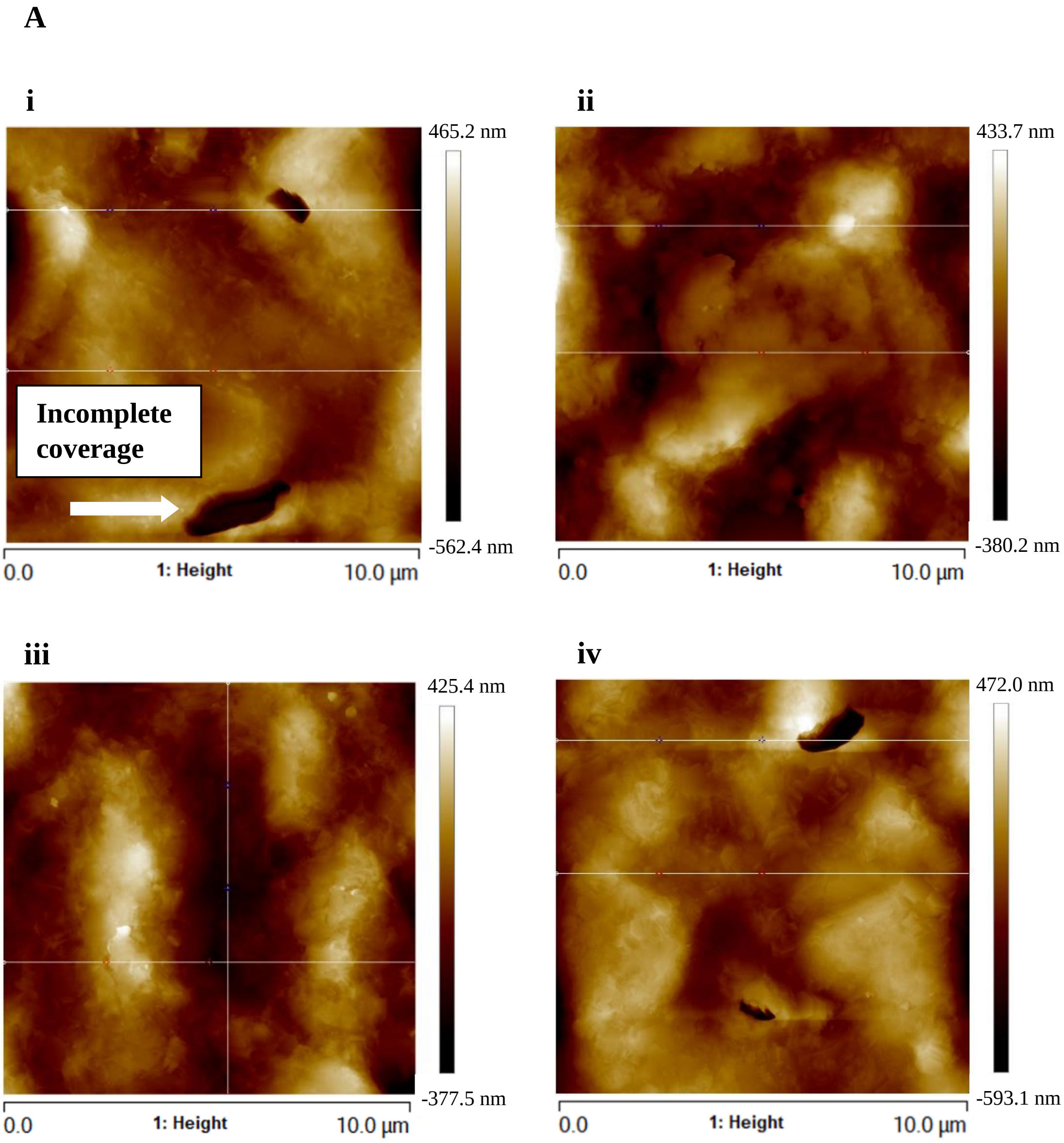
A
i
465.2 nm
-562.4 nm
Incomplete coverage
0.0
1: Height
10.0 µm
ii
433.7 nm
-380.2 nm
0.0
1: Height
10.0 µm
iii
425.4 nm
-377.5 nm
0.0
1: Height
10.0 µm
iv
472.0 nm
-593.1 nm
0.0
1: Height
10.0 µm

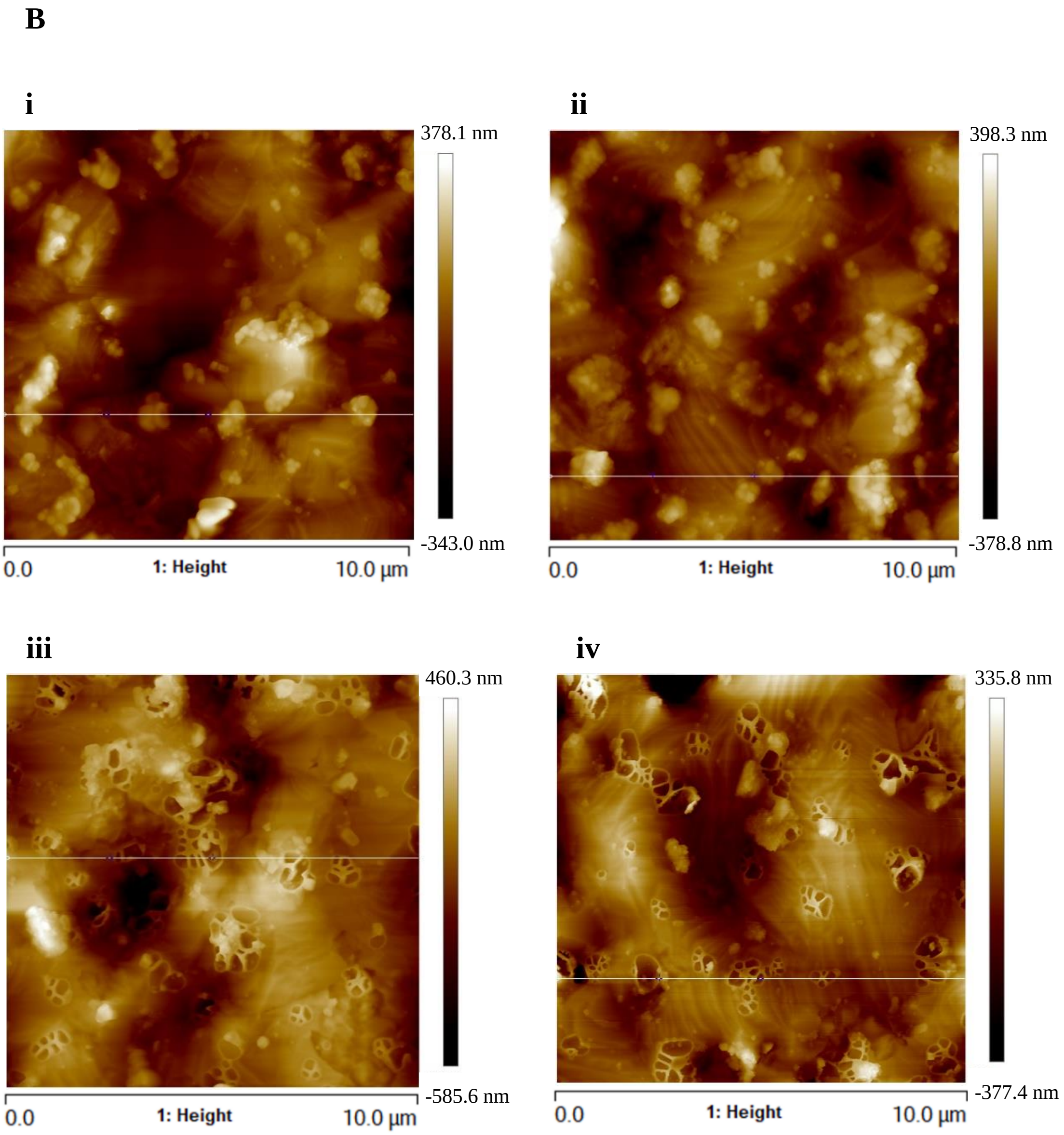

Figure 3.9: Section AFM analysis of Electrodes 2 and Electrodes 3 under different pretreatments. Ten µm scan-size AFM images were taken and assessed with NanoScope (ver 9.4). **A**, Electrodes 2 and **B**, Electrodes 3 for the different pretreatments: non-pretreated (**i**), ethanol (**ii**), CV in H_2SO_4 (**iii**) and CV in H_2SO_4 + ethanol (**iv**).

3.3. Discussion & Conclusions

In this chapter, CV in H_2SO_4, CV in H_2SO_4 + ethanol and ethanol have been assessed for pretreatment of two types of commercial SPGEs. Electrode 2, from Metrohm DropSens, and Electrode 3, from BVT Technologies, were functionalised with POc, POc-Ab, 11-MUA SAM, and bare surface for each pretreatment and non-pretreatment.

This research employed CV, EIS, AFM, and XPS to evaluate the amount of polymer and SAM coating the SPGEs, reproducibility, topography of the SPGEs' surface, and composition. Here, 3 different electrode pretreatments and non-pretreatments were compared. After the extensive analysis, it was concluded that there was no standard method for SPGE pretreatment.

Extensive gold surface pretreatment studies have been carried out. CV in H_2SO_4 appears to be among the most common gold surface pretreatment in literature for bare gold surfaces. However, different studies corroborated the best pretreatment performance of other pretreatments. (Fischer et al., 2009) found that KOH + H_2O_2 and KOH sweep method left the cleanest surface, whereas CV in H_2SO_4 yielded just acceptable surface; (Lamas-ardisana et al., 2015) discovered that the application of a fixed potential $HClO_4$ 1 M for 1 min yielded a flat gold wire electrode surface compared to gold surfaces pretreated with anodic and potentials in H_2SO_4.

However, the application of potentials in H_2SO_4 in joint pretreatment for gold surfaces yielded some successful SAM formation. Specific pretreatments have been researched for the SAM formation over gold surfaces. (Carvalhal et al., 2005) demonstrated that the best gold surface pretreatment for SAM formation was through mechanical polishing, chemical (piranha) and electrochemical (consecutive scans between redox potentials in H_2SO_4) pretreatments. Similar or related pretreatments have been used to construct electrochemical biosensors over a gold surface. (Dulay et al., 2011) employed a combination of mechanical, chemical and CV in H_2SO_4 to treat gold electrode surfaces. The gold surface was then coated with SAM for the electrochemical immunosensor detection of anti-tissue transglutaminase antibodies detection. The application of potentials in H_2SO_4 have been applied to pretreat gold electrodes for SAM formation as joint pretreatment in other different studies (Rosales-Rivera et al., 2011; Bandyopadhyay et al., 2013; Motaghedifard et al., 2014; Mossanha et al., 2015)

Gold pretreatments were also studied for thiol-modified DNA oligopeptide SAMs. An extensive study was carried out to show the best gold pretreatment for impedimetric aptasensors biosensors. Mechanical polishing and exposure in 50 mM KOH/H_2O_2 (3:1) was the best pretreatment compared to the rest, including CV in H_2SO_4 and combined acidic pretreatments (L. S. J. Ho et al., 2019).

Common gold electrode pretreatments include mechanical, chemical, electrochemical, UV/O_3, ethanol, etc. Some studies do not indicate any pretreatment procedure. Up to date, there are no in-depth studies about the SPGE pretreatments.

Recently, a more elaborated study about the most suitable pretreatment for SPGEs was carried out by (Stan et al., 2022). They recommend a pretreatment based on CV in 5 mM $K_4[Fe(CN)_6]/K_3[Fe(CN)_6]$. However, a solution of H_2O_2 with the application of multiple CV appeared to be the most efficient pretreatment. A brief study was carried out to develop a *Streptococcus pyogenes* biosensor (Ahmed et al., 2013). CV in H_2SO_4 was found to be better SPGE pretreatment than piranha solution and ethanol sonication. Nonetheless, CV in H_2SO_4 showed the possibility of creating gold electrode surface modifications that could affect the quality and reproducibility of their surfaces.

The literature suggests CV in H_2SO_4 as one of the best candidates, confirmed by several studies using it before biosensor construction (Radi et al., 2009; Escamilla-Gómez et al., 2008; Sakamoto et al., 2018; Loaiza et al., 2008; Aghaei et al., 2017; Ndiaye et al., 2016; Pagliarini et al., 2019; Cardoso et al., 2016; Kuralay et al., 2011; Escamilla-Gómez et al., 2009). Moreover, SPGE manufacturers such as Metrohm DropSens (Metrohm Dropsens), Micrux (Micrux Technologies) and Pine (PINE Research, 2016) accept CV in H_2SO_4 as a pretreatment for their commercial SPGEs.

This research has shown that under certain circumstances, CV in H_2SO_4 + ethanol or just ethanol pretreatments for SPGE could be better than CV in H_2SO_4 pretreatment. The pretreatment has been shown to depend on several factors such as composition and the surface coating, as had been previously concluded in literature. Specifically, degeneration, R_{ct}, C_{dl}, the gold electrode composition and the surface coating deposited or created over the electrode. Therefore, these results conclude that the best way of proceeding is to identify which one best suits your particular electrodes to produce the best stability and reproducibility.

Chapter 4

Fabrication and optimisation of an impedimetric immunosensor for *Escherichia coli* determination

Chapter 4: Fabrication and optimisation of an impedimetric immunosensor for *Escherichia coli* determination

4.1. Overview

This chapter reports on the first stages of the PhD in which an immunosensor against *E. coli* was investigated. The overall goal of the PhD project was to fabricate and optimise a biosensor based on the ECM protein-adhesin interaction (**Chapters 5 & 6**). The SPGEs to be used were purchased shortly after the commencing of the project. Nonetheless, the material's contact, purchase, and shipping would take months. Therefore, before any investigation in the novel area employing the ideal electrodes, an impedimetric immunosensor for *E. coli* detection was first investigated with older SPGE available in Millner's lab, Metrohm DropSens CX2223AT (Electrodes 1). Step-by-step optimisation of an immunosensor against whole bacteria was first considered to gain experience using the most common characterisation and analytical techniques, namely CV and EIS and main microbiological methods. The immunosensor would be later compared with the novel ECM protein-adhesin-based biosensor, corresponding to the main aim of the PhD project.

Optimisation of a classic immunosensor against whole *E. coli* was planned following on from previous investigations from former PhD students. In this chapter, a full antibody-based biosensor was investigated for whole bacteria determination using the bacteria strains employed by Dr. Natalie Hirst, who used bacteria donated by Mr John Wright, School of Molecular and Cellular Biology, University of Leeds. The donated bacteria comprised of a mixture of different *E. coli* strains, namely, BL21, 35218, DH5a, HGB101, and NCTC10418. One of the critical investigations of the biosensor researched in this chapter was the antibody attachment to the polymer. A successful protocol previously developed for antibody oxidation was followed (Shamsuddin, 2018).

In this chapter, several parameters were investigated until achieving a complete immunosensor construction, namely: selecting the correct solvent to dissolve the monomers, tyramine and octopamine; the monomer concentration for each polymer candidate; an adequate antibody concentration; and the type of polymer. Electrodes 1 were employed to optimise each *E. coli* impedimetric immunosensor construction level. EIS and CV were used as main electrochemical characterisation and analyte detection techniques.

In this research, EIS and CV analysis determined that PB + DMSO solvent was the most suitable to dissolve both monomer candidates. Both polymers showed their best performance at 0.1 M monomer in PB + DMSO. Tyramine was a better candidate than octopamine at the antibody concentration step, which showed the best performance at 0.1 mg/mL of antibodies. The final biosensor platform (**Figure 4.1**) successfully detected *E. coli* from 1x10^4 to 1x10^8 cfu/mL compared to the control sample containing just PBS. However, unspecific binding was detected just as highly as specific binding when using the control anti-Protein A antibodies against *E. coli*. Therefore, the biosensor could detect bacteria compared to control samples with only PBS and therefore, the biosensor also detected non-specific bacteria.

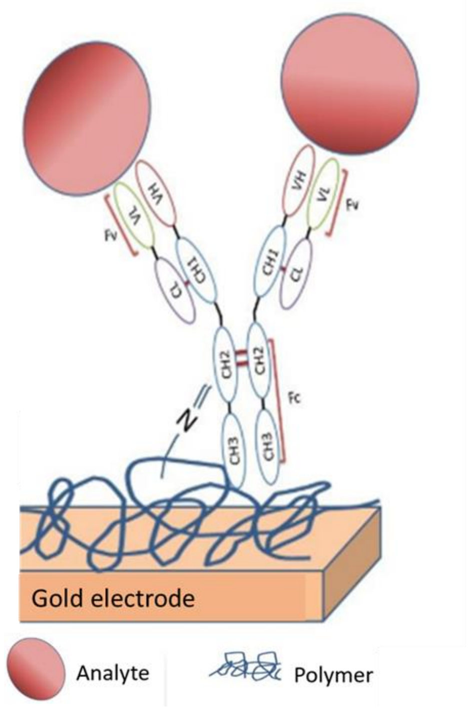

Figure 4.1: Replicate of Figure 2.4A for clarity. Immobilisation of antibodies to the polymer through reactive aldehyde of oxidised oligosaccharide on the Fc region reacting to polymer amine groups to form a covalent bond. Adapted and reproduced from (Shamsuddin, 2018).

4.2. Results

4.2.1. Optimisation of monomer-solvent

The first optimisation step consisted of selecting the best solvent to dissolve the two monomer candidates. Tyramine had been previously dissolved in different solvents. Tyramine dissolved in PBS was used for glucose biosensor development (Liu et al., 2007); in methanol with NaOH: for the development of an impedimetric biosensor for PEP gene detection (Yang et al., 2012), for *S. pyogenes* detection (Ahmed et al., 2013). Octopamine was dissolved in PB with DMSO for the cancer biomarker carcinoembryonic antigen detection (Shamsuddin et al., 2021). Therefore, tyramine and octopamine were dissolved in different solvents to determine which solvent allowed the best electropolymerisation.

First, Electrodes 1 were pretreated by conducting CV for 5 cycles of 1 M H_2SO_4 using Autolab workstation. Twenty-five mM of tyramine and 25 mM of octopamine were dissolved separately in: 10 mM PBS, methanol + 0.3 M NaOH, 100 mM PB + DMSO 20 % (v/v), 1 M HCl, 100 % methanol and electropolymerised as detailed in **Section 2.2.5.1**. Tyramine and octopamine electropolymerisation was achieved when characteristic oxidation peaks around +0.45 V to +0.6 V were observed (Ahmed et al., 2013; Shamsuddin et al., 2021). **Figures 4.2A-E & 4.3A-E** show the first and second CV cycles for octopamine and tyramine electropolymerisation for each solvent, respectively. In the first CV cycle, a characteristic oxidation peak can be observed for successful electropolymerisation. In the second CV cycle, the oxidation peak is then absent. Where peaks are small, a zoomed-in insert of +0.3 to +0.7 V is shown. Oxidation current during electropolymerisation was observed for both octopamine and tyramine dissolved in 10 mM PBS, in 100 mM PB + DMSO 20 % (v/v), and methanol + 0.3 M NaOH. Oxidation current was also observed in the electropolymerisation of tyramine dissolved in methanol (**Figure 4.3C**). In their second CV cycle, no oxidative peaks were observed and thus confirmed the polymerisation over the electrode surface.

POc and Ptyr-coated electrodes underwent EIS assessment, which provided information about the relative amount of polymer coating the electrode surface. **Figure 4.2F** shows the EIS analysis for POc-coated surfaces after electropolymerisation of octopamine dissolved in each solvent. The EIS analysis showed highly capacitive Nyquist curves for PBS and PB + DMSO solvents (red and green). The high impedance showed by these two solvents could imply a relatively thick and insulating layer. For the rest of the solvents tested (dark blue, light blue and teal), a slight or barely visible curve was observed only at high frequencies followed by linearity. These plot shapes can be explained by the limited diffusion process occurring at the electrode surface instead of the semi-circular shape of PBS and PB + DMSO, which indicates a charge-transfer limited process (Fernández-Sánchez et al., 2005). The charge-transfer limited process can especially be a drawback in determining conclusive resistive information as it is difficult to establish any definitive R_{ct} data. Well-shaped Nyquist curves can yield a more accurate Randles' equivalent fit, thus providing more precise R_{ct} data as it is obtained at lower frequencies.

Figure 4.3F shows the EIS analysis for Ptyr-coated surfaces after electropolymerisation of tyramine dissolved in each solvent. The EIS analysis for Ptyr-coated surfaces was similar to POc-coated ones and showed a very capacitive profile for PBS solvent (red). A more resistive Nyquist was observed for methanol (light blue), which interestingly achieved a successful electropolymerisation, unlike that observed for POc. Following methanol, PB + DMSO solvent (green) presented a precise well-shaped Nyquist fit in Randle's equivalent circuit and a less capacitive system than PBS and methanol. Despite the satisfactory Nyquist shape, methanol + 0.3 M NaOH showed a very small Nyquist curve. Finally, similarly to previously observed POc profiles, the HCl solvent gave a minimal curve.

PB + DMSO was the best solvent candidate for both monomers after the electropolymerisation and EIS analysis. Nyquist plots from electrodes coated with Ptyr and POc dissolved in PB + DMSO showed a characteristic semi-circle curve, not too capacitive, and resistive enough to indicate an insulating polymeric layer over the electrode that could provide accurate R_{ct} data at low frequencies. EIS profiles in PB + DMSO were ideal to proceed with further investigations.

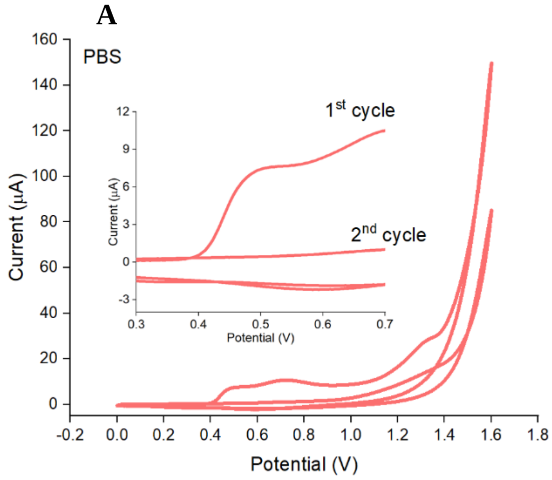
A
PBS
Current (μA)
Potential (V)
160
140
120
100
80
60
40
20
0
-0.2
0.0
0.2
0.4
0.6
0.8
1.0
1.2
1.4
1.6
1.8
1st cycle
2nd cycle
Current (μA)
Potential (V)
12
9
6
3
0
-3
0.3
0.4
0.5
0.6
0.7

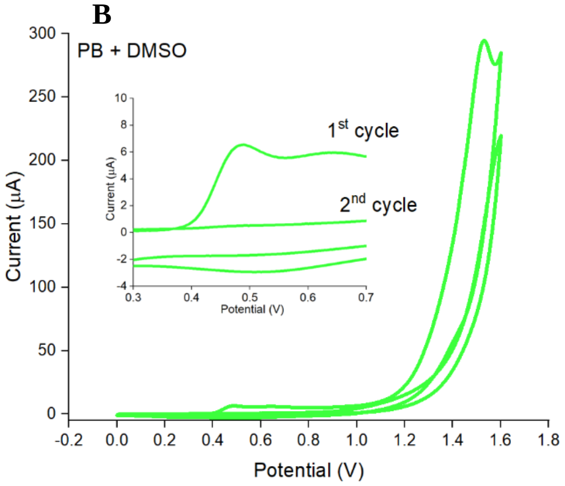
B
PB + DMSO
Current (μA)
Potential (V)
300
250
200
150
100
50
0
-0.2
0.0
0.2
0.4
0.6
0.8
1.0
1.2
1.4
1.6
1.8
1st cycle
2nd cycle
Current (μA)
Potential (V)
10
8
6
4
2
0
-2
-4
0.3
0.4
0.5
0.6
0.7

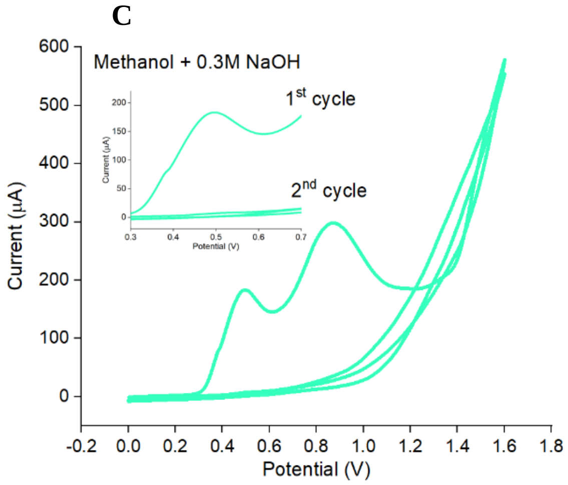
C
Methanol + 0.3M NaOH
Current (μA)
Potential (V)
600
500
400
300
200
100
0
-0.2
0.0
0.2
0.4
0.6
0.8
1.0
1.2
1.4
1.6
1.8
1st cycle
2nd cycle
Current (μA)
Potential (V)
200
150
100
50
0
0.3
0.4
0.5
0.6
0.7

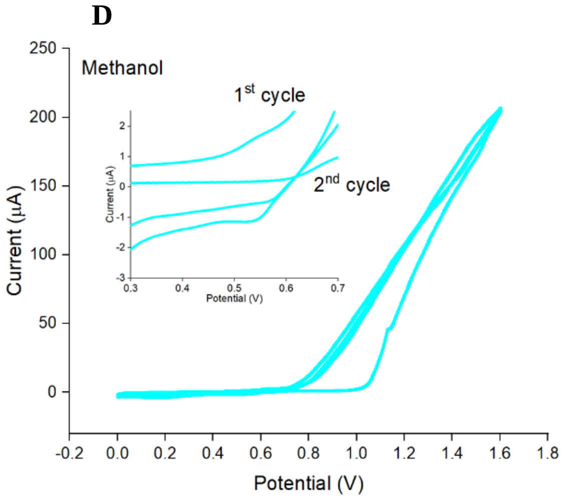
D
Methanol
Current (μA)
Potential (V)
250
200
150
100
50
0
-0.2
0.0
0.2
0.4
0.6
0.8
1.0
1.2
1.4
1.6
1.8
1st cycle
2nd cycle
Current (μA)
Potential (V)
2
1
0
-1
-2
-3
0.3
0.4
0.5
0.6
0.7

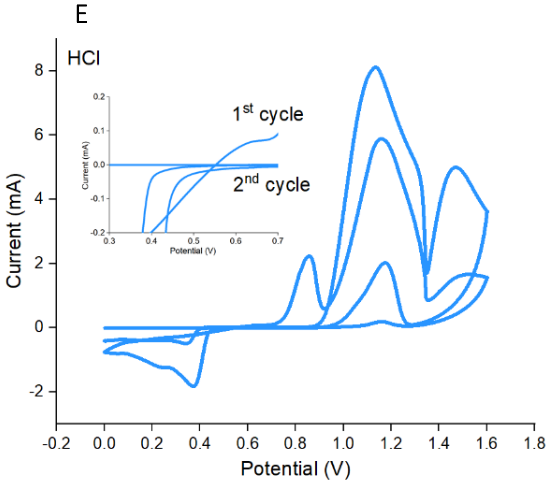
E
HCl
Current (mA)
Potential (V)
8
6
4
2
0
-2
-0.2
0.0
0.2
0.4
0.6
0.8
1.0
1.2
1.4
1.6
1.8
1st cycle
2nd cycle
Current (mA)
Potential (V)
0.2
0.1
0.0
-0.1
-0.2
0.3
0.4
0.5
0.6
0.7

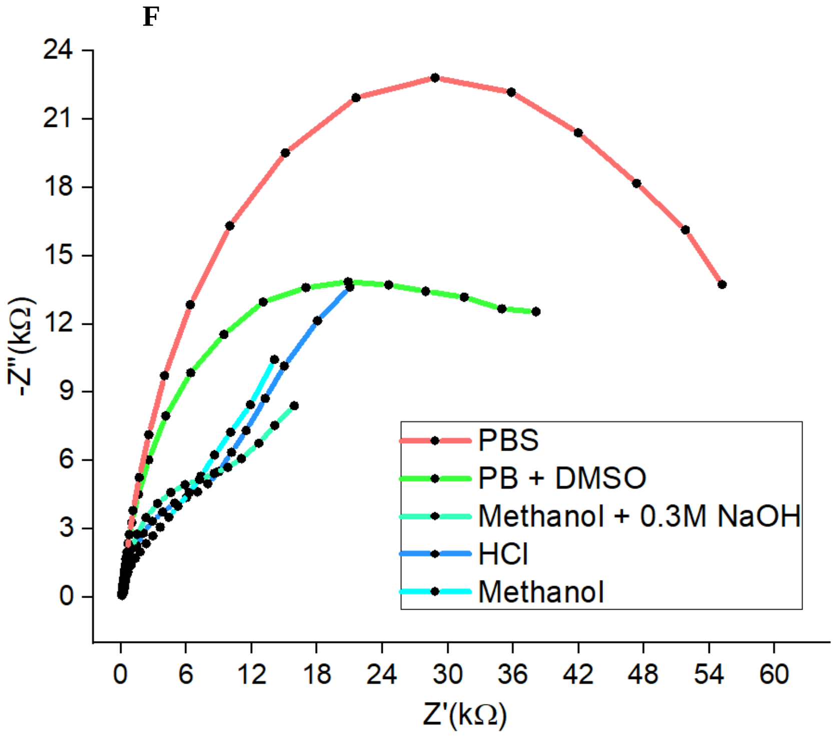

Figure 4.2: 25 mM octopamine electropolymerisation CV and POc-coated surfaces' Nyquist profiles for octopamine dissolved in different solvents. Twenty-five mM octopamine solutions were cycled over Electrodes 1 from 0.0 V to +1.6 V for 2 cycles using Autolab workstation in **A**, 10 mM PBS; in **B**, 100 mM PB + DMSO 20 % (v/v); in **C**, methanol + 0.3 M NaOH; in **D**, in methanol; and in **E**, 1 M HCl. The zoomed-in inserts of +0.3 V to +0.7 V are shown for each electropolymerisation profile. **F**, Nyquist profiles derived from EIS measurements in 10 mM $[Fe(CN)_6]^{3-/4-}$ in 100 mM PBS pH 7.2. EIS was recorded at 0.0 V over a frequency range of +2.5 kHz to +0.25 Hz, with a modulation voltage of +10 mV as described in **Section 2.2.5.1**. Averaged curves shown with number of repeats, n=4.

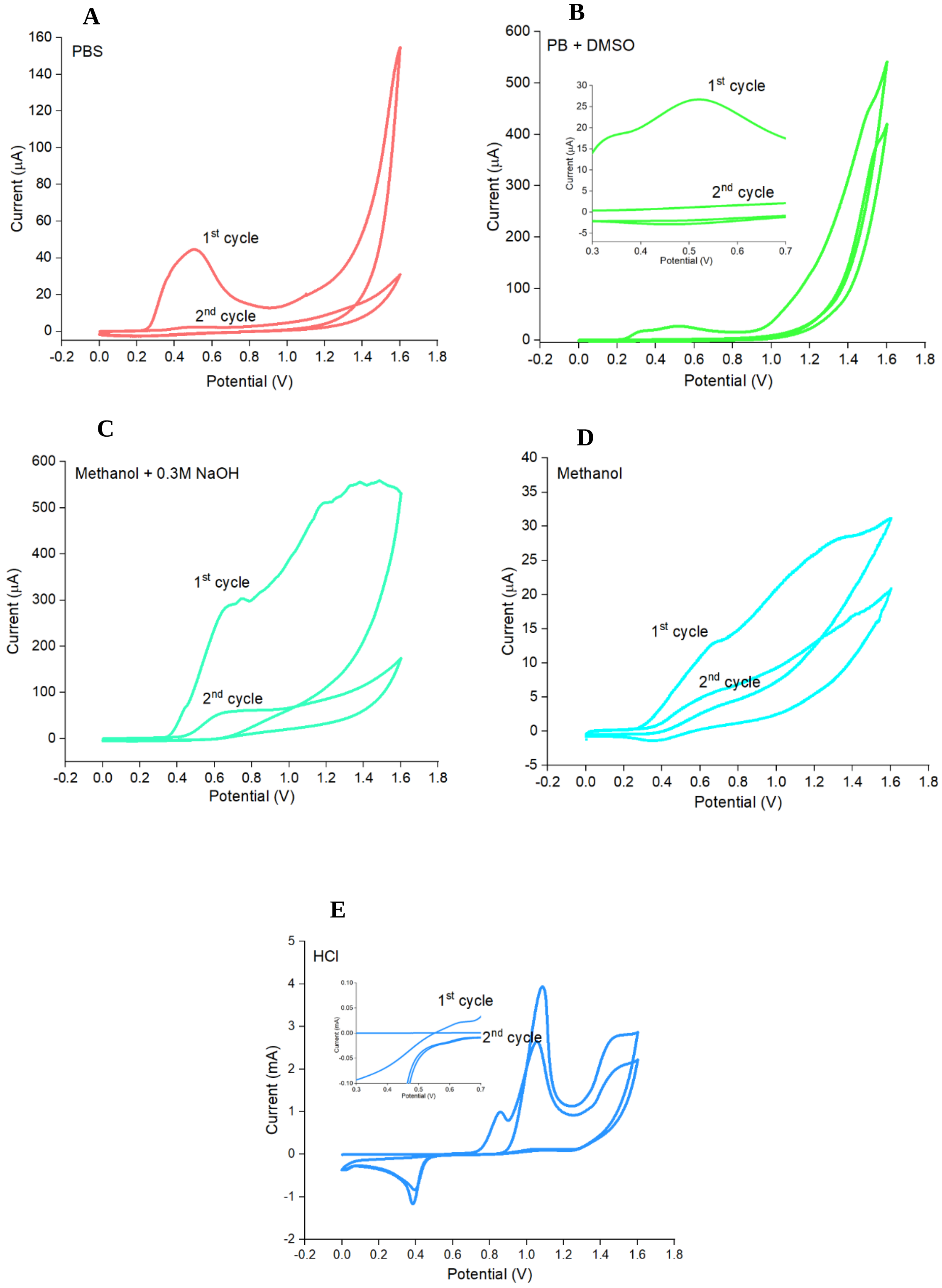
A
PBS
Current (μA)
160
140
120
100
80
60
40
20
0
1st cycle
2nd cycle
-0.2
0.0
0.2
0.4
0.6
0.8
1.0
1.2
1.4
1.6
1.8
Potential (V)
B
PB + DMSO
Current (μA)
600
500
400
300
200
100
0
1st cycle
2nd cycle
Current (μA)
30
25
20
15
10
5
0
-5
0.3
0.4
0.5
0.6
0.7
Potential (V)
-0.2
0.0
0.2
0.4
0.6
0.8
1.0
1.2
1.4
1.6
1.8
Potential (V)
C
Methanol + 0.3M NaOH
Current (μA)
600
500
400
300
200
100
0
1st cycle
2nd cycle
-0.2
0.0
0.2
0.4
0.6
0.8
1.0
1.2
1.4
1.6
1.8
Potential (V)
D
Methanol
Current (μA)
40
35
30
25
20
15
10
5
0
-5
1st cycle
2nd cycle
-0.2
0.0
0.2
0.4
0.6
0.8
1.0
1.2
1.4
1.6
1.8
Potential (V)
E
HCl
Current (mA)
5
4
3
2
1
0
-1
-2
1st cycle
2nd cycle
Current (mA)
0.10
0.05
0.00
-0.05
-0.10
0.3
0.4
0.5
0.6
0.7
Potential (V)
-0.2
0.0
0.2
0.4
0.6
0.8
1.0
1.2
1.4
1.6
1.8
Potential (V)

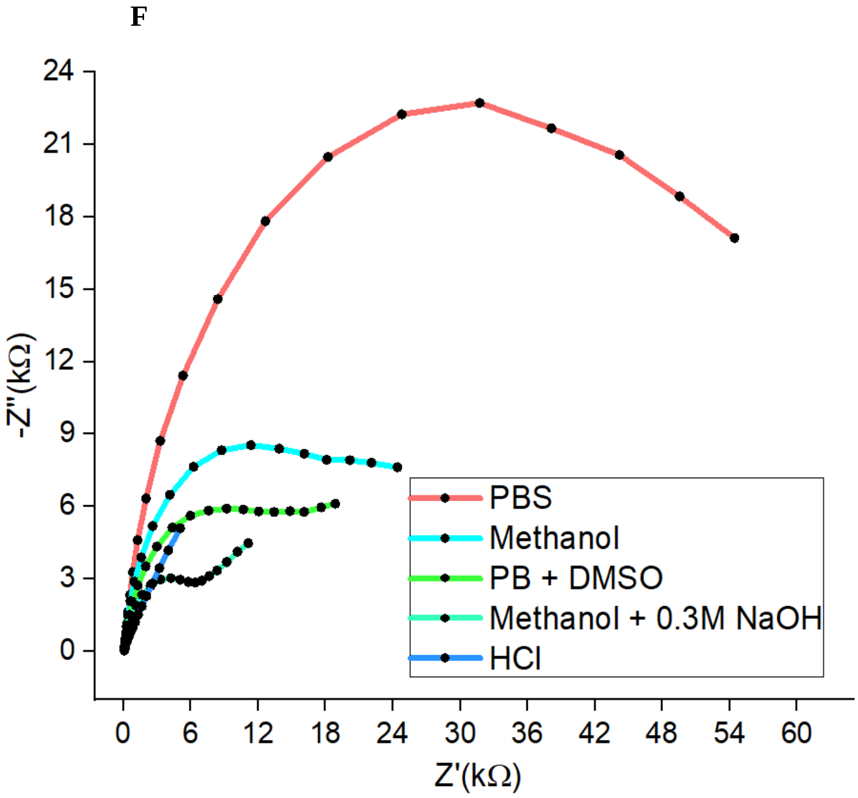

Figure 4.3: 25 mM tyramine electropolymerisation CV and Ptyr-coated surfaces' Nyquist profiles for tyramine dissolved in different solvents. Twenty-five mM tyramine solutions were cycled over Electrodes 1 from 0.0 V to +1.6 V for 2 cycles using Autolab workstation in **A**, 10 mM PBS; in **B**, 100 mM PB + DMSO 20 % (v/v); in **C**, methanol + 0.3 M NaOH; in **D**, in methanol; and in **E**, 1 M HCl. The zoomed-in inserts of +0.3 V to +0.7 V are shown for PB + DMSO and HCl. **F**, Nyquist profiles derived from EIS measurements in 10 mM $[Fe(CN)_6]^{3-/4-}$ in 100 mM PBS pH 7.2. EIS was recorded at 0.0 V over a frequency range of +2.5 kHz to +0.25 Hz, with a modulation voltage of +10 mV as described in **Section 2.2.5.1**. Averaged curves shown with number of repeats, n=4.

4.2.2. Optimisation of octopamine and tyramine concentration

First, electrodes were pretreated, washed and dried. Then, four concentrations of each monomer, 0.01 M, 0.025 M, 0.05 M, and 0.1 M, were dissolved in 100 mM PB + DMSO 20 % (v/v) and electropolymerised onto the electrodes as detailed in **Section 2.2.5.1** for subsequent EIS analysis (**Section 2.2.7**). **Figures 4.4A & 4.5A** show the electropolymerisation profiles for octopamine and tyramine respectively. The first cycle shows a characteristic oxidation peak for all polymer concentrations except for the control. No oxidation cycle was observed in the second peak, indicating successful electrodeposition for both polymer ranges of concentration.

Afterwards, the coated electrodes underwent EIS analysis to obtain information about the relative amount of polymer coating them. A control without any polymer was also assessed for comparison. **Figures 4.4B & 4.5B** show the Nyquist plots for systems using POc and Ptyr respectively for all range of concentrations. Similar EIS behaviour was observed for surfaces coated with both polymers. When monomer concentrations increased, their system's Nyquist curves increased too. The highest Nyquist plot for POc and Ptyr-coated surfaces was achieved at 0.1 M of their respective monomer concentration (light blue). Particularly in the POc-coated surface; the Nyquist plot represented a more considerable resistance and capacitance. The POc systems' Nyquist plots showed a steady increase in their curves. That behaviour was not observed for Ptyr systems, whose Nyquist overlaps with the control at 0.01 M (orange) and 0.025 M (green).

Nyquist plots were fitted to Randle's equivalent circuit to obtain R_{ct} values (**Figures 4.4C & 4.5C**). As the octopamine concentration increased, a consistent increase was noticed for POc systems' R_{ct} values. These results were in accordance with the previous Nyquist curves analysis. The POc systems with the two lowest octopamine concentrations, 0.01 M (orange) and 0.025 M (green), with 9.57 ± 0.27 kΩ and 9.76 ± 0.35 kΩ respectively, showed similar R_{ct} values with overlapping error bars. A remarkable increase was observed for POc-coated surfaces with 0.05 M octopamine (teal), 12.12 ± 1.01 kΩ, although a relatively large error bar was presented. The POc-coated surfaces with highest octopamine concentration, 0.1M (light blue) with 13.80 ± 0.32 kΩ, clearly differed from POc-coated systems with the lower octopamine concentrations R_{ct} and showed a small error bar (**Figure 4.4C**). Concerning R_{ct} values for Ptyr-coated electrodes (**Figure 4.5C**), there was no difference between the control (red), 8.53 ± 0.65 kΩ, and the two Ptyr-coated surfaces with the lowest tyramine concentrations, 0.01 M (orange) and 0.025 M (green), 8.50 ± 0.22 kΩ and 10.38 ± 1.97 kΩ respectively. Nonetheless, a differentiated increase was observed from system with 0.05 M tyramine (teal), 11.90 ± 1.26 kΩ, to 0.1 M tyramine (light blue), 14.54 ± 0.33 kΩ. Overall, the R_{ct} assessment provided similar information to the previous Nyquist plots analysis. The surfaces coated with lower monomer concentrations were close to the control (red) or even non-distinguishable in the R_{ct} analysis. Then, an R_{ct} increase for surfaces coated with POc and Ptyr was observed from 0.025 M (green) to 0.1 M (light blue). This behaviour was similarly presented by the oxidation current peaks observed in the electropolymerisation profiles (**Figures 4.4A & 4.5A**). After considering the electropolymerisation voltammograms, Nyquist profiles and reproducibility of R_{ct} values, a concentration of 0.1 M (light blue) for both polymers was chosen for further experiments.

A

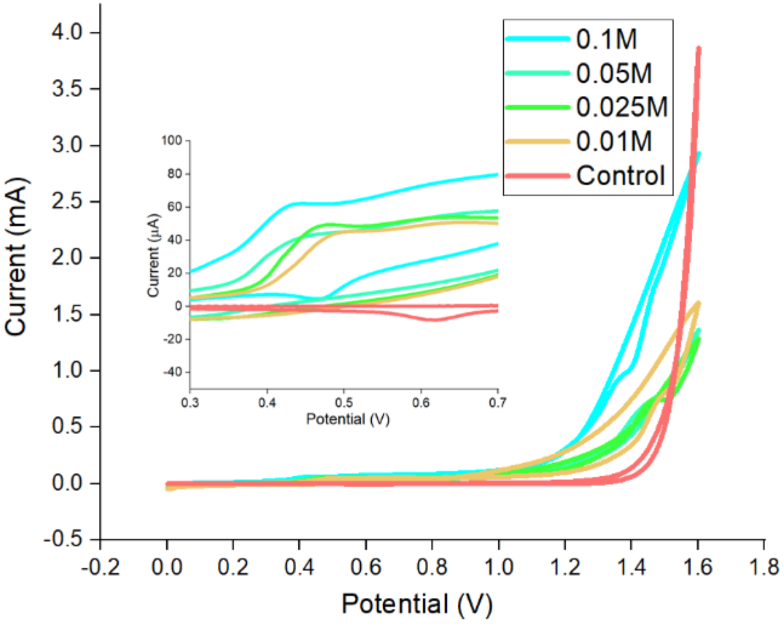
Current (mA)
Potential (V)
4.0
3.5
3.0
2.5
2.0
1.5
1.0
0.5
0.0
-0.5
-0.2
0.0
0.2
0.4
0.6
0.8
1.0
1.2
1.4
1.6
1.8
0.1M
0.05M
0.025M
0.01M
Control
Current (µA)
Potential (V)
100
80
60
40
20
0
-20
-40
0.3
0.4
0.5
0.6
0.7

B

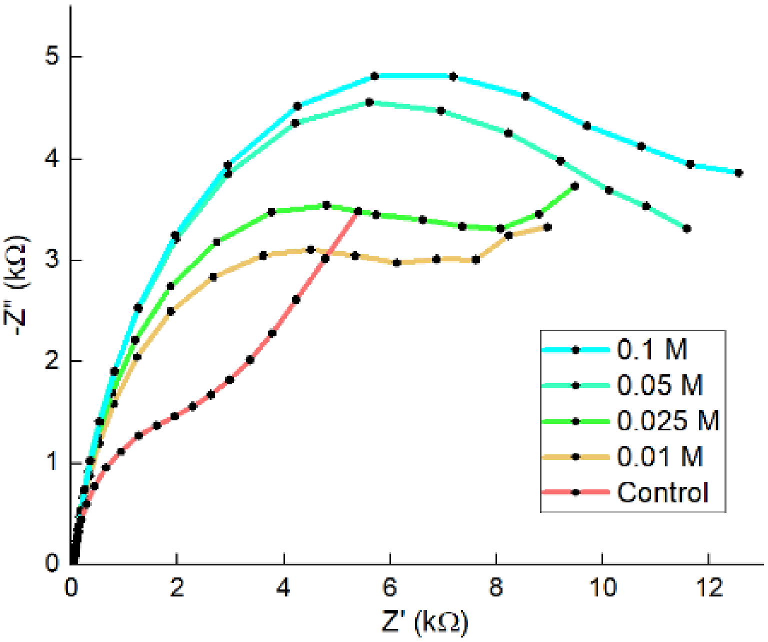
-Z'' (kΩ)
Z' (kΩ)
5
4
3
2
1
0
0
2
4
6
8
10
12
0.1 M
0.05 M
0.025 M
0.01 M
Control

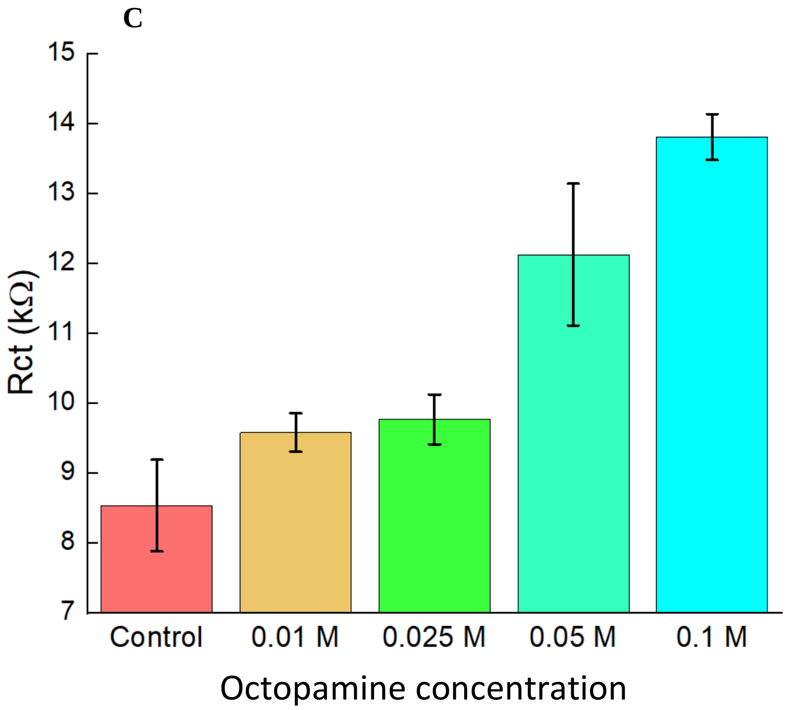

Figure 4.4: Octopamine electropolymerisation; CV, Nyquist plot and R_{ct} values for POc-coated surfaces. Different concentrations of octopamine, namely, 0.01, 0.025, 0.05 and 0.1 M were dissolved in 100 mM PB + DMSO 20 % (v/v). **A**, Different concentrations were cycled over Electrodes 1 from 0.0 V to +1.6 V for 2 cycles using Autolab workstation (**Section 2.2.5.1**). **B**, The Nyquist profiles derived from EIS measurements in 10 mM $[Fe(CN)_6]^{3-/4-}$ in 100 mM PBS pH 7.2. EIS was recorded at 0.0 V over a frequency range of +2.5 kHz to +0.25 Hz, with a modulation voltage of +10 mV (**Section 2.2.7**). **C**, R_{ct} values were obtained from the Randles' equivalent circuits fitting. CVs and Nyquist shown with number of repeats, n=4. The bars represent data from n=4 ± SD.

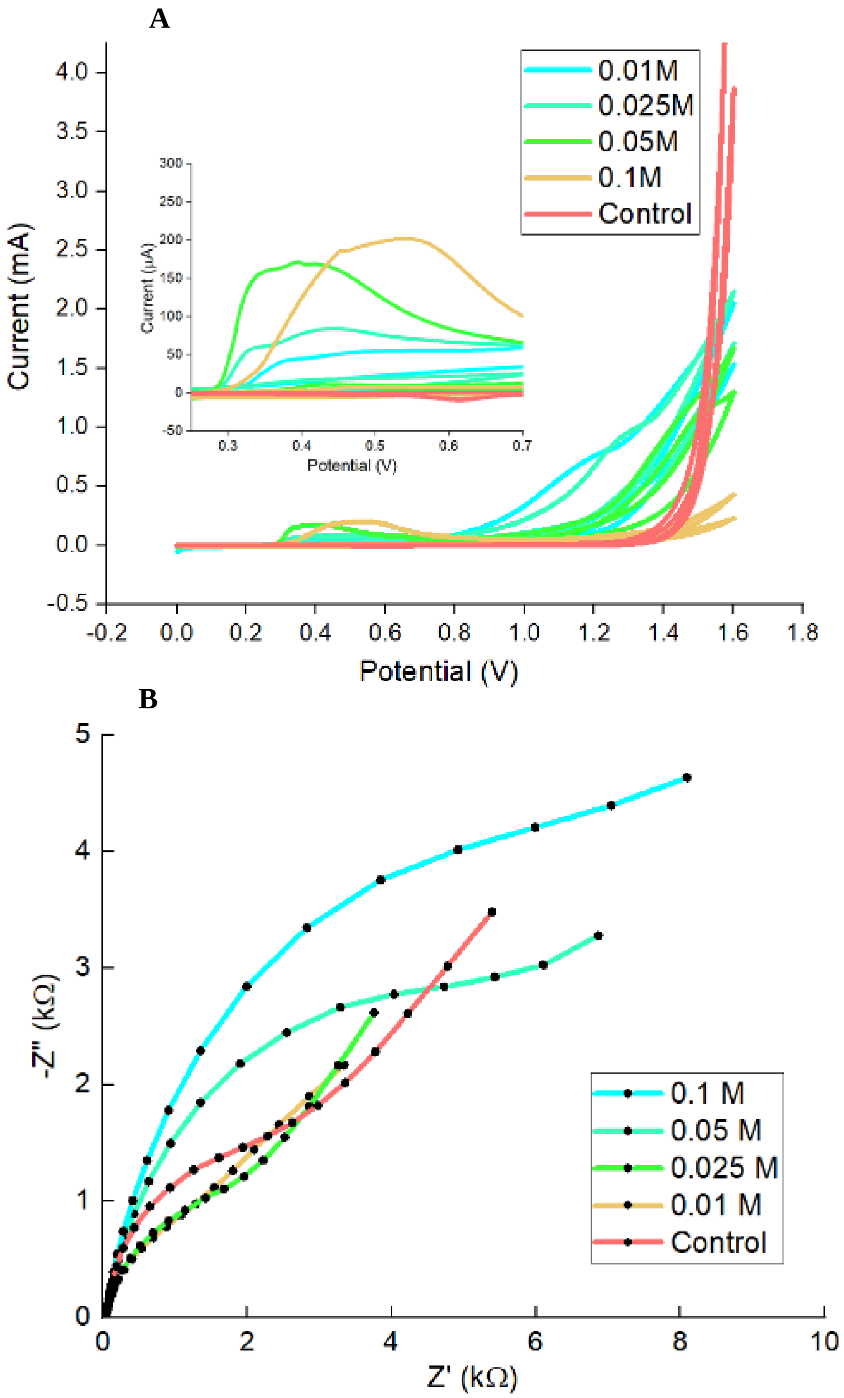
A
Current (mA)
4.0
3.5
3.0
2.5
2.0
1.5
1.0
0.5
0.0
-0.5
-0.2
0.0
0.2
0.4
0.6
0.8
1.0
1.2
1.4
1.6
1.8
Potential (V)
0.01M
0.025M
0.05M
0.1M
Control
Current (µA)
300
250
200
150
100
50
0
-50
0.3
0.4
0.5
0.6
0.7
Potential (V)
B
-Z'' (kΩ)
5
4
3
2
1
0
0
2
4
6
8
10
Z' (kΩ)
0.1 M
0.05 M
0.025 M
0.01 M
Control

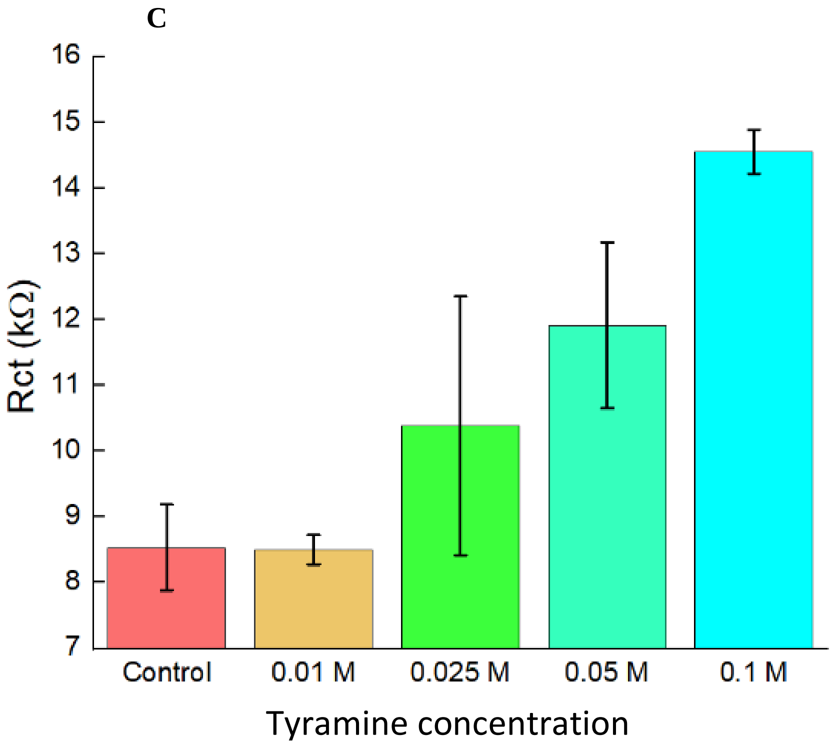

Figure 4.5: Tyramine electropolymerisation; CV, Nyquist plot and R_{ct} values for Ptyr-coated surfaces. Different concentrations of tyramine, namely, 0.01, 0.025, 0.05 and 0.1 M were dissolved in 100 mM PB + DMSO 20 % (v/v). **A**, Different concentrations were cycled over Electrodes 1 from 0.0 V to +1.6 V for 2 cycles using Autolab workstation (**Section 2.2.5.1**). **B**, The Nyquist profiles derived from EIS measurements in 10 mM $[Fe(CN)_6]^{3-/4-}$ in 100 mM PBS pH 7.2. EIS was recorded at 0.0 V over a frequency range of +2.5 kHz to +0.25 Hz, with a modulation voltage of +10 mV (**Section 2.2.7**). **C**, R_{ct} values were obtained from the Randles' equivalent circuits fitting. CVs and Nyquist shown with number of repeats, n=4. The bars represent data from n=4 ± SD.

4.2.3. *E. coli*-antibody affinity by EIS

The bacteria and the antibodies used in this section were provided by Dr. Natalie Hirst. A mixture of 5 different bacterial strains, *E. coli* BL21, 35218, DH5a, HGB101, and NCTC10418, were used and detected using polyclonal antibodies raised in rabbits against a mixture of *E. coli* strains **(Section 2.1.2)**. This section aimed to assess whether the polyclonal antibodies had more affinity to the mixture of all bacteria or to one strain in particular. Therefore, a mix of all bacterial strains and each of the strains were tested for two different bacterial concentrations of 10^5 cfu/mL and 10^8 cfu/mL and control without bacteria. Up to this point, the immunosensor was being developed and not fully optimised. Therefore, a different successful protocol for whole bacteria detection from Millner's lab was used to detect the bacteria (Ahmed et al., 2013) (**Figure 2.4B**).

First, electrodes were pretreated, washed, dried, and subsequently functionalised until complete biosensor construction. Briefly, 0.025 M tyramine was dissolved in methanol with 0.3 M NaOH and electropolymerised. In order to immobilise the antibodies to the sensor surface using biotin-Neutravidin attachment, the polymerised working electrodes were incubated with biotin-NHS and followed by Neutravidin. Finally, the biotinylated antibodies were attached to the biosensors and ready for bacterial testing. Next, 5 µL of *E. coli* was applied to both working electrodes, which were incubated in a moist chamber for 15 min. Once completed, electrodes were washed and analysed through EIS (**Section 2.2.7**). This process was carried out for n=4 for 1x10^5 cfu/mL and 1x10^8 cfu/mL *E. coli*, using a new electrode for each measurement. The control was carried out without bacteria, only PBS (**Section 2.2.5.1**).

Figure 4.6 shows the EIS results a mix of all bacteria strains (**Figure 4.6A**) and individual strains (**Figures 4.6B-F**). Mixed bacteria and strain HB101 presented an almost identical Nyquist curve for both *E. coli* tested concentrations (**Figure 4.6A-B**). The bacteria strains in **Figures 4.6C-F** showed differences in Nyquist curves between the two concentrations and also from the control curve. Bacteria DH5a (**Figure 4.6D**) and 35218 (**Figure 4.6C**) showed the clearest analytical signal: the Nyquist plots showed differentiated signals for the two different *E. coli* tested concentrations between them and compared to the controls. BL21 (**Figure 4.6E**) showed differentiated binding for the tested *E. coli* concentrations. However, DH5a showed a clear analytical signal and is typically used for a wide variety of applications, particularly in synthetic biology and cloning. Therefore, it was decided to continue with DH5a for further experiments.

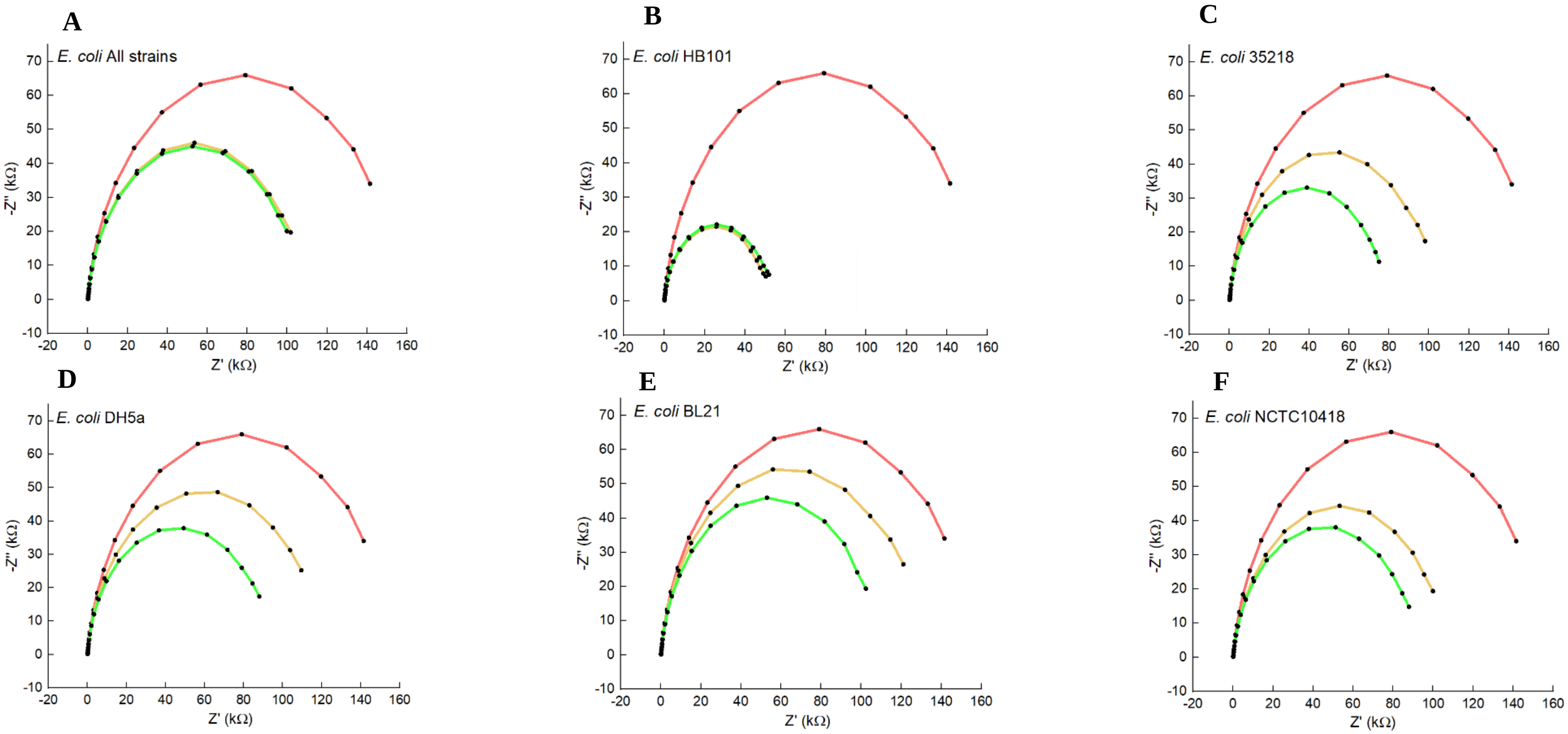

Figure 4.6: EIS analysis assessed bacterial binding compared to control for all mixed bacteria strains and each bacteria strain. To construct this biosensor over Electrodes 1, a different model biosensor was already optimised and can be followed in detail in (Ahmed et al., 2013). **A**, a mix of all bacteria strains; **B**, strain HB101; **C**, strain 35218; **D**, strain DH5a; **E**, strain BL21 and **F**, strain NCTC10418, were assessed for binding for 10^5 cfu/mL (🟨), 10^8 cfu/mL (🟩) and PBS (🟥). The Nyquist profiles derived from EIS measurements in 10 mM $[Fe(CN)_6]^{3-/4-}$ in 100 mM PBS pH 7.2. EIS was recorded at 0.0 V over a frequency range of +2.5 kHz to +0.25 Hz, with a modulation voltage of +10 mV using Autolab workstation (**Section 2.2.7**). Averaged curves shown with number of repeats, n=4.

4.2.4. Optimisation of antibody concentration

The previous step employed an already successful optimised protocol for whole bacteria detection. This allowed determining which bacterial strain was more suitable for further experiments. For the next steps until the final optimised biosensor, the research consisted of keeping on developing an optimised protocol for whole bacteria detection. So far, 0.1 M monomer dissolved in 100 mM PB + DMSO 20 % (v/v) and the use of *E. coli* DH5a was optimised. The antibody concentration and polymer still needed to be studied. Antibody concentration is considered a critical optimisation parameter as it determines the amount of bioreceptor (antibody) attached to the biosensor's surface. The next step in the biosensor construction, therefore, consisted of immobilising different anti-*E. coli* IgG concentrations onto the polymer-coated electrode surface.

First, electrodes were pretreated, washed and dried. Then, three typical antibody as bioreceptor concentrations, namely, 0.1 mg/mL, 0.5 mg/mL and 1 mg/mL anti-*E. coli* IgG was oxidised to create reactive aldehyde groups to achieve a covalent bond with the polymer amine groups as detailed in **Section 2.2.5.1**. Once the antibodies were adhered to the POc-coated SPGE surface, EIS analysis was conducted (**Section 2.2.7**).

Figure 4.7A shows the Nyquist plot for antibody functionalised POc-coated SPGEs at different antibody concentrations 0.1 mg/mL (orange), 0.5 mg/mL (green) and 1 mg/mL (teal) and a control (red) without antibody, just polymer coating. The Nyquist plot curves increased according to an increase in antibody concentration. The control's Nyquist plot (red) appeared to be the smallest curve. **Figure 4.7B** shows the R_{ct} values of the different antibody concentrations and the control obtained from fitting the Nyquist plots to Randle's equivalent circuit. The lowest antibody concentration, 0.1 mg/mL (orange), presented the smallest R_{ct} value, 11.67 ± 0.44 kΩ. R_{ct} control (red), 13.80 ± 0.32 kΩ, showed to be as large as 0.5 mg/mL (green) and 1 mg/mL (teal), with 13.78 ± 0.90 kΩ and 14.50 ± 0.22 kΩ. These differences between the Nyquist and the R_{ct} analysis could be explained by the control's low-frequency values, which complicated Randles' equivalent circuit fitting.

Then, the same study was carried out for antibody functionalised Ptyr-coated SPGEs. **Figure 4.8A** shows the Nyquist plot for antibody functionalised Ptyr-coated SPGEs at different antibody concentrations 0.1 mg/mL (orange), 0.5 mg/mL (green) and 1 mg/mL (teal) and a control (red). The antibody functionalised Ptyr-coated SPGEs showed a decrease in their Nyquist curve, starting from the control, followed by a higher antibody concentration. Likewise, the same trend was observed in the R_{ct} analysis (**Figure 4.8B**), which exhibited a decrease in R_{ct} magnitude as the antibody concentration increased. The addition of antibodies to the Ptyr-coated surface was manifested by decreased impedance. This behaviour was also observed for Ptyr-coated SPGEs in

(Ahmed et al., 2013). This effect could be explained by the stretchy net behaviour adopted by the polymer. The polymer net tenses after the antibody binding, thus creating more space for the electron mediators to reach the electrode surface. As octopamine and tyramine are slightly different polymers, the attachment of antibodies may saturate their surfaces in different ways.

The best polymer candidate was chosen by the best impedimetric performance with the optimum antibody concentration. Ptyr was selected as the best polymer after considering the reproducibility and consistency in R_{ct} and Nyquist analysis along with 0.1 mg/mL of antibody. In addition, the antibody immobilisation over Ptyr showed an impedimetric behaviour already observed in a successful biosensor for *S. pyogenes* detection (Ahmed et al., 2013).

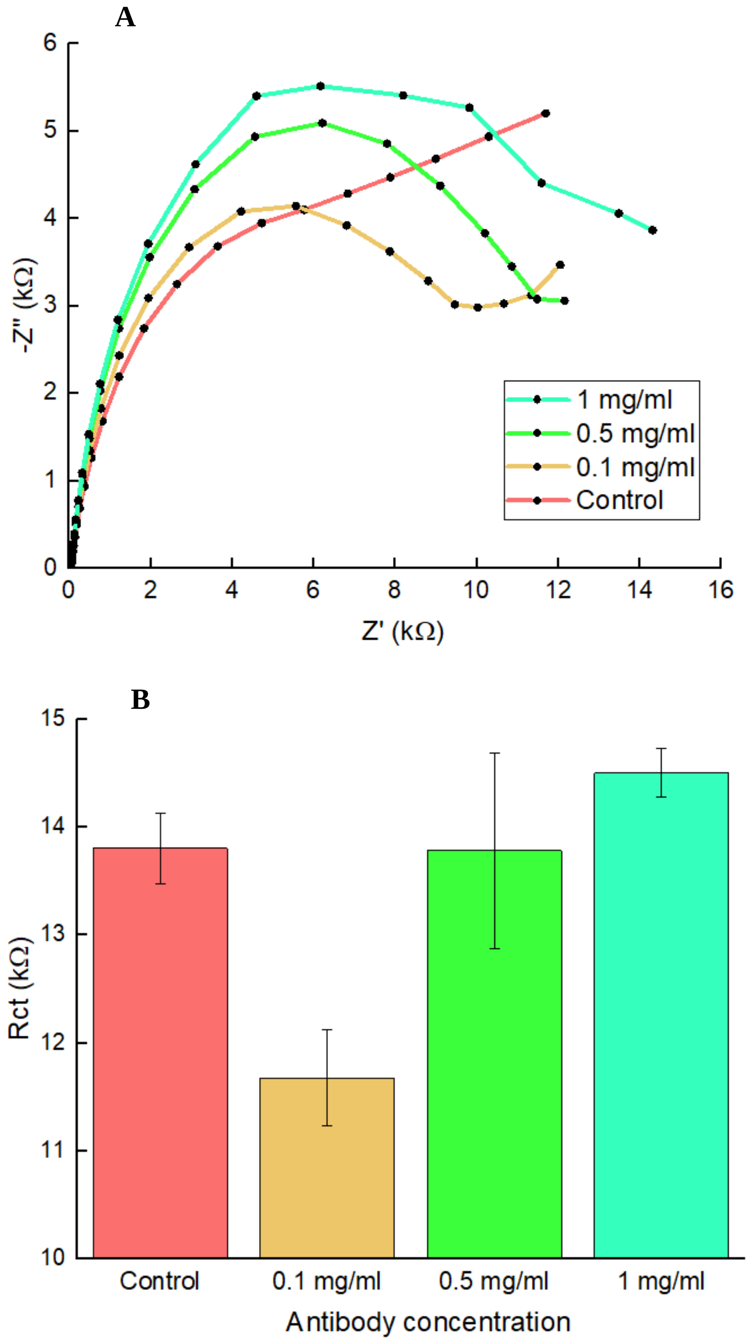

Figure 4.7: Nyquist plots and R_{ct} bar chart for antibody functionalised POc-coated SPGEs at different antibody concentrations. Different anti-*E. coli* IgG concentrations, namely, 0.1, 0.5, and 1 mg/mL, were oxidised to create reactive aldehyde groups to achieve a covalent bond with the polymer amine groups as detailed in **Section 2.2.5.1**. Once the antibodies were adhered to the POc-coated Electrodes 1, EIS analysis was conducted. **A**, The Nyquist profiles derived from EIS measurements in 10 mM $[Fe(CN)_6]^{3-/4-}$ in 100 mM PBS pH 7.2. EIS was recorded at 0.0 V over a frequency range of +2.5 kHz to +0.25 Hz, with a modulation voltage of +10 mV using Autolab workstation (**Section 2.2.7**). **B**, to obtain the R_{ct} values, each Nyquist plot was fitted into Randle's equivalent circuit model. Averaged curves shown with number of repeats, n=4. The bars represent data from n=4 ± SD.

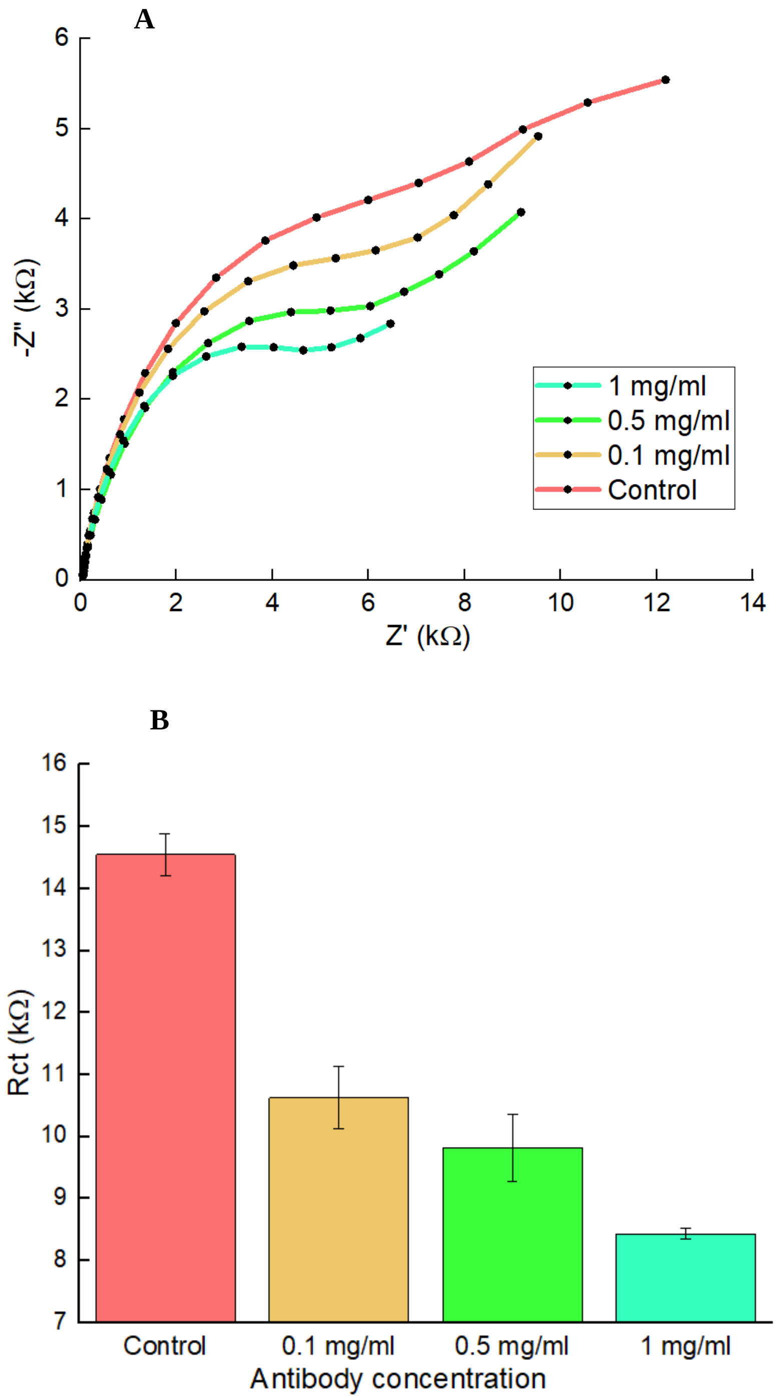

Figure 4.8: Nyquist plots and R_{ct} bar chart for antibody functionalised Ptyr-coated SPGEs at different antibody concentrations. Different anti-*E. coli* IgG concentrations, namely, 0.1, 0.5, and 1 mg/mL, were oxidised to create reactive aldehyde groups to achieve a covalent bond with the polymer amine groups as detailed in **Section 2.2.5.1**. Once the antibodies were adhered to the Ptyr-coated Electrodes 1, EIS analysis was conducted. **A**, the Nyquist profiles derived from EIS measurements in 10 mM $[Fe(CN)_6]^{3-/4-}$ in 100 mM PBS pH 7.2. EIS was recorded at 0.0 V over a frequency range of +2.5 kHz +0.25 Hz, with a modulation voltage of +10 mV using Autolab workstation (**Section 2.2.7**). **B**, to obtain the R_{ct} values, each Nyquist plot was fitted into Randle's equivalent circuit model. Averaged curves shown with number of repeats, n=4. The bars represent data from n=4 ± SD.

4.2.5. Full *Escherichia coli* immunosensor

The optimum conditions for the *E. coli* immunosensor construction were: 0.1 M of tyramine dissolved in 100 mM PB + 20 % (v/v) DMSO and an antibody concentration of 0.1 mg/mL.

Next, electrodes were pretreated, washed and dried. Then, 0.1 mg/mL anti-*E. coli* IgG, for analyte detection, and 0.1 mg/mL anti-protein A antibody, as a control, were covalently attached to the Ptyr-coated SPGE surface. After that, 5 µL of *E. coli* was placed over both working electrodes incubated in a moist chamber for 15 min. Once completed, electrodes were rinsed and analysed through EIS (**Section 2.2.7**). This process was carried out for n=4 for $1x10^3$ cfu/mL concentrations to $1x10^8$ cfu/mL *E. coli*, using a new electrode for each measurement as detailed in **Section 2.2.5.1**.

Figure 4.9A shows the Nyquist plots after the EIS analysis of the optimised biosensor for a range of concentrations of *E. coli*. Sensors with specific anti-*E. coli* IgG, cells consistently bound and detected bacteria. Nyquist plots showed a consistent trend in which the Nyquist plots increased with the bacterial concentration. **Figure 4.9C** shows the R_{ct} values of the different antibody concentrations and the control obtained from fitting the Nyquist plots to Randle's equivalent circuit. Similarly to the Nyquist results, a consistent increase in R_{ct} values with increasing bacteria concentration was tested despite relatively large error bars (**Figure 4.9C**). However, bacterial binding was also detected when control antibodies were employed despite no consistent trend with bacterial concentration (**Figures 4.9B-C**).

Smaller impedance, either in Nyquist or R_{ct}, was expected when testing bacteria with control antibodies. However, impedance levels showed that bacterial detection using control antibodies was higher than for specific antibodies against *E. coli* for most of the analysis. This could have its explanation in the origin of the antibody optimisation step where only anti-*E. coli* was tested. The control antibody, anti-protein A, could have presented different attachments to the Ptyr-coated surface. There is a clear, logical trend expected when using anti-*E. coli*: the Nyquist plots and R_{ct} values increase with increasing bacterial concentration (**Figures 4.9A & C**). No logical trend was observed for the anti-Protein A (**Figures 4.9B-C**).

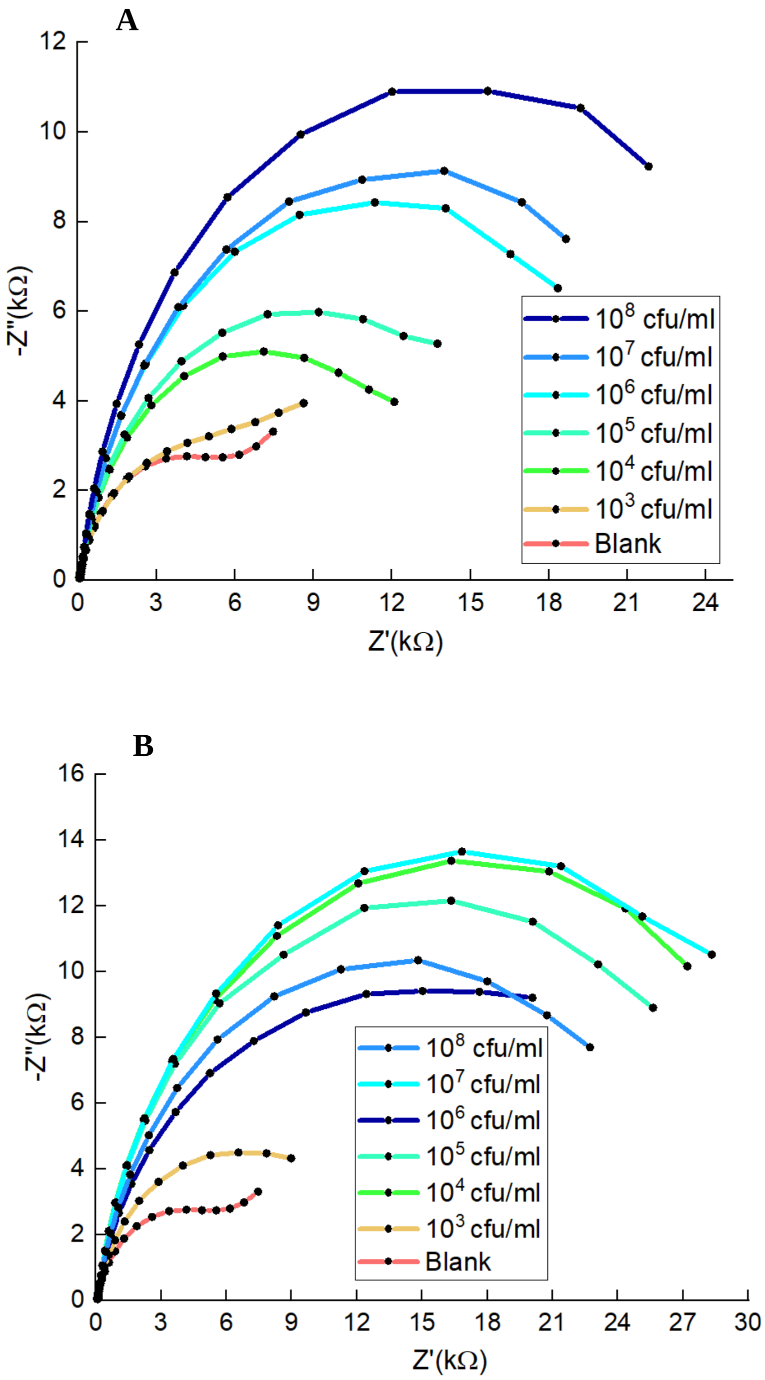
A
12
10
8
6
4
2
0
-Z''(kΩ)
0
3
6
9
12
15
18
21
24
Z'(kΩ)
10^8 cfu/ml
10^7 cfu/ml
10^6 cfu/ml
10^5 cfu/ml
10^4 cfu/ml
10^3 cfu/ml
Blank
B
16
14
12
10
8
6
4
2
0
-Z''(kΩ)
0
3
6
9
12
15
18
21
24
27
30
Z'(kΩ)
10^8 cfu/ml
10^7 cfu/ml
10^6 cfu/ml
10^5 cfu/ml
10^4 cfu/ml
10^3 cfu/ml
Blank

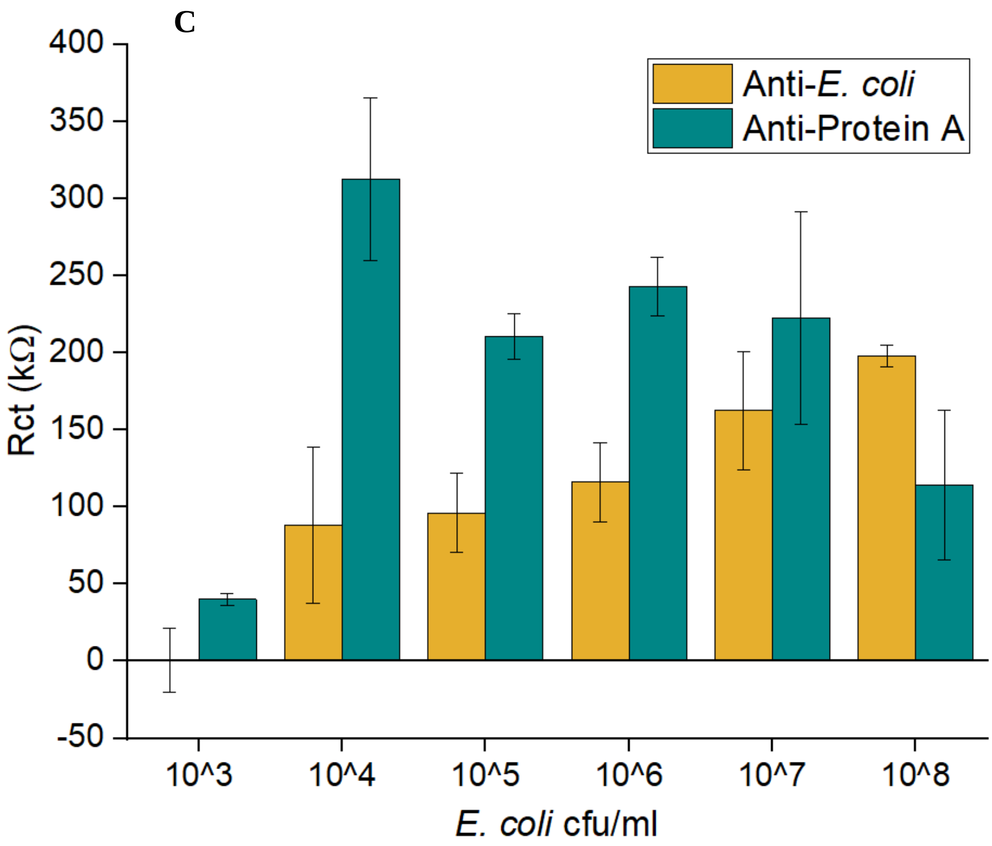

Figure 4.9: Bacterial detection through EIS represented by Nyquist and R_{ct} for a range of bacterial concentrations from 10^3 to 10^8 cfu/mL. The biosensor was fully constructed and tested with 5 µL of *E. coli*, incubated for 15 min and washed. Then, the biosensors were analysed by EIS. This process was carried out for $1x10^3$ cfu/mL to $1x10^8$ cfu/mL *E. coli*, using a new electrode for each measurement as detailed in **Section 2.2.5.1**. All Nyquist profiles derived from EIS measurements over Electrodes 1 in 10 mM $[Fe(CN)_6]^{3-/4-}$ in 10 mM PBS pH 7.2 using Autolab workstation. EIS was recorded at 0.0 V over a frequency range of +2.5 kHz to +0.25 Hz, with a modulation voltage of +10 mV (**Section 2.2.7**). **A**, representing the bacterial binding using anti-*E. coli* and **B**, using anti-protein A as a control. **C**, Represents the R_{ct} values for *E. coli* against the specific anti-*E. coli* and for the control anti-Protein A for the different bacterial concentrations. Averaged curves shown with number of repeats, n=4. The bars represent data from n=4 ± SD.

4.3. Discussion & Conclusions

A basic impedimetric antibody-based immunosensor for *E. coli* detection was constructed. Different parameters were optimised, and the best candidates were taken for further steps: 0.1 M of tyramine dissolved in 100 mM PB + 20 % (v/v) DMSO and an antibody concentration of 0.1 mg/mL. The performance of the biosensor was shown to detect bacteria from 10^4 cfu/mL to 10^8 cfu/mL when using anti-*E. coli* against *E. coli* DH5a strain. A steady increase in the R_{ct} values was observed with increasing bacterial concentrations. Nonetheless, bacteria tested with anti-Protein A showed an abnormal performance. An increase in R_{ct} was observed but not steadily and with huge variability. This could be caused by the anti-protein A conformation when attaching to the Ptyr surface. This is not observed in the anti-*E. coli* as they were employed for the antibody optimisation step. Anti-protein A attachment to the biosensor should be studied to improve biosensor detection further. In addition, non-specific binding could be decreased if adding a blocking agent optimisation step. Typically, blocking agents can be added to the surface after the IgG addition to minimise the unspecific binding. However, (Shamsuddin, 2018) concluded that no blocking step was needed for that protocol. Therefore, at this stage, blocking agents were not investigated.

The biosensor optimisation could have been improved in different ways. The first step, optimisation, consisted in choosing the most suitable solvent for the polymer. CV and EIS were employed to assess it, and PB + DMSO was selected for further steps. However, the electrochemical analysis could not have been enough to choose the best buffer. The adequate polymerisation does not indicate the proven availability of NH_2 groups at their surface, essential to bind the oxidised antibodies. It was confirmed by further experiments the attachment of the antibodies. However, chemiluminescence experiments could have helped observe which solvent candidate allowed more NH_2 groups to be present at the polymer surface.

Better performance could have been obtained in the antibody optimisation: antibodies must be kept in the dark with ice. However, these conditions could not be maintained throughout the entire experiment. When opening the Eppendorf's, the antibodies were exposed to light, and tearing the aluminium foil would compromise the dark conditions after the oxidation procedure. This could have led to a differential confirmation of each batch of oxidised antibodies across different experimental repeats. Some pitfalls presented during the biosensor construction or full biosensor could have been avoided by planning the experiments differently. Rather than using anti-protein A as a control, a control bacteria could have been tested against the specific anti-*E. coli* IgG. In addition, typical blocking agents such as BSA or casein could have been assessed to prevent non-specific binding. Other chemicals such as ethanolamine could have been beneficial in blocking any nonspecific and undesirable interactions of other abundant contaminating molecules (Foubert et al., 2019). In addition, the optimum antibody concentration should have included a wider range of concentrations. Also, choosing the best bacterial strain for its affinity to anti-*E. coli* should have been decided by other techniques such as Dot Blot, at least for validation.

In addition, some optimisation steps and the analyte testing could have yielded better analytical signals by analysing the increase in % R_{ct} rather than testing the R_{ct} at the end of the process. This implies testing the R_{ct} before and after the analyte addition, allowing to obtain better analytical signals, which would improve the performance of the final biosensor.

Chapter 5

Preliminary biosensor optimisation

Chapter 5: Preliminary biosensor optimisation

5.1. Overview

Research and characterisation of Metrohm DropSens CX2223AT (Electrodes 1) and Metrohm DropSens CX2220AT (Electrodes 2) had been carried out using Autolab workstation in Millner´s lab. In **Chapter 4,** Electrodes 1 from Metrohm DropSens and Autolab workstation were employed. However, as explained in **Section 9.4**, BVT-AC1.W1.RS.Dw2 (Electrodes 3) and Palmsens workstation equipment were purchased to continue the project (**Chapters 5-7**). The electrode composition of one type of gold electrode can vary from one manufacturer to another. In addition, SPGEs from the same manufacturer and model can present variations among different batches. Therefore, essential electrochemical characterisation and exploration of the Electrodes 3 employing Palmsens workstation were carried out.

The new Electrodes 3 and electrochemical workstation consisted of a new setup, including the potentiostat, adapter, multiplexer, and electrodes. **Figure 5.1** shows a photograph of the Palmsens workstation instrumentation. The electrochemical setup was different: multiple electrodes were connected simultaneously to an adapter and multiplexer, which could run them simultaneously for EIS and consecutively for CV. In addition, given the setup structure, the electrolyte solution was placed as 50 µL onto the working electrode to be analysed. This differed from the former Autolab workstation in which the electrodes were assessed individually by immersing them in electrolyte solution (**Figure 5.2**).

Several characterisation experiments for Electrodes 3 using Palmsens workstation were carried out: buffer concentration of the electrolyte solution, CV effect over EIS and vice versa, the polymer electrodeposition after 24 h in solution, the electrochemical assessment using both electrochemical workstations, Electrodes 3 pretreatment using Palmsens workstation and bare electrode characterisation.

It is essential to clarify that the Electrodes 3 pretreatment optimisation found in this chapter does not relate to the one in **Chapter 3**. In **Chapter 3,** Electrodes 2 and Electrodes 3 were analysed with Autolab workstation. In this chapter, only Electrodes 3 were assessed employing Palmsens workstation. The reason to have evaluated Electrodes 3 with another electrochemical workstation is due to electrochemical analysis differences presented when different electrochemical setups are used, as explained in **Section 5.2.5**. Despite both electrochemical workstations giving different analytical signals one to another under the same conditions, the outcome as per the pretreatment to use was the same, concluding that ethanol pretreatment suited best Electrodes 3 coated with POc.

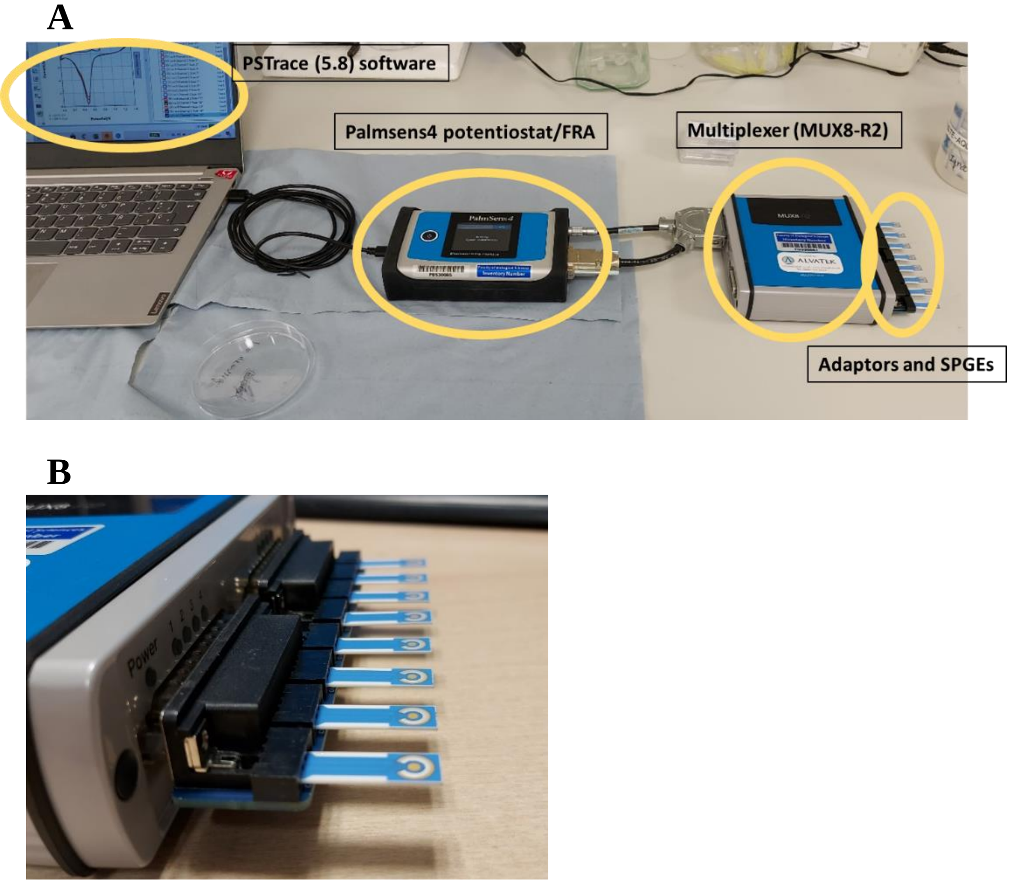

Figure 5.1: Replicate of Figure 2.3 for clarity. A, Palmsens4 potentiostat, galvanostat and frequency response analyser (FRA) coupled to a multiplexer (MUX8-R2) with adaptors connected to 8 different Electrodes 3. The potentiostat was controlled through PSTrace 5.8 software. **B**, a closer image corresponding to the adapter and the set of 8 SPGEs.

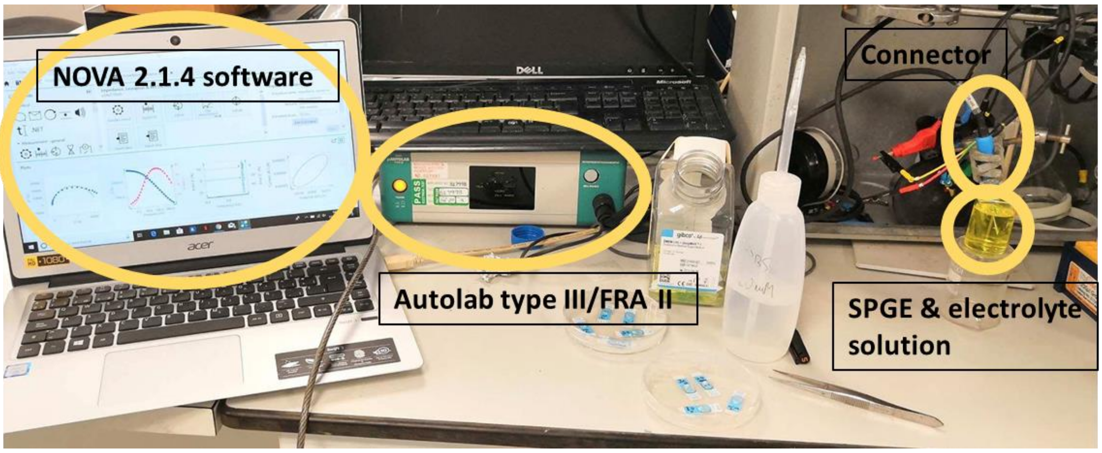

Figure 5.2: Replicate of Figure 2.2 for clarity. The Autolab type III Fra II potentiostat connected to a single Electrode 2 through a connector and immersed in an electrolyte solution. The potentiostat is controlled by NOVA 2.1.4 software.

5.2. Results

5.2.1. Buffer concentration for electrolyte solution

The electron mediator solution was one of the first conditions to be assessed. Typically, a solution of 10 mM $[Fe(CN)_6]^{3-/4-}$ was dissolved in either 10 mM or 100 mM PBS for impedimetric biosensor measurements (Ahmed et al., 2013; Thangsunan, 2018; Shamsuddin, 2018). A solution of 10 mM $[Fe(CN)_6]^{3-/4-}$ in 100 mM PBS pH 7.2 was employed for **Chapters 4 & 8.** This decision was based upon the use of the Metrohm DropSens SPGEs and Autolab potentiostat, which was the same electrochemical equipment as reported in (Thangsunan, 2018) and (Shamsuddin, 2018) as they used that electrolyte and buffer concentration.

Once Electrodes 3 and Palmsens4 workstation arrived, 10 mM $[Fe(CN)_6]^{3-/4-}$ in 100 mM PBS pH 7.2 was kept as electrolyte solution. When analysing CV voltammograms for POc-coated Electrodes 3 under 10 mM $[Fe(CN)_6]^{3-/4-}$ in 100 mM PBS pH 7.2, a white precipitate was observed over the working electrode. This had a negative effect on the reproducibility of the scans. The white precipitate also appeared for EIS analysis. In this case, the electrodes were simultaneously assessed and the precipitate appeared during the analysis. As a result, the first frequencies presented a typical Nyquist profile that went abnormal with the appearance of the white precipitate. It was hypothesed that the white precipitate could be caused by salt precipitates due to a high PBS concentration. Therefore, the electrolyte was dissolved in a lower concentrated buffer solution; 10 mM $[Fe(CN)_6]^{3-/4-}$ was dissolved in 10 mM PBS pH 7.2, tried for comparison and no precipitate was observed for EIS or CV analysis. As a reminder, no precipitate employing Electrodes 1 and 2 with Autolab workstation (**Chapters 4 & 8**) was observed when the electrodes were immersed in the electrolyte solution at 100 mM PBS. In the current system, Electrodes 3 with Palmsens workstation, the white precipitate appeared at 100 mM PBS in a 50 µL sample. A possible explanation could be that the 50 µL quickly evaporated given the high surface-to-volume ratio. The 100 mM PBS is already relatively concentrated and the dissolved salts became more concentrated with increasing evaporation. As a result, an increase in NaCl concentration also yielded an increase in Na^+ concentration, which had driven the equilibrium to the left according to Le Châtelier's principle, $Na_2HPO_4 \leftrightarrow Na^{2+} + HPO_4^{2-}$, causing the formation of Na_2HPO_4, thus forming the white precipitate.

Although the white precipitate appeared with 10 mM $[Fe(CN)_6]^{3-/4-}$ in 100 mM PBS, CV and EIS profiles could be obtained. This was achieved by analysing the electrodes individually rather than consecutively or simultaneously, as the CV and EIS analysis time was short enough not to allow the precipitate to appear. Then, the electrolyte solution was placed over the electrode just before starting each analysis.

Therefore, 10 mM $[Fe(CN)_6]^{3-/4-}$ dissolved in 10 mM PBS and in 100 mM PBS pH 7.2 were analysed for comparison over a POc-coated surface. Electrodes 3 were coated with 2.5 mM POc in 10 mM PB pH 7.2 as described in **Section 2.2.5.3** and characterised through CV and EIS (**Sections 2.2.6 & 2.2.7**).

Figure 5.3A showed the CV analysis of the 10 mM $[Fe(CN)_6]^{3-/4-}$ redox profiles for each of the two PBS concentrations, 10 mM and 100 mM. More conductive profile for 10 mM $[Fe(CN)_6]^{3-/4-}$ in 100 mM PBS (orange) than in 10 mM PBS (red) was observed. On the one hand, 10 mM $[Fe(CN)_6]^{3-/4-}$ in 100 mM PBS showed clearly the oxidation and reduction current peaks and an apparent reversible redox reaction. On the other hand, the analysis with 10 mM $[Fe(CN)_6]^{3-/4-}$ in 10 mM PBS showed a less conductive CV profile in which the reduction and oxidative peaks could not be observed. These results were in accordance with the Nyquist plots (**Figure 5.3B**), in which 10 mM $[Fe(CN)_6]^{3-/4-}$ in 10 mM PBS (red) showed a more impedimetric profile than 10 mM $[Fe(CN)_6]^{3-/4-}$ in 100 mM PB. These results could be explained by 100 mM PBS providing more free ions to the solution than 10 mM PBS. These free ions could behave as electrolytes as well. This was avoided by lowering the concentration of PBS to 10 mM, which depicted a more logical profile for a non-conducting polymer layer.

The Nyquist plot for 10 mM PBS shows two larger semicircles, of which the second one corresponds to finite Warburg impedance, investigated in **Section 5.2.5**.

These experiments showed that the CV and EIS measurements were negatively affected when dissolving 10 mM $[Fe(CN)_6]^{3-/4-}$ in 100 mM PBS. The electrodes suffered from a white precipitate over the working electrode under consecutive CV and simultaneous EIS analysis. The electrodes were assessed individually to avoid the precipitate appearance. Dissolving the electrolyte in 10 mM PBS presented a more insulating surface whereas a more conductive layer was presented when dissolving the electrolyte in 100 mM PBS.

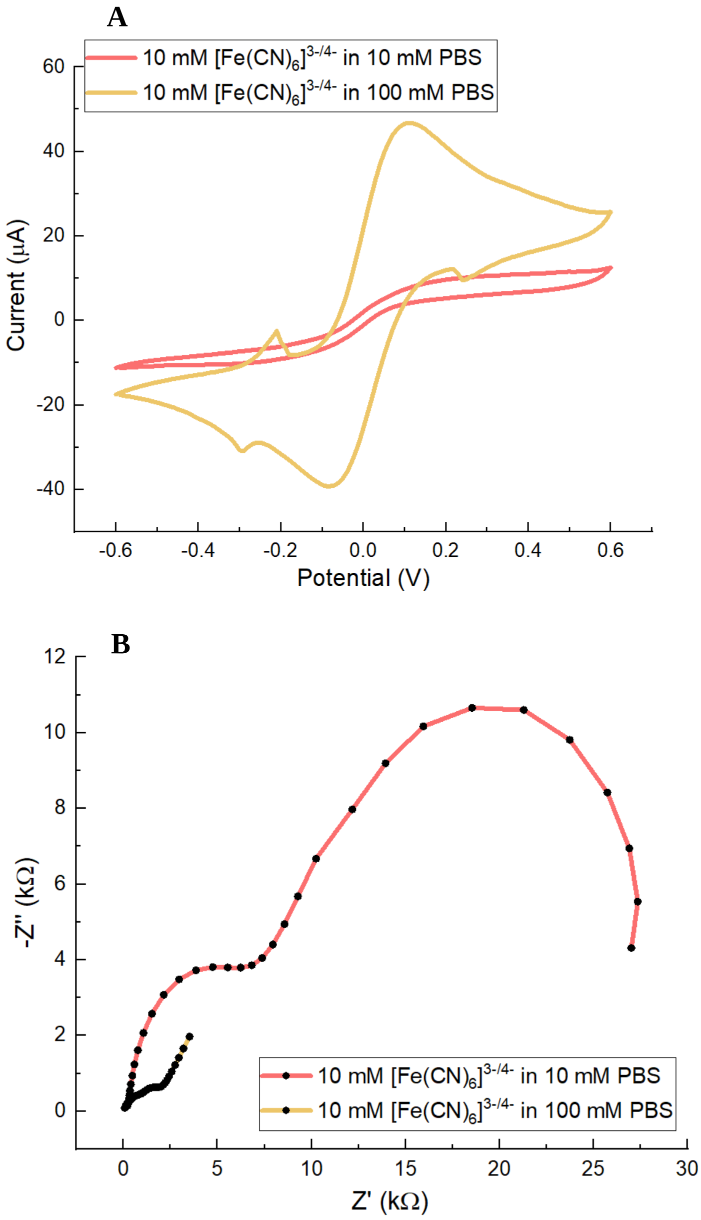

Figure 5.3: Electrochemical assessment of 2.5 mM POc-coated electrode with 10 mM $[Fe(CN)_6]^{3-/4-}$ in either 10 or 100 mM PBS pH 7.2. A, shows the cyclic voltammogram profile of a 2.5 mM POc-coated gold working electrode surface of Electrodes 3 for two conditions. The CVs were cycled from -0.6 V to +0.6 in 10 mM $[Fe(CN)_6]^{3-/4-}$ in 10 mM PBS, in red, and in 100 mM PBS, in orange, at pH 7.2 as described in **Section 2.2.6**. **B**, the Nyquist profiles derived from EIS measurements in 10 mM $[Fe(CN)_6]^{3-/4-}$ in 10 mM, in red, and in 100 mM PBS, in orange, at pH 7.2. EIS was recorded at 0.0 V over a frequency range of +5 kHz to +0.1 Hz, with a modulation voltage of +10 mV as described in **Section 2.2.7**. CV and EIS analysis were performed with Palmsens workstation. The CV and Nyquist plots show averaged readings from n≥6.

5.2.2. CV effect over EIS and vice versa over POc-coated SPGEs stability

CV and EIS were employed for the biosensor optimisation and fabrication. To achieve the best consistency and information about the state of the electrode surface at any step, it was relevant to understand the possible effect that CV measurements could have over subsequent EIS measurements and vice versa. This study aimed to assess whether applying CV over a POc-coated surface yields the same analysis if previously an EIS analysis had been taken, and vice versa. It was of interest to understand how the first technique applied could modify the coated electrode surface and how distant the second technique's analysis could be from a direct theoretical measurement. If the experimental results show no differences regarding the position in which the two techniques are employed, the electrodes could be sequentially assessed with CV and EIS or vice versa. Otherwise, two coated surfaces had to be created in parallel and separately assess by CV and EIS.

First, 2.5 mM octopamine dissolved in 10 mM PB pH 7.2 was electropolymerised over the electrodes as detailed in **Section 2.2.5.3**. Next, 10 cycles of CV from -0.6 to + 0.6 V in 10 mM $[Fe(CN)_6]^{3-/4-}$ in 10 mM PBS pH 7.2 solution were taken over POc-coated electrodes as detailed in **Section 2.2.6**. After that, 3 consecutive EIS measurements were taken over the same electrodes as described in **Section 2.2.7**. The opposite process was carried out for comparison: new electrodes were functionalised by coating the surface with POc as described in **Section 2.2.5.3**. Next, 3 EIS measurements were taken as described in **Section 2.2.7** and subsequently analysed with 10 CV measurements as detailed in **Section 2.2.6**.

The CV analysis involves 10 consecutive cycles. However, only the second cycle is used for comparison; a second cycle will show the state at the beginning of the analysis. Nonetheless, the CV cycle is extended to the 10th to study the effect over the EIS.

Figure 5.4A shows a comparison between CV analysis just after electrode functionalisation and CV analysis after 3 EIS measurements. The plots illustrate the second CV cycle mean ± SD. The CV just after the electrode functionalisation in red presented an insulating profile with small SD. In orange, the CV analysis after 3 EIS measurements showed more conductivity and less reproducibility given its substantially larger SD, which overlapped some parts with the red one. The results showed that previous EIS measurements had a large impact over the coated electrode surface. The stabilisation of the signal through EIS measurements changes the surface's state, thus compromising the subsequent CV measurements. Speculatively, this might be explained because there is a natural loss of coating with time and because the interaction between the electron mediators with the deposited polymer after EIS analysis causes polymer detachment. The oxidation and reduction current of the CV profiles were also analytically assessed and shown in **Figure 5.4B**. Similarly to the CV plots, the oxidation and reduction current was higher for the CV analysis after 3 EIS measurements and presented a compromised reproducibility.

The effect of CV analysis over EIS measurements was also assessed to study how previous CV analysis could affect the POc-coated electrode surface over a subsequent EIS analysis. Electrodes were coated with POc (**Section 2.2.5.3**) and underwent 10 consecutive CV cycles (**Section 2.2.6**) to subsequently be tested through 3 EIS measurements (**Section 2.2.7**). For comparison, new electrodes were functionalised with POc coating (**Section 2.2.5.3**) and assessed with 3 EIS (**Section 2.2.7**). **Figure 5.4C** shows direct EIS measurement without any previous CV analysis (red) compared to EIS analysis after 10 CV cycles (orange). A notable difference between the two Nyquist can be observed. On the one hand, a clear impedimetric surface was obtained when assessing the electrodes directly with EIS, without previous CV measurements. On the other hand, the impedance shown for EIS measurement after 10 CV analysis appeared smaller, indicating a clear, more conductive surface. This might be explained because there is a natural loss of coating with time and because the interaction between the electron mediators with the deposited polymer after CV analysis causes detachment. In addition, the electrodeposition of POc occurs between +0.45 to +0.6 V and the last voltage sweep is reductive from +0.6V to -0.6, which could cause some polymer reduction.

The results obtained in this section showed that EIS and CV analysis had to be carried out separately. The impact of one technique on another was sufficiently notable to consider functionalising new electrodes for a single CV or EIS analysis.

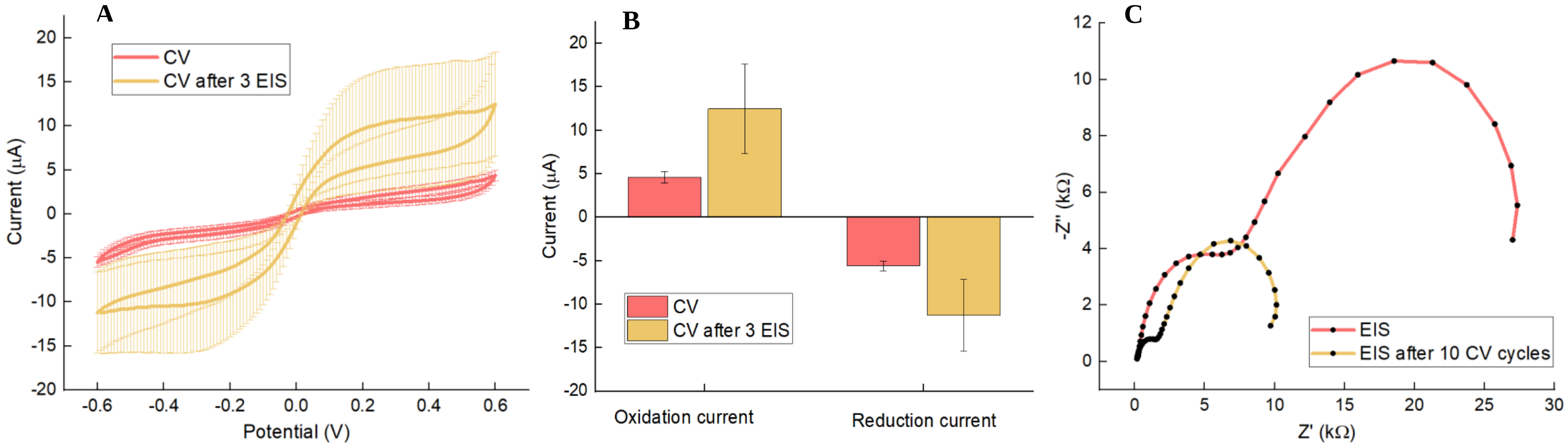

Figure 5.4: Study of EIS measurements over CV analysis and vice versa through electrochemical assessment of 2.5 mM POc-coated Electrodes 3. A, in red, shows the cyclic voltammogram profiles of a 2.5 mM POc-coated gold working electrode surface. In orange, it shows the cyclic voltammogram profiles of a 2.5 mM POc-coated gold working electrode surface after 3 EIS measurements. The CVs were cycled from -0.6 V to +0.6 in 10 mM $[Fe(CN)_6]^{3-/4-}$ in 10 mM PBS pH 7.2 (**Section 2.2.6**). **B**, oxidation and reduction currents are represented in bar graphs. In red, CV, and in orange, CV after 3 EIS. The bars represent the mean of n≥6 ± SD. **C**, in red, Nyquist profile, and EIS in orange after 10 CV cycles. The Nyquist profiles were derived from EIS measurements in 10 mM $[Fe(CN)_6]^{3-/4-}$ in 10 mM pH 7.2. EIS was recorded at 0.0 V over a frequency range of +5 kHz to +0.1 Hz, with a modulation voltage of +10 mV (**Section 2.2.7**). EIS and CV analysis were performed with Palmsens workstation. The CV plots and bars show averaged readings from n≥6; errors bars indicate standard deviation (± SD). Averaged curves shown with number of repeats n≥6.

5.2.3. Polymer stability after 24 h in solution

Before investigating the optimum polymer concentration, it was relevant to study how the time of polymer in solution affected the surface coating. It was essential to consistently reproduce the same amount of surface coating to achieve the best biosensor optimisation. This could be better achieved by using the same polymer solution for all the experiments. However, before employing the same octopamine solution for the rest of the biosensor optimisation, the reproducibility of the polymer electrodeposition and its further electrochemical assessment had to be investigated for a freshly made octopamine solution and compared to the same octopamine solution after a certain time. Therefore, a comparative electrochemical study was carried out for a freshly made octopamine solution compared to a 24 h octopamine solution at the same concentration. First, 2.5 mM octopamine was dissolved in 10 mM PB pH 7.2 and electropolymerised as detailed in **Section 2.2.5.3**. Once the electrodes were functionalised, a CV and EIS analysis were performed in the presence of the 10 mM $[Fe(CN)_6]^{3-/4-}$ redox couple solution (**Sections 2.2.6 & 2.2.7**).

The same solution containing the 2.5 mM octopamine was left overnight until accomplishing 24 h from its creation. After that, new electrodes were again functionalised and subsequently assessed through CV and EIS equally as before. The results compared the CV and EIS analysis of electrodes coated with freshly made polymer to electrodes functionalised with polymer from a 24 h solution. The voltammograms from **Figure 5.5A** showed more conducting surface for electrode surfaces coated with polymer from 24 h solution than the ones at 0 h freshly made. **Figure 5.5B** showed the Nyquist plots derived from EIS analysis, performed in parallel to validate the previous CV analysis. The results were in line with the previous CV voltammograms since Nyquist plots of POc-coated surface from freshly made solution appeared to be notably larger, thus confirming a more insulating layer than the 24 h candidate one. This could be explained by octopamine oxidation during the 24 h in solution which impedes the further electrodeposition.

The results obtained in this section suggested that the time during which POc was dissolved in 10 mM PB pH 7.2 buffer affected the system's reproducibility. For the rest of the POc electrode’s functionalisation, a new freshly made polymer solution was created at the beginning of each optimisation process. A POc solution was never used for longer than one-day experiments to seek consistency and reproducibility.

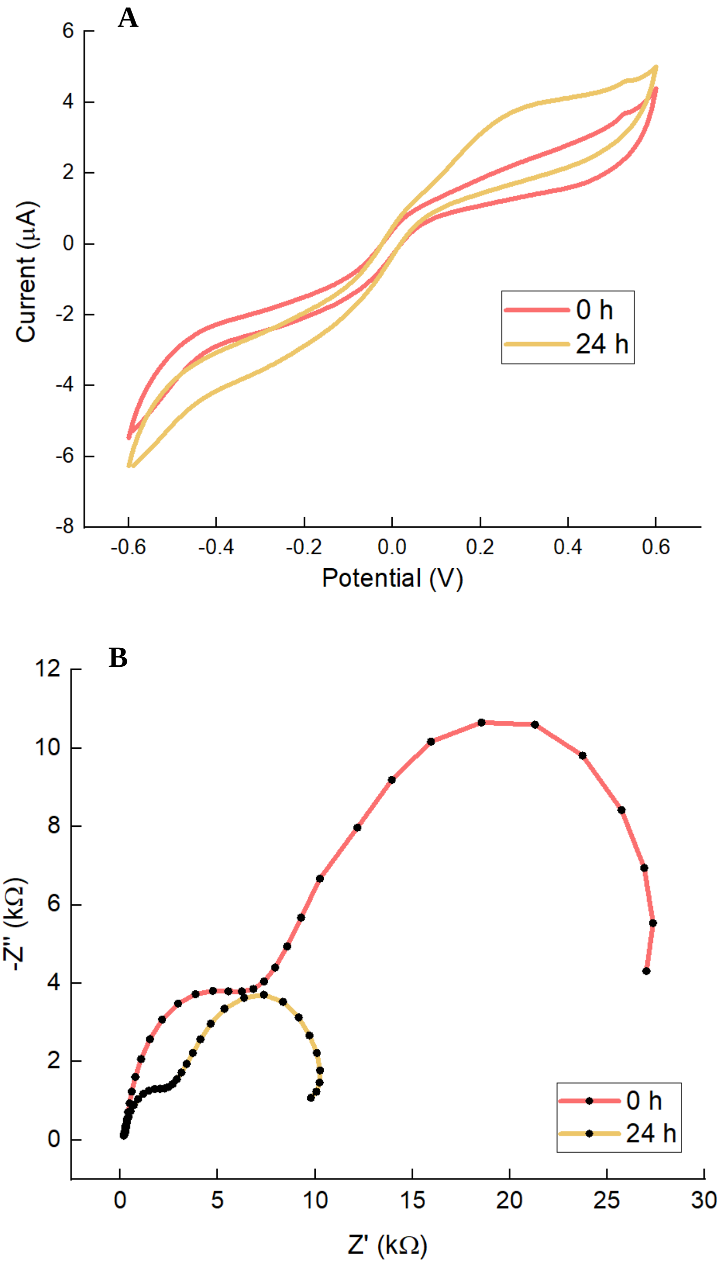

Figure 5.5: CV and EIS analysis of 2.5 mM POc-coated Electrodes 3 surface with a 0 h or 24 h POc made solution. A, shows the cyclic voltammograms of a 2.5 mM octopamine dissolved in 10 mM PB pH 7.2 electrodes coated surfaces. In red, the 2.5 mM octopamine was immediately electropolymerised after dissolving in PB buffer. In orange, the 2.5 mM octopamine solution was electropolymerised after 24 h dissolved. The CVs were cycled from -0.6 V to +0.6 V in 10 mM $[Fe(CN)_6]^{3-/4-}$ in 10 mM PBS pH 7.2 as detailed in **Section 2.2.6**. **B**, in red, Nyquist profile for 2.5 mM octopamine that has been immediately electropolymerised after dissolving in PB buffer, and in orange, 2.5 mM octopamine solution was electropolymerised after 24 h dissolved. The Nyquist profiles were derived from EIS measurements in 10 mM $[Fe(CN)_6]^{3-/4-}$ in 10 mM pH 7.2. EIS was recorded at 0.0 V over a frequency range of +5 kHz to +0.1 Hz, with a modulation voltage of +10 mV as described in **Section 2.2.7**. CV and EIS analysis were performed with Palmsens workstation. The CV and Nyquist plots show averaged readings from $n \geq 6$.

5.2.4. Demonstration of POc non-conductivity

The non-conductivity of polymer had already been demonstrated by characterising POc electrodeposition over Electrodes 1 (Shamsuddin, 2018; Shamsuddin et al., 2021). There, POc was electrodeposited through different cycles and varying scan rates in the electrodeposition CV. EIS measurements were taken as part of the characterisation. It was found that the optimum POc electrodeposition conditions over SPGE were 2 CV cycles at 100 mV/s. In addition, the existence of oriented amine groups at the surface was confirmed through chemiluminescence by (Shamsuddin, 2018). As part of my PhD, I collaborated on demonstrating the non-conductivity of POc by CV characterisation after polymer electrodeposition and corroborated previous EIS results. These experiments were then published in (Shamsuddin et al., 2021).

To be consistent with previous research, the experimental conditions were exclusively different for this section: Electrodes 1 and Autolab workstation were used. The electrodes did not undergo any pretreatment before the electropolymerisation and 5 mM octopamine was dissolved in 100 mM PB pH 7.5 and 20 % (v/v) DMSO and polymerised testing different cycles, namely, 2, 4, and 6 at 100 mV/s (Shamsuddin et al., 2021).

It was expected that an increase of scans during electrodeposition would increase polymer coating, manifested by a decrease in conductivity. **Figure 5.6A** shows the electropolymerisation CV for 5 mM octopamine after 2, 4 and 6 scans. After the first scan, all tested samples showed the octopamine oxidation peak, as most of the coating occurs in the first cycle. An increase in polymer deposition was expected with an increasing number of scans. Ptyr electrodeposition profile was added to **Figure 5.6A** for comparison. This data was generated by Dr S. Shamsuddin.

After that, the electrodes were washed and immersed in 10 mM $[Fe(CN)_6]^{3-/4-}$ redox probes to undergo a CV analysis. **Figure 5.6B** shows the CV analysis for 5 mM octopamine electropolymerised at a different number of scans. The systems in which the POc electrodeposition was made with 2 electrodeposition cycles provided more conductive CV profiles than those created through 4 and 6 electrodeposition cycles. The observed trend is that the more electrodeposition scans, the more insulating CV provided.

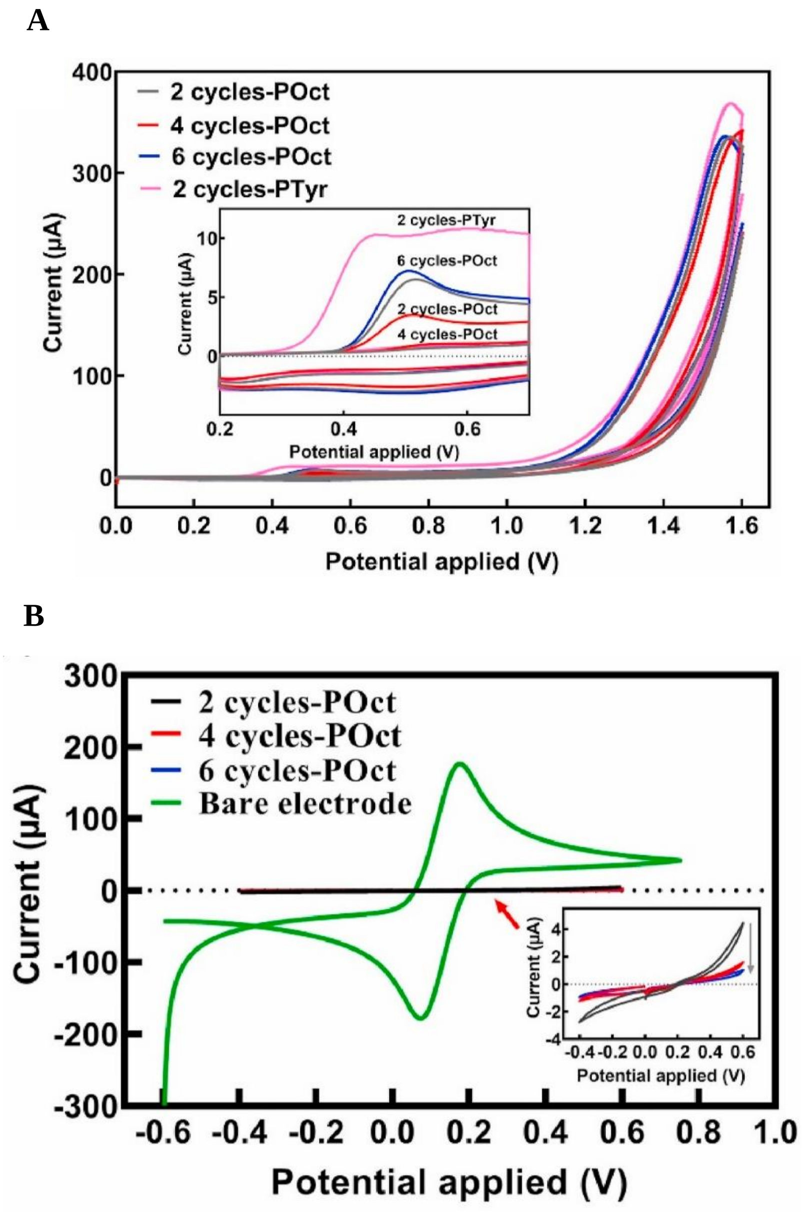

Figure 5.6: Electropolymerisation CV profile and CV analysis for a different number of electropolymerisation scans of 5 mM octopamine: The methodology is detailed in (Shamsuddin et al., 2021). **A**, 5 mM octopamine were dissolved in 100 mM PB pH 7.5 and 20% (v/v) DMSO and electropolymerised onto Electrodes 1 through CV. The electropolymerisation consisted of cycling from 0.0 V to +1.6 V for 2 cycles. The zoomed-in insert shows the current from +0.2 V to +0.7 V. The 2-cycle Ptyr data was generated by Dr S. Shamsuddin. **B**, the CV profiles of the coated electrode surfaces in 5 mM $[Fe(CN)_6]^{3-/4-}$ in 100 mM PBS pH 7.1 for different electrodeposition scan cycles. The zoomed-in insert shows the current from -0.4 V to +0.6 V. These experiments were published in (Shamsuddin et al., 2021).

5.2.5. Differences between Autolab and Palmsens workstations

Commercial Electrodes 3 and Palmsens workstation implied different setup conditions compared to any of the Metrohm DropSens electrodes (Electrodes 1 and 2) and Autolab workstation previously employed. Those differences were the electrolyte volume, SPGEs adapter/multiplexer and connectors, number of working electrodes, SPGEs composition, etc. As a result of all these changes, the Nyquist profiles derived from EIS measurements differed depending on the SPGEs and electrochemical workstation. Polymer-coated Electrodes 3 have shown two-semicircle-shaped Nyquist after EIS analysis using Palmsens workstation, for instance, as observed in **Figures 5.3B, 5.4C & 5.5B**. In contrast, just one-semicircle-shaped Nyquist using any of the Metrohm DropSens electrodes and Autolab workstation was obtained, for instance, as observed in **Chapter 4** with Electrodes 1 (**Figures 4.2F, 4.3F, 4.4B & 4.5B**).

To understand where this difference was originally from, 5 mM octopamine in 10 mM PB pH 7.2 was electropolymerised over Electrodes 3 using Autolab and Palmsens workstations following the same approaches as in **Section 2.2.2.2** & **2.2.5.3** respectively. **Figure 5.7** shows the Nyquist plots derived from 5 mM POc-coated Electrodes 3 using the two different electrochemical workstations. Two different Nyquist profiles were obtained for the same polymer and concentration for the same SPGEs but employing different electrochemical workstations. The Autolab workstation (red) exhibited a first semicircle followed by a typical semi-infinite shaped Warburg impedance. This is not observed in the Nyquist plot when the Palmsens4 workstation (orange) was employed. Instead, a first semicircle is observed and followed by another semicircle, which coincides with a finite-length Warburg impedance (Nguyen & Breitkopf, 2018). This data was sent to Alvatek Ltd, from which the Electrodes 3 and Palmsens4 workstation were purchased. They agreed that it was a case of finite-length Warburg. They agreed that even if the electrodeposition conditions and EIS analysis were the same for both electrochemical workstations, the different electrochemical set up such as connectors, adaptors or multiplexers could play a role in the input and output signal.

These findings conclude that the robustness of a biosensor could be affected by the electrochemical equipment used, in this case, potentiostat, connectors and multiplexer. Therefore, these results strongly support using the same electrochemical equipment for the same study as it could be an added variability in the biosensor fabrication.

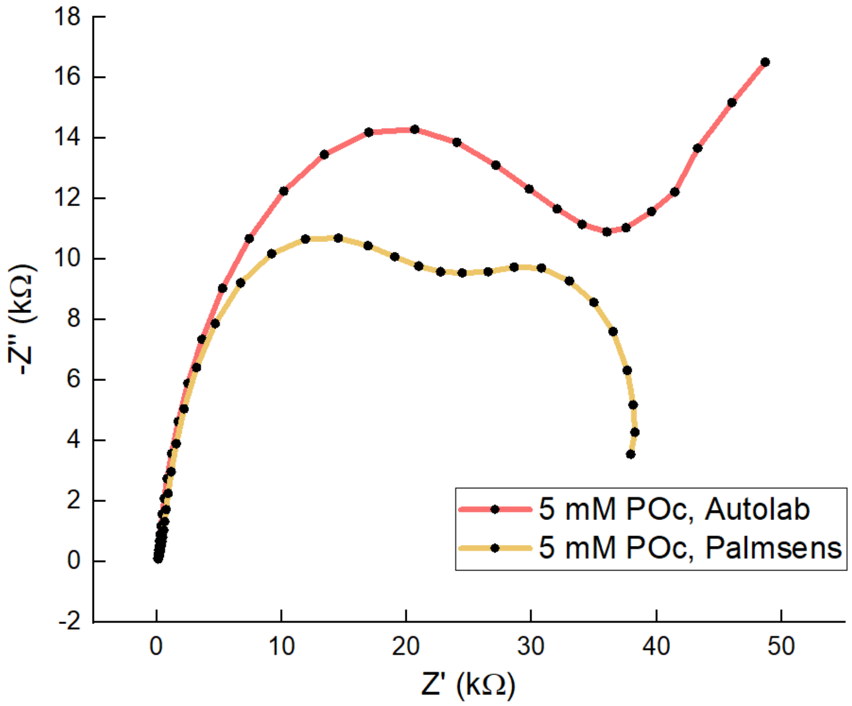

Figure 5.7: Nyquist plots derived from EIS assessment of 5 mM POc-coated Electrodes 3 using two different electrochemical workstations. In red, POc-coated electrode's Nyquist plots using Autolab workstation, and in orange, Palmsens workstation. The 5 mM octopamine dissolved in 10 mM PB pH 7.2 was electropolymerised. The Nyquist profiles were derived from EIS measurements in 10 mM $[Fe(CN)_6]^{3-/4-}$ in 10 mM pH 7.2. EIS was recorded for both potentiostats, at 0 V over a frequency range of +5 kHz to +0.1 Hz, with a modulation voltage of +10 mV. Nyquist plot averaged curves shown with number of repeats, n≥6.

5.2.6. Pretreatment

This section assessed the stability and reproducibility of Electrodes 3 for 3 different pretreatments compared to non-pretreated. POc-coated gold working electrode surfaces were evaluated for the following pretreatments: CV in H_2SO_4; CV in H_2SO_4 followed by immersion in ethanol; and only immersion in ethanol. Non-pretreated electrodes were also assessed for comparison. The current Electrodes 3 and Electrodes 2 had already been studied for pretreatment characterisation in **Chapter 3**. There, the mentioned pretreatments were employed to assess, among others, POc-coated surfaces. However, the electrochemical set-up employed in **Chapter 3** consisted of Autolab workstation and individual electrode measurements with a single connector. As a consequence of obtaining different electrochemical analyses using different electrochemical workstation in the previous **Section 5.2.5**, a study for POc-coated Electrodes 3 using Palmsens workstation was considered necessary.

The coated electrode surfaces were evaluated after the pretreatments with 0.1 M H_2SO_4 at 15 cycles at a scan rate of 50 mv/s; the same electrochemical procedure for H_2SO_4 cycling potential followed 30 min immersion in ethanol; a 30 min of immersion in ethanol, all described in **Section 2.2.1**; or without pretreating the electrodes.

After each pretreatment, 2.5 mM octopamine was electropolymerised over the SPGE as detailed in **Section 2.2.5.3**. **Figure 5.8A** shows all octopamine electropolymerisation profiles after each pretreatment. A typical octopamine oxidation peak was observed for the non-pretreated (red) and ethanol (teal) pretreated electropolymerisation profiles. Electropolymerisation CV profiles showing different abnormal shapes appeared when employing CV in H_2SO_4 with (green) or without (orange) ethanol. The different shapes suggest that some other compounds could have participated in the octopamine electropolymerisation and compromised the electrode surface. This could be explained by the chemical change of the surface after CV in H_2SO_4 or by the deposition of dielectric material during CV in H_2SO_4. Although some oxidation peaks are observed in the CV in H_2SO_4 and CV in H_2SO_4 pretreated + ethanol electrodes, the accomplished surface passivation could only be assessed with further CV or EIS analysis. In addition, the POc electrodeposition profiles were individually plotted for each pretreatment ($n \geq 6$) to highlight the reproducibility, which can be assessed by the SD and shown in **Figures 5.8B-E**. The results indicated that more reproducible systems were obtained for non-pretreated and ethanol pretreated electrodes compared to CV in H_2SO_4 pretreated systems, with or without ethanol. Non-pretreated and ethanol pretreated 2.5 mM octopamine electropolymerisation profiles showed a more reproducible SD (**Figures 5.8B & E**) than those pretreated with CV in H_2SO_4 with or without ethanol (**Figures 5.8C-D**).

Then, the same electrodes were assessed with CV to observe the redox current and thus evaluate the surface's conductivity. **Figure 5.9A** shows the CV profiles of a 2.5 mM POc-coated gold working electrode surface for different electrode pretreatments. The non-pretreated (red) and ethanol (teal) pretreated electrodes for POc-coated surfaces presented a more insulating layer than those involving CV in H_2SO_4 in the pretreatment. These findings suggest that the successful POc coating was accomplished with non-pretreatment and ethanol pretreatment. Moreover, the non-conductive profiles shown by non-pretreated (red) and ethanol (teal) pretreated in **Figure 5.9A** confirms the unsuitability of CV in H_2SO_4 as pretreatments in this case. POc electrodeposition profiles on CV in H_2SO_4 and CV in H_2SO_4 + ethanol (**Figures 5.8C-D**) pretreated appeared abnormal; if any of the oxidation peaks had been octopamine, the surface would be insulating as the current peaks are higher than the ones in non-pretreated and ethanol pretreated. Even if some of the peaks partially corresponded to octopamine, the electropolymerisation processes were interfered by possible contaminant or non-favourable electrode surfaces' change after both CV in H_2SO_4 pretreatments. Moreover, the oxidation and reduction peaks reproducibility of the electron mediators were derived from the CV analysis and were plotted in **Figure 5.9B**. The results indicated more reproducibility for the non-pretreated and ethanol pretreated systems.

After the CV analysis, EIS analysis was performed. New electrodes were taken, pretreated with the respective pretreatment (**Section 2.2.1**) and electropolymerised with 2.5 mM octopamine in 10 mM PB as detailed in **Section 2.2.5.3**. Next, the electrodes were put in the $[Fe(CN)_6]^{3-/4-}$ solution to perform EIS measurements to obtain information about the resistance offered at the electrode surface interface to the flow of the electrons. **Figure 5.9C** shows the Nyquist plots for 2.5 mM POc-coated electrodes for different pretreatments. More impedimetric profiles were obtained for non-pretreated and ethanol pretreated systems compared to CV in H_2SO_4 pretreatments. These results were in line with previous results obtained by CV analysis. In detail, the non-pretreated surface showed a more insulating CV profile than ethanol (**Figure 5.9A**) whereas the non-pretreated appeared less impedimetric according to Nyquist plots in **Figure 5.9C**. The Nyquist plots were fit into a Randles' equivalent circuit to obtain the R_{ct} values (**Figure 5.9D**) and plotted with SD for $n \geq 6$. The values appeared proportional to the Nyquist curves. In addition, the ethanol and non-pretreated electropolymerised electrodes' SD values are smaller than those involving CV in H_2SO_4.

This section concluded that a better electropolymerisation was achieved for 2.5 mM octopamine in 10 mM PB pH 7.2 for non-pretreated and ethanol pretreated electrodes. Their CV and EIS analysis under the redox mediators indicate better insulating layers than the CV in H_2SO_4 pretreated ones. The nature of only the electrode coating and the reproducibility of the electrodes were assessed. Therefore, ethanol pretreated SPGEs appeared to be the most suitable pretreatment for further biosensor functionalisation and optimisation experiments.

A

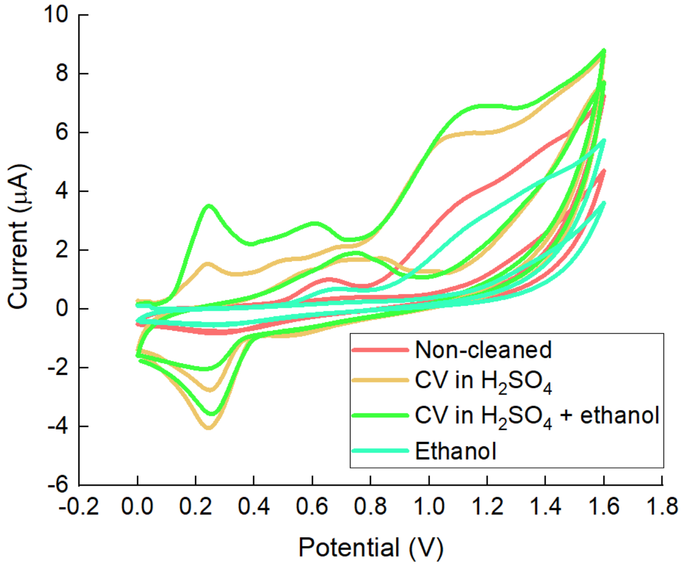
Current (µA)
10
8
6
4
2
0
-2
-4
-6
-0.2
0.0
0.2
0.4
0.6
0.8
1.0
1.2
1.4
1.6
1.8
Potential (V)
Non-cleaned
CV in H_2SO_4
CV in H_2SO_4 + ethanol
Ethanol

B

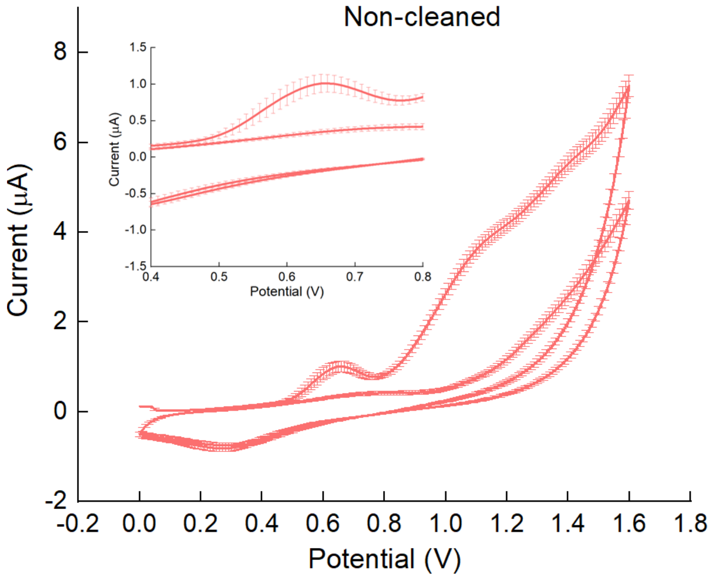
Non-cleaned
Current (µA)
8
6
4
2
0
-2
-0.2
0.0
0.2
0.4
0.6
0.8
1.0
1.2
1.4
1.6
1.8
Potential (V)
Current (µA)
1.5
1.0
0.5
0.0
-0.5
-1.0
-1.5
0.4
0.5
0.6
0.7
0.8
Potential (V)

C

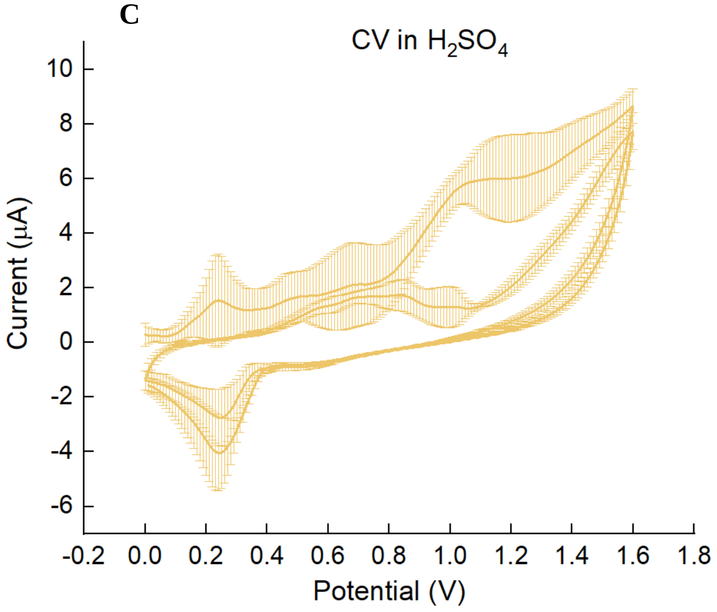
CV in H_2SO_4
Current (µA)
10
8
6
4
2
0
-2
-4
-6
-0.2
0.0
0.2
0.4
0.6
0.8
1.0
1.2
1.4
1.6
1.8
Potential (V)

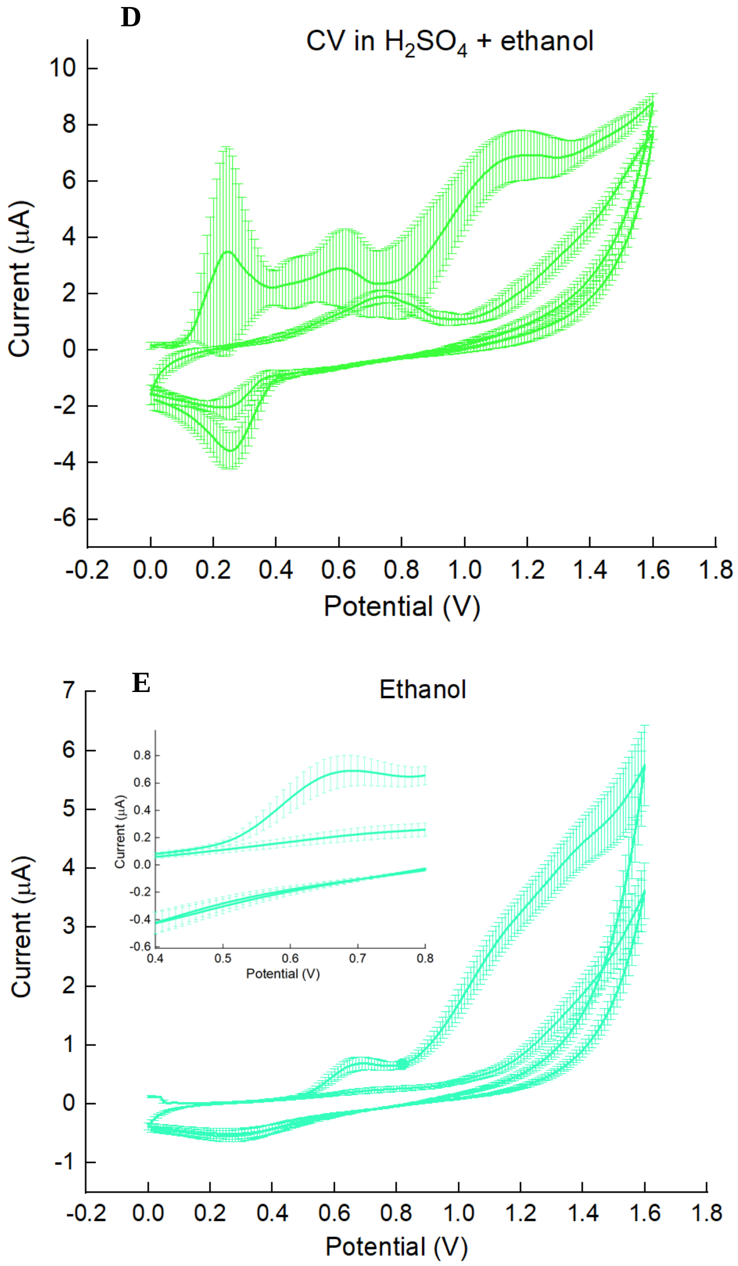

Figure 5.8: 2.5 mM octopamine electropolymerisation profiles upon different Electrode 3 pretreatments. The electropolymerisation of 2.5 mM octopamine was cycled from 0.0 V to +1.6 V for 2 cycles (**Section 2.2.5.3**) for different pretreated surfaces (**Section 2.2.1**). **A**, shows all electropolymerisation CV profiles. **B**, **C**, **D** and **E**, show the electropolymerisation CV mean ± SD for non-pretreated electrodes, CV in H_2SO_4, CV in H_2SO_4 + ethanol, and ethanol pretreated electrodes, respectively. The SPGEs employed were Electrodes 3 along with Palmsens workstation. The CV plots show averaged readings from n≥6; errors bars indicate standard deviation (± SD).

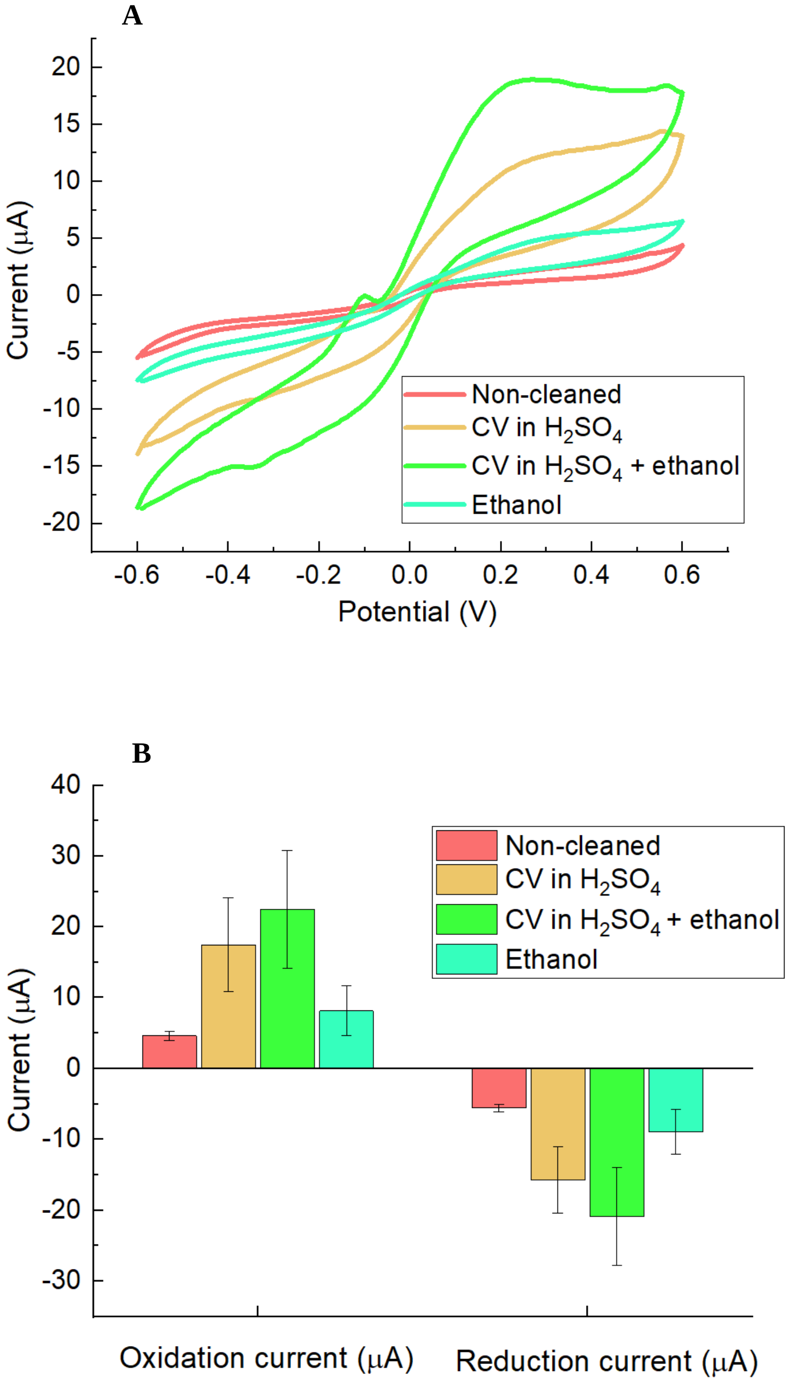
A
Current (µA)
20
15
10
5
0
-5
-10
-15
-20
-0.6
-0.4
-0.2
0.0
0.2
0.4
0.6
Potential (V)
Non-cleaned
CV in H_2SO_4
CV in H_2SO_4 + ethanol
Ethanol
B
Current (µA)
40
30
20
10
0
-10
-20
-30
Non-cleaned
CV in H_2SO_4
CV in H_2SO_4 + ethanol
Ethanol
Oxidation current (µA)
Reduction current (µA)

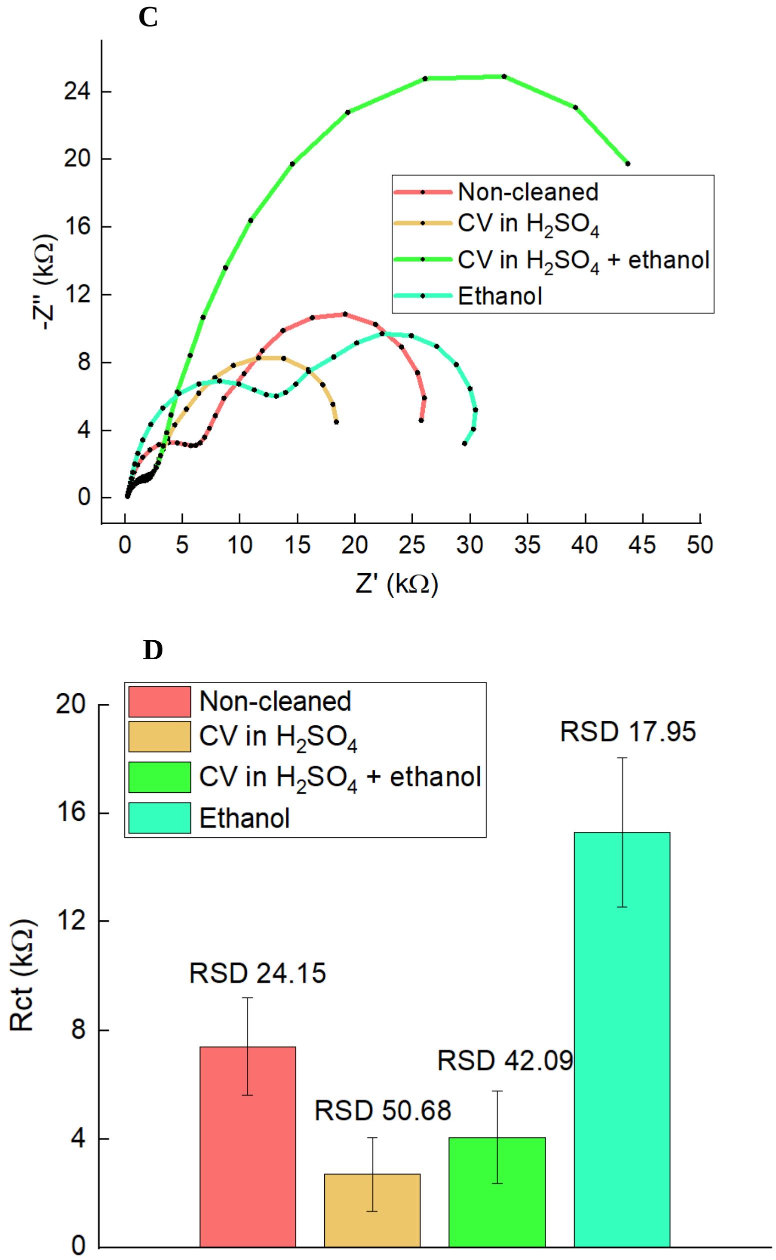

Figure 5.9: Study of the CV and EIS for 2.5 mM POc-coated electrodes for different Electrode 3 pretreatments. A, shows the CV profiles of a 2.5 mM POc-coated gold working electrode surface (**Section 2.2.5.3**) for different electrode pretreatments, namely CV in H_2SO_4, CV in H_2SO_4 + ethanol, and ethanol pretreated (**Section 2.2.1**). The CVs were cycled from -0.6 V to +0.6 in 10 mM $[Fe(CN)_6]^{3-/4-}$ in 10 mM PBS pH 7.2, as described in **Section 2.2.6** employing Palmsens workstation. **B**, corresponds to the oxidation and reduction currents represented in bar graphs, representing the mean ± SD. **C**, the Nyquist profile of 2.5 mM POc-coated surfaces upon the mentioned pretreatments and non-pretreated. The Nyquist profiles were derived from EIS measurements in 10 mM $[Fe(CN)_6]^{3-/4-}$ in 10 mM pH 7.2. EIS was recorded at 0.0 V over a frequency range of +5 kHz to +0.1 Hz, with a modulation voltage of +10 mV as detailed in **Section 2.2.7**. **D**, the R_{ct} analysis was obtained from fitting the Nyquist plot into Randles equivalent circuit. CV and Nyquist plots show averaged curves shown with number of repeats, n≥6. Figure **B** shows bars from n≥6 ± SD and Figure D shows bars from n≥6 ± RSD.

5.2.7. Characterisation of the bare electrodes

As the primary layer of the biosensor fabrication was the POc, the electrode pretreatment was chosen according to the first POc layer. Then, bare electrode characterisation was carried out by first pretreating the electrodes with immersion in ethanol as detailed in **Section 2.2.1**. Next, the electrodes were analysed with CV and EIS for characterisation (**Sections 2.2.6 & 2.2.7**).

Figure 5.10A shows the CV profile of typical $[Fe(CN)_6]^{3-/4-}$, showing a reversible redox reaction with clear oxidative and reduction current peaks. The Nyquist plot (**Figure 5.10B**) shows a barely impedimetric profile. The semicircle appeared followed by a straight line representing the Warburg impedance. Compared to the previous POc-coated surface on which the impedance appeared in the order of kΩ, the ethanol pretreated bare electrode seems to be in the order of the Ωs.

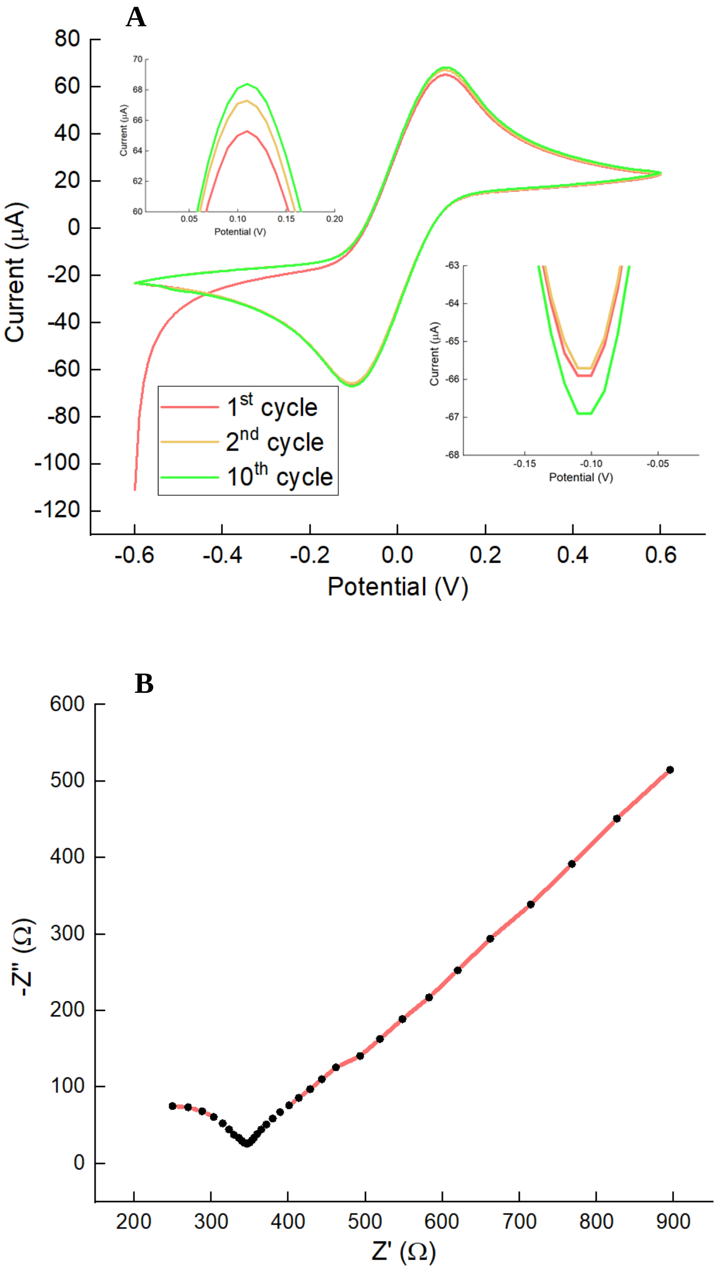

Figure 5.10: Electrochemical characterisation of ethanol pretreated bare electrodes. A, shows the CV profile of ethanol pretreated (**Section 2.2.1**) Electrodes 3. The CVs were cycled from -0.6 V to +0.6 in 10 mM $[Fe(CN)_6]^{3-/4-}$ in 10 mM PBS pH 7.2 (**Section 2.2.6**). **B**, the Nyquist profiles derived from EIS measurements in 10 mM $[Fe(CN)_6]^{3-/4-}$ in 10 mM PBS pH 7.2. EIS was recorded at 0.0 V over a frequency range of +5 kHz to +0.1 Hz, with a modulation voltage of +10 mV (**Section 2.2.7**). EIS and CV analysis were performed with Palmsens workstation. The CV and Nyquist plots show averaged readings from n≥6.

5.3. Discussion & Conclusions

Commercial Electrodes 3 underwent preliminary characterisation and testing before proceeding with the biosensor fabrication. The following parameters were investigated: the buffer concentration for electrolyte, comparison of CV and EIS analysis, the effect of the polymer after 24 h, polymer non-conductivity, EIS analysis of polymer-coated electrodes for different workstations, the most suitable pretreatment and the bare electrode characterisation. These first approach characterisation of the electrodes, along with previous studies showing the non-conducting POc properties (Shamsuddin, 2018), allowed moving to the next stage of the biosensor fabrication.

Former studies in Millner's group employed $[Fe(CN)_6]^{3-/4-}$ as electrolyte dissolved in PBS buffer, using either 10 mM or 100 mM PBS. At the beginning of my research, belonging to **Chapter 4**, Electrodes 1 were employed with the Autolab workstation. The research was carried out using 10 mM $[Fe(CN)_6]^{3-/4-}$ in 100 mM PBS as electrolyte. However, the new Electrodes 3 with the Palmsens workstation showed a white precipitate which only appeared with the 100 mM PBS. In addition, the CV and EIS experiments had to be performed separately as each analysis had a notable impact on the other. To complete the experiments, the polymer solution had to be freshly made every day. This made to be very precise always to match the same concentration to keep consistency. The best pretreatment for the Electrodes 3 employing Palmsens workstation system were also determined, and bare electrode characterisation was evaluated.

The pretreatment experiments in **Section 5.2.6** had been previously reproduced in **Chapter 3**. In **Chapter 3**, CV in H_2SO_4 and CV in H_2SO_4 + ethanol pretreated electrodes presented good octopamine electropolymerisation profiles, less conductive and more impedimetric profiles compared to non-pretreated and ethanol pretreated electrodes. However, Autolab workstation was employed in **Chapter 3**. CV and EIS measurements were undertaken by submerging the electrodes in the electrolyte solution detailed in **Sections 2.2.6 & 2.2.7**. In this current section, the electrodes were connected to the multiplexer/adaptor from Palmsens workstation and spread 50 µL electrolyte solution over the working electrodes. In addition, in **Chapter 3,** the experiments employed 5 mM octopamine to coat the electrodes after each pretreatment, whereas in this chapter, 2.5 mM octopamine was employed. The studies carried out in **Chapter 3** and in this chapter were carried out with the same Electrodes 3, but belonging to a different batch of electrodes, could show different compositions (**Appendix I**).

The second semicircles found in Nyquist plots using Palmsens workstation were finite-length Warburg impedance. It was corroborated by Alvatek (private communication). These findings conclude that the robustness of a biosensor could be affected by the electrochemical equipment used. Therefore, the findings reported in **Section 5.2.5** strongly support using the same electrochemical equipment for the same study as it could be an added variability in biosensor fabrication.

Chapter 6

Fabrication and optimisation of an impedimetric ECM protein-adhesin biosensor for whole pathogen detection

Chapter 6: Fabrication and optimisation of an impedimetric ECM protein-adhesin biosensor for whole pathogen detection

6.1. Overview

The objective was to develop a novel electrochemical biosensor based on the ECM protein-adhesin interaction to capture whole bacteria. Two biosensors were designed to detect pathogenic adhesion employing collagen binding to adhesins recombinantly expressed in *E. coli*. The first biosensor was fabricated to prove collagen-adhesin binding through an impedimetric biosensor. A collagen-polymer matrix was used as a bioreceptor to capture whole bacteria and showed a detection range of $8x10^5$ cfu to $8x10^7$ cfu in a 10 µL sample (**Figure 6.1**). The second biosensor corresponds to a step-by-step full optimised biosensor (**Figure 6.2**). The collagen was directly attached to POc through EDC/sulfo-NHS, a well-known cross-linker commonly used in bioconjugation (Greg T. Hermanson, 1996). Each optimisation step was characterised with CV and EIS, and the collagen attachment was validated with the Midland blotting technique (Rushworth, 2013). The biosensor detected bacteria from $8x10^4$ cfu to $8x10^7$cfu in a 10 µL sample. To validate the electrochemical biosensors, a fluorescent binding assay was performed by Ina Meuskens, a collaborator ESR on ITN ViBrANT based at University of Oslo. The bacterial control samples were non-induced *E. coli* and were included in electrochemical and fluorescent binding assays.

This research has investigated another alternative for a bioreceptor. Commonly, antibodies, proteins, oligonucleotides, and others have been employed for full pathogen detection. This study demonstrates that ECM proteins can also be used based on the ECM protein-adhesin interaction. The most prevalent configuration for a biosensor contains the bioreceptors attached to the transducer surface. The transducer surface changes and is subsequently monitored upon the analyte-bioreceptor interaction. Choosing the bioreceptor is thus essential for the architecture and fabrication of the biosensor. The choice of the bioreceptor strongly depends on its affinity and specificity to the analyte, which can range from small biomolecules such as drugs and peptides to whole organisms such as bacteria or viruses. Generally, antibodies have been used as bioreceptors as the gold standard to detect the whole pathogen, given the specificity derived from the antibody-antigen interaction (Birch & Racher, 2006). Other types of molecules have been employed as bioreceptors for whole pathogen detection, for instance, DNA or RNA. Some biosensors using them as bioreceptors can be found in (Wu et al., 2019) concerning the detection of foodborne pathogens. Other common bioreceptors are proteins, such as lectins (Xi et al., 2011); phage, which was used for detecting bacteria using *E. coli* specific T4 bacteriophages (Shabani et al., 2008);

and sol-gel bacterial imprinted films employed for *E. coli* impedimetric detection (Jafari et al., 2019). Adhesins have been previously used in electrochemical biosensors as bioreceptors (Su et al., 2018; Xi et al., 2011) or as analyte (Hai et al., 2017). However, the use of ECM proteins as bioreceptors for pathogen detection has not been extensively studied. Different alternatives have emerged to antibodies for electrochemical biosensors for complete pathogen detection. This project presents collagen as an ECM protein alternative for electrochemical biosensors bioreceptor for whole pathogen detection through pathogenic adhesins target.

In this project, an ECM protein-adhesin-based electrochemical biosensor for whole pathogen detection is investigated. Two biosensors were assessed. Collagen was employed as ECM protein targeting the $\text{YadA}_{\text{O:8}}$-expressing bacteria. YadA is naturally expressed in *Yersinia enterocolitica* and *Yersinia pseudotuberculosis*, widely spread in nature and also located in human intestinal and cause enteritis. Both biosensors have been entirely constructed and characterised using CV and EIS. The bacterial binding has been monitored through EIS and validated with the fluorescent assay. The collagen-protein matrix-based biosensor detected bacteria from 10^5 cfu to 10^7 cfu in a 10 µL sample. The collagen direct attachment biosensor detected bacteria from 10^4 cfu to 10^7 cfu in a 10 µL sample.

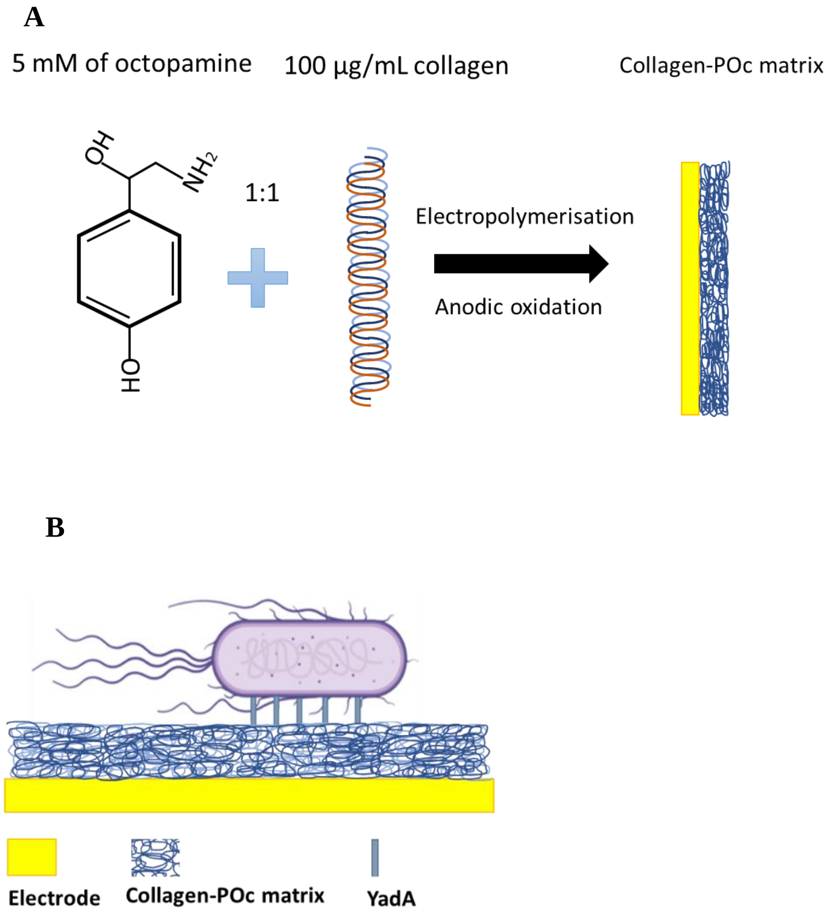

Figure 6.1: Schematic of collagen-POc matrix biosensor. A, schematic representation of step-by-step fabrication of collagen-POc matrix biosensor and **B**, final biosensor architecture.

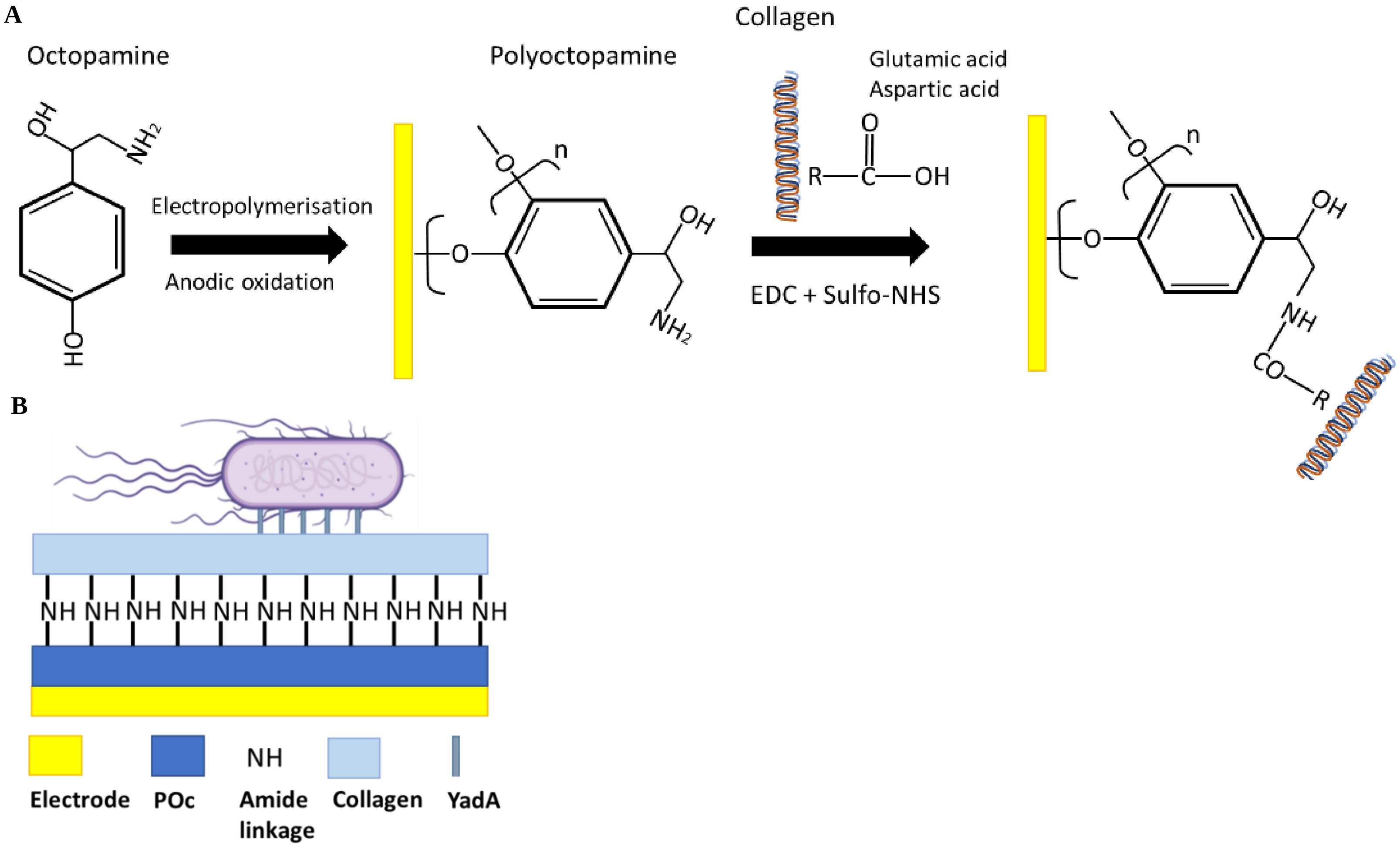

Figure 6.2: Schematic collagen direct attachment biosensor. A, schematic representation of step-by-step fabrication of collagen direct attachment biosensor and **B**, final biosensor architecture.

6.2. Results

6.2.1. Collagen-polymer matrix biosensor

6.2.1.1. Electrochemical characterisation

Before the biosensor fabrication, the characterisation of BVT-AC1.W1.RS.Dw2 (Electrodes 3) with the collagen-POc matrix bioreceptor surface was carried out. First, the SPGEs were pretreated with ethanol as detailed in **Section 2.2.1**. Next, a collagen-POc matrix was immobilised as a bioreceptor through electrodeposition as described in **Section 2.2.5.2** and characterised by CV and EIS as described in **Sections 2.2.6 & 2.2.7**. The exact process involved bare electrodes, and electrodes only coated with POc for comparison.

Figure 6.3A-B shows the octopamine and collagen-octopamine electropolymerisation CV profiles, respectively. Octopamine electropolymerisation occurs at an oxidation peak around +0.6 V (Shamsuddin et al., 2021). A current peak around +0.6 V appeared for only POc-coated electrodes, whereas a clear increase in current in the collagen-POc matrix occurred at the same potential. For both, no oxidative current related to octopamine oxidation was observed in the second cycle at the mentioned potential, thus confirming the electrode surface coating. These results indicated that the polymer electrodeposition was achieved in the first cycle and then impeded the flow of electrons in the second cycle**.** Next, the coated electrodes underwent CV analysis in the presence of 10 mM $[Fe(CN)_6]^{3-/4-}$ in 10 mM PBS as detailed in **Section 2.2.6** for each of the systems and compared to the bare surface.

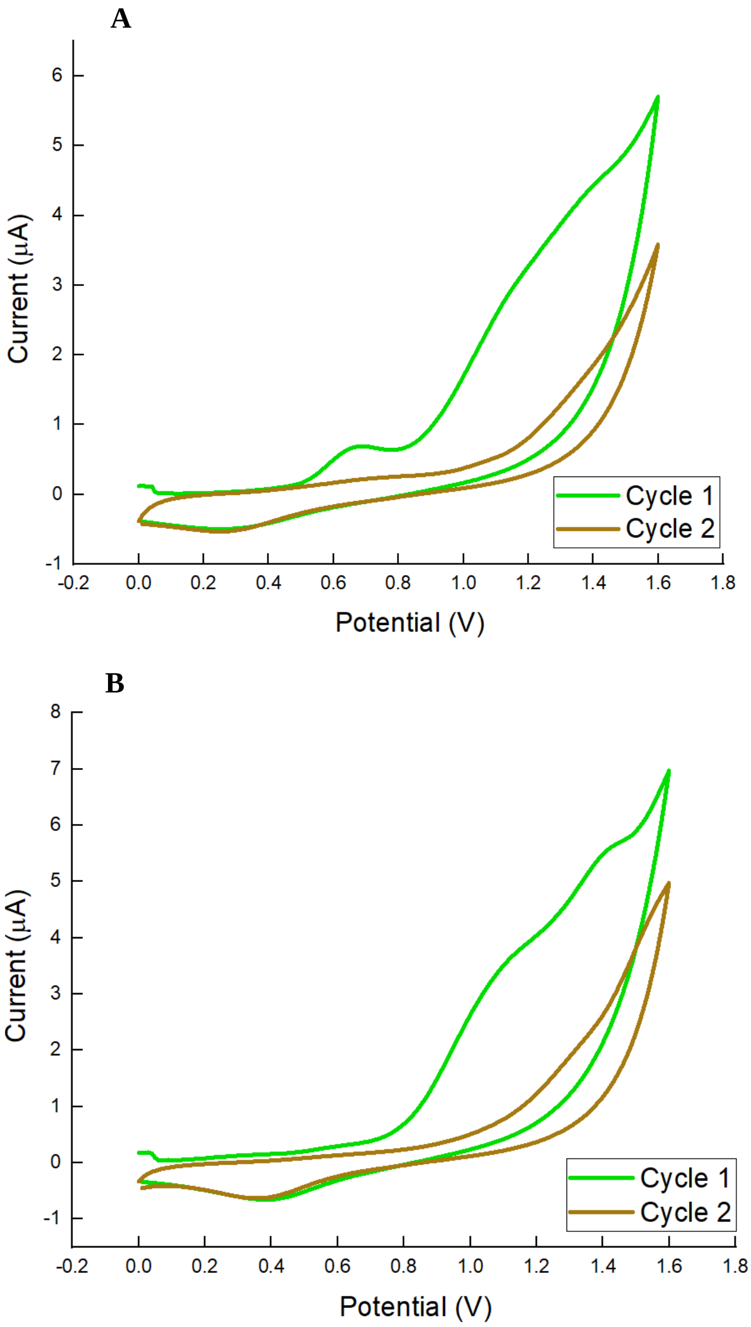

Figure 6.3: Octopamine and collagen-octopamine electropolymerisation CV profiles. A, shows the electropolymerisation of 2.5 mM octopamine in 10 mM PB pH 7.2 (**Section 2.2.5.3**). The electrode was cycled from 0.0 V to +1.6 V for 2 cycles as detailed in **Section 2.2.6**. **B**, shows the electropolymerisation of 2.5 mM octopamine with 100 µg/mL collagen (**Section 2.2.2.3**). The electrode was cycled from 0.0 V to +1.6 V for 2 cycles as described in **Section 2.2.6**. CV and EIS analysis were performed with Palmsens workstation. Electrodes 3 were employed. The CV plots show averaged readings from n≥6.

Figure 6.4A-B shows further CV and EIS analysis respectively for POc and collagen-POc matrix, including bare electrode surface. The bare electrodes CV voltammogram (dark blue) shows the two peaks of oxidation and reduction current at clear oxidation and reduction potential, showing a clear redox reversible reaction. This indicated proper electron flow at the gold bare electrode surface. The POc CV voltammogram (green) indicated oxidation and reduction currents of + 5.32 µA and - 4.17 µA, respectively, and oxidation and reduction potentials at 0.3 V and -0.20 V. This meant a more insulating voltammogram profile compared to bare electrodes. Once octopamine was electropolymerised, the redox pair in the solution could not properly reach the electrode surface to carry out the electrons exchange. The collagen-POc matrix CV voltammogram (brown) showed electrochemical properties in line with the surface coating: the collagen-POc composite most likely presented a more open nanostructure than only POc. Therefore, it gave a more conductive surface coating that allowed the electron mediators to reach the surface easier than the POc system. The oxidation and reduction peaks were + 9.61 µA and - 9.93 µA, respectively. These results were in line with the electrodeposition profiles previously assessed in **Figure 6.3**.

To assess the impedance properties of the systems, new electrodes were again pretreated with ethanol as detailed in **Section 2.2.1**, and collagen-POc matrix and 2.5 mM POc were electrodeposited as described in **Section 2.2.5.2**. Next, the electrodes underwent EIS analysis as described in **Section 2.2.7**.

The EIS results (**Figure 6.4B**) showed that the POc Nyquist curve was the largest, followed by the collagen-POc matrix and finally the bare electrode. This order of impedance was expected as POc is the most insulating system. The collagen-POc matrix Nyquist profile appeared smaller than just POc. The EIS results were in line with previous electrodeposition profiles (**Figure 6.3**) and CV voltammograms (**Figure 6.4A**):

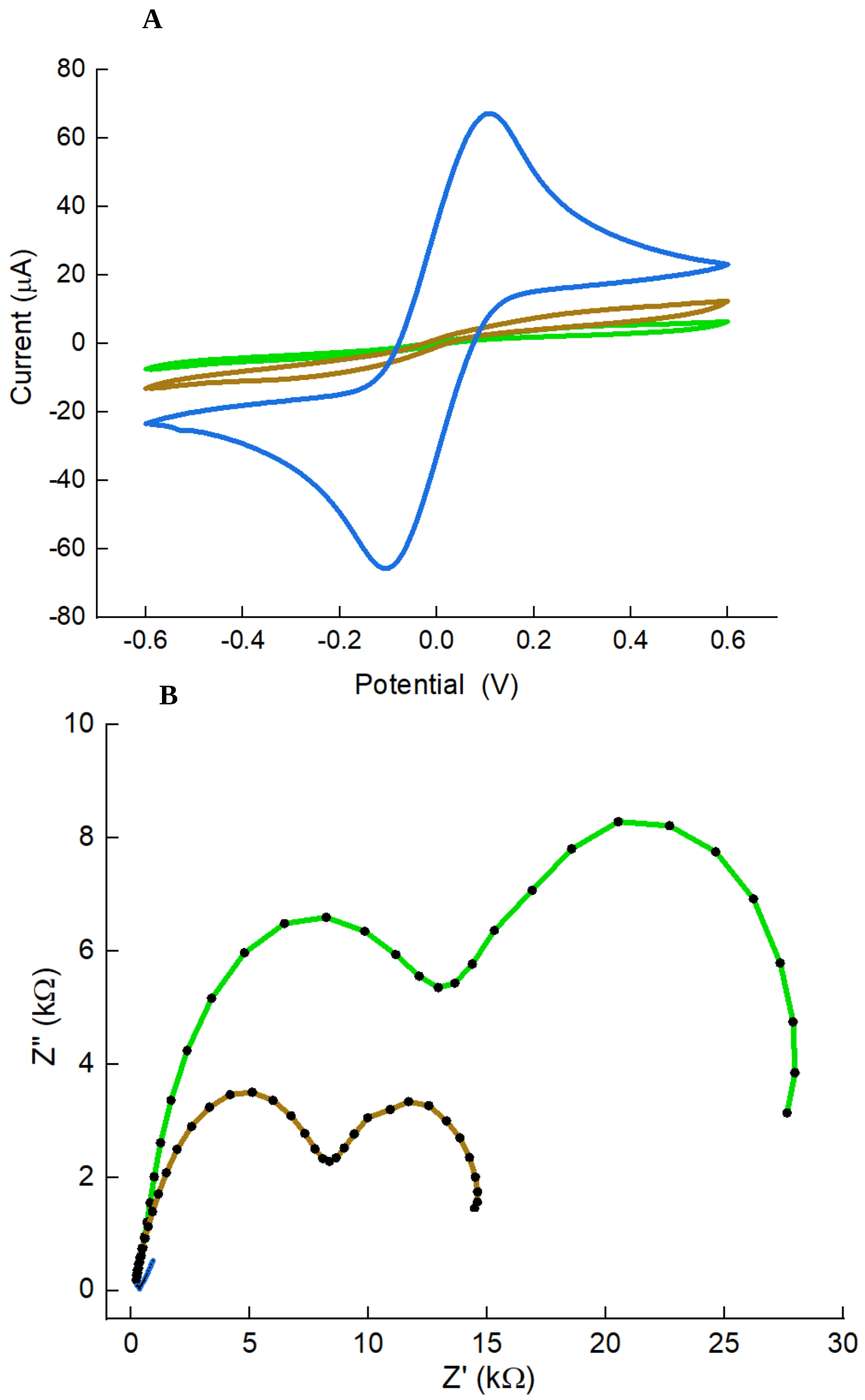

Figure 6.4: Electrochemical characterisation of collagen-POc matrix biosensor with CV and EIS. A, a cyclic voltammogram of the bare electrode surface (━━━), POc (━━━) and collagen-POc matrix (━━━) coated surfaces. The CV was cycled from -0.6 V to +0.6 at 100 mv/s in 10 mM $[Fe(CN)_6]^{3-/4-}$ in 10 mM PBS pH 7.2 as detailed in **Section 2.2.6**. **B**, Nyquist plot of bare, POc and collagen-POc functionalised electrodes, all Nyquist profiles derived from EIS measurements in 10 mM $[Fe(CN)_6]^{3-/4-}$ in 10 mM PBS pH 7.2. EIS was recorded at 0.0 V over a frequency range of + 5 kHz to + 0.1 Hz, with a modulation voltage of +10 mV as detailed in **Section 2.2.7**. CV and EIS analysis were performed with Palmsens workstation. Electrodes 3 were employed. The CV and Nyquist plots show averaged readings from n≥6.

6.2.1.2. Detection of bacteria

The electrochemical detection of the bacteria analyte was carried out. Electrodes 3 were pretreated with ethanol as detailed in **Section 2.2.1**. Then, a collagen-POc matrix was immobilised as a bioreceptor through electrodeposition as described in **Section 2.2.5.2**. Ten µL of a particular bacteria concentration was placed over the biosensor for electrochemical detection. The bacteria binding was determined by assessing the $\%\Delta R_{ct}$ determined by **Equation 2.1** with EIS analysis before and after analyte addition as described in **Section 2.2.5.2**. A new biosensor was used for each new bacterial concentration. A range from 8×10^2 to 8×10^7 cfu YadA-expressing *E. coli* samples were incubated for 30 mins at RT and tested as described in **Section 2.2.5.2**. The controls consisted of testing non-induced bacteria for the same bacterial concentrations as YadA-expressing *E. coli* and employing the new fully functionalised electrodes.

Figure 6.5 shows bacterial detection through EIS assessed by $\Delta\%R_{ct}$, obtained by fitting the Nyquist plots into Randle's equivalent circuit before and after the analyte addition. The data in **Figure 6.5** shows that the YadA-expressing *E. coli* binding compared to non-induced *E.coli* binding was significantly different ($p \leq 0.001$) from 8×10^5 cfu to 8×10^7 cfu. The lower YadA-expressing *E. coli* sample detected compared to non-induced bacteria was 8×10^5 cfu with $\Delta\%R_{ct}$ of 63.20 ± 12.18 for induced and 24.20 ± 8.78 for non-induced. For lower concentration samples, similar values of $\Delta\%R_{ct}$ were shown for both induced and non-induced samples.

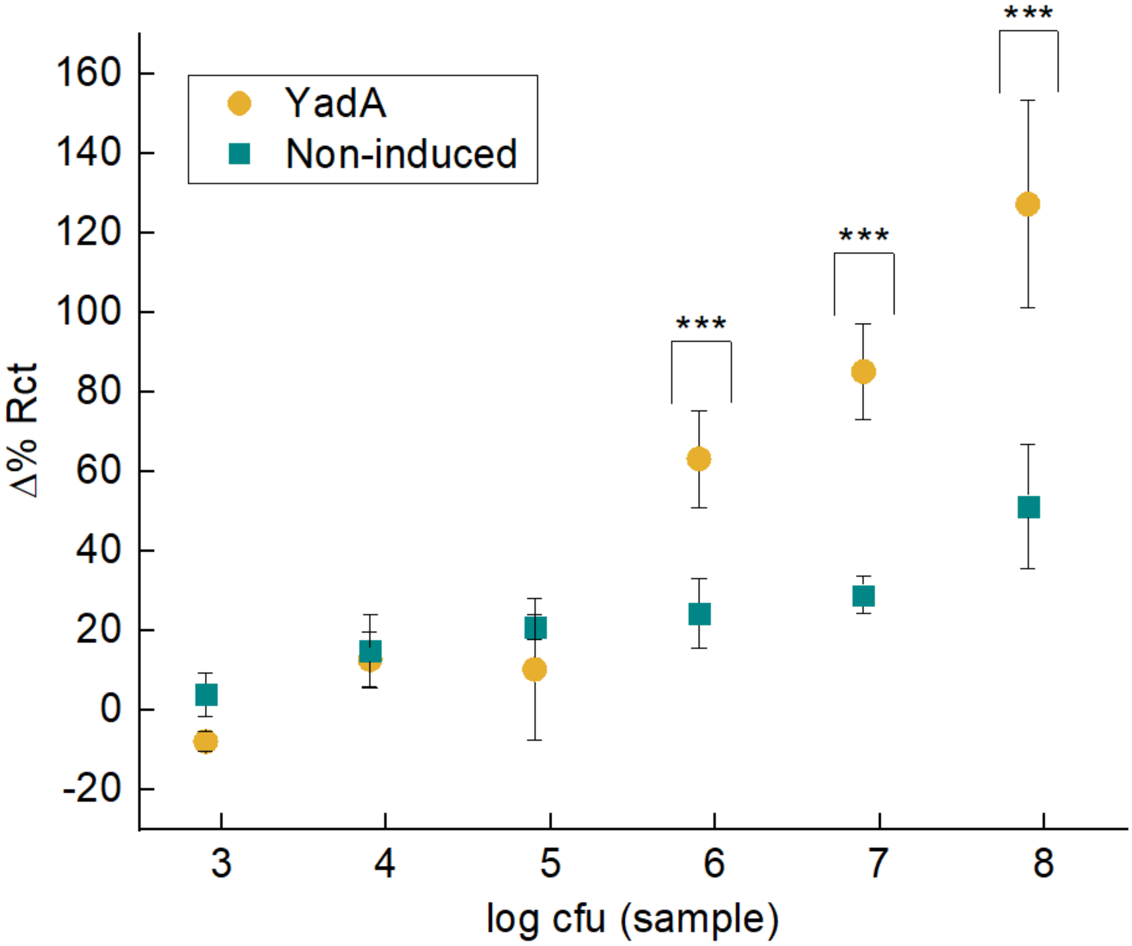

Figure 6.5: Bacterial detection through EIS assessed by Δ%R_{ct}. Bacterial binding for collagen-POc-based biosensor for expressed in Δ%R_{ct} calculated with **Equation 2.1**. A range from 8x10^2 to 8x10^7 cfu YadA-expressing *E. coli* and non-induced bacterial samples were incubated for 30 min at RT and tested as described in **Section 2.2.5.2**. EIS analyses were performed with Palmsens workstation. Electrodes 3 were employed. The data is shown as average from n≥6 ± SD. Statistical analysis was performed using ANOVA, and data with $p < 0.001$ are indicated by ***.

6.2.2. Collagen direct attachment biosensor

6.2.2.1. Polymer characterisation by electrodeposition CV profile and EIS

First, electrodes were pretreated with ethanol as detailed in **Section 2.2.1**. Subsequently, different concentrations of octopamine dissolved in 10 mM PB pH 7.2 from 1 to 250 mM as described in **Section 2.2.5.3** were electropolymerised. In addition, a sample with only 10 mM PB pH 7.2 underwent electrodeposition analysis to assess components from the buffer solution. Bare electrode characterisation was also performed for comparison. The electropolymerisation of the different octopamine concentrations (**Figure 6.6**) was successfully achieved. The typical octopamine oxidation peak was observed (Shamsuddin et al., 2021) on the first cycle and absent in the second, which indicated an irreversible reaction.

Once each electrode was coated with the corresponding POc concentration, EIS analysis was performed (**Figure 6.7A**) for impedance assessment as detailed in **Section 2.2.7**. The Nyquist plot diameters increased until reaching a POc concentration of 5 mM. Then, for higher POc-coated electrode concentration, the Nyquist diameter decreased. This indicated more conductive electrode surfaces at higher POc concentrations. This could be explained by the POc self-aggregation at high concentrations when dissolved in 10 mM PB pH 7.2. These results showed that the most insulating POc coating was achieved at 5 mM POc.

The different POc concentrations for electrode coating were also assessed by CV in 10 mM $[Fe(CN)_6]^{3-/4-}$ in 10 mM PBS pH 7.2 (**Figure 6.7B**). New electrodes were first pretreated with ethanol (**Section 2.2.1**), electropolymerised (**Section 2.2.5.3**) and then assessed by a CV (**Section 2.2.6)**. Similarly to EIS results, 5 mM POc appeared to be one of the most insulating electrode surfaces, and higher concentrations showed more conductive profiles. Both EIS and CV results are by the magnitude of the oxidation current observed in the electropolymerisation profiles (**Figure 6.6A).**

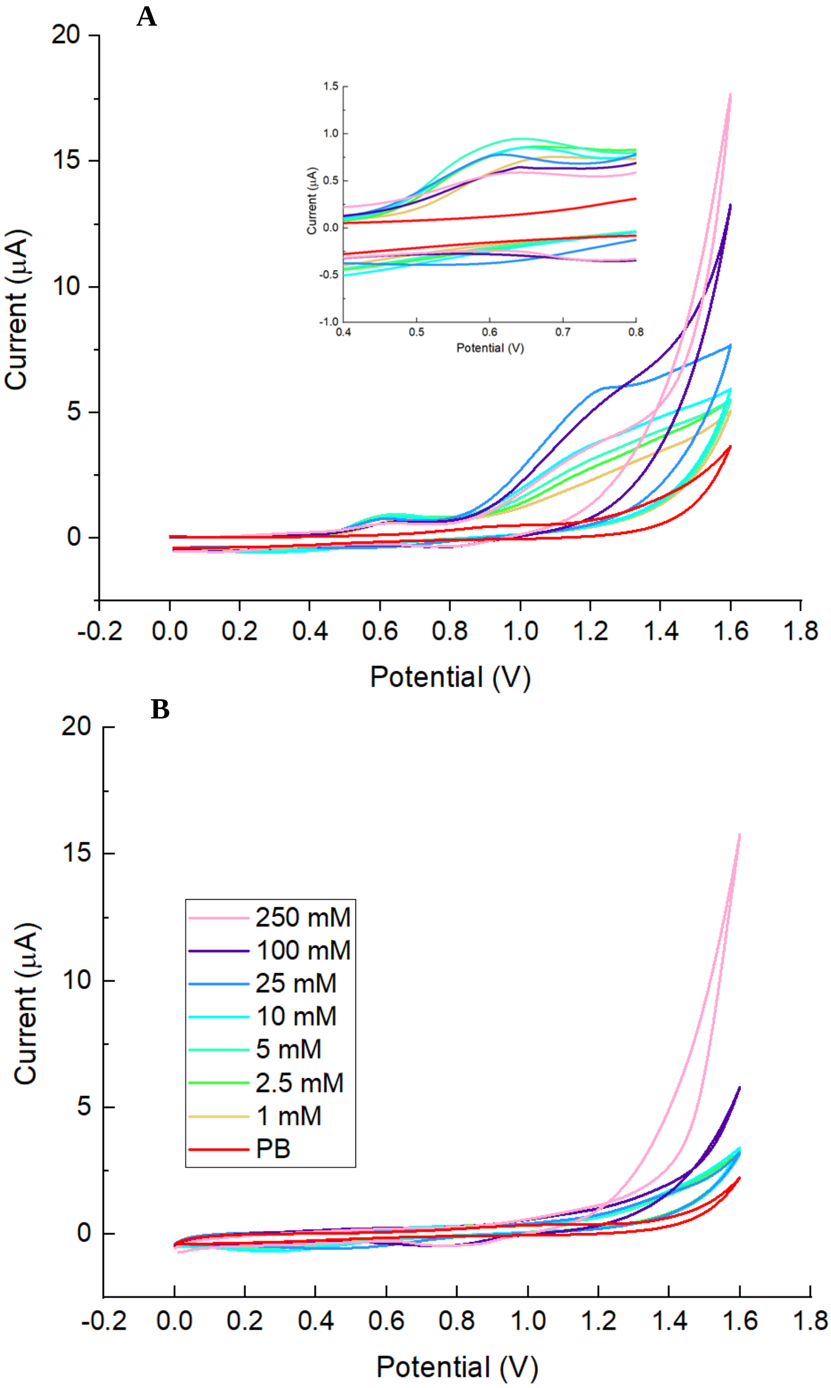

Figure 6.6: Electropolymerisation profiles for different octopamine concentrations. Electropolymerisation of different octopamine concentrations dissolved in 10 mM PB pH 7.2 namely: 1 mM (▬), 2.5 mM (▬), 5 mM (▬), 10 mM (▬), 25 mM (▬), 100 mM (▬), 250 mM (▬) and only PB (▬) (**Section 2.2.5.3**). The electrode was cycled from 0.0 V to +1.6 V for 2 cycles as detailed in **Section 2.2.6**. **A**, shows the first cycle of the electropolymerisation and **B**, shows the second cycle of the electropolymerisation. The zoom-in insert at **A** shows the oxidative current between +0.4 to +0.8 V. CV analyses were performed with Palmsens workstation. Electrodes 3 were employed. The CV plots show averaged readings from n≥6.

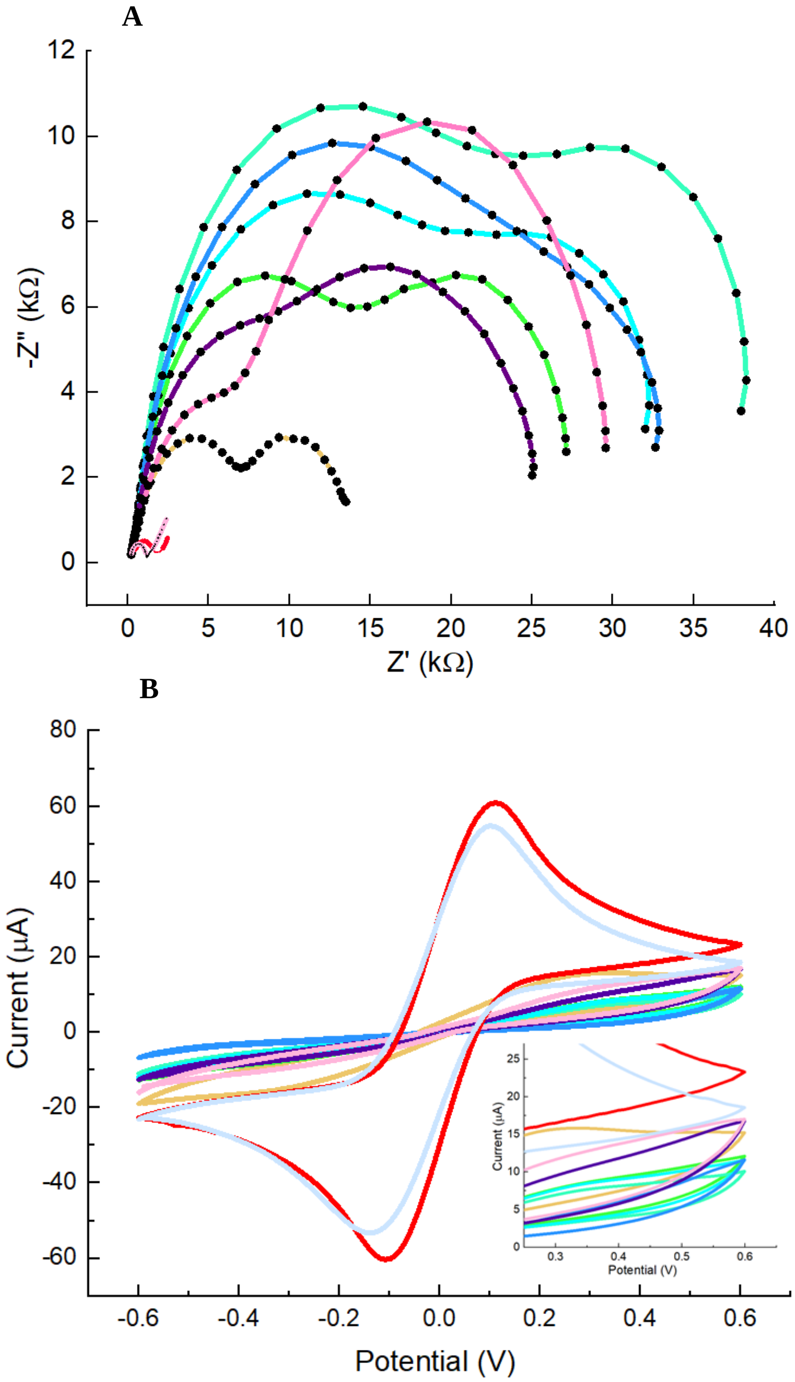

Figure 6.7: Electrochemical characterisation of POc-coated Electrodes 3 at different concentrations. **A**, Nyquist plot of bare electrode, PB buffer, and a range of POc concentrations, namely, 1 mM (▬), 2.5 mM (▬), 5 mM (▬), 10 mM (▬), 25 mM (▬), 100 mM (▬), 250 mM (▬), only PB (▬) and bare electrode (▬) as detailed in **Section 2.2.5.3**, all Nyquist profiles derived from EIS measurements in 10 mM $[Fe(CN)_6]^{3-/4-}$ in 10 mM PBS pH 7.2. EIS was recorded at 0.0 V over a frequency range of +5 kHz to +0.1 Hz, with a modulation voltage of +10 mV as detailed in **Section 2.2.7**. **B**, cyclic voltammogram of the bare electrode surface, PB buffer, and a range of POc concentrations from 1 mM to 250 mM POc following the same colouring system. The CV was cycled from -0.6 V to +0.6 V in 10 mM $[Fe(CN)_6]^{3-/4-}$ in 10 mM PBS pH 7.2 as described in **Section 2.2.6**. The zoomed-in insert shows the current between +0.2 V to +0.7 V for each CV profile. CV and EIS analysis were performed with Palmsens workstation. Electrodes 3 were employed. The CV and Nyquist plots show averaged readings from n≥6.

The CV and EIS characterisation showed that the optimum polymer concentration was 5 mM POc. Then, the 5 mM POc CV voltammograms under 10 mM $[Fe(CN)_6]^{3-/4-}$ in 10 mM PBS and EIS analysis were plotted separately to the rest of the POc concentrations and compared with bare electrodes (**Figure 6.8**).

Figure 6.8A shows the CV voltammogram of 5 mM POc and bare electrode. The POc CV voltammogram (orange) showed oxidative and reductive current peaks of -6.20 µA and +7.56 µA, respectively, at -0.30 V and +0.34 V. These values indicated a clear insulating electrode compared to the bare one (red). The EIS analysis (**Figures 6.8B**) shows a non-conducting behaviour again for 5 mM POc-coated electrode. The Nyquist curve appeared noticeably larger than the Nyquist semi-circle from bare electrodes.

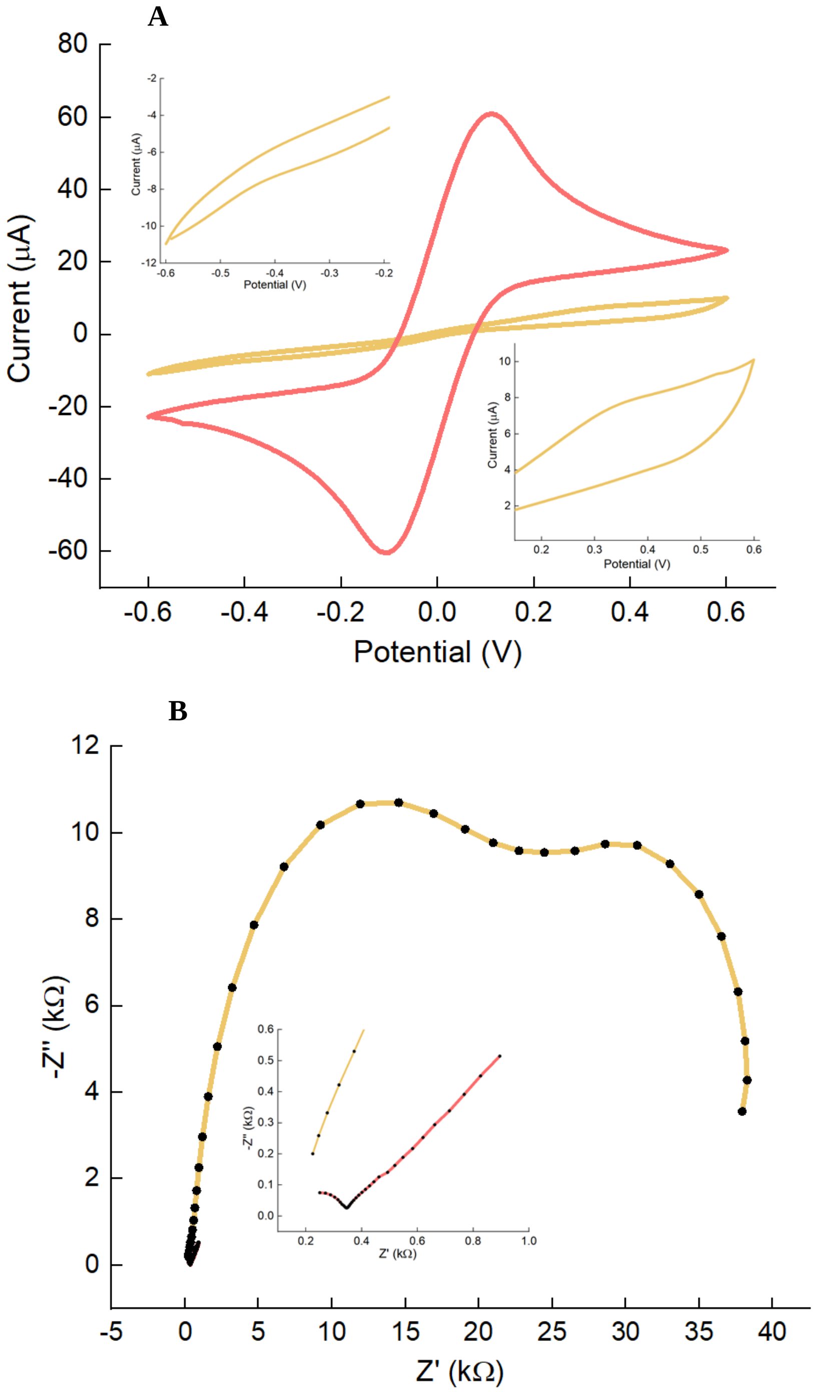

Figure 6.8: Electrochemical characterisation of 5 mM octopamine compared to bare electrodes. A, CV of 5 mM POc-coated (🟨) and bare (🟥) electrode surface. The CV was cycled from -0.6 V to +0.6 in 10 mM $[Fe(CN)_6]^{3-/4-}$ in 10 mM PBS pH 7.2 as described in **Section 2.2.6**. The zoomed-in insert shows the current for 5 mM POc from -0.6 to -0.2 V and from +0.1 to +0.6 V. **B**, Nyquist plot of 5 mM POc-coated and the bare electrode surface. The Nyquist profiles derived from EIS measurements in 10 mM $[Fe(CN)_6]^{3-/4-}$ in 10 mM PBS pH 7.2. EIS was recorded at 0.0 V over a frequency range of +5 kHz to +0.1 Hz, with a modulation voltage of +10 mV as described in **Section 2.2.7**. The zoomed-in insert from 0.0 kΩ to +0.6 kΩ (-Z’’) and from +0.1 kΩ to +1.0 kΩ (Z’). CV and EIS analysis were performed with Palmsens workstation. Electrodes 3 were employed. The CV and Nyquist show averaged readings from n≥6.

6.2.2.2. Characterisation of EDC/sulfo-NHS coupling conditions

EDC/sulfo-NHS were employed as cross-linker and catalyst, respectively, between the POc and the collagen. An amide linkage between the primary amines of the POc and the carboxylic acid from glutamic acid and aspartic acid is created by the intervention of this crosslinker. Then, the presence of sulfo-NHS is essential as its hydrophilic nature allows targeting the amines presented by POc quickly and then creating stable amide linkages (Greg T. Hermanson, 1996).

Seeking a correct protocol is crucial for bioconjugation success. Depending on the conditions of the system, the involvement of a peptide can cause precipitation. This can be a consequence of amine groups and activated carboxylates from collagen reacting, thus causing precipitation. This was considered as collagen is a protein.

Three protocols were tested to find the best way to bind collagen to POc. These protocols are detailed in **Section 2.2.5.3**. All three protocols aimed to create a final solution of 100 µg/mL collagen solution in 50 mM MES pH 5.5 at 2 mM EDC and 6 mM sulfo-NHS to then incubate with a surface coated with 5 mM POc. The first protocol created a 1 mg/mL collagen dissolved in 0.01 M acetic acid and another solution of EDC and sulfo-NHS were dissolved in 50 mM MES pH 5.5. Both solutions were then mixed to make a final solution of 100 µg/mL collagen solution in 50 mM MES pH 5.5 at 2 mM EDC and 6 mM sulfo-NHS which was left for 30 mins incubation. Just before proceeding with the next step, it was observed that the bioconjugate had precipitated. As explained above, the precipitation could be a consequence of activated carboxylates from collagen reacting with amine groups also present in collagen.

A second protocol was followed. Again, the collagen dissolved in acetic acid was added to the EDC/sulfo-NHS solution, yielding a 100 µg/mL collagen solution in 50 mM MES pH 5.5 at 2 mM EDC and 6 mM sulfo-NHS. The bioconjugate solution was not left for 30 mins incubation as in the first protocol. Instead, the bioconjugate solution was immediately placed over the 5 mM POc-coated electrodes and left for a 2 h incubation. No precipitation was observed. The electrodes were then washed 3 times with 50 mM MES pH 5.5. A final 100 mM Tris buffer was employed to block any reactive carboxylate group left. Next, the functionalised electrodes underwent electrochemical assessment through CV and EIS (**Sections 2.2.6 & 2.2.7**).

A third protocols was also tested. The third protocol was similar to the second one. However, this time the collagen was dissolved in 50 mM MES pH 5.5. The rest of the procedure remained the same as detailed in **Section 2.2.5.3**. Next, the functionalised electrodes underwent electrochemical assessment through EIS and CV (**Sections 2.2.6 & 2.2.7**).

The first protocol employed yielded bioconjugation conjugate precipitation; thus, no electrochemical assessment could be performed. The second and third employed protocols allowed complete functionalisation of the electrodes and were electrochemically assessed. They both differed in the buffer used to dissolve collagen, acetic acid for the second protocol and MES for the third. As a result, the second and third protocols yielded POc-coated surfaces with covalently attached collagen and underwent EIS and CV characterisation (**Figure 6.9**).

Figure 6.9A shows the Nyquist profiles derived from EIS analysis for collagen bound to POc-coated surfaces for the second and third protocols. Collagen dissolved in MES Nyquist's (brown) showed less impedance than the collagen dissolved in acetic acid (green). Both Nyquist plots showed semicircle shapes. The Nyquist plot from collagen dissolved in MES showed to be less impedimetric but more resistive profile than the one from collagen dissolved in acetic acid. A more resistive profile is more relevant as it will provide more accurate impedance data at lower frequencies. The impedance decrease could result from the polymer acting as a soft and stretchy net. Any attachment onto the polymer can create more space for the electron mediator to reach the surface. This behaviour has also been reported in another non-conducting polymer biosensor study (Ahmed et al., 2013).

After the EIS analysis, new electrodes were again functionalised following the second and third protocols. Next, CV assessment in 10 mM $[Fe(CN)_6]^{3-/4-}$ in 10 mM PBS pH 7.2 was carried out for both systems and shown in **Figure 6.9B**. The collagen dissolved in MES functionalised electrode voltammogram presented more conductive profile compared to the collagen dissolved in acetic acid functionalised system. These results were in line with the previous ones obtained with EIS analysis.

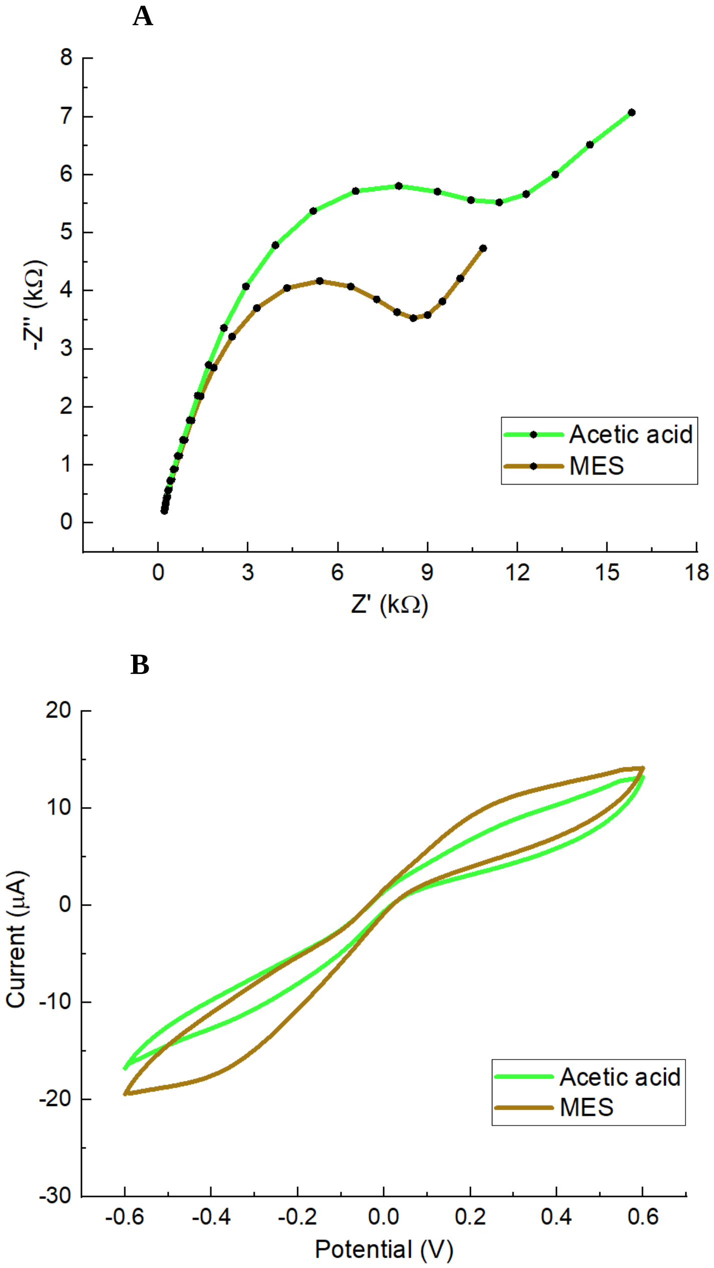

Figure 6.9: Electrochemical characterisation of collagen directly bound to POc through EDC/sulfo-NHS employing two protocols. The second protocol was employed in which the collagen was first dissolved in 0.01M acetic acid solution (🟩). The third protocol was employed in which the collagen was first dissolved in MES solution (🟧). **A**, the Nyquist profiles derived from EIS measurements in 10 mM $[Fe(CN)_6]^{3-/4-}$ in 10 mM PBS pH 7.2. EIS was recorded at 0.0 V over a frequency range of +5 kHz to +0.1 Hz, with a modulation voltage of +10 mV as described in **Section 2.2.7**. **B**, the CV was cycled from -0.6 V to +0.6 V in 10 mM $[Fe(CN)_6]^{3-/4-}$ in 10 mM PBS pH 7.2 as described in **Section 2.2.6**. CV and EIS analysis were performed with Palmsens workstation. Electrodes 3 were employed. The CV and Nyquists plots show averaged readings from n≥6.

6.2.2.3. Collagen concentration optimisation

Collagen binding to POc was achieved by employing EDC/sulfo-NHS, which bound the POc amine group to the carboxylic group from the collagen. The assessment of collagen concentration resulted in a crucial step of the biosensor construction as determined the amount of bioreceptor presence on the surface. Different collagen concentration solutions were tested between 5 µg/mL and 1000 µg/mL. The solutions were created by dissolving collagen in 50 mM MES pH 5.5, to which a final concentration of 2 mM EDC and 6 mM sulfo-NHS in 50 mM MES pH 5.5 was added as described in **Section 2.2.5.3**. Next, the solution was immediately put over the 5 mM POc-coated electrode and left for incubation.

Figure 6.10A shows the Nyquist plots derived from EIS analysis of POc-coated electrodes with different collagen concentrations. Decreasing impedance was observed for increasing collagen concentration. The Nyquist plots presented a steady decrease up to 100 µg/mL (light blue), from which higher collagen concentrations did not show further impact on impedance. Then, new electrodes were pretreated (**Section 2.2.1**), coated with 5 mM POc, and again functionalised with different collagen concentrations as detailed in (**Section 2.2.5.3**) and were subjected to CV assessment under 10 mM $[Fe(CN)_6]^{3-/4-}$ in 10 mM PBS pH 7.2 redox pair as described in (**Section 2.2.6**). The voltammograms (**Figure 6.10B**), in line with the impedimetric results, showed an increase in intensity with increasing collagen concentrations. These results confirmed more conductive systems with higher collagen concentrations.

Midland blotting (Rushworth et al., 2013) was employed to validate the collagen direct attachment to POc through EDC/sulfo-NHS. New electrodes were pretreated with ethanol (**Section 2.2.1**), coated with 5 mM POc and functionalised with 100 µg/mL collagen (**Section 2.2.5.3**). To test the presence of the collagen, the surface was incubated with rabbit anti-type I collagen antibodies. Next, goat anti-rabbit IgG HRP conjugate was added to the electrodes. Finally, ECL reagent was added to the samples to reveal the chemiluminescence detected via the G:BOX imager. Negative controls were carried out by not adding primary antibodies. Two more control samples consisting of 5 mM POc-coated and bare electrodes were also employed. The Midland blotting methodology is followed in (**Section 2.2.10**) and the results are shown in **Figure 6.11**.

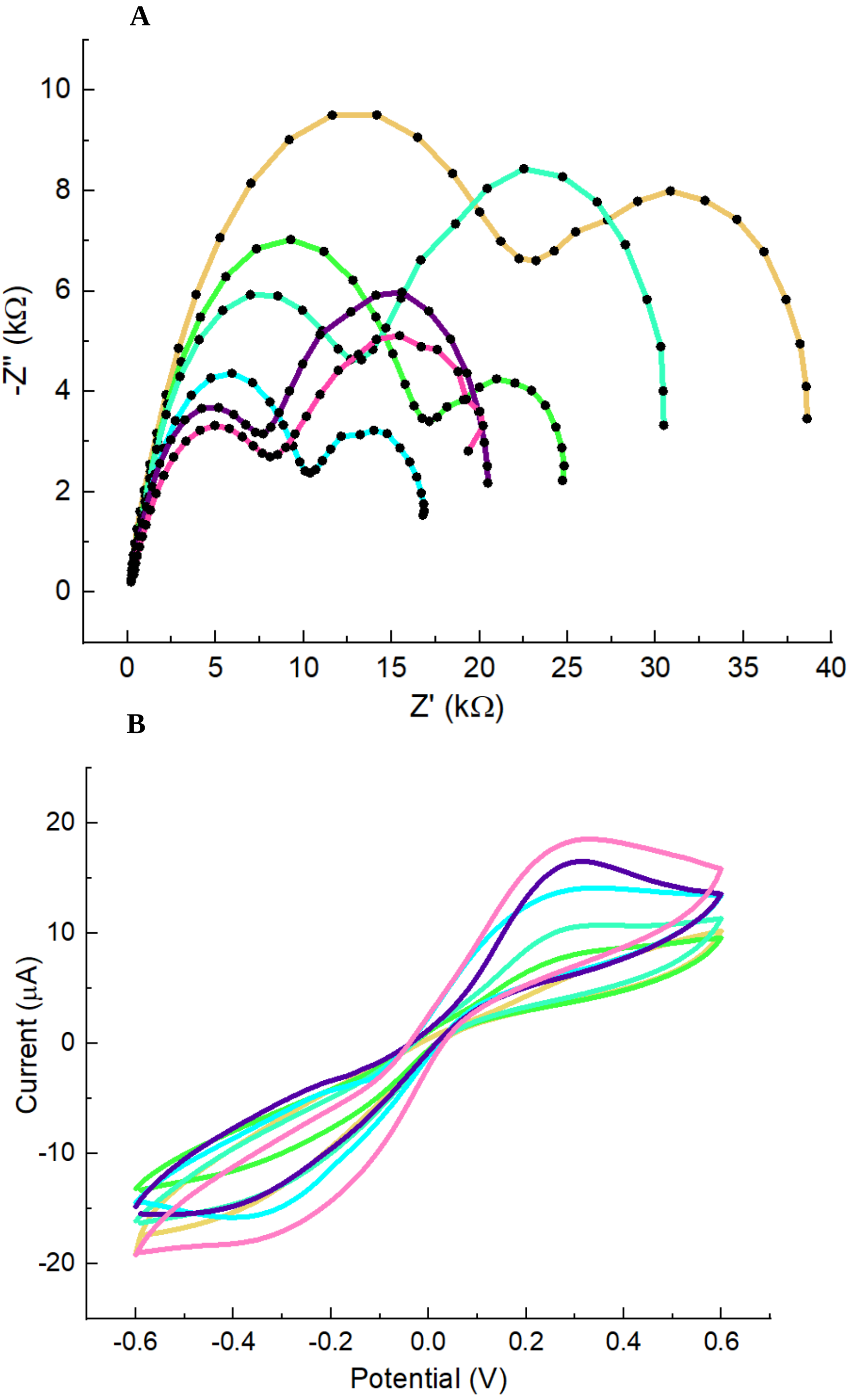

Figure 6.10: Electrochemical characterisation of different collagen concentrations. Different collagen concentrations were directly bound to 5 mM POc, namely, 5 µg/mL (▬), 10 µg/mL (▬), 50 µg/mL (▬), 100 µg/mL (▬), 500 µg/mL (▬) and 1000 µg/mL (▬) of collagen to 5 mM POc via EDC/sulfo-NHS as detailed in **Section 2.2.5.3** and assessed by EIS and CV. **A**, Nyquist profiles derived from EIS measurements in 10 mM $[Fe(CN)_6]^{3-/4-}$ in 10 mM PBS pH 7.2. EIS was recorded at 0.0 V over a frequency range of +5 kHz to +0.1 Hz, with a modulation voltage of +10 mV (**Section 2.2.7**). **B**, the CV was cycled from -0.6 V to +0.6 in 10 mM $[Fe(CN)_6]^{3-/4-}$ in 10 mM PBS pH 7.2 as detailed in **Section 2.2.6**. CV and EIS analysis were performed with Palmsens workstation. Electrodes 3 were employed. The CV and Nyquist plots show averaged readings from n≥6.

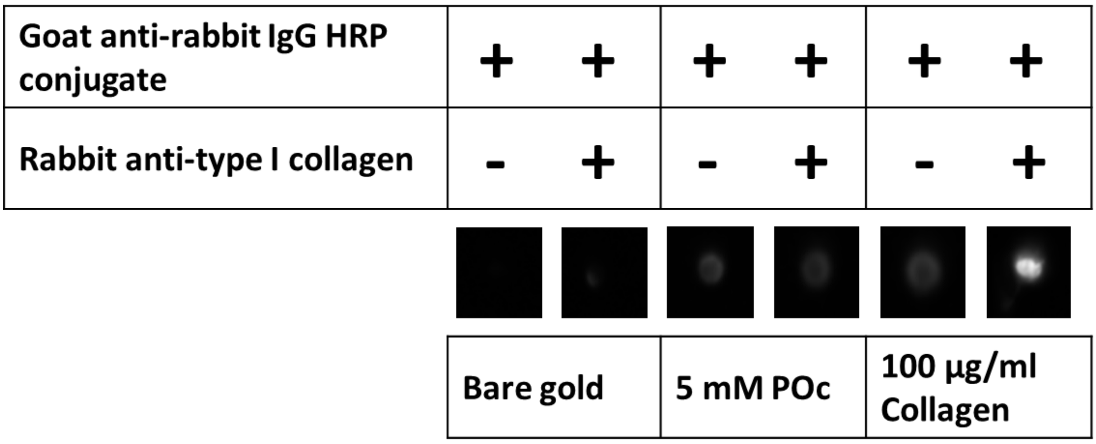

Figure 6.11: Midland blotting for collagen direct attachment to POc validation. Midland blotting was employed to validate the direct collagen binding to POc through EDC/sulfo-NHS cross-linkers. Three different systems were tested. One system consisted of functionalised electrodes with 100 µg/mL collagen (**Section 2.2.5.3**). Two more systems consisting of 5 mM POc and bare electrodes were tested as controls. Then, all systems were prepared by adding 1 mg/mL primary rabbit anti-type I collagen from bovine and human over the electrodes and left for incubation. Next, the electrodes were washed and added 1:1000 in PBS of secondary goat anti-rabbit HRP antibodies. Next, the electrodes were washed and added ECL for chemiluminescence detection using G: BOX as described in **Section 2.2.10**.

6.2.2.4. Optimisation of incubation time with analyte

Different bacterial incubation times were optimised, from 5 min to 60 min. Electrodes were pretreated with ethanol (**Section 2.2.1**), coated with 5 mM POc, and 100 µg/mL collagen was directly attached to POc through EDC/sulfo-NHS as described in **Section 2.2.5.3**. Next, the functionalised electrodes were tested with 10 µL of 8x10^6 cfu YadA-expressing bacteria for each incubation time as detailed in **Section 2.2.5.3**. In this case, the Nyquist plot after analyte addition was used to assess the optimum time of incubation rather than %ΔR_{ct}.

Figure 6.12 shows the Nyquist plots derived from EIS analysis of the different analyte incubation times. The lowest impedance appeared for YadA-expressing bacteria at 5 mins of incubation, as observed from the Nyquist plot. Then, a substantial increase in the size of the Nyquist plot happened for 15-min incubation. Longer incubation times did not make much difference and therefore, 15 mins seemed the most efficient incubation time.

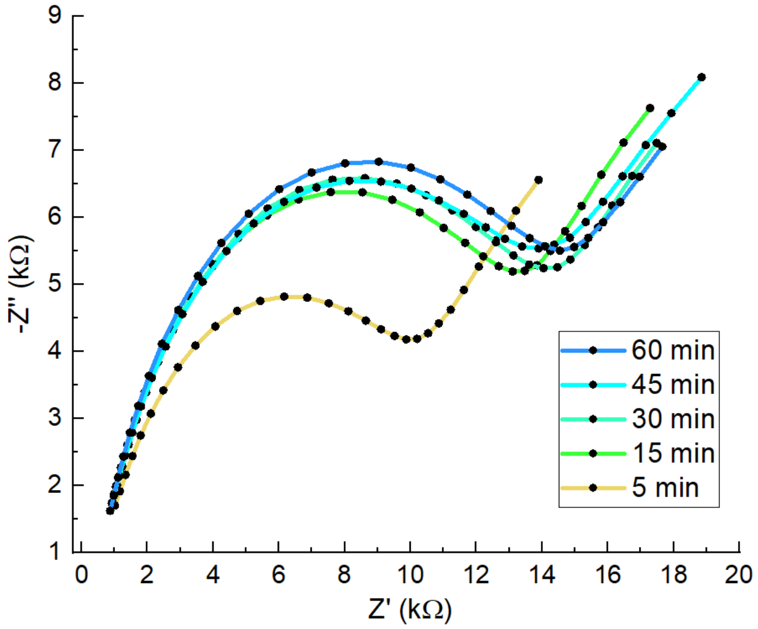

Figure 6.12: Electrochemical assessment of bacterial binding for different incubation times. Different bacterial incubation times were analysed through EIS for 5 min, 15 min, 30 min, 45 min and 60 min of incubation. The electrodes were left incubating with 8x10^6 cfu in a 10 µL sample of YadA-induced *E.coli*. All Nyquist profiles derived from EIS measurements in 10 mM $[Fe(CN)_6]^{3-/4-}$ in 10 mM PBS pH 7.2. EIS was recorded at 0.0 V over a frequency range of +5 kHz to +0.1 Hz, with a modulation voltage of +10 mV as detailed in **Section 2.2.7**. Warburg impedance was avoided for clarity. EIS analyses were performed with Palmsens workstation. Electrodes 3 were employed. Averaged curves shown with number of repeats, n≥6.

6.2.2.5. Assessment of blocking agents

Blocking agents were also assessed as part of the optimisation process to improve selectivity and sensitivity. BSA and casein were considered to block the non-binding sites of the biosensor before bacterial addition. First, new electrodes were pretreated with ethanol (**Section 2.2.1**), coated with 5 mM POc, and 100 µg/mL collagen was directly attached to POc through EDC/sulfo-NHS. Next, the corresponding blocking agent, 1.5 mg/mL BSA or 1.5 mg/mL casein, both in 10 mM PBS, was left for 1 h incubation over the biosensor surface, washed with PBS buffer with 0.05 % Tween-20, and tested with 10 µL of $8x10^6$ cfu YadA-expressing bacteria and non-induced as control as described in **Section 2.2.5.3**. The same procedure was executed without including any blocking agent for comparison. The bacteria binding was assessed using the $\%\Delta R_{ct}$, calculated following **Equation 2.1**.

Figure 6.13 shows the bacterial binding expressed in $\Delta\%R_{ct}$ ± SD for blocked systems compared to non-blocked. BSA and casein blocked biosensors showed bacterial binding testing YadA-expressing bacteria expressed in $\%\Delta R_{ct}$ of 54.89 % ± 12.93 and 41.31 % ± 15.71, respectively. These results show substantial binding as the non-blocked biosensor surface with $\%\Delta R_{ct}$ of 61.61 % ± 7.80. The biosensors employing blocking agents presented notable bacterial binding, but their SD appeared to be higher than non-blocked biosensors. Control, non-induced bacteria showed less non-specific binding for BSA and casein, 11.45 % ± 10.25 and 9.87 % ± 13.31 respectively. The non-blocked surface showed a $\%\Delta R_{ct}$ of 26.12 % ± 5.95. Similarly to YadA-expressing bacteria, BSA and casein blocked biosensors showed substantially larger SD for non-induced samples. Therefore, the use of blocking agents did prevent non-specific binding, but the reproducibility of the blocked systems appeared to be more affected than non-blocked systems.

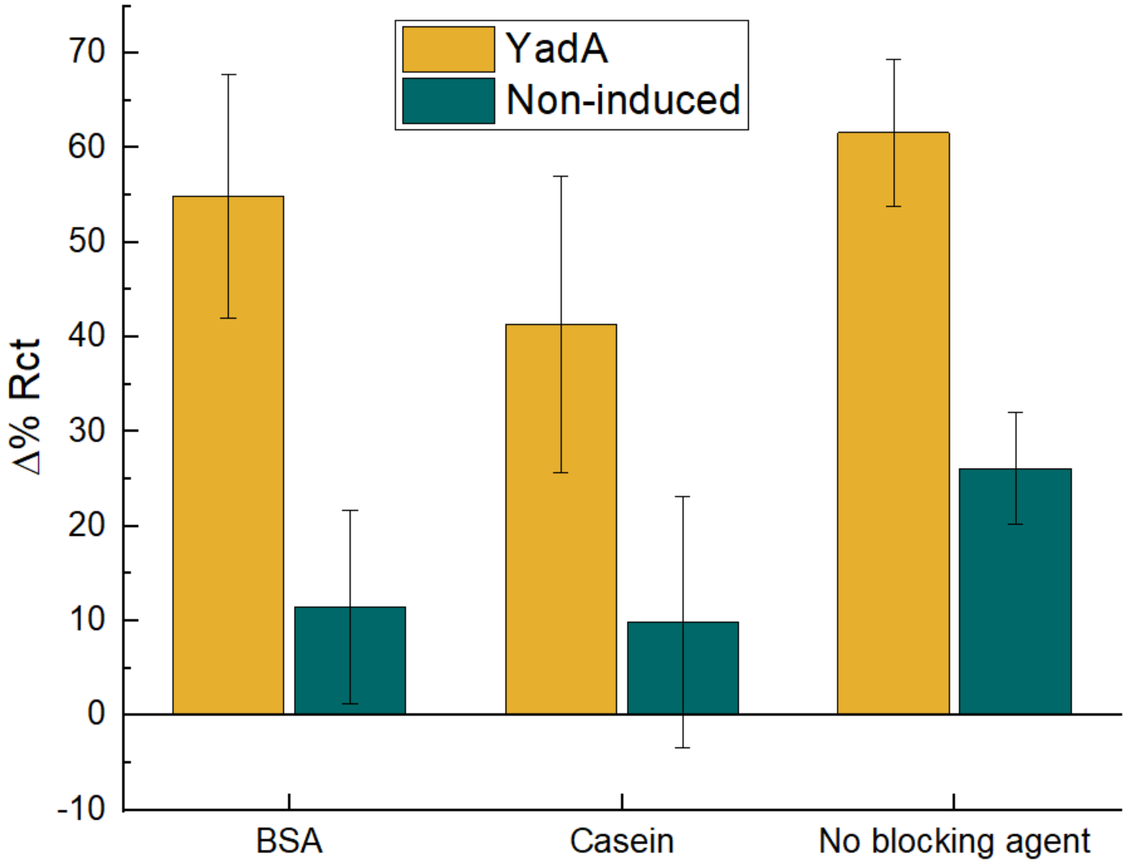

Figure 6.13: Electrochemical bacterial binding assessment employing blocking agents compared to non-blocked. Fully functionalised electrodes were blocked with 1.5 mg/mL BSA and 1.5 mg/mL casein both in 10 mM PBS. Then, the biosensors were incubated for 15 min with 8x10^6 cfu of YadA-expressing bacteria and non-induced in a 10 µL as detailed in **Section 2.2.5.3**. Another system was also assessed in which a non-blocking agent was added for comparison. Before and after the analyte, EIS measurements were taken to assess bacterial binding through Δ%R_{ct}, calculated with **Equation 2.1**. EIS analyses were performed with Palmsens workstation. Electrodes 3 were employed. The bars represent data from n≥6 ± SD.

6.2.2.6. Bacterial detection with optimised sensor

Finally, a fully step-by-step optimised biosensor was analysed to test bacterial determination. First, electrodes were pretreated with ethanol (**Section 2.2.1**), coated with 5 mM POc, and 100 µg/mL collagen was directly attached to POc through EDC/sulfo-NHS. After that, YadA-expressing bacteria were analysed at different bacterial samples ranging from $8x10^2$ to $8x10^7$ cfu. Ten µL of the bacterial sample was placed over the fully functionalised biosensor for 15 min (**Section 2.2.5.3**). After that, the biosensor was washed with PBS and measured with EIS. The EIS measurements before and after the analyte addition allowed assessing the signal through $\Delta\%R_{ct}$. The exact process of biosensor fully construction was carried out and tested for non-induced bacteria.

The bar chart in **Figure 6.14** represents the different $\Delta\%R_{ct}$ ± SD for induced and non-induced bacteria. The two lowest bacteria samples of $8x10^2$ and $8x10^3$ cfu were not detected. Then, from $8x10^4$ cfu induced and non-induced, with $\Delta\%R_{ct}$ 38.98 % ± 3.04 and 15.20 % ± 4.95 respectively, to larger samples, a differentiated analyte response appeared compared to lower cfu samples. From $8x10^4$ to $8x10^7$ cfu, the YadA-expressing *E. coli* showed binding significantly different from non-induced bacteria, $p<0.001$. The YadA-expressing bacteria bar charts presented a steady increase in $\%\Delta R_{ct}$. The non-induced bacterial samples presented non-specific binding. However, higher non-induced bacterial binding gave a lower SD than lower bacterial cfu. The trend shown for non-induced bacteria appears to show a plateau.

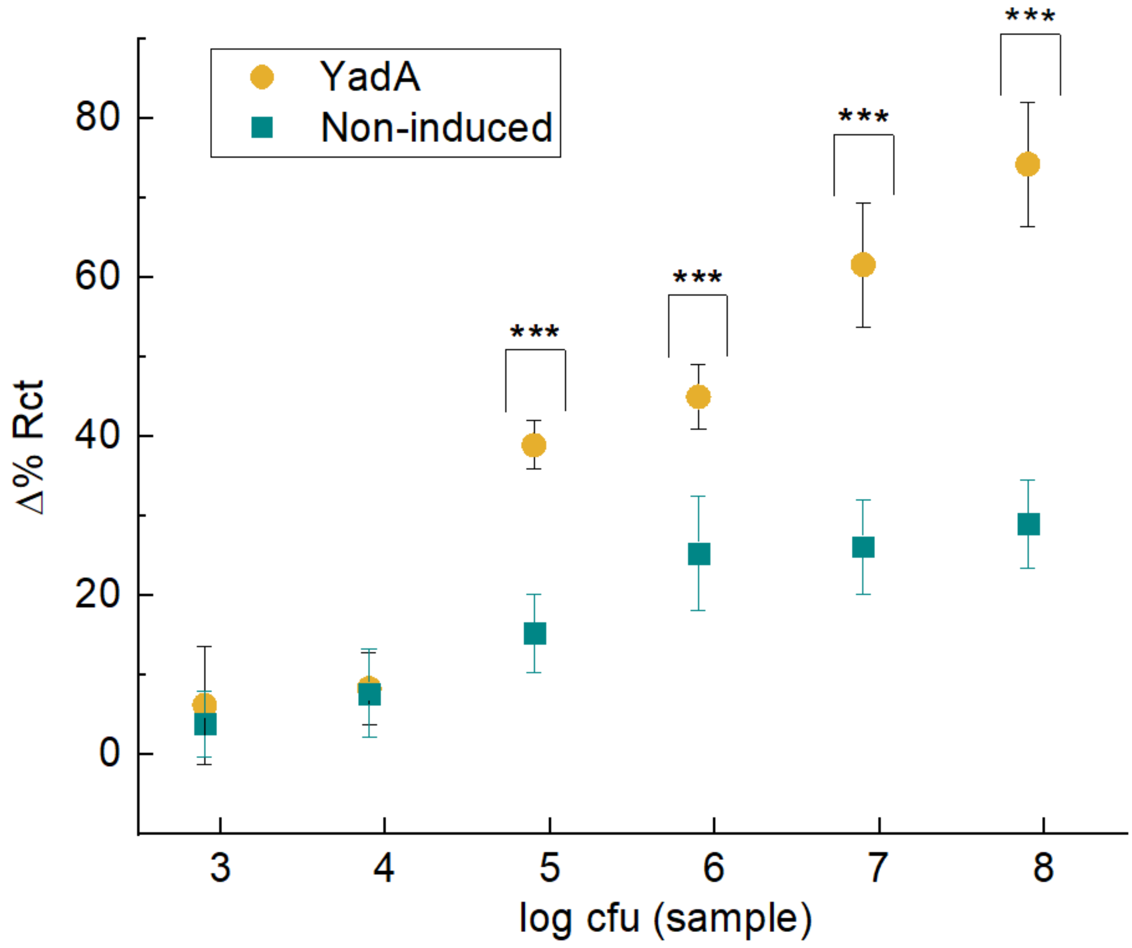

Figure 6.14: Electrochemical bacterial binding assessment for YadA-expressing bacteria and non-induced. Fully constructed biosensors were tested with YadA-expressing bacteria and non-induced. A range of cfu bacterial samples from 8x10^2 cfu to 8x10^7 cfu in 10 µL were incubated for 15 min as detailed in **Section 2.2.5.3** for YadA-expressing bacteria and non-induced. Then, the $\Delta\%R_{ct}$ was calculated with **Equation 2.1**. Electrodes 3 and Palmsens workstastion were employed. The data is represented as the average from $n \geq 6 \pm$ SD. Statistical analysis was performed using ANOVA, and data with $p < 0.001$ are indicated by ***.

6.2.2.7. Fluorescent assay as a validation technique

A validation technique for collagen-YadA-expressing bacteria was carried out through a fluorescent technique. Early-Stage Researcher (PhD student) Ina Meuskens carried out these collaborative experiments at the University of Oslo. The materials and methods can be followed in **Section 2.2.13.1**. The fluorescent assay (**Figure 6.15**) showed specific YadA-expressing *E. coli* binding compared to non-induced bacteria. The bacterial binding was detected as low as 8x10^6 cfu ($p \leq 0.001$) as more diluted samples did not present significant differences between induced and non-induced bacteria. This could be explained by non-specific binding to the well material.

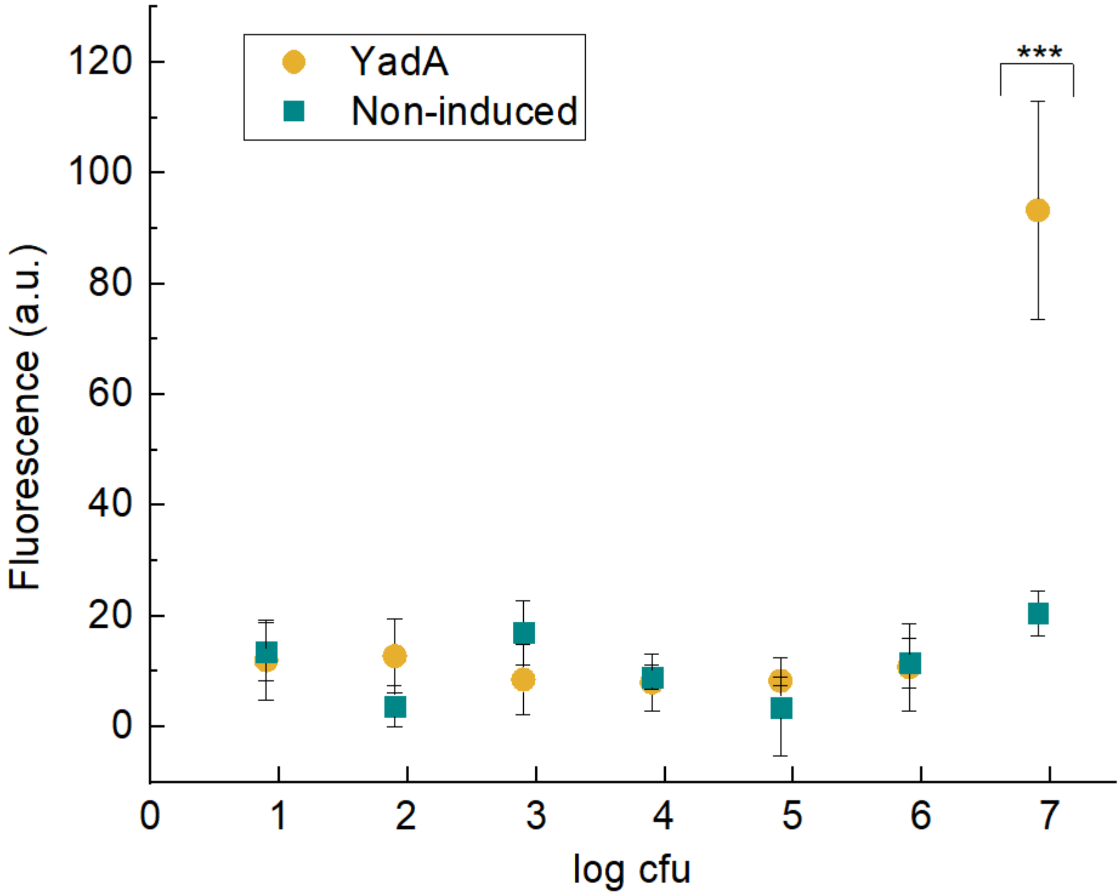

Figure 6.15: Fluorescence assay for bacterial detection. As detailed in **Section 2.2.13.1**, Fluorescence assay based on sfGFP-expressing *E. coli* attaching to wells coated with collagen. A range of different cfu bacterial samples of fluorescent *E. coli*, either expressing or not YadA, were added to collagen-coated wells, and fluorescence was assessed after washing. The data is represented as the average from n=4 ± SD. Statistical analysis was performed using ANOVA, and data with $p < 0.001$ are indicated by ***.

6.3. Discussion & Conclusions

This research presented collagen as a potential bioreceptor candidate for a rapid diagnostic electrochemical biosensor. Two different biosensors were created and tested for bacterial binding. The first system consisted of a non-optimised collagen-POc matrix bioreceptor. This biosensor could detect $8x10^5$ cfu to $8x10^7$ cfu in a 10 µL sample of YadA-expressing *E. coli.* The second system was fully optimised and employed collagen directly bound to POc through EDC/sulfo-NHS as a bioreceptor. This system detected $8x10^4$ cfu to $8x10^7$ cfu in a 10 µL sample of YadA expressing *E. coli.*

ECM-protein biosensors have been able to specifically detect bacteria. However, ECM protein biosensors still need to improve to compete with classic immunosensors, showing LODs of at least two orders of magnitude (**Table 1.2**) smaller than the collagen-adhesin biosensors.

This project aimed to demonstrate that ECM proteins-adhesin interaction could be used for whole pathogen detection in electrochemical biosensors. The use of ECM protein as bioreceptors could offer pan-specificity. This means that the biosensor could detect a group of organisms instead of a specific organism. Detecting a group of organisms could be helpful for clinicians who could perform a rapid diagnostic test to start a treatment before a more time-consuming technique to test the exact species. The main advantage of the antibody-based biosensor is the high specificity for a pathogen. However, being too specific to a particular pathogen could miss other species detection. A balance in specificity could provide more accurate diagnostics results for clinicians.

Pathogenic bacteria have adhesins to target host cells (Meuskens et al., 2019). Generally, adhesins show specificities for different targets. This could be exploited for diagnostics purposes in the future. For instance, a device could use different ECM protein molecules coating and host surfaces to capture or identify bacteria based on their adhesins.

The designed and fabricated ECM protein-adhesin-based biosensor will likely not replace other techniques such as mass spectrometry. However, a rapid biosensor test can achieve a fast approach, quickly indicating which type of infection is present and giving a quicker pathway to initiate the correct clinical actions. Compared to other techniques such as mass spectrometry or media-based testing, these biosensors do not require pathogen growth on plates (Croxatto et al., 2012). In addition, ECM protein-coated biosensors could offer more economical solutions compared to antibody-based biosensors.

Chapter 7

YadA$_{O:9}$ binds directly to heparin

Chapter 7: YadA$_{O:9}$ binds directly to heparin

7.1. Overview

This chapter aimed to demonstrate, through an electrochemical biosensor, that the YadA$_{O:9}$-expressing bacteria direct bind to heparin. This research belongs to a collaboration with Early-Stage Researcher (PhD student) Ina Meuskens and Prof. Dirk Linke, both part of ITN ViBrANT based at University of Oslo. They researched the adhesin YadA$_{O:9}$ interaction with ECM proteins through the direct attachment of YadA$_{O:9}$ to glycan moieties. They studied the interaction between YadA$_{O:9}$ to vitronectin (Vn) and its exclusive interaction with its N-linked glycans. In addition, YadA$_{O:9}$ showed to bind to GAGs through glycan moieties, such as heparin. The study demonstrated that YadA$_{O:9}$ from *Yersinia enterocolitica* interacts with vitronectin through its glycosyl groups. This study was the first time YadA$_{O:9}$ has been shown to interact with glycan moieties of proteins of the ECM or GAGs. As a collaborative project, we participated by providing supporting techniques to their findings by showing that YadA$_{O:9}$-expressing bacteria bind to heparin via electrochemical biosensor. An impedimetric biosensor using heparin as a bioreceptor was fabricated and characterised. The analyte tested in this study was YadA$_{O:9}$-expressing *E.coli* with non-induced cells as control. Another control was also carried out by testing the induced and non-induced bacterial serotype YadA$_{O:8}$.

Ina Meuskens studied the YadA$_{O:9}$-expressing bacteria binding to heparin through a fluorescence assay. In addition, she purified the YadA$_{O:9}$ domain heads to perform a Dot blot and some ELISA-like binding assays. Therefore, a validation technique was still needed for whole bacteria, unlike the protein purified assays, for which different methods were employed. Thus, my participation in this study provided supporting evidence of the entire YadA$_{O:9}$-expressing bacteria direct binding to heparin. The electrochemical binding assay consisted of a biosensor that monitored bacterial binding through EIS. For that, a biosensor was built, so the heparin functioned as a bioreceptor to capture YadA$_{O:9}$-expressing bacteria.

To choose the best biosensor architecture, the manner of attaching the heparin to the electrodes had to be considered. For this, different types of heparin were investigated. Biotin-tagged heparin appeared to be the best candidate as it had been used frequently for biosensor construction in the Millner laboratory and is well established. The complete biosensor construction consisted of the same architecture as the one employed in (Ahmed et al., 2013), but using biotinylated heparin instead of antibodies, a scheme of which can be observed in **Figure 7.1**.

Two different bacterial concentrations were tested to provide more conclusive information, 10^6 and 10^7 cfu, which were placed in 10 µL samples over the functionalised electrodes. Different types of bacteria were tested to ensure the validity of the results. First, the YadA$_{O:9}$ serotype was tested. Another serotype, $\mathrm{YadA}_{\mathrm{O:8}}$, was used as a control. Both serotypes were tested for induced and non-induced bacteria. As expected, $\mathrm{YadA}_{\mathrm{O:9}}$-expressing bacteria showed binding to heparin compared to non-induced cells and to the $\mathrm{YadA}_{\mathrm{O:8}}$ serotype. The whole investigation yielded a publication (Meuskens et al., 2022) that is referenced for Ina’s materials and methodological procedure as well as results figures.

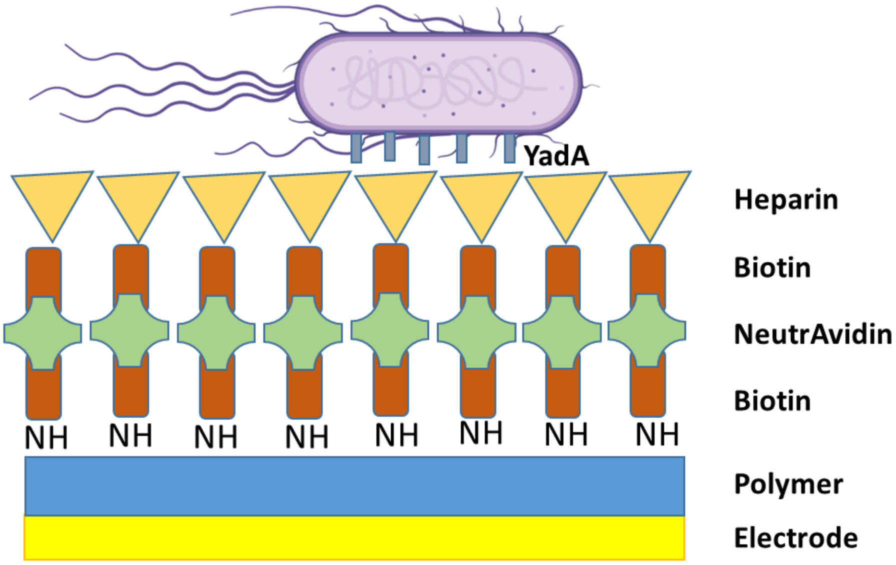

Figure 7.1: Replicate of Figure 2.5 for clarity. The biosensor layer-by-layer construction comprises an electrode, POc film, biotin, NeutrAvidin, and biotinylated heparin.

7.2. Results

7.2.1. Heparin-binding fluorescence assay for whole bacteria

First, through absorbance, a heparin-binding assay was performed to test the specific binding of whole bacteria expressing $\text{YadA}_{O:9}$ to heparin. This assay was carried out by Ina Meuskens and confirmed the entire bacteria expressing $\text{YadA}_{O:9}$ binding to heparin. The interaction between *E. coli* AS75 expressing $\text{YadA}_{O:9}$ and heparin was done by immobilising bacteria in a 96-well plate. The immobilised $\text{YadA}_{O:9}$-expressing bacteria, bound to biotinylated heparin. As a control, $\text{YadA}_{O:8}$-expressing bacteria were used, for which minimal binding to biotinylated heparin was observed (**Figure 7.2**).

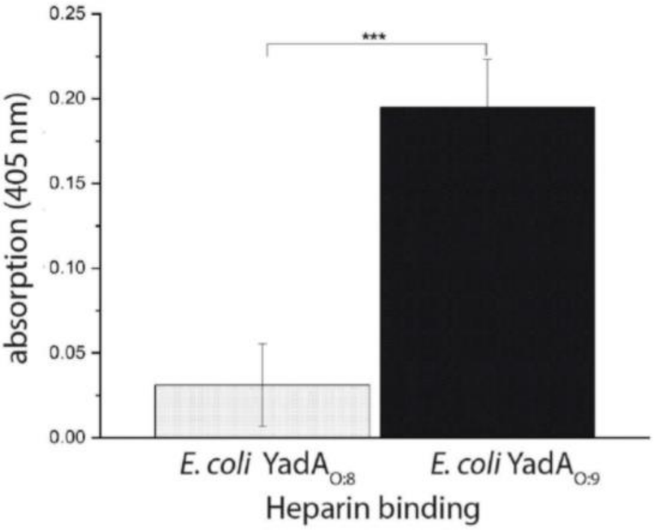

Figure 7.2: Fluorescence binding assay for whole-cell bacteria expressing $\text{YadA}_{O:8}$ or $\text{YadA}_{O:9}$. In this assay, heparin-binding to whole bacteria is measured and analysed in terms of absorbance at 405 nm (**Section 2.2.13.2**). $p < 0.001$ is indicated with ***. Figure reproduced from (Meuskens et al., 2022).

7.2.2. EIS detection of whole bacteria expressing YadA$_{O:9}$

7.2.2.1. Characterisation of the biosensor: layer-by-layer construction

First, BVT-AC1.W1.RS.Dw2 (Electrodes 3) were pretreated by immersion in ethanol, washed with diH$_2$O, and dried with N$_2$. Next, electrodes were coated using 2.5 mM octopamine through electropolymerisation, washed with PBS and dried with Ar. Next, the POc-coated surface was biotinylated and NeutrAvidin was added. Finally, 10 µL of 1 mg/mL heparin-biotin was incubated over the surface for 1 h, washed with PBS and dried with Ar (**Section 2.2.5.4**). **Figure 7.3** shows the EIS and CV measurements taken at each functionalisation step that assessed and confirmed the layer-by-layer construction of the biosensor: starting from the bare electrode to the fully functionalised biosensor with heparin ready to detect YadA expressing bacteria.

Figure 7.3A shows the 2.5 mM POc electrodeposition voltammogram. As expected, an oxidation peak current in the first CV cycle (green). No oxidative current was observed in the second cycle (red), thus confirming the passivation of the electrode. **Figure 7.3B** shows the Nyquist plots derived from EIS analysis at each step of the biosensor construction. The bare electrode showed the smallest Nyquist semi-circle as there was no coating on the electrode, thus allowing the electrode mediators to reach the surface without resistance (red). As the electrode was functionalised with more layers, the Nyquist curves became more resistive, manifested by a steady increase in their semicircles from the non-functionalised surface to the biotinylated heparin attachment. In parallel, the same functionalisation steps were assessed with CV (**Figure 7.3C**). In the CV profiles, the oxidation and reduction peaks of the electron mediator's intensity were used as surface functionalisation indicators. The most impedimetric surface showed the smallest oxidation and reduction peaks. This can be observed from the different interfaces of the biosensor, starting from the bare one, which matches with a characteristic $[Fe(CN)_6]^{3-/4-}$ CV profile. The more functionalised layers were added to the biosensor, the less current was observed in the $[Fe(CN)_6]^{3-/4-}$ redox peaks. The CV results showed to be in line with that observed in the Nyquist plots.

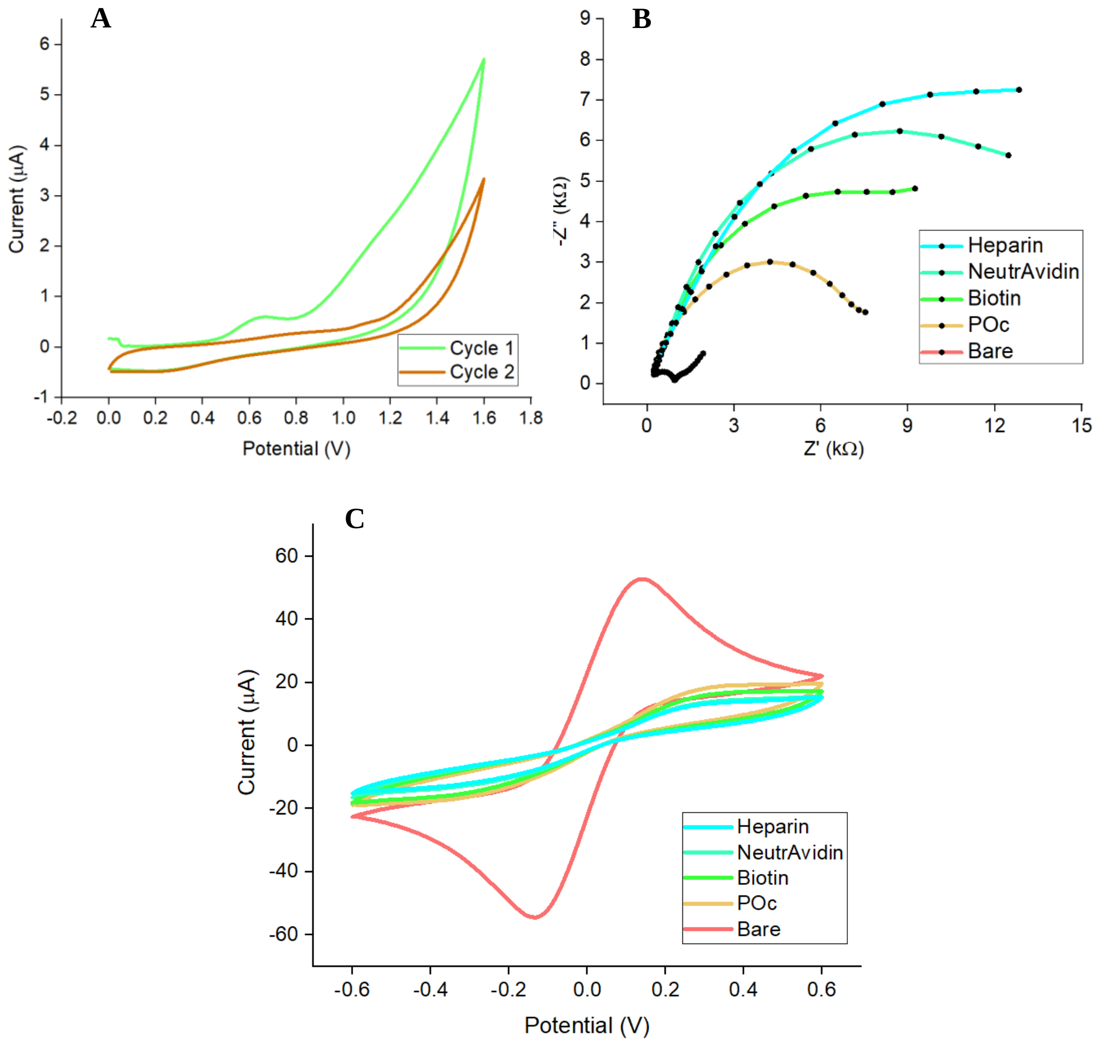

Figure 7.3: Electrochemical layer-by-layer characterisation of the impedimetric biosensor with heparin-immobilised-bioreceptor for whole bacteria detection. A, corresponds to the electropolymerisation of 2.5 mM octopamine over Electrodes 3 cycled from 0.0 V to +1.6 V for two cycles as the first layer of the biosensor (**Section 2.2.5.4**). **B**, shows the Nyquist plot of layer-by-layer biosensor construction: bare gold working electrode surface, POc, biotin, NeutrAvidin and heparin. All Nyquist profiles derived from EIS measurements in 10 mM $[Fe(CN)_6]^{3-/4-}$ in 10 mM PBS pH 7.2. EIS was recorded at 0.0 V over a frequency range of +5 kHz to +0.1 Hz, with a modulation voltage of +10 mV using Palmsens workstation as described in **Section 2.2.7**. **C**, shows the cyclic voltammogram profile of layer-by-layer biosensor construction of bare gold working electrode surface, POc, biotin, NeutrAvidin and heparin. The CV was cycled from -0.6 V to +0.6 V in 10 mM $[Fe(CN)_6]^{3-/4-}$ in 10 mM PBS pH 7.2 using Palmsens workstation as detailed in **Section 2.2.6**. These data, within **Figures 3A, 3B & 3C** were published in (Meuskens et al., 2022). The CV and the Nyquist plots show averaged readings from n≥6.

7.2.2.2. Analyte detection

Whole bacteria expressing YadA for both serotypes, $YadA_{O:9}$ and $YadA_{O:8}$, were tested, including non-induced samples as controls. Then, two different cfu samples were employed, 10^6 and 10^7 cfu in 10 µL. Fully functionalised biosensors were tested before the analyte with 3 EIS measurements for signal stabilisation. After that, samples for both $YadA_{O:9}$ and $YadA_{O:8}$ were left for 30 min incubation, washed, and analysed with EIS (**Section 2.2.5.4**).

Figure 7.4 shows the $\Delta\%R_{ct}$ derived from EIS measurements before and after analyte addition and calculated as shown in **Equation 2.1** and used as analytical signal to assess bacterial binding. $YadA_{O:9}$-expressing bacteria (teal) and non-induced cells (green) were tested and showed binding for the adhesin-expressing bacteria. It showed binding for both 10^6 and 10^7 cfu samples, showing an increase in signal with increasing bacterial cfu. Contrarily, $YadA_{O:8}$-expressing bacteria (orange) and non-induced cells (red) did not show binding for any samples. These results are in line with the observations of Ina Meuskens in the fluorescent assays (**Figure 7.2**), thus validating $YadA_{O:9}$-expressing bacteria binding to heparin.

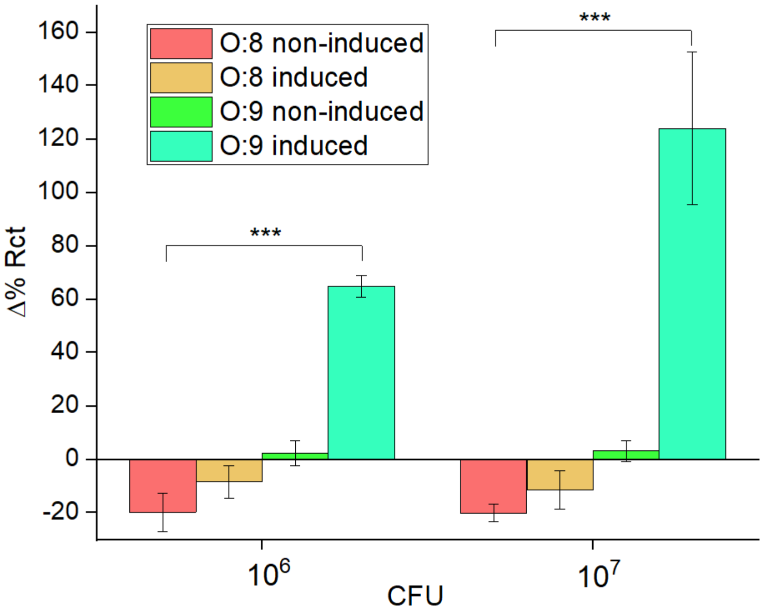

Figure 7.4: EIS bacterial detection represented by $\Delta\%R_{ct}$ for two bacterial samples of 10^6 to 10^7 cfu in 10 µL. $\Delta\%R_{ct}$ before and after analyte incubation with non-induced O:8 and O:9 *E. coli* or *E. coli* expressing $YadA_{O:8}$ or $YadA_{O:9}$ for two different bacterial samples containing 10 µL of 10^6 and 10^7 cfu to surface-coated heparin Electrodes 3. Incubation was for 30 min, and $\Delta\%R_{ct}$ was calculated with **Equation 2.1** (**Section 2.2.5.4**). EIS measurements were conducted in 10 mM $[Fe(CN)_6]^{3-/4-}$ in 10 mM PBS pH 7.2. EIS was recorded at 0.0 V over a frequency range of +5 kHz to +0.1 Hz, with a modulation voltage of +10 mV using Palmsens workstation as described in **Section 2.2.7**. Data published in (Meuskens et al., 2022). The bars represent data from $n \geq 6 \pm$ SD. Statistical analysis was performed using ANOVA, and $p < 0.001$ is indicated with ***.

The first studies corresponded to bacterial binding assays, fluorescent and electrochemical, to assess if whole bacteria expressing $\text{YadA}_{\text{O:9}}$ bound to heparin. Then, Ina Meuskens proceeded with fluorescent binding assays to determine whether purified $\text{YadA}_{\text{O:9}}$ head domains bond to heparin. These experiments showed that the binding came purely from the $\text{YadA}_{\text{O:9}}$ protein rather than other factors associated with the bacteria expressing it. These results can be observed in **Appendix II**, **Figure $\mathbf{A_{II}}$1**.

The initial aim of the work was to implement the sensors into a lab-on-a-chip design. However, due to many restrictions, including the impact of Covid-19, this meant only preliminary work could take place. This is presented in the next results section.

7.3. Microfluidics overview

As part of the biosensor research, one crucial element to consider was the miniaturisation, compatibility and portability of the device, all of which could be obtained through microfluidics. As part of the ITN, the University of Hull offered secondments involving microfluidics. By the time secondments started in Hull, the biosensor was close to being finished so that it could be integrated and optimised in a customised microfluidic device. Following the implementation of these techniques, factors affecting the device, including incubation, reagents use and waste produced, could all be optimised. Ideally, the microfluidics component would have been studied towards the end of the project. Therefore, secondment at the University of Hull started. A customised design suitable for the employed electrodes was arranged, and some basic microfluidics experiments were researched. The few experiments demonstrated different electropolymerisation profiles off-chip than on-chip. On-chip fluid was pumped using syringe and pressure pump. The syringe pump system administers fluid at a determined flow rate. The pressure pump is regulated by a pressure controller that creates constant pressure and is connected to the microfluidic device. The effect of varying flow rates was analysed and showed the CV signal’s impact. The oxidative and reductive potential differences were observed for the oxidative and reductive peak currents.

7.4. Microfluidic Results

The first interaction with microfluidics was working with the interfacing of the chip with the fluid pumping instrumentation. Chip 1 (**Figure 7.5A**) served as a model on which to practice interfacing the device with the pumping system while a new device, Chip 2 (**Figure 7.5B**), was being designed and fabricated by Dr Alex Iles, experimental officer at University of Hull, to fit the electrodes for further electrochemical analysis on-chip. Therefore, in the meantime, Chip 1 observed in **Figure 7.5A** served as a model on which to practice interfacing the device with the pumping system. Once Chip 2 was fabricated (**Figure 7.5B**), some electrochemical characterisation were carried out such as the polymer electrodeposition and coated surfaces CV characterisation. The fluids were pumped through Chip 2 by a syringe pump system. The pressure pump system was also tried using the Fluigent system but the results were not accurate due to faulty accessories. Off-chip experiments were run in parallel for comparison.

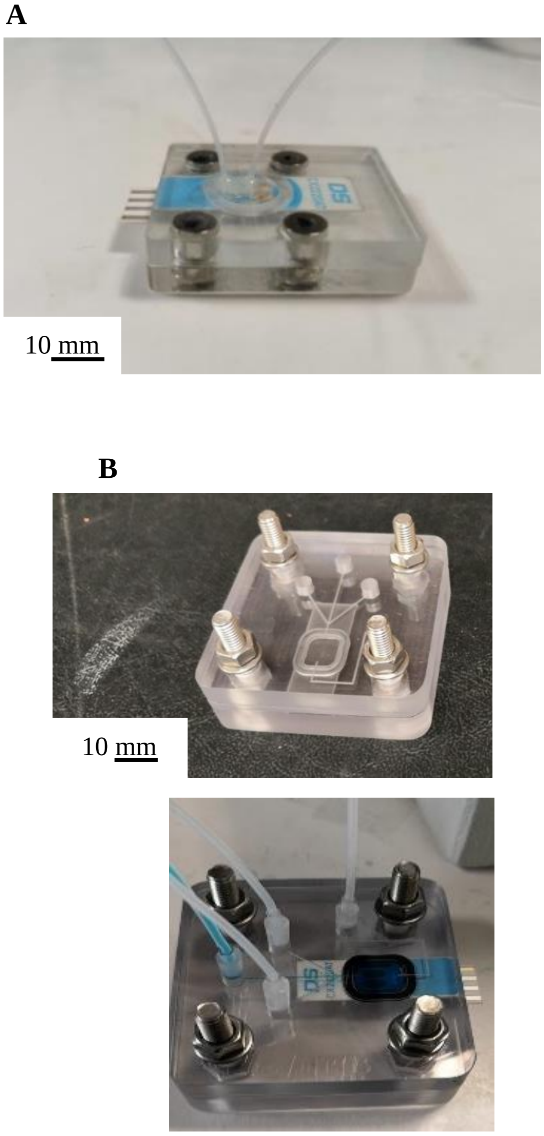

Figure 7.5: Replicate of Figure 2.6 for clarity. A, the chip was designed and fabricated as described in (Patinglag et al., 2020). **B**, the chip was made of PC fabricated using CNC machine milling. The sample chamber (7.5 mm wide, 9 mm long, and 0.2 mm depth) is connected with the inlet channels (7.5 mm wide, 22.5 mm long, 0.2 mm depth). An O-ring made of nitrile rubber with a 10.1 mm bore and 13.3 mm outer was employed. PTFE Teflon tubing (1.58mm od x 0.5mm id) were inserted into inlets and outlet through a 2.5 mL syringe luer adaptor and glued with Araldite.

7.4.1. Electropolymerisation off-chip, syringe and Fluigent system

Non-conducting polymer electrodeposition over SPGEs was assessed on-chip and off-chip. On the one hand, the off-chip system had the monomer solution steady during electropolymerisation. On the other hand, the on-chip system had the monomer solution flowing through the chamber during the electropolymerisation. On-chip electropolymerisation was evaluated using a syringe pump and pressure pumping through the Fluigent system. First, Metrohm DropSens CX2220AT (Electrodes 2) were pretreated with CV in H_2SO_4 as in **Section 2.2.5.1**. Next, 2.5 mM octopamine was electropolymerised over the electrodes as described in **Section 2.2.2.2** for each of the systems. The syringe pump's flow rate was 5 µL/min, and the pressure was 10 mbar through the Fluigents system (**Section 2.2.9**).

Figure 7.6 shows a similar octopamine electropolymerisation profiles for the off-chip and on-chip systems. The octopamine oxidation peak appeared at the expected oxidation potential between +0.45 V to +0.6 V at the first CV scan for off-chip and both on-chip evaluated systems. A flat CV was observed in the second scan for all systems, thus indicating the passivation of the electrode surface. However, the electropolymerisation profiles showed different reproducibility, as observed in **Figures 7.6B-D**. Off-chip octopamine electropolymerisation showed just slightly better reproducibility than both on-chip systems using syringe or pressure pump systems. Polymer-coating on-chip was successfully achieved, and their reproducibility was comparable to the off-chip. Further experiments to improve the octopamine electropolymerisation reproducibility on-chip could be performed.

The results derived from the Fluigent pump system are plotted although the Fluigent system demonstrated multiple problems. The flow rate controller accessory appeared to be faulty and the flow rate could not be controlled. Altogether that caused the fluid to not be pumped at an accurate constant flow rate. Therefore, a syringe pump was employed to ensure flow rate control for the next experiment.

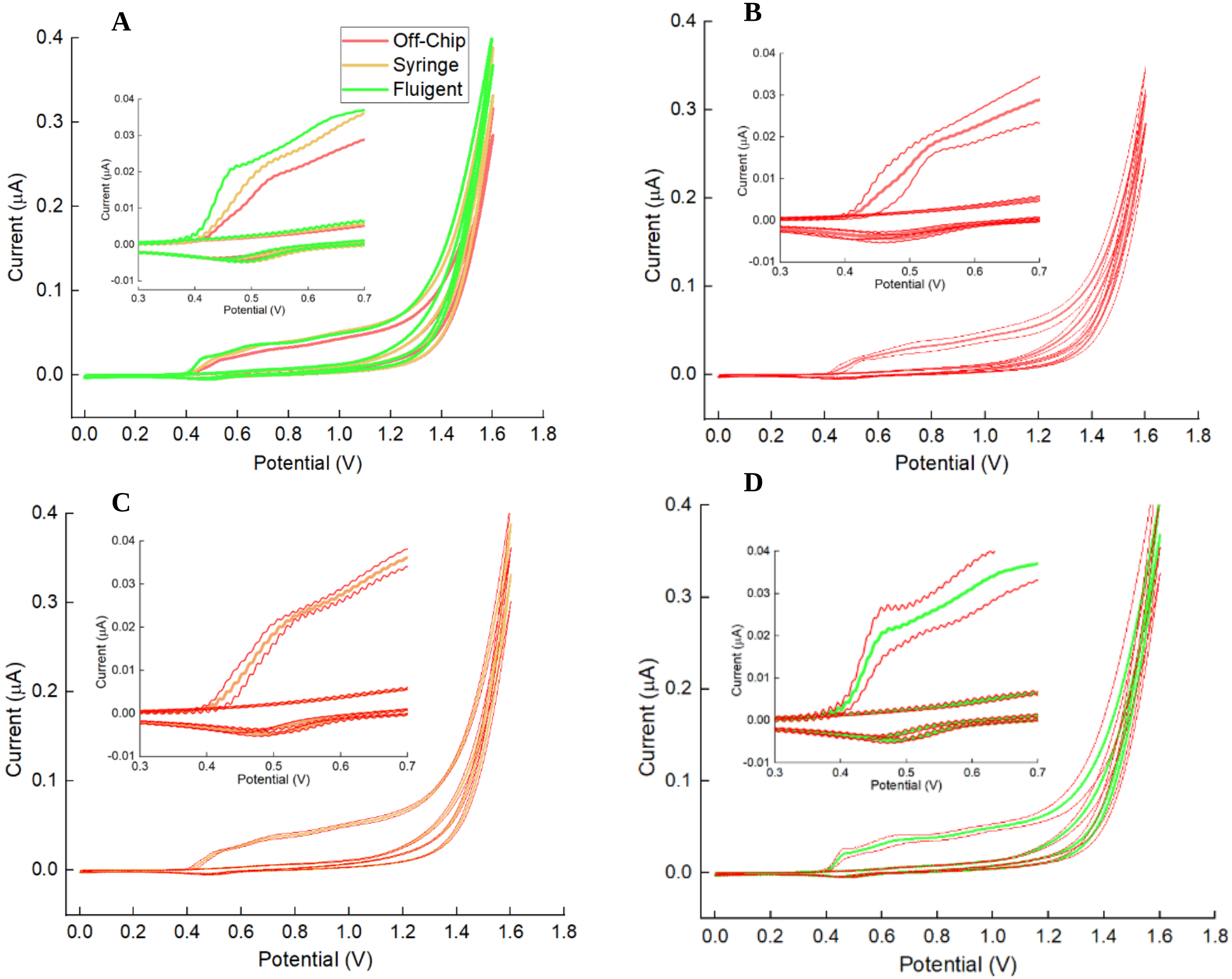

Figure 7.6: Electropolymerisation CV profiles for 2.5 mM octopamine in 10 mM PB pH 7.2: A, off-chip, syringe pump, and Fluigent (pressure pump) octopamine electropolymerised Electrodes 2 as described in **Section 2.2.2.2** using Autolab workstation. The syringe pump's flow rate was 5 µL/min, and the pressure for the Fluigent was 10 mbar. The sample time on the chip was of 150 s. **B**, off-chip, **C**, syringe pump, and **D**, Fluigent. The CV plots averaged readings from n=4; SD, represented in red line.

7.4.2. Polymer-coated electrodes; CV characterisation for different flow rates

Before proceeding with biosensor optimisation, studying the flow rate's effect on the electrochemical measurements was carried out. First, Electrodes 2 were pretreated with CV in H_2SO_4 as detailed in **Section 2.2.5.1**. Then, bare electrodes were cycled between -0.6 V to +0.6 V in 10 mM $[Fe(CN)_6]^{3-/4-}$ in 100 mM PBS solution (**Section 2.2.6**) for flow rates between 1 µL/min and 500 µL/min. An on-chip electrode without flow was also assessed for comparison. To assess how the flow rate affected the electrochemistry, at each flow rate the oxidation and reduction potential and intensity were recorded.

In **Figure 7.7A**, off-chip and on-chip without flow CV analysis can be observed. Both CV voltammograms show a reversible redox $[Fe(CN_6)]^{3-/4-}$ pair reaction. Then, CV analysis was applied on-chip under flow conditions as detailed in **Section 2.2.6** and run for 1 µL/min to 500 µL/min flow rates. The oxidation and reduction peaks and potentials for each flow rate were plotted.

Figure 7.7B shows the reduction potential for different flow rates. The reduction potential appeared at the lowest levels at +0.141 V for 0 µL/min and most of the lowest flow rates until 15 µL/min. Then, the reduction potential jumped from +0.141 V to +0.144 V at 20 µL/min and kept this value until 100 µL/min, increasing to +0.146 V for the highest flow rates. This indicated that the flow rate affected the reduction potential of $[Fe(CN_6)]^{3-/4-}$ pair, in which the higher the flow rate, the greater the reduction potential was.

Figure 7.7C shows that the effect of the flow rates over the oxidative potential differs from the observed reduction potential. The initial flow rate, 0 µL/min shows a value of +0.229 V, but it increases with the two lowest flow rates until they reach +0.234 V, maintained until 10 µL/min. Larger flow rates were shown to decrease the signal until +0.232 V. Unlike what was observed for reduction potential, the flow rate for the oxidation potential, especially the highest, seems to stabilise the signal.

The reductive and oxidative current represents the minimum and the maximum current observed, respectively. In **Figure 7.7D**, the minimum current can be seen to demonstrate a general increase with the increasing flow rates, whereas the maximum current decreases in **Figure 7.7E**. Although the differences described a quite small, they were consistently observed.

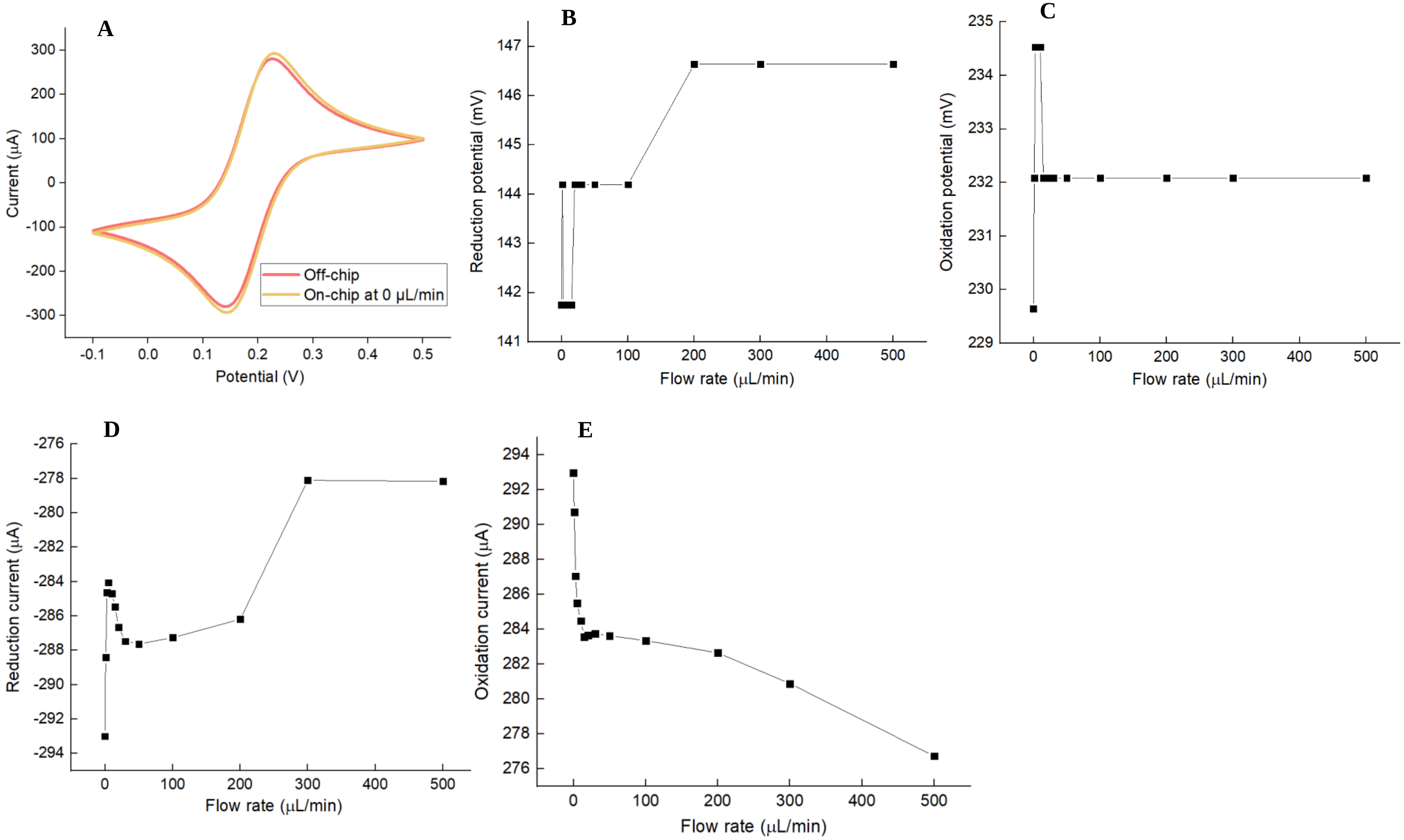

Figure 7.7: **Bare electrodes CV characterisation off-chip and with different flow rates. A**, cyclic voltammogram of bare electrodes for off-chip and on-chip at 0 µL/min. The CV was cycled from -0.6 V to +0.6 V in 10 mM $[Fe(CN)_6]^{3-/4-}$ in 100 mM PBS pH 7.2 (**Section 2.2.6**). **B** and **C** show the reduction and oxidation potential peaks, respectively, for the different flow rates 1, 3, 5, 10, 15, 20, 30, 50, 100, 200, 300 and 500 µL/min. **D** and **E** show the oxidation and reduction current peaks, respectively, for the previously mentioned flow rates. The data show averaged readings from n=4.

7.5. Discussion & Conclusions

Ina Meuskens and Prof. Dirk Linke showed that YadA$_{O:9}$ binds to glycan moieties. They demonstrated that the interaction is not specific for a certain glycan but occurs with a variety of them. The primary research showed this interaction between the YadA$_{O:9}$ and Vn and heparin, both components of the ECM. The collaboration was focused on the YadA$_{O:9}$ to heparin binding. We provided experimental validation to the whole YadA$_{O:9}$-expressing bacteria binding to heparin through an electrochemical biosensor. The biosensor was fabricated, so it had heparin attached as a bioreceptor and whole bacteria expressing YadA$_{O:9}$ and YadA$_{O:8}$ were tested for both induced and non-induced. Once whole bacteria was tested, and proved YadA$_{O:9}$ binding to heparin, the YadA$_{O:9}$ binding to heparin was tested using purified YadA domains. This collaborative research between University of Oslo and University of Leeds yielded a publication (Meuskens et al, 2022). All related to materials and methods employed by Ina Meuskens for her research have been referenced as well as the figures from her experimental part.

The fact that the binding occurred with YadA$_{O:9}$ and not with YadA$_{O:8}$ supports the model in which the YadA$_{O:9}$ loop is responsible for the glycan interactions. The interaction is hypothesised due to electrical charges: the loop contains seven positively charged residues (Arg and Lys) while heparin shows heavily negatively charged sulphate moieties (Rabenstein, 2002). This suggests that the interaction between the positively charged YadA$_{O:9}$ loop and the negatively charged functional groups in glycans is crucial to the binding between YadA$_{O:9}$ and glycans.

Regarding microfluidics, experiments focused on the octopamine electropolymerisation behaviour off-chip and on-chip (**Figure 7.6**) and the differences in the oxidative and reductive potentials and peak currents (**Figure 7.7**). Unfortunately, fewer than the expected number of experiments could be conducted using the microfluidic chip. Several factors influenced the lack of time to optimise the on-chip biosensor. A notification from the University of Oslo indicated that the bacteria previously employed to optimise the biosensor off-chip were mutated. This brought the secondment project to an end. It was decided that the best decision would be to move back to Leeds to start with new experimental planning.

Chapter 8

Overall discussion

Chapter 8: Overall discussion

8.1. Commercial screen-printed gold electrodes: pretreatment, composition and reproducibility

A general pretreatment for gold surface has been extensively studied. Each gold electrode type undergoes a different fabrication process, composition, shape, different interface to be created, molecule to be detected, etc. Extensive research on gold pretreatment has been carried out to facilitate SAM formation and derivative surfaces. However, little about gold pretreatment for polymer electrodeposition was found. In addition, barely any information was found on the pretreatment of SPGEs. The availability of commercial SPGEs has increased in the last decades. Different conditions can alter the electrochemical SPGE performance, such as printing ink composition, and variable temperature conditions during curing and printing processes. Another valuable consideration is the non-clean room conditions in that electrodes are exposed. Electrode contamination can alter thiols' binding kinetics, for instance, and other electrochemical events (Kang & Rowntree, 2007).

Recently, a study about SPGEs pretreatment was carried out by (Stan et al., 2022). They recommend CV in 5 mM $K_4[Fe (CN)_6]/K_3[Fe(CN)_6]$ as SPGE pretreatment. However, a solution of H_2O_2 with the application of multiple CV appeared to be the most efficient pretreatment. Metallic surfaces are still commonly pretreated with CV in H_2SO_4. However, topological alterations have been observed after using CV in H_2SO_4 for gold pretreatment (Burke & Hopkins, 1984; Izumi et al., 1991). Some pretreatments were studied during a *Streptococcus pyogenes* biosensor development. CV in H_2SO_4 was found to be a better SPGE pretreatment than piranha solution and sonication in ethanol. However, CV in H_2SO_4 was considered to create surface modifications that could affect the quality and reproducibility of the surfaces. Moreover, SPGE suppliers and manufacturers accept CV in H_2SO_4 as a pretreatment; these suppliers include Metrohm DropSens (Metrohm Dropsens), Micrux (Micrux Technologies) and Pine (PINE Research, 2016). Other companies suggest acidic cycling potentials, such as Zimmer and Peacock (Zimmer & Peacock AS, 2020) or the use of high anodic and cathodic potentials such as Basi (BASi).

Therefore, in this project, a study with two different types of commercial SPGEs was carried out. CV in H_2SO_4, CV in H_2SO_4 + ethanol, and ethanol alone were used to pretreat Electrodes 2 from Metrohm DropSens, and Electrodes 3, from BVT Technologies. To assess how the gold pretreatment affected the gold surface, different functionalisation were carried out with POc, POc-Ab, 11-MUA SAM, and bare surface for each pretreatment and non-pretreated. CV, EIS, AFM, and XPS evaluated the reproducibility of the systems, the amount of polymer coating, the topography of the SPGEs' surface, and their composition.

After the research, it was concluded that there is no specific optimal pretreatment for SPGEs. As previously mentioned, every commercial electrode is manufactured with the manufacturer's own techniques. Printing ink composition, variable temperature conditions during curing and printing processes and so on, makes every electrode type unique. In addition, using the same manufacturer and model, the composition among different batches can vary. This was the case of the purchased electrodes that showed to be faulty (**Appendix I**). From results in **Chapter 3**, it was observed that some pretreatments were better than others depending on the type of electrode and surface coating. Therefore, a short pretreatment study before using commercial SPGE is recommended. In line with the results from gold pretreatment experiments, **Chapter 5** tested different pretreatments for Electrodes 3 for POc coating.

Other findings were significant: observing a contaminant layer over Electrode 2. A film was observed through AFM, and XPS confirmed the presence of Bi, which could only be revealed with CV in H_2SO_4. Electrode type's A manufacturer, Metrohm DropSens, interestingly commercial bismuth oxide screen-printed carbon electrodes on their website, which led us to suspect cross-contamination during the manufacturing process. It is interesting to mention that a SAM was only removed for one Electrodes 3 just under CV in H_2SO_4. However, the reproducibility was likely compromised due to the molecularly flat surface needed for a good quality SAM.

This study showed that adequate SPGE pretreatment depends on several factors such as electrode composition and surface coating, as had been previously concluded from previous literature. Specifically, degeneration, R_{ct}, C_{dl}, the gold electrode composition and the surface coating deposited or created over the electrode all depend on the particular pretreatment. These results conclude that the best way of proceeding is to identify which one best suits your particular electrodes to produce the best stability and reproducibility.

8.2. Different EIS profiles are shown for POc-coated Electrodes 3 with different electrochemical workstations

When EIS analysis was conducted over POc-coated BVT-AC1.W1.RS.Dw2 (Electrodes 3) employing Palmsens workstation, notable differences were observed compared to formerly used Metrohm DropSens CX2220AT (Electrodes 2) and Autolab workstation. The difference mainly consisted in the two-semicircle shaped Nyquist plot obtained with Electrodes 3 and Palmsens workstation compared to just one-semicircle shaped Nyquist using Electrodes 2 and Autolab workstation.

Electrodes 3 were coated with POc and assessed with the two electrochemical workstations. It was concluded that a two-semicircle shape appeared only when using Palmsens workstation, which seemed to be a typical finite length shaped Warburg impedance (Nguyen & Breitkopf, 2018). On consultation with Alvatek they agreed with this assessment of the data. Alvatek agreed that the electrochemical set-up such as connectors, adaptors or multiplexers could play a role in the signal input and output.

The Palmsens workstation offered the possibility to run several electrodes simultaneously. The electrochemical characterisation and biosensor fabrication show that Palmsens workstation appeared as valid and functional as the Autolab workstation set up. Nevertheless, these results imply that an optimised system could have a different outcome depending on the electrochemical workstation employed. While optimisation and fabrication of a biosensor can be carried out with one type of electrochemical workstation, it does not guarantee the same performance as other electrochemical workstations. This observation casts doubts on the robustness of biosensors from one system to another.

8.3. ECM protein-based biosensor compared to antibody-based biosensor

The main goal of this project was to research an alternative bioreceptor for a pathogen detecting biosensor. Typically, antibodies, proteins and oligonucleotides are used for whole pathogen detection. In **Chapter 6**, ECM protein-adhesin interaction is explored for two types of biosensors. The collagen-protein matrix-based was fabricated following a protocol from ELISHA Ltd. There, collagen was dissolved with octopamine and electropolymerised, thus entrapping the collagen. The performance of this biosensor indicated the possibility of creating a rapid biosensor. Then, a slightly more sophisticated biosensor was fabricated. Electrodes 3 were coated with POc and covalently bound to collagen through EDC/sulfo-NHS. All the steps were optimised, as can be seen from **Chapter 6.** Typically, the bacterial samples are quantified by concentration. However, using the cfu in a 10 µL sample was the unit used in this thesis, to emphasize the very small sample size. The majority of biosensors reported in the literature employ concentration. However, most of them use larger volumes than those employed in this project.

The collagen-polymer matrix captured bacteria in 8×10^5 cfu to 8×10^7 cfu in a 10 µL sample whereas the collagen direct attachment biosensor detected bacteria over 8×10^4 cfu to 8×10^7cfu in a 10 µL sample. The collagen direct attachment system improved by one order of magnitude the detection of YadA-expressing bacteria compared to the collagen-polymer matrix one. The collagen-polymer matrix system could have hindered a great portion of collagen binding sites since the collagen orientation could not be controlled. The use of blocking agents is usually beneficial for classic immunosensor construction. However, as assessed in **Chapter 6**, the use of a blocking agent comprised the reproducibility of the biosensor. While ECM-protein biosensors showed the ability to capture bacteria specifically, they still need to improve to compete with classic immunosensors, showing LODs of at least two orders of magnitude (**Table 1.2**) smaller than the collagen-adhesin biosensors. However, ECM protein as a bioreceptor could detect a *group* of organisms rather than a specific organism. This pan-specificity could be helpful to clinicians who could run a rapid test to start treatment while moving onto more specific identification techniques.

8.4. A reflection on challenges encountered

Three main obstacles affected the course of my PhD studentship.

The first main setback was a mutation found in bacteria YadA$_{O:8}$. The cloned bacteria used for the project were obtained from Dirk Linke's lab. However, Early-Stage Researcher (PhD student) Ina Meuskens discovered a mutation in the YadA vector. The second main obstacle to my PhD was the purchase of Metrohm DropSens electrodes that proved to be faulty. After recommencing my work in the lab after the lockdown, we received the new electrodes and electrochemical equipment-the new Electrodes 3 and the new electrochemical equipment Palmsens workstation. The third major obstacle in my PhD was the Covid-19 Pandemic. The consequences of the Covid-19 pandemic have affected my PhD, not only the seeking new suppliers for electrodes and new equipment but also the limited space in the laboratory and not being able to work in the office.

8.5. Future work

Further research in the development of ECM molecule-based biosensor is needed, such as optimising a biosensor for a specific pathogen, or group of pathogens, or combining different ECM protein binding patterns to determine a pathogen in a complex sample.

Analogous to YadA expressed on *Yersinia* species, other bacteria also have adhesins that target single ligands or a variety of host cell structures (Meuskens et al., 2019; Westerlund & Korhonen, 1993). Biosensors have the potential to be designed with different ECM molecules coatings to identify pathogens based on their adhesion patterns. An ECM molecule-based biosensor could be used as first approach to identify which type of infection is present. Biosensors, unlike other commonly employed diagnostics techniques such as mass spectrometry or media-based testing, do not require traditional culture-based methods (Senior, 1997; Croxatto, Prod'hom & Greub, 2012). Also, biosensors coated with ECM molecules could be a cheaper alternative to antibody-based biosensors. ECM protein-based biosensors, therefore, could be an additional, rapid diagnostics for pathogens that could help fast decision making to treat with the correct antibiotic.

Moreover, the biosensor insertion into a microfluidic chip could improve its performance, give less reagent consumption and bring other benefits such as decreased risk of contamination, and improved sensitivity and specificity (Lei, 2012). Microfluidic devices could also be employed for sample pretreatment and further sampling manipulation which can decrease the time of analysis. Particularly in the case of the biosensor researched in this project, the washing step could be automated with microfluidics, thus removing human error. All these mentioned factors could be optimised on-chip.

Chapter 9

References

Chapter 9: References

Adkins, J.A. and Henry, C.S. 2015. Electrochemical detection in paper-based analytical devices using microwire electrodes. *Analytica Chimica Acta*. **891**, pp.247–254.

Aghaei, F., Seifati, S.M. and Nasirizadeh, N. 2017. Development of a DNA biosensor for the detection of phenylketonuria based on a screen-printed gold electrode and hematoxylin. *Analytical Methods*. **9**(6), pp.966–973.

Ahmed, A. 2015. *Fabrication of electrochemical biosensors for detection of microorganisms. PhD thesis, University of Leeds, Leeds.*

Ahmed, A., Rushworth, J. V., Wright, J.D. and Millner, P.A. 2013. Novel impedimetric immunosensor for detection of pathogenic bacteria *Streptococcus pyogenes* in human saliva. *Analytical Chemistry*. **85**(24), pp.12118–12125.

Akter, R., Jeong, B., Lee, Y.M., Choi, J.S. and Rahman, M.A. 2017. Femtomolar detection of cardiac troponin I using a novel label-free and reagent-free dendrimer enhanced impedimetric immunosensor. *Biosensors and Bioelectronics*. **91**, pp.637–643.

Alshehri, N., Eissa, S., Balobaid, L., Abdel Rahman, A.M., Dasouki, M. and Zourob, M. 2017. Electrochemical immunosensors for the rapid screening of Cystic Fibrosis and Duchenne Muscular Dystrophy. *Electroanalysis*. **29**(8), pp.1911–1917.

Asav, E. and Sezgintürk, M.K. 2014. A novel impedimetric disposable immunosensor for rapid detection of a potential cancer biomarker. *International Journal of Biological Macromolecules*. **66**, pp.273–280.

Aslam, B., Wang, W., Arshad, M.I. and Khurshid, M. 2018. Antibiotic resistance : a rundown of a global crisis. . **11**, pp.1645–1658.

Bahadir, E.B. and Sezgintürk, M.K. 2016. A review on impedimetric biosensors. *Artificial Cells, Nanomedicine and Biotechnology*. **44**(1), pp.248–262.

Bain, C.D., Troughton, E.B., Tao, Y.T., Evall, J., Whitesides, G.M. and Nuzzo, R.G. 1989. Formation of monolayer films by the spontaneous assembly of organic thiols from solution onto gold. *Journal of the American Chemical Society*. **111**(1), pp.321–335.

Bandyopadhyay, S., Mukherjee, S. and Dey, A. 2013. Modular synthesis, spectroscopic characterization and in situ functionalization using ‘click’ chemistry of azide terminated amide containing self-assembled monolayers. *RSC Advances*. **3**(38), pp.17174–17187.

Bard, A.J. and Faulkner, L.R. 2001. *Electrochemical methods* 2nd ed. (D. Harris, E. Swain, & E. Aiello, eds.). John Wiley & Sons, inc.

Barlett, P.N. and Cooper, J.M. 1993. A review of the immobilization of enzymes in electropolymerized films. *Journal of Electroanalytical Chemistry*. **362**(1–2), pp.1–12.

Barreiros dos Santos, M., Azevedo, S., Agusil, J.P., Prieto-Simón, B., Sporer, C., Torrents, E., Juárez, A., Teixeira, V. and Samitier, J. 2015. Label-free ITO-based immunosensor for the detection of very low concentrations of pathogenic bacteria. *Bioelectrochemistry*. **101**, pp.146–152.

BASi n.d. No Title. [Accessed 9 February 2020]. Available from: https://www.basinc.com/products/ec/faqele#Polish.

Bekir, K., Barhoumi, H., Braiek, M., Chrouda, A., Zine, N., Abid, N., Maaref, A., Bakhrouf, A., Ouada, H. Ben, Jaffrezic-Renault, N. and Mansour, H. Ben 2015. Electrochemical impedance immunosensor for rapid detection of stressed pathogenic *Staphylococcus aureus* bacteria. *Environmental Science and Pollution Research*. **22**, pp.15796–15803.

Bekir, K., Bousimma, F., Barhoumi, H., Fedhila, K., Maaref, A., Bakhrouf, A., Ouada, H. Ben, Namour, P., Jaffrezic-Renault, N. and Mansour, H. Ben 2015. An investigation of the well-water quality: immunosensor for pathogenic *Pseudomonas aeruginosa* detection based on antibody-modified poly(pyrrole-3 carboxylic acid) screen-printed carbon electrode. *Environmental Science and Pollution Research*. **22**, pp.18669–18675.

Bernalte, E., Marín-Sánchez, C., Pinilla-Gil, E. and Brett, C.M.A. 2013. Characterisation of screen-printed gold and gold nanoparticle-modified carbon sensors by electrochemical impedance spectroscopy. *JOURNAL OF ELECTROANALYTICAL CHEMISTRY*. **709**, pp.70–76.

Billah, M.M., Hays, H.C.W., Hodges, C.S., Ponnambalam, S., Vohra, R. and Millner, P.A. 2012. Mixed self-assembled monolayer (mSAM) based impedimetric immunosensors for cardiac troponin I (cTnI) and soluble lectin-like oxidized low-density lipoprotein receptor-1 (sLOX-1). *Sensors and Actuators, B: Chemical*. **173**, pp.361–366.

Birch, J.R. and Racher, A.J. 2006. Antibody production. *Advanced Drug Delivery Reviews*. **58**(5–6), pp.671–685.

Boozer, C., Chen, S. and Jiang, S. 2006. Controlling DNA orientation on mixed ssDNA/OEG SAMs. *Langmuir*. **22**(10), pp.4694–4698.

Boubour, E. and Lennox, R.B. 2000. Potential-induced defects in n-alkanethiol self-assembled monolayers monitored by impedance spectroscopy. *Journal of Physical Chemistry B*. **104**(38), pp.9004–9010.

Bourigua, S., Hnaien, M., Bessueille, F., Lagarde, F., Dzyadevych, S., Maaref, A., Bausells, J., Errachid, A. and Renault, N.J. 2010. Impedimetric immunosensor based on SWCNT-COOH modified gold microelectrodes for label-free detection of deep venous thrombosis biomarker. *Biosensors and Bioelectronics*. **26**(4), pp.1278–1282.

Breton, M.D., Kanapka, L.G., Beck, R.W., Ekhlaspour, L., Forlenza, G.P., Cengiz, E., Schoelwer, M., Ruedy, K.J., Jost, E., Carria, L., Emory, E., Hsu, L.J., Oliveri, M., Kollman, C.C., Dokken, B.B., Weinzimer, S.A., DeBoer, M.D., Buckingham, B.A., Cherñavvsky, D. and Wadwa, R.P. 2020. A randomized trial of closed-loop control in children with type 1 diabetes. *New England Journal of Medicine*. **383**(9), pp.836–845.

Burke, L.D. and Hopkins, G.P. 1984. Hydrous oxide formation on gold in base under potential cycling conditions. *Journal of Applied Electrochemistry*. **14**, pp.679–686.

Burke, L.D., Lyons, M.E. and Murphy, O.J. 1982. Formation of hydrous oxide films on cobalt under potential cycling conditions. *Journal of Electroanalytical Chemistry*. **132**, pp.247–261.

Burke, L.D. and Nugent, P.F. 1998. Multicomponent hydrous oxide films grown on gold in acid solution. *Journal of Electroanalytical Chemistry*. **444**, pp.19–29.

Campbell, S.B., Wu, Q., Yazbeck, J., Liu, C., Okhovatian, S. and Radisic, M. 2021. Beyond polydimethylsiloxane: Alternative materials for fabrication of organ-on-a-chip devices and microphysiological Systems. *ACS Biomaterials Science and Engineering*. **7**(7), pp.2880–2899.

Cardoso, A.R., Moreira, F.T.C., Fernandes, R. and Sales, M.G.F. 2016. Novel and simple electrochemical biosensor monitoring attomolar levels of miRNA-155 in breast cancer. *Biosensors and Bioelectronics*. **80**, pp.621–630.

Carvalhal, R.F., Freire, R.S. and Kubota, L.T. 2005. Polycrystalline gold electrodes: A comparative study of pretreatment procedures used for cleaning and thiol self-assembly monolayer formation. *Electroanalysis*. **17**(14), pp.1251–1259.

Caygill, R.L., Hodges, C.S., Holmes, J.L., Higson, S.P.J., Blair, G.E. and Millner, P.A. 2012.

Novel impedimetric immunosensor for the detection and quantitation of Adenovirus using reduced antibody fragments immobilized onto a conducting copolymer surface. *Biosensors and Bioelectronics*. **32**(1), pp.104–110.

Cesewski, E. and Johnson, B.N. 2020. Electrochemical biosensors for pathogen detection. *Biosensors and Bioelectronics*. **159**, p.112214.

Chaubey, A. and Malhotra, B.D. 2002. Mediated biosensors. *Biosensors and Bioelectronics*. **17**, pp.441–456.

Chen, K., Lu, G., Chang, J., Mao, S., Yu, K., Cui, S. and Chen, J. 2012. Hg(II) ion detection using thermally reduced graphene oxide decorated with functionalized gold nanoparticles. *Analytical Chemistry*. **84**(9), pp.4057–4062.

Chen, Q., Wang, D., Cai, G., Xiong, Y., Li, Y., Wang, M., Huo, H. and Lin, J. 2016. Fast and sensitive detection of foodborne pathogen using electrochemical impedance analysis, urease catalysis and microfluidics. *Biosensors and Bioelectronics*. **86**, pp.770–776.

Chen, S.H., Chuang, Y.C., Lu, Y.C., Lin, H.C., Yang, Y.L. and Lin, C.S. 2009. A method of layer-by-layer gold nanoparticle hybridization in a quartz crystal microbalance DNA sensing system used to detect dengue virus. *Nanotechnology*. **20**, p.215501.

Chen, Y., Wang, Z., Liu, Y., Wang, X., Li, Y., Ma, P., Gu, B. and Li, H. 2018. Recent advances in rapid pathogen detection method based on biosensors. *European Journal of Clinical Microbiology and Infectious Diseases*. **37**, pp.1021–1037.

Chiang, W.H., Chen, P.Y., Nien, P.C. and Ho, K.C. 2011. Amperometric detection of cholesterol using an indirect electrochemical oxidation method. *Steroids*. **76**(14), pp.1535–1540.

Chowdhury, A.D., De, A., Chaudhuri, C.R., Bandyopadhyay, K. and Sen, P. 2012. Label free polyaniline based impedimetric biosensor for detection of *E. coli* O157:H7 Bacteria. *Sensors and Actuators, B: Chemical*. **171**–**172**, pp.916–923.

Chowdhury, A.D., Ganganboina, A.B., Park, E.Y. and Doong, R. 2018. Impedimetric biosensor for detection of cancer cells employing carbohydrate targeting ability of Concanavalin A. *Biosensors and Bioelectronics*. **122**, pp.95–103.

Ciani, I., Schulze, H., Corrigan, D.K., Henihan, G., Giraud, G., Terry, J.G., Walton, A.J., Pethig, R., Ghazal, P., Crain, J., Campbell, C.J., Bachmann, T.T. and Mount, A.R. 2012. Development of immunosensors for direct detection of three wound infection biomarkers at point of care using electrochemical impedance spectroscopy. *Biosensors and Bioelectronics*. **31**, pp.413–418.

Clark, L.C. and Lyons, C. 1962. Electrode systems for continuous monitoring in cardiovascular surgery. *Annals of the New York Academy of Sciences*. **102**, pp.29–45.

Clements, A., Young, J.C., Constantinou, N. and Frankel, G. 2012. Infection strategies of enteric pathogenic *Escherichia coli*. *Gut Microbes*. **3**(2), pp.71–87.

Conroy, P.J., Hearty, S., Leonard, P. and O'Kennedy, R.J. 2009. Antibody production, design and use for biosensor-based applications. *Seminars in Cell and Developmental Biology*. **20**, pp.10–26.

Creager, S.E., Hockett, L.A. and Rowe, G.K. 1992. Consequences of microscopic surface roughness for molecular self-assembly. *Langmuir*. **8**(3), pp.854–861.

Croxatto, A., Prod'hom, G. and Greub, G. 2012. Applications of MALDI-TOF mass spectrometry in clinical diagnostic microbiology. *FEMS Microbiology Reviews*. **36**(2), pp.380–407.

Croxen, M.A., Law, R.J., Scholz, R., Keeney, K.M., Wlodarska, M. and Finlay, B.B. 2013.

Recent advances in understanding enteric pathogenic *Escherichia coli*. *Clinical Microbiology Reviews*. **26**(4), pp.822–880.

Cui, H., Li, S., Yuan, Q., Wadhwa, A., Eda, S., Chambers, M., Ashford, R., Jiang, H. and Wu, J. 2013. An AC electrokinetic impedance immunosensor for rapid detection of tuberculosis. *Analyst*. **138**(23), pp.7188–7196.

Cui, M., Wang, Y., Wang, H., Wu, Y. and Luo, X. 2017. A label-free electrochemical DNA biosensor for breast cancer marker BRCA1 based on self-assembled antifouling peptide monolayer. *Sensors and Actuators, B: Chemical*. **244**, pp.742–749.

Custidiano, E., Piovano, S., Arvia, A.J., Chialvo, A.C. and Ipohorski, M. 1987. Electrochemical faceting and preferred crystallographic orientation of rhodium electrodes. *Journal of Electroanalytical Chemistry*. **221**(1–2), pp.229–238.

Dellinger, R.P., Levy, M.M., Rhodes, A., Annane, D., Gerlach, H., Opal, S.M., Sevransky, J.E., Sprung, C.L., Douglas, I.S., Jaeschke, R., Osborn, T.M., Nunnally, M.E., Townsend, S.R., Reinhart, K., Kleinpell, R.M., Angus, D.C., Deutschman, C.S., Machado, F.R., Rubenfeld, G.D., Webb, S.A., Beale, R.J., Vincent, J.L., Moreno, R., Aitken, L., Al Rahma, H., Bernard, G.R., Bion, J.F., Biban, P., Calandra, T., Carcillo, J.A., Clemmer, T.P., Divatia, J. V., Fujishima, S., Du, B., Gando, S., Guyatt, G., Goodyear-Bruch, C., Hazelzet, J.A., Hollenberg, S.M., Hirasawa, H., Jacobi, J., Kacmarek, R.M., Jenkins, I., Jimenez, E., Jones, A.E., Kern, W., Koh, S.O., Kotani, J., Machado, F., Marini, J., Marshall, J.C., Masur, H., Mehta, S., Muscedere, J., Napolitano, L.M., Parker, M.M., Parrrillo, J.E., Qiu, H., Randolph, A.G., Rello, J., Resende, E., Rivers, E.P., Schorr, C.A., Shukri, K., Silva, E., Soth, M.D., Thompson, A.E., Vender, J.S., Welte, T. and Zimmerman, J.L. 2013. Surviving sepsis campaign: International guidelines for management of severe sepsis and septic shock: 2012. *Critical Care Medicine*. **41**(2), pp.580–637.

Deshmukh, S.S. and Goswami, A. 2020. Hot embossing of polymers - A review. *Materials Today: Proceedings*. **26**(2), pp.405–414.

Detante, O., Valable, S., de Fraipont, F., Grillon, E., Barbier, E.L., Moisan, A., Arnaud, J., Moriscot, C., Segebarth, C., Hommel, M., Remy, C. and Richard, M.-J. 2012. Magnetic resonance imaging and fluorescence labeling of clinical-grade mesenchymal stem cells without impacting their phenotype: Study in a rat model of stroke. *Stem Cells Translational Medicine*. **1**(4), pp.333–340.

Dinçkaya, E., Kinik, Ö., Sezgintürk, M.K., Altuĝ, Ç. and Akkoca, A. 2011. Development of an impedimetric aflatoxin M1 biosensor based on a DNA probe and gold nanoparticles. *Biosensors and Bioelectronics*. **26**(9), pp.3806–3811.

Dougan, G. and Baker, S. 2014. *Salmonella enterica* Serovar Typhi and the pathogenesis of Typhoid Fever. *Annual Review of Microbiology*. **68**(1), pp.317–336.

Douterelo, I., Boxall, J.B., Deines, P., Sekar, R., Fish, K.E. and Biggs, C.A. 2014. Methodological approaches for studying the microbial ecology of drinking water distribution systems. *Water Research*. **65**, pp.134–156.

Drevets, D.A. and Bronze, M.S. 2008. *Listeria monocytogenes*: epidemiology, human disease, and mechanisms of brain invasion. *FEMS Immunology and Medical Microbiology*. **53**(2), pp.151–165.

Dulay, S., Lozano-Sánchez, P., Iwuoha, E., Katakis, I. and O'Sullivan, C.K. 2011. Electrochemical detection of celiac disease-related anti-tissue transglutaminase antibodies using thiol based surface chemistry. *Biosensors and Bioelectronics*. **26**(9), pp.3852–3856.

Dutta, G., Jo, K., Lee, H., Kim, B., Young Woo, H. and Yang, H. 2012. Time-dependent decrease in the enhanced electrocatalytic activities observed after three different pretreatments of gold electrodes. *JOURNAL OF ELECTROANALYTICAL CHEMISTRY*. **675**, pp.41–46.

Elshafey, R., Tavares, A.C., Siaj, M. and Zourob, M. 2013. Electrochemical impedance immunosensor based on gold nanoparticles-protein G for the detection of cancer marker epidermal growth factor receptor in human plasma and brain tissue. *Biosensors and Bioelectronics*. **50**, pp.143–149.

Elshafey, R., Tlili, C., Abulrob, A., Tavares, A.C. and Zourob, M. 2013. Label-free impedimetric immunosensor for ultrasensitive detection of cancer marker Murine double minute 2 in brain tissue. *Biosensors and Bioelectronics*. **39**, pp.220–225.

Enomoto, J., Kageyama, T., Myasnikova, D., Onishi, K., Kobayashi, Y., Taruno, Y., Kanai, T. and Fukuda, J. 2018. Gold cleaning methods for preparation of cell culture surfaces for self-assembled monolayers of zwitterionic oligopeptides. *Journal of Bioscience and Bioengineering*. **125**(5), pp.606–612.

Escamilla-Gómez, V., Campuzano, S., Pedrero, M. and Pingarrón, J.M. 2008. Electrochemical immunosensor designs for the determination of *Staphylococcus aureus* using 3,3-dithiodipropionic acid di(N-succinimidyl ester)-modified gold electrodes. *Talanta*. **77**(2), pp.876–881.

Escamilla-Gómez, V., Campuzano, S., Pedrero, M. and Pingarrón, J.M. 2009. Gold screen-printed-based impedimetric immunobiosensors for direct and sensitive *Escherichia coli* quantisation. *Biosensors and Bioelectronics*. **24**(11), pp.3365–3371.

Everley, R.A., Mott, T.M., Wyatt, S.A., Toney, D.M. and Croley, T.R. 2008. Liquid chromatography/mass spectrometry characterization of *Escherichia coli* and *Shigella* species. *Journal of the American Society for Mass Spectrometry*. **19**(11), pp.1621–1628.

Fàbrega, A. and Vila, J. 2012. *Yersinia enterocolitica*: Pathogenesis, virulence and antimicrobial resistance. *Enfermedades Infecciosas y Microbiología Clínica*. **30**(1), pp.24–32.

Fagan, D.T., Hu, I.F. and Kuwana, T. 1985. Vacuum heat treatment for activation of glassy carbon electrodes. *Analytical Chemistry*. **57**(14), pp.2759–2763.

Fan, H.C., Blumenfeld, Y.J., El-Sayed, Y.Y., Chueh, J. and Quake, S.R. 2009. Microfluidic digital PCR enables rapid prenatal diagnosis of fetal aneuploidy. *American Journal of Obstetrics and Gynecology*. **200**(5), pp.543–543.

Fan, X., White, I.M., Shopova, S.I., Zhu, H., Suter, J.D. and Sun, Y. 2008. Sensitive optical biosensors for unlabeled targets: A review. *Analytica Chimica Acta*. **620**(1–2), pp.8–26.

Farka, Z., Juřík, T., Pastucha, M., Kovář, D., Lacina, K. and Skládal, P. 2016. Rapid immunosensing of *Salmonella typhimurium* using electrochemical impedance spectroscopy: the effect of sample treatment. *Electroanalysis*. **28**(8), pp.1803–1809.

Fealy, R.J., Ackerman, S.R. and Ferguson, G.S. 2011. Mechanism of spontaneous formation of monolayers on gold from alkyl thiosulfates. *Langmuir*. **27**(9), pp.5371–5376.

Feng, G., Niu, T., You, X., Wan, Z., Kong, Q. and Bi, S. 2011. Studies on the effect of electrode pretreatment on the coverage of dodecanethiol on gold by electrochemical reductive desorption determination. *Analyst*. **136**(23), pp.5058–5063.

Fernández-Sánchez, C., McNeil, C.J. and Rawson, K. 2005. Electrochemical impedance spectroscopy studies of polymer degradation: application to biosensor development. *TrAC - Trends in Analytical Chemistry*. **24**(1), pp.37–48.

Fischer, L.M., Tenje, M., Heiskanen, A.R., Masuda, N., Castillo, J., Bentien, A., Émneus, J., Jakobsen, M.H. and Boisen, A. 2009. Gold cleaning methods for electrochemical detection applications. *Microelectronic Engineering*. **86**(4–6), pp.1282–1285.

La Flamme, K.E., Popat, K.C., Leoni, L., Markiewicz, E., La Tempa, T.J., Roman, B.B., Grimes, C.A. and Desai, T.A. 2007. Biocompatibility of nanoporous alumina membranes for immunoisolation. *Biomaterials*. **28**(16), pp.2638–2645.

Foubert, A., Beloglazova, N. V., Hedström, M. and De Saeger, S. 2019. Antibody immobilization strategy for the development of a capacitive immunosensor detecting zearalenone. *Talanta*. **191**, pp.202–208.

Garcia-Mutio, D., Gomez-Caballero, A., Guerreiro, A., Piletsky, S., Goicolea, M.A. and Barrio, R.J. 2016. Solid-phase synthesis of imprinted nanoparticles grafted on gold substrates for voltammetric sensing of 4-ethylphenol. *Sensors and Actuators, B: Chemical*. **236**, pp.839–848.

García, R., Fernández, M.T., Pernía, A. and Costa-García, A. 2008. Electrochemical characterization of different screen-printed gold electrodes. *Electrochimica Actca*. **53**, pp.3242–3249.

Gebala, M. and Schuhmann, W. 2010. Controlled orientation of DNA in a binary SAM as a key for the successful determination of DNA hybridization by means of electrochemical impedance spectroscopy. *ChemPhysChem*. **11**(13), pp.2887–2895.

Gibson, D.G., Young, L., Chuang, R.Y., Venter, J.C., Hutchison, C.A. and Smith, H.O. 2009. Enzymatic assembly of DNA molecules up to several hundred kilobases. *Nature Methods*. **6**(5), pp.343–345.

Goode, J., Dillon, G. and Millner, P.A. 2016. The development and optimisation of nanobody based electrochemical immunosensors for IgG. *Sensors and Actuators, B: Chemical*. **234**, pp.478–484.

Greg T. Hermanson 1996. *Bioconjugate Techniques*. 2nd Edition. Elsevier.

Grieshaber, D., MacKenzie, R., Voros, J. and Reimhult, E. 2008. Electrochemical biosensors - sensor principles and architectures. *Kunststoffe International*. **8**(3), pp.1400–1458.

Gschwend, G.C. and Girault, H.H. 2020. Discrete Helmholtz model: a single layer of correlated counter-ions. Metal oxides and silica interfaces, ion-exchange and biological membranes. *Chemical Science*. **11**(38), pp.10304–10312.

Guan, J.-G., Miao, Y.-Q. and Zhang, Q.-J. 2004. Impedimetric biosensors. *Journal of Bioscience and Bioengineering*. **97**(4), pp.219–226.

Guntupalli, R., Lakshmanan, R.S., Johnson, M.L., Hu, J., Huang, T.-S., Barbaree, J.M., Vodyanoy, V.J. and Chin, B.A. 2007. Magnetoelastic biosensor for the detection of *Salmonella typhimurium* in food products. *Sensing and Instrumentation for Food Quality and Safety*. **1**(1), pp.3–10.

Guo, L.H., Facci, J.S., McLendon, G. and Mosher, R. 1994. Effect of Gold Topography and Surface Pretreatment on the Self-Assembly of Alkanethiol Monolayers. *Langmuir*. **10**(12), pp.4588–4593.

Gutiérrez-Zúñiga, G.G. and Hernández-López, J.L. 2016. Sensitivity improvement of a sandwich-type ELISA immunosensor for the detection of different prostate-specific antigen isoforms in human serum using electrochemical impedance spectroscopy and an ordered and hierarchically organized interfacial supramolecu. *Analytica Chimica Acta*. **902**, pp.97–106.

Hai, W., Goda, T., Takeuchi, H., Yamaoka, S., Horiguchi, Y., Matsumoto, A. and Miyahara, Y. 2017. Specific recognition of human influenza virus with pedot bearing sialic acid-terminated trisaccharides. *ACS Applied Materials and Interfaces*. **9**(16), pp.14162–14170.

Hamelin, A. 1996. Cyclic voltammetry at gold single-crystal surfaces. Part 1. Behaviour at low-index faces. *Electroanalytical chemistry*. **407**, pp.1–11.

Hansen, A.G., Mortensen, M.W., Andersen, J.E.T., Ulstrup, J., Kühle, A., Garnæs, J. and Boisen, A. 2001. Stress formation during self-assembly of alkanethiols on differently pre-treated gold surfaces. *Probe Microscopy*. **2**, pp.139–149.

He, F., Zhang, L., Zhao, J., Hu, B. and Lei, J. 2002. A TSM immunosensor for detection of *M. tuberculosis* with a new membrane material. *Sensors and Actuators, B: Chemical*. **85**(3), pp.284–290.

Heise, T. and Dersch, P. 2006. Identification of a domain in *Yersinia* virulence factor YadA that is crucial for extracellular matrix-specific cell adhesion and uptake. *Proceedings of the National Academy of Sciences of the United States of America*. **103**(9), pp.3375–3380.

Hiatt, L.A. and Cliffel, D.E. 2012. Real-time recognition of *Mycobacterium tuberculosis* and lipoarabinomannan using the quartz crystal microbalance. *Sensors and Actuators, B: Chemical*. **174**, pp.245–252.

Hirst, N.A., Hazelwood, L.D., Jayne, D.G. and Millner, P.A. 2013. An amperometric lactate biosensor using H_2O_2 reduction via a Prussian Blue impregnated poly(ethyleneimine) surface on screen printed carbon electrodes to detect anastomotic leak and sepsis. *Sensors and Actuators, B: Chemical*. **186**, pp.674–680.

Hoogvliet, J.C., Dijksma, M., Kamp, B. and Bennekom, W.P. Van 2000. Electrochemical Pretreatment of polycrystalline gold electrodes to produce a reproducible surface roughness for self-assembly : a study in phosphate buffer pH 7.4. *Analytical Chemistry*. **72**(9), pp.2016–2021.

Hou, L., Cui, Y., Xu, M., Gao, Z., Huang, J. and Tang, D. 2013. Graphene oxide-labeled sandwich-type impedimetric immunoassay with sensitive enhancement based on enzymatic 4-chloro-1-naphthol oxidation. *Biosensors and Bioelectronics*. **47**, pp.149–156.

Huck, W.T.S. 2007. Self-assembly meets nanofabrication: recent developments in microcontact printing and dip-pen nanolithography. *Angewandte Chemie - International Edition*. **46**(16), pp.2754–2757.

Ilver, D., Frick, I., Ilver, D., Arnqvist, A., Johan, O., Kersulyte, D., Incecik, E.T., Berg, D.E., Covacci, A., Engstrand, L. and Bore, T. 2012. *Helicobacter pylori* adhesin binding fucosylated histo-blood group antigens revealed by retagging. *Science.* **279**(1998), pp.373–377.

Ilyin, A.M. 2017. *Chapter 11 - Auger Electron Spectroscopy A2 - Thomas, Sabu* [Online]. Elsevier Inc. Available from: https://www.sciencedirect.com/science/article/pii/B9780323461412000110.

Ishida, T., Tsuneda, S., Nishida, N., Hara, M., Sasabe, H. and Knoll, W. 1997. Surface-conditioning effect of gold substrates on octadecanethiol self-assembled monolayer growth. *Langmuir*. **13**(17), pp.4638–4643.

Izumi, T., Watanabe, I. and Yokoyama, Y. 1991. Activation of a gold electrode by electrochemical oxidation-reduction pretreatment in hydrochloric acid. *Journal of Electroanalytical Chemistry*. **303**, pp.151–160.

J.C.Hoogvliet, C.M.B.van den Beld, C.J.van der Poel, W.P. va. B. 1986. Influence of polishing and of electrochemical pretreatment on the performance of glassy-carbon electrodes in electrochemical detection. *Journal of Electroanalytical Chemistry*. **201**, pp.11–21.

Jadhav, S.A., Biji, P., Panthalingal, M.K., Murali Krishna, C., Rajkumar, S., Joshi, D.S. and Sundaram, N. 2021. Development of integrated microfluidic platform coupled with Surface-enhanced Raman Spectroscopy for diagnosis of COVID-19. *Medical Hypotheses*. **146**, 110356.

Jafari, H., Amiri, M., Abdi, E., Navid, S.L., Bouckaert, J., Jijie, R., Boukherroub, R. and Szunerits, S. 2019. Entrapment of uropathogenic *E. coli* cells into ultra-thin sol-gel matrices on gold thin films: A low cost alternative for impedimetric bacteria sensing. *Biosensors and Bioelectronics*. **124–125**(October 2018), pp.161–166.

Jarocka, U., Wasowicz, M., Radecka, H., Malinowski, T., Michalczuk, L. and Radecki, J. 2011. Impedimetric immunosensor for detection of plum pox virus in plant extracts. *Electroanalysis*. **23**(9), pp.2197–2204.

Jean, H., Saha, T., Tey, T., Siang, W. and Wei, C. 2020. Quartz crystal microbalance-based biosensors as rapid diagnostic devices for infectious diseases. *Biosensors and Bioelectronics*. **168**, 112513.

Rushworth, J.V., Ahmed, A and Millner P.A. 2013. Midland Blotting: a rapid, semi-quantitative method for biosensor surface characterization. *Journal of Biosensors & Bioelectronics*. **04**(05).

Johari-Ahar, M., Rashidi, M.R., Barar, J., Aghaie, M., Mohammadnejad, D., Ramazani, A., Karami, P., Coukos, G. and Omidi, Y. 2015. An ultra-sensitive impedimetric immunosensor for detection of the serum oncomarker CA-125 in ovarian cancer patients. *Nanoscale*. **7**(8), pp.3768–3779.

John Ho, L.S., Fogel, R. and Limson, J.L. 2020. Generation and screening of histamine-specific aptamers for application in a novel impedimetric aptamer-based sensor. *Talanta*. **208**, p.120474.

Joung, C.K., Kim, H.N., Im, H.C., Kim, H.Y., Oh, M.H. and Kim, Y.R. 2012. Ultra-sensitive detection of pathogenic microorganism using surface-engineered impedimetric immunosensor. *Sensors and Actuators, B: Chemical*. **161**(1), pp.824–831.

Joung, C.K., Kim, H.N., Lim, M.C., Jeon, T.J., Kim, H.Y. and Kim, Y.R. 2013. A nanoporous membrane-based impedimetric immunosensor for label-free detection of pathogenic bacteria in whole milk. *Biosensors and Bioelectronics*. **44**(1), pp.210–215.

Kadara, R.O., Jenkinson, N. and Banks, C.E. 2009. Characterisation of commercially available electrochemical sensing platforms. *Sensors and Actuators, B: Chemical*. **138**(2), pp.556–562.

Kanayeva, D.A., Wang, R., Rhoads, D., Erf, G.F., Slavik, M.F., Tung, S. and Li, Y. 2012. Efficient separation and sensitive detection of *Listeria monocytogenes* using an impedance immunosensor based on magnetic nanoparticles, a microfluidic chip, and an interdigitated microelectrode. *Journal of Food Protection*. **75**(11), pp.1951–1959.

Kang, J. and Rowntree, P.A. 2007. Gold film surface preparation for self-assembled monolayer studies. *Langmuir*. **23**(2), pp.509–516.

Kaper, J.B., Nataro, J.P. and Mobley, H.L.T. 2004. Pathogenic *Escherichia coli*. *Nature Reviews Microbiology*. **2**(2), pp.123–140.

Kayali, G., Ahmed, K., El-Shesheny, R., Kayed, A., Maatouq, A., Cai, Z., McKenzie, P., Webby, R., El Rafaey, S., Kandeel, A. and Ali, M. 2016. Avian Influenza A(H5N1) Virus in Egypt. *Emerging Infectious Diseases*. **22**(3), pp.379–388.

Kelley, S.O., Barton, J.K., Jackson, N.M. and Hill, M.G. 1997. Electrochemistry of methylene blue bound to a DNA-modified electrode. *Bioconjugate Chemistry*. **8**(1), pp.31–37.

Khan, R., Pal, M., Kuzikov, A. V., Bulko, T., Suprun, E. V. and Shumyantseva, V. V. 2016. Impedimetric immunosensor for detection of cardiovascular disorder risk biomarker. *Materials Science and Engineering C*. **68**, pp.52–58.

Kim, J., Woo, Y.Y., Moon, J. and Kim, B. 2008. A new wideband adaptive digital predistortion technique employing feedback linearization. *IEEE Transactions on Microwave Theory and Techniques*. **56**(2), pp.385–392.

Kohli, R. 2019. *Applications of UV-Ozone Cleaning Technique for Removal of Surface Contaminants* [Online]. Elsevier Inc. Available from: http://dx.doi.org/10.1016/B978-0-12-815577-6.00009-8.

Kokkinos, C., Economou, A. and Prodromidis, M.I. 2016. Electrochemical immunosensors: Critical survey of different architectures and transduction strategies. *TrAC - Trends in Analytical Chemistry*. **79**, pp.88–105.

Kudinha, T. 2017. The pathogenesis of *Escherichia coli* urinary tract infection. IntechOpen. *Intech*.

Kuralay, F., Campuzano, S., Haake, D.A. and Wang, J. 2011. Highly sensitive disposable nucleic acid biosensors for direct bioelectronic detection in raw biological samples. *Talanta*. **85**(3), pp.1330–1337.

Kveton, F., Blšáková, A., Hushegyi, A., Damborsky, P., Blixt, O., Jansson, B. and Tkac, J. 2017. Optimization of the small glycan presentation for binding a tumor-associated antibody: application to the construction of an ultrasensitive glycan biosensor. *Langmuir*. **33**(11), pp.2709–2716.

L.D. Burke and T.A M. Twomey 1984. Voltammetric behaviour of nickel in base with particular reference to thick oxide growth. *Journal of Electroanalytical Chemistry*. **162**, pp.101–119.

Lamas-ardisana, P.J., Fanjul-bolado, P. and Costa-garcía, A. 2015. Hydrogen evolution : electrochemical pretreatment for voltammetric analysis with gold electrodes short communication. *Electroanalysis.* **27**, pp.1073–1077.

Lan, Y. bin, Wang, S. zhou, Yin, Y. guang, Hoffmann, W.C. and Zheng, X. zhe 2008. Using a surface plasmon resonance biosensor for rapid detection of salmonella typhimurium in chicken carcass. *Journal of Bionic Engineering*. **5**(3), pp.239–246.

Laxminarayan, R., Duse, A., Wattal, C., Zaidi, A.K.M., Wertheim, H.F.L., Sumpradit, N., Vlieghe, E., Hara, G.L., Gould, I.M., Goossens, H., Greko, C., So, A.D., Bigdeli, M., Tomson, G., Woodhouse, W., Ombaka, E., Peralta, A.Q., Qamar, F.N., Mir, F., Kariuki, S., Bhutta, Z.A., Coates, A., Bergstrom, R., Wright, G.D., Brown, E.D. and Cars, O. 2013. Antibiotic resistance-the need for global solutions. *The Lancet Infectious Diseases*. **13**(12), pp.1057–1098.

Lefort, A., Panhard, X., Clermont, O., Woerther, P.L., Branger, C., Mentré, F., Fantin, B., Wolff, M. and Denamur, E. 2011. Host factors and portal of entry outweigh bacterial determinants to predict the severity of *Escherichia coli* bacteremia. *Journal of Clinical Microbiology*. **49**(3), pp.777–783.

Lei, K.F. 2012. Microfluidic systems for diagnostic applications: A review. *Journal of Laboratory Automation*. **17**(5), pp.330–347.

Leo, J.C., Elovaara, H., Bihan, D., Pugh, N., Kilpinen, S.K., Raynal, N., Skurnik, M., Farndale, R.W. and Goldman, A. 2010. First analysis of a bacterial collagen-binding protein with collagen toolkits: Promiscuous binding of YadA to collagens may explain how YadA interferes with host processes. *Infection and Immunity*. **78**(7), pp.3226–3236.

Leo, J.C., Elovaara, H., Brodsky, B., Skurnik, M. and Goldman, A. 2008. The *Yersinia* adhesin YadA binds to a collagenous triple-helical conformation but without sequence specificity. *Protein Engineering, Design and Selection*. **21**(8), pp.475–484.

Leo, J.C., Grin, I. and Linke, D. 2012. Type V secretion: Mechanism(S) of autotransport through the bacterial outer membrane. *Philosophical Transactions of the Royal Society B: Biological Sciences*. **367**(1592), pp.1088–1101.

Leung, J.M. and Gallant, C.V. 2014. *Infections due to Escherichia and Shigella* [Online]. Elsevier Inc. Available from: http://dx.doi.org/10.1016/B978-0-12-801238-3.05090-X.

Leva-bueno, J., Meuskens, I., Linke, D., Millner, P.A. and Peyman, S.A. 2022. A novel, proof-of-concept electrochemical impedimetric biosensor based on extracellular matrix protein–

adhesin interaction. *Sensors & Diagnostics, in the press*. DOI:10.1039/d2sd00075j

Leva-Bueno, J., Peyman, S.A. and Millner, P.A. 2020. A review on impedimetric immunosensors for pathogen and biomarker detection. *Medical Microbiology and Immunology*. **209**(3), pp.343–362.

Li, G., Zhu, M., Ma, L., Yan, J., Lu, X., Shen, Y. and Wan, Y. 2016. Generation of small single domain nanobody binders for sensitive detection of testosterone by electrochemical impedance spectroscopy. *ACS Applied Materials and Interfaces*. **8**(22), pp.13830–13839.

Li, J., Wu, Z., Wang, H., Shen, G. and Yu, R. 2005. A reusable capacitive immunosensor with a novel immobilization procedure based on 1,6-hexanedithiol and nano-Au self-assembled layers. *Sensors and Actuators, B: Chemical*. **110**(2), pp.327–334.

Li, Z., Fu, Y., Fang, W. and Li, Y. 2015. Electrochemical impedance immunosensor based on self-assembled monolayers for rapid detection of *Escherichia coli* O157:H7 with signal amplification using lectin. *Sensors*. **15**(8), pp.19212–19224.

Li, Z., Zhang, L., Zeng, S., Zhang, M., Du, E. and Li, B. 2014. Effect of surface pretreatment on self-assembly of thiol-modified DNA monolayers on gold electrode. *JOURNAL OF ELECTROANALYTICAL CHEMISTRY*. **722–723**, pp.131–140.

Liao, S., He, Y., Chu, Y., Liao, H. and Wang, Y. 2019. Solvent-resistant and fully recyclable perfluoropolyether-based elastomer for microfluidic chip fabrication. *Journal of Materials Chemistry A*. **7**(27), pp.16249–16286.

Lim, J.Y., Yoon, J.W. and Hovde, C.J. 2010. A brief overview of *Escherichia coli* O157:H7 and its plasmid O157. *Journal of Microbiology and Biotechnology*. **20**(1), pp.1–10.

Lima, D., Inaba, J., Clarindo Lopes, L., Calaça, G.N., Los Weinert, P., Lenzi Fogaça, R., Ferreira de Moura, J., Magalhães Alvarenga, L., Cavalcante de Figueiredo, B., Wohnrath, K. and Andrade Pessôa, C. 2019. Label-free impedimetric immunosensor based on arginine-functionalized gold nanoparticles for detection of DHEAS, a biomarker of pediatric adrenocortical carcinoma. *Biosensors and Bioelectronics*. **133**, pp.86–93.

Lin, D., Tang, T., Jed Harrison, D., Lee, W.E. and Jemere, A.B. 2015. A regenerating ultrasensitive electrochemical impedance immunosensor for the detection of adenovirus. *Biosensors and Bioelectronics*. **68**, pp.129–134.

Lin, J., Wang, R., Jiao, P., Li, Yuntao, Li, Yanbin, Liao, M., Yu, Y. and Wang, M. 2015. An impedance immunosensor based on low-cost microelectrodes and specific monoclonal antibodies for rapid detection of avian influenza virus H5N1 in chicken swabs. *Biosensors and Bioelectronics*. **67**, pp.546–552.

Linke, D., Riess, T., Autenrieth, I.B., Lupas, A. and Kempf, V.A.J. 2006. Trimeric autotransporter adhesins: variable structure, common function. *Trends in Microbiology*. **14**(6), pp.264–270.

Li, Z. Niu, T. Zhang, Z. Feng, G. Bi, S. 2012. Effect of monovalent cations (Li + , Na + , K + , Cs +) on self-assembly of thiol-modified double-stranded and single-stranded DNA on gold electrode. *Analyst.* **137**, pp.1680–1691.

Li, Z. Niu, T. Zhang, Z. Chen, R. Feng, G. Bi, S. 2011. Electrochemical studies on the permeable characteristics of thiol-modified double-stranded DNA self-assembled monolayers on gold. *Analyst.* **136**, pp.2090–2099.

Lis, H. and Sharon, N. 1998. Lectins: Carbohydrate-specific proteins that mediate cellular recognition. *Chemical Reviews*. **98**(2), pp.637–674.

Liu, M.Q., Jiang, J.H., Feng, Y.L., Shen, G.L. and Yu, R.Q. 2007. Glucose biosensor based on immobilization of glucose oxidase in electrochemically polymerized polytyramine film and overoxidised polypyrrole film on platinized carbon paste electrode. *Chinese Journal of*

Analytical Chemistry. **35**(10), pp.1435–1438.

Loaiza, Ó.A., Campuzano, S., Pedrero, M. and Pingaron, J.M. 2008. Designs of enterobacteriaceae lac Z gene DNA gold screen printed biosensors. *Electroanalysis*. **20**(13), pp.1397–1405.

Lu, L., Chee, G., Yamada, K. and Jun, S. 2013. Electrochemical impedance spectroscopic technique with a functionalized microwire sensor for rapid detection of foodborne pathogens. *Biosensors and Bioelectronics*. **42**(1), pp.492–495.

Lvovich, V.F. 2012. *Impedance Spectroscopy: Applications to Electrochemical and Dielectric Phenomena*. John Wiley & Sons, inc.

M. Barreiros dos Santos, J.P. Agusil, B. Prieto-Simon, C. Sporer, V. Teixeira, J.S. 2013. Highly sensitive detection of pathogen *Escherichia coli* O157:H7 by electrochemical impedance spectroscopy. *Biosensors and Bioelectronics*. **45**(1), pp.174–180.

Mahdavi, J., Sonde, B., Olfat, F.O., Forsberg, L., Roche, N., Larsson, T., Teneberg, S., Karlsson, K., Altraja, S., Wadstro, T., Kersulyte, D., Berg, D.E., Dubois, A., Petersson, C., Magnusson, K. and Norberg, T. 2007. *Helicobacter pylori* SabA adhesin in persistent infection and chronic inflammation. *Science*. **573**(2002), pp.573–579.

Mahjoub-Messai, F., Bidet, P., Caro, V., Diancourt, L., Biran, V., Aujard, Y., Bingen, E. and Bonacorsi, S. 2011. *Escherichia coli* isolates causing bacteremia via gut translocation and urinary tract infection in young infants exhibit different virulence genotypes. *Journal of Infectious Diseases*. **203**(12), pp.1844–1849.

Makaraviciute, A., Xu, X., Nyholm, L. and Zhang, Z. 2017. systematic approach to the development of microfabricated biosensors: relationship between gold surface pretreatment and thiolated molecule binding. *ACS Applied Materials & Interfaces*. **9**, pp.26610–26621.

Malvano, F., Pilloton, R. and Albanese, D. 2018. Sensitive detection of *Escherichia coli* O157:H7 in food products by impedimetric immunosensors. *Sensors*. **18**(7), pp.1–11.

Metkar, S.K. and Girigoswami, K. 2019. Diagnostic biosensors in medicine – A review. *Biocatalysis and Agricultural Biotechnology*. **17**(October 2018), pp.271–283.

Metrohm Dropsens n.d. No Title. *Electrodes*. [Online]. [Accessed 9 February 2020]. Available from: http://www.dropsens.com/en/faqs_dropsens.html.

Meuskens, I., Leva-bueno, J., Millner, P., Schütz, M., Peyman, S.A. and Linke, D. 2022. The trimeric autotransporter adhesin YadA of *Yersinia enterocolitica* serotype O : 9 binds glycan moieties. *Frontiers in Microbiology*. **12**(February), pp.1–12.

Meuskens, I., Saragliadis, A., Leo, J.C. and Linke, D. 2019. Type V secretion systems: An overview of passenger domain functions. *Frontiers in Microbiology*. **10**, pp.1–19.

Micrux Technologies n.d. No Title. [Accessed 9 February 2020]. Available from: https://www.micruxfluidic.com/en/shop/electrochemical-solutions/thin-film-electrochemical-sensors/single-electrodes-se/.

Mirsaleh-Kohan, N., Bass, A.D. and Sanche, L. 2010. X-ray photoelectron spectroscopy analysis of gold surfaces after removal of thiolated DNA oligomers by ultraviolet/ozone treatment. *Langmuir*. **26**(9), pp.6508–6514.

Mishra, S.K., Srivastava, A.K., Kumar, D. and Rajesh 2014. Bio-functionalized Pt nanoparticles based electrochemical impedance immunosensor for human cardiac myoglobin. *RSC Advances*. **4**(41), pp.21267–21276.

Monošík, R., Streďanský, M. and Šturdík, E. 2012. Biosensors - classification, characterization and new trends. *Acta Chimica Slovaca*. **5**(1), pp.109–120.

Monteiro, M.C.O. and Koper, M.T.M. 2019. Alumina contamination through polishing and its effect on hydrogen evolution on gold electrodes. *Electrochimica Acta*. **325**, p.134915.

Montrose, A., Cargou, S., Nepveu, F., Manczak, R., Gué, A.M. and Reybier, K. 2013. Impedimetric immunosensor for the detection of circulating pro-inflammatory monocytes as infection markers. *Biosensors and Bioelectronics*. **49**, pp.305–311.

Mossanha, R., Soc, J.E., Mossanha, R., Ramos, M.K., Santos, C.S. and Andrade, C. 2015. Mixed self-assembled monolayers of mercaptoundecanoic acid and thiolactic acid for the construction of an enzymatic biosensor for hydroquinone determination. *Journal of the Electrochemical Society*. **162**(7), pp.145–151

Motaghedifard, M., Behpour, M. and Ghoreishi, S.M. 2014. Sensors and Actuators B : Chemical self-assembling monolayer of Schiff ' s base formed between o-methoxyphenyl methyl ketone and 2-aminothiophenol at the surface of gold electrode for electrochemical impedimetric sensing of uranyl cations. *Sensors & Actuators: B. Chemical*. **203**, pp.802–811.

Mühlenkamp, M., Oberhettinger, P., Leo, J.C., Linke, D. and Schütz, M.S. 2015. *Yersinia* adhesin A (YadA) - Beauty & beast. *International Journal of Medical Microbiology*. **305**(2), pp.252–258.

Mühlenkamp, M.C., Hallström, T., Autenrieth, I.B., Bohn, E., Linke, D., Rinker, J., Riesbeck, K., Singh, B., Leo, J.C., Hammerschmidt, S., Zipfel, P.F. and Schütz, M.S. 2017. Vitronectin binds to a specific stretch within the head region of *yersinia* adhesin a and thereby modulates *Yersinia enterocolitica* host interaction. *Journal of Innate Immunity*. **9**(1), pp.33–51.

Muyzer, G. and Stams, A.J.M. 2008. The ecology and biotechnology of sulphate-reducing bacteria. *Nature Reviews Microbiology*. **6**(6), pp.441–454.

Nanduri, V., Bhunia, A.K., Tu, S.I., Paoli, G.C. and Brewster, J.D. 2007. SPR biosensor for the detection of *L. monocytogenes* using phage-displayed antibody. *Biosensors and Bioelectronics*. **23**(2), pp.248–252.

Naomi, R., Ridzuan, P.M. and Bahari, H. 2021. Current insights into collagen type i. *Polymers*. **13**(16), pp.1–19.

Naresh, V. and Lee, N. 2021. A review on biosensors and recent development of nanostructured materials-enabled biosensors. *Sensors*. **21**(4), pp.1–35.

Narimani, R., Azizi, M., Esmaeili, M., Rasta, S.H. and Khosroshahi, H.T. 2020. An optimal method for measuring biomarkers: colorimetric optical image processing for determination of creatinine concentration using silver nanoparticles. *3 Biotech*. **10**(10), pp.1–9.

Ndiaye, A.L., Delile, S., Brunet, J., Varenne, C. and Pauly, A. 2016. Electrochemical sensors based on screen-printed electrodes: The use of phthalocyanine derivatives for application in VFA Detection. *Biosensors*. **6**(3).

Nge, P.N., Rogers, C.I. and Woolley, A.T. 2013. Advances in micro fluidic materials, functions, integration, and applications. *Chemical Reviews*. **113**, pp.2550–2583

Nguyen, H.H., Lee, S.H., Lee, U.J., Fermin, C.D. and Kim, M. 2019. Immobilized enzymes in biosensor applications. *Materials*. **12**(1), pp.1–34.

Nguyen, H.H., Park, J., Kang, S. and Kim, M. 2015. Surface plasmon resonance: A versatile technique for biosensor applications. *Sensors*. **15**(5), pp.10481–10510.

Nguyen, P.D., Tran, T.B., Nguyen, D.T.X. and Min, J. 2014. Magnetic silica nanotube-assisted impedimetric immunosensor for the separation and label-free detection of *Salmonella typhimurium*. *Sensors and Actuators, B: Chemical*. **197**, pp.314–320.

Nguyen, T.Q. and Breitkopf, C. 2018. Determination of diffusion coefficients using impedance spectroscopy data. *Journal of The Electrochemical Society*. **165**(14), pp.826–831.

Niculescu, A.G., Chircov, C., Bîrcă, A.C. and Grumezescu, A.M. 2021. Fabrication and applications of microfluidic devices: A review. *International Journal of Molecular Sciences*. **22**(4), pp.1–26.

Nielsen, J.B., Hanson, R.L., Almughamsi, H.M., Pang, C., Fish, T.R. and Woolley, A.T. 2020. Microfluidics: innovations in materials and their fabrication and functionalization. *Analytical Chemistry*. **92**(1), pp.150–168.

Nishi, K., Isobe, S.I., Zhu, Y. and Kiyama, R. 2015. Fluorescence-based bioassays for the detection and evaluation of food materials. *Sensors*. **15**(10), pp.25831–25867.

Nummelin, H., Merckel, M.C., Leo, J.C., Lankinen, H., Skurnik, M. and Goldman, A. 2004. The *Yersinia* adhesin YadA collagen-binding domain structure is a novel left-handed parallel β-roll. *EMBO Journal*. **23**(4), pp.701–711.

Nummelin, H., El Tahir, Y., Ollikka, P., Skurnik, M. and Goldman, A. 2002. Expression, purification and crystallization of a collagen-binding fragment of *Yersinia* adhesin YadA. *Acta Crystallographica Section D: Biological Crystallography*. **58**(6 II), pp.1042–1044.

Nuzzo, R.G. and Allara, D.L. 1983. Adsorption of bifunctional organic disulfides on gold surfaces. *Journal of the American Chemical Society*. **105**(13), pp.4481–4483.

O'Neill, J. 2016. Tackling drug-resistant infections globally: final report and recommendations. *Review on Antimicrobial Resistance*.

Oblath, E.A., Henley, W.H., Alarie, J.P. and Ramsey, J.M. 2013. A microfluidic chip integrating DNA extraction and real-time PCR for the detection of bacteria in saliva. *Lab on a Chip*. **13**(7), pp.1325–1332.

Ogończyk, D., Wgrzyn, J., Jankowski, P., Dąbrowski, B. and Garstecki, P. 2010. Bonding of microfluidic devices fabricated in polycarbonate. *Lab on a Chip*. **10**(10), pp.1324–1327.

van Oss, C.J., Good, R.J. and Chaudhury, M.K. 2002. Nature of the antigen-antibody interaction. *Journal of Chromatography B: Biomedical Sciences and Applications*. **376**, pp.111–119.

Pagliarini, V., Neagu, D., Scognamiglio, V., Pascale, S., Scordo, G., Volpe, G., Delibato, E., Pucci, E., Notargiacomo, A., Pea, M., Moscone, D. and Arduini, F. 2019. Treated gold screen-printed electrode as disposable platform for label-free immunosensing of *Salmonella typhimurium*. *Electrocatalysis*. **10**(4), pp.288–294.

Pal, N., Sharma, S. and Gupta, S. 2016. Sensitive and rapid detection of pathogenic bacteria in small volumes using impedance spectroscopy technique. *Biosensors and Bioelectronics*. **77**, pp.270–276.

Pan, L.J., Tu, J.W., Ma, H.T., Yang, Y.J., Tian, Z.Q., Pang, D.W. and Zhang, Z.L. 2018. Controllable synthesis of nanocrystals in droplet reactors. *Lab on a Chip*. **18**(1), pp.41–56.

Park, J.H., Cho, Y.W. and Kim, T.H. 2022. Recent advances in surface plasmon resonance sensors for sensitive optical detection of pathogens. *Biosensors*. **12**(3).

Patinglag, L., Esfahani, M.M.N., Ragunathan, K., He, P., Brown, N.J., Archibald, S.J., Pamme, N. and Tarn, M.D. 2020. On-chip electrochemical detection of glucose towards the miniaturised quality control of carbohydrate-based radiotracers. *Analyst*. **145**(14), pp.4920–4930.

Peyman, S.A., Iles, A. and Pamme, N. 2009. Mobile magnetic particles as solid-supports for rapid surface-based bioanalysis in continuous flow. *Lab on a Chip*. **9**(21), pp.3110–3117.

PINE Research 2016. No Title. [Accessed 9 February 2020]. Available from:

https://pineresearch.com/shop/wp-content/uploads/sites/2/2016/10/DRP10036-Screen-Printed-Electrodes-Overview-REV004.pdf.

Pisoschi, A.M. 2016. Potentiometric biosensors: concept and analytical applications-an editorial. *Biochemistry & Analytical Biochemistry*. **5**(3), pp.19–20.

Pizarro-Cerdá, J. and Cossart, P. 2006. Bacterial adhesion and entry into host cells. *Cell*. **124**(4), pp.715–727.

Pournaras, A. V., Koraki, T. and Prodromidis, M.I. 2008. Development of an impedimetric immunosensor based on electropolymerized polytyramine films for the direct detection of *Salmonella typhimurium* in pure cultures of type strains and inoculated real samples. *Analytica Chimica Acta*. **624**(2), pp.301–307.

Promdromidis, M.I. 2010. Impedimetric immunosensors-A review. *Electrochimica Acta*. **55**(14), pp.4227–4233.

Qi, X., Chen, T., Lu, D. and Chen, B. 2017. Graphene-Au nanoparticle based electrochemical immunosensor for fish pathogen Aphanomyces invadans detection. *Fullerenes Nanotubes and Carbon Nanostructures*. **25**(1), pp.12–16.

Quan, X., Fischer, L.M., Boisen, A. and Tenje, M. 2011. Development of nanoporous gold electrodes for electrochemical applications. *Microelectronic Engineering*. **88**(8), pp.2379–2382.

Rabenstein, D.L. 2002. Heparin and heparan sulfate: Structure and function. *Natural Product Reports*. **19**(3), pp.312–331.

Radi, A.E., Muñoz-Berbel, X., Cortina-Puig, M. and Marty, J.L. 2009. An electrochemical immunosensor for ochratoxin A based on immobilization of antibodies on diazonium-functionalized gold electrode. *Electrochimica Acta*. **54**(8), pp.2180–2184.

Raghuraman, H., Chatterjee, S. and Das, A. 2019. Site-directed fluorescence approaches for dynamic structural biology of membrane peptides and proteins. *Frontiers in Molecular Biosciences*. **6**, pp.1–25.

Raiber, K., Terfort, A., Benndorf, C., Krings, N. and Strehblow, H.H. 2005. Removal of self-assembled monolayers of alkanethiolates on gold by plasma cleaning. *Surface Science*. **595**(1–3), pp.56–63.

Rajesh, Sharma, V., Tanwar, V.K., Mishra, S.K. and Biradar, A.M. 2010. Electrochemical impedance immunosensor for the detection of cardiac biomarker Myogobin (Mb) in aqueous solution. *Thin Solid Films*. **519**(3), pp.1167–1170.

Randviir, E.P. and Banks, C.E. 2013. Electrochemical impedance spectroscopy: An overview of bioanalytical applications. *Analytical Methods*. **5**(5), pp.1098–1115.

Rivet, C., Lee, H., Hirsch, A., Hamilton, S. and Lu, H. 2011. Microfluidics for medical diagnostics and biosensors. *Chemical Engineering Science*. **66**(7), pp.1490–1507.

Rodriguez-Mateos, P., Ngamsom, B., Dyer, C.E., Iles, A. and Pamme, N. 2021. Inertial focusing of microparticles, bacteria, and blood in serpentine glass channels. *Electrophoresis*. **42**(21–22), pp.2246–2255.

Ron, H., Matlis, S. and Rubinstein, I. 1998. Self-assembled monolayers on oxidized metals. 2. Gold surface oxidative pretreatment, monolayer properties, and depression formation. *Langmuir*. **14**(5), pp.1116–1121.

Rosales-Rivera, L.C., Acero-Sánchez, J.L., Lozano-Sánchez, P., Katakis, I. and O'Sullivan, C.K. 2011. Electrochemical immunosensor detection of antigliadin antibodies from real human serum. *Biosensors and Bioelectronics*. **26**(11), pp.4471–4476.

Rushworth, J. V, Ahmed, A. and Millner, P.A. 2013. Midland Blotting: a rapid, semi-quantitative method for biosensor surface characterization. *Journal of Biosensors & Bioelectronics*. **04**(05).

Rushworth, J. V., Ahmed, A., Griffiths, H.H., Pollock, N.M., Hooper, N.M. and Millner, P.A. 2014. A label-free electrical impedimetric biosensor for the specific detection of Alzheimer's amyloid-beta oligomers. *Biosensors and Bioelectronics*. **56**, pp.83–90.

Rushworth, J. V., Hirst, N.A. and Goode, J.A. 2013. *Impedimetric Biosensors for Medical Applications: Current Progress and Challenges*. New York, USA: ASME Press.

Sakamoto, S., Putalun, W., Vimolmangkang, S., Phoolcharoen, W., Shoyama, Y., Tanaka, H. and Morimoto, S. 2018. Enzyme-linked immunosorbent assay for the quantitative/qualitative analysis of plant secondary metabolites. *Journal of Natural Medicines*. **72**(1), pp.32–42.

Sanzò, G., Taurino, I., Puppo, F., Antiochia, R., Gorton, L., Favero, G., Mazzei, F., Carrara, S. and De Micheli, G. 2017. A bimetallic nanocoral Au decorated with Pt nanoflowers (bio)sensor for H_2O_2 detection at low potential. *Methods*. **129**, pp.89–95.

Saragliadis, A. and Linke, D. 2019. Assay development for the discovery of small-molecule inhibitors of YadA adhesion to collagen. *Cell Surface*. **5**, p.100025.

Schultsz, C., Van den Ende, J., Cobelens, F., Vervoort, T., Van Gompel, A., Wetsteyn, J.C.F.M. and Dankert, J. 2000. Diarrheagenic *Escherichia coli* and acute and persistent diarrhea in returned travelers. *Journal of Clinical Microbiology*. **38**(10), pp.3550–3554.

Senior, B.W. 1997. Media and tests to simplify the recognition and identification of members of the Proteeae. *Journal of Medical Microbiology*. **46**(1), pp.39–44.

Seymour, J.P., Langhals, N.B., Anderson, D.J. and Kipke, D.R. 2011. Novel multi-sided, microelectrode arrays for implantable neural applications. *Biomedical Microdevices*. **13**(3), pp.441–451.

Shabani, A., Zourob, M., Allain, B., Marquette, C.A., Lawrence, M.F. and Mandeville, R. 2008. Bacteriophage-modified microarrays for the direct impedimetric detection of bacteria. *Analytical Chemistry*. **80**(24), pp.9475–9482.

Shamsuddin, S.H. 2018. Biosensors for detection of colorectal cancer. *PhD thesis, University of Leeds, Leeds.*

Shamsuddin, S.H., Gibson, T.D., Tomlinson, D.C., McPherson, M.J., Jayne, D.G. and Millner, P.A. 2021. Reagentless Affimer- and antibody-based impedimetric biosensors for CEA-detection using a novel non-conducting polymer. *Biosensors and Bioelectronics*. **178**, p.113013.

Shoulders, M.D. and Raines, R.T. 2009. Collagen structure and stability. *Annual Review of Biochemistry*. **78**, pp.929–958.

Shrivastav, A.M., Cvelbar, U. and Abdulhalim, I. 2021. A comprehensive review on plasmonic-based biosensors used in viral diagnostics. *Communications Biology*. **4**(1), pp.1–12.

Song, S., Wang, L., Li, J., Fan, C. and Zhao, J. 2008. Aptamer-based biosensors. *TrAC - Trends in Analytical Chemistry*. **27**(2), pp.108–117.

St, L., Ho, J., Limson, J.L. and Fogel, R. 2019. Certain methods of electrode pretreatment create misleading responses in impedimetric aptamer biosensors. *ACS Omega*. **4**, pp.5839–5847.

Stan, Dana, Mirica, A.C., Iosub, R., Stan, Diana, Mincu, N.B., Gheorghe, M., Avram, M., Adiaconita, B., Craciun, G. and Mateescu, A.L.B. 2022. What is the optimal method for cleaning screen-printed electrodes? *Processes*. **10**(4), 723.

Steeland, S., Vandenbroucke, R.E. and Libert, C. 2016. Nanobodies as therapeutics: Big opportunities for small antibodies. *Drug Discovery Today*. **21**(7), pp.1076–1113.

Su, H., Li, S., Terebiznik, M., Guyard, C. and Kerman, K. 2018. Biosensors for the detection of interaction between *Legionella pneumophila* collagen-like protein and glycosaminoglycans. *Sensors*. **18**(8).

Sun, S.G., Clavilier, J. and Bewick, A. 1988. The mechanism of electrocatalytic oxidation of formic acid on Pt (100) and Pt (111) in sulphuric acid solution: an emirs study. *Journal of Electroanalytical Chemistry*. **240**(1–2), pp.147–159.

El Tahir, Y. and Skurnik, M. 2001. YadA, the multifaceted *Yersinia* adhesin. *International Journal of Medical Microbiology*. **291**(3), pp.209–218.

Tan, F., Leung, P.H.M., Liu, Z. Bin, Zhang, Y., Xiao, L., Ye, W., Zhang, X., Yi, L. and Yang, M. 2011. A PDMS microfluidic impedance immunosensor for *E. coli* O157:H7 and Staphylococcus aureus detection via antibody-immobilized nanoporous membrane. *Sensors and Actuators, B: Chemical*. **159**(1), pp.328–335.

Taylor, A.D., Yu, Q., Chen, S., Homola, J. and Jiang, S. 2005. Comparison of *E. coli* O157:H7 preparation methods used for detection with surface plasmon resonance sensor. *Sensors and Actuators, B: Chemical*. **107**, pp.202–208.

Tercero, N., Wang, K., Gong, P. and Levicky, R. 2009. Morpholino monolayers: Preparation and label-free DNA analysis by surface hybridization. *Journal of the American Chemical Society*. **131**(13), pp.4953–4961.

Thakur, O.P. and Singh, A.K. 2008. Application of various physical laws and its suitability at Interface in nanometric dielectrics. *International Journal of Material Science*. **3**(2), pp.105–111.

Thangsunan, P. 2018. Affimer-based impedimetric biosensors: the new analytical platform for biorecognition applications. *PhD thesis, University of Leeds, Leeds.*

Thomas, J.P., Zhao, L., Ding, K., Heinig, N.F. and Leung, K.T. 2012. Near-surface oxidized sulfur modifications and self-assembly of thiol-modified aptamer on Au thin film substrates influenced by piranha treatment. *ACS Applied Materials and Interfaces*. **4**(11), pp.5945–5948.

Tiede, C., Bedford, R., Heseltine, S.J., Smith, G., Wijetunga, I., Ross, R., Alqallaf, D., Roberts, A.P.E., Balls, A., Curd, A., Hughes, R.E., Martin, H., Needham, S.R., Zanetti-Domingues, L.C., Sadigh, Y., Peacock, T.P., Tang, A.A., Gibson, N., Kyle, H., Platt, G.W., Ingram, N., Taylor, T., Coletta, L.P., Manfield, I., Knowles, M., Bell, S., Esteves, F., Maqbool, A., Prasad, R.K., Drinkhill, M., Bon, R.S., Patel, V., Goodchild, S.A., Martin-Fernandez, M., Owens, R.J., Nettleship, J.E., Webb, M.E., Harrison, M., Lippiat, J.D., Ponnambalam, S., Peckham, M., Smith, A., Ferrigno, P.K., Johnson, M., McPherson, M.J. and Tomlinson, D.C. 2017. Affimer proteins are versatile and renewable affinity reagents. *eLife*. **6**(c), pp.1–35.

Tiede, C., Tang, A.A.S., Deacon, S.E., Mandal, U., Nettleship, J.E., Owen, R.L., George, S.E., Harrison, D.J., Owens, R.J., Tomlinson, D.C. and McPherson, M.J. 2014. Adhiron: A stable and versatile peptide display scaffold for molecular recognition applications. *Protein Engineering, Design and Selection*. **27**(5), pp.145–155.

Tkac, J. and Davis, J.J. 2008. An optimised electrode pre-treatment for SAM formation on polycrystalline gold. *Journal of Electroanalytical Chemistry*. **621**(1), pp.117–120.

Tothill, I.E., Newman, J.D., White, S.F. and Turner, A.P.F. 1997. Monitoring of the glucose concentration during microbial fermentation using a novel mass-producible biosensor suitable for on-line use. *Enzyme and Microbial Technology*. **20**(8), pp.590–596.

Tunuli, M.S. 1988. Gold - chloride electrodes for voltammetric analyses. *Analyst*. **113**(8), pp.1339–1340.

Tunuli, M.S. and Armendariz, L. 1987. Electrocatalytic chloride modified gold electrodes for electroanalyses. *Journal of The Electrochemical Society*. **134**(10), pp.2641–2642.

Vakurov, A., Pchelintsev, N.A., Forde, J., ’Fgin, C., Gibson, T. and Millner, P. 2009. The preparation of size-controlled functionalized polymeric nanoparticles in micelles. *Nanotechnology*. **20**(29).

Varshney, M., Li, Y., Srinivasan, B. and Tung, S. 2007. A label-free, microfluidics and interdigitated array microelectrode-based impedance biosensor in combination with nanoparticles immunoseparation for detection of *Escherichia coli* O157:H7 in food samples. *Sensors and Actuators, B: Chemical*. **128**(1), pp.99–107.

Vig, J.R. 1985. UV/ozone cleaning of surfaces. *Proceedings - The Electrochemical Society*. **90**(9), pp.105–113.

Walgama, C., Nguyen, M.P., Boatner, L.M., Richards, I. and Crooks, R.M. 2020. Hybrid paper and 3D-printed microfluidic device for electrochemical detection of Ag nanoparticle labels. *Lab on a Chip*. **20**(9), pp.1648–1657.

Wan, J., Ai, J., Zhang, Y., Geng, X., Gao, Q. and Cheng, Z. 2016. Signal-off impedimetric immunosensor for the detection of *Escherichia coli* O157:H7. *Scientific Reports*. **6**, pp.2–7.

Wan, Y., Lin, Z., Zhang, D., Wang, Y. and Hou, B. 2011. Biosensors and Bioelectronics Impedimetric immunosensor doped with reduced graphene sheets fabricated by controllable electrodeposition for the non-labelled detection of bacteria. *Biosensors and Bioelectronics*. **26**(5), pp.1959–1964.

Wan, Y., Zhang, D. and Hou, B. 2009. Monitoring microbial populations of sulfate-reducing bacteria using an impedimetric immunosensor based on agglutination assay. *Talanta*. **80**(1), pp.218–223.

Wan, Y., Zhang, D., Wang, Y. and Hou, B. 2010. A 3D-impedimetric immunosensor based on foam Ni for detection of sulfate-reducing bacteria. *Electrochemistry Communications*. **12**(2), pp.288–291.

Wang, J. 2001. Glucose biosensors: 40 Years of advances and challenges. *Electroanalysis*. **13**(12), pp.983–988.

Wang, R., Dong, W., Ruan, C., Kanayeva, D., Lassiter, K., Tian, R. and Li, Y. 2008. TiO_2 Nanowire bundle microelectrode based impedance immunosensor for rapid and sensitive detection of *Listeria monocytogenes*. *Nano Letters*. **8**(9), pp.2625–2631.

Wang, R., Lum, J., Callaway, Z., Lin, J., Bottje, W. and Li, Y. 2015. A label-free impedance immunosensor using screen-printed interdigitated electrodes and magnetic nanobeads for the detection of *E. coli* O157:H7. *Biosensors*. **5**(4), pp.791–803.

Wang, R., Wang, Y., Lassiter, K., Li, Y., Hargis, B., Tung, S., Berghman, L. and Bottje, W. 2009. Interdigitated array microelectrode based impedance immunosensor for detection of avian influenza virus H5N1. *Talanta*. **79**(2), pp.159–164.

Wang, Renjie, Xu, Y., Sors, T., Irudayaraj, J., Ren, W. and Wang, Rong 2018. Impedimetric detection of bacteria by using a microfluidic chip and silver nanoparticle based signal enhancement. *Microchimica Acta*. **185**(3).

Wang, Y., Ping, J., Ye, Z., Wu, J. and Ying, Y. 2013. Impedimetric immunosensor based on gold nanoparticles modified graphene paper for label-free detection of *Escherichia coli* O157: H7. *Biosensors and Bioelectronics*. **49**, pp.492–498.

Wangmaung, N., Chomean, S., Promptmas, C., Mas-oodi, S., Tanyong, D. and Ittarat, W. 2014. Silver quartz crystal microbalance for differential diagnosis of Plasmodium falciparum and Plasmodium vivax in single and mixed infection. *Biosensors and Bioelectronics*. **62**, pp.295–301.

Weltin, A., Kieninger, J. and Urban, G.A. 2016. Microfabricated, amperometric, enzyme-based biosensors for in vivo applications. *Analytical and Bioanalytical Chemistry*. **408**(17), pp.4503–4521.

Wen, T., Wang, R., Sotero, A. and Li, Y. 2017. A portable impedance immunosensing system for rapid detection of *Salmonella Typhimurium*. *Sensors*. **17**(9), pp.1–15.

Westerlund, B. and Korhonen, T.K. 1993. Bacterial proteins binding to the mammalian extracellular matrix. *Molecular Microbiology*. **9**, pp.687–694.

Widrig, C.A., Chung, C. and Porter, M.D. 1991. The electrochemical desorption of n-alkanethiol monolayers from polycrystalline Au and Ag electrodes. *Journal of Electroanalytical Chemistry*. **310**(1–2), pp.335–359.

Wilson, G.S. and Gifford, R. 2005. Biosensors for real-time in vivo measurements. *Biosensors and Bioelectronics*. **20**(12), pp.2388–2403.

Worley, C.G. and Linton, R.W. 1995. Removing sulfur from gold using ultraviolet/ozone cleaning. *Journal of Vacuum Science & Technology A: Vacuum, Surfaces, and Films*. **13**(4), pp.2281–2284.

Wu, M. and Li, X. 2015. *Klebsiella pneumoniae* and *Pseudomonas aeruginosa* [Online] Second Edi. (Y.-W. Tang, M. Sussman, D. Liu, I. Poxton, & J. Schwartzman, eds.). Academic Press. Available from: http://dx.doi.org/10.1016/B978-0-12-397169-2.00087-1.

Wu, Q., Zhang, Y., Yang, Q., Yuan, N. and Zhang, W. 2019. Review of electrochemical DNA biosensors for detecting food borne pathogens. *Sensors*. **19**(22), p.4916.

Xi, F., Gao, J., Wang, J. and Wang, Z. 2011. Discrimination and detection of bacteria with a label-free impedimetric biosensor based on self-assembled lectin monolayer. *Journal of Electroanalytical Chemistry*. **656**(1–2), pp.252–257.

Xia, S., Zhu, P., Pi, F., Zhang, Y., Li, Y., Wang, J. and Sun, X. 2017. Development of a simple and convenient cell-based electrochemical biosensor for evaluating the individual and combined toxicity of DON, ZEN, and AFB1. *Biosensors and Bioelectronics*. **97**, pp.345–351.

Xu, X., Makaraviciute, A., Abdurakhmanov, E., Wermeling, F. and Li, S. 2020. Estimating detection limits of potentiometric DNA sensors using surface plasmon resonance analyses. *ACS Sensors*. **5**, pp.217–224.

Xu, X., Makaraviciute, A., Pettersson, J., Zhang, S., Nyholm, L. and Zhang, Z. 2019. Sensors and Actuators B : Chemical Revisiting the factors influencing gold electrodes prepared using cyclic voltammetry. *Sensors & Actuators: B. Chemical*. **283**(December 2018), pp.146–153.

Yan, X.F., Wang, M.H. and An, D. 2011. Progress of interdigitated array microelectrodes based impedance immunosensor. *Fenxi Huaxue/ Chinese Journal of Analytical Chemistry*. **39**(10), pp.1601–1610.

Yang, J., Deng, S., Lei, J., Ju, H. and Gunasekaran, S. 2011. Electrochemical synthesis of reduced graphene sheet-AuPd alloy nanoparticle composites for enzymatic biosensing. *Biosensors and Bioelectronics*. **29**(1), pp.159–166.

Yang, T., Zhou, N., Li, Q., Guan, Q., Zhang, W. and Jiao, K. 2012. Highly sensitive electrochemical impedance sensing of PEP gene based on integrated Au-Pt alloy nanoparticles and polytyramine. *Colloids and Surfaces B: Biointerfaces*. **97**, pp.150–154.

Yang, W. and Lai, R.Y. 2011. Effect of diluent chain length on the performance of the electrochemical DNA sensor at elevated temperature. *Analyst*. **136**(1), pp.134–139.

Yang, Z., Gonzalez-cortes, A., Jourquin, G., Vire, J. and Kauffmann, J. 1995. Analytical application of self assembled monolayers on gold electrodes : critical importance of surface pretreatment. *Biosensors and Bioelectronics*. **10**, pp.789–795.

Yao, C., Xiang, Y., Deng, K., Xia, H. and Fu, W. 2013. Sensitive and specific HBV genomic DNA detection using RCA-based QCM biosensor. *Sensors and Actuators, B: Chemical*. **181**, pp.382–387.

Yoo, E.H. and Lee, S.Y. 2010. Glucose biosensors: an overview of use in clinical practice. *Sensors*. **10**(5), pp.4558–4576.

Zhao, X., Li, M. and Xu, Z. 2018. Detection of foodborne pathogens by surface enhanced Raman spectroscopy. *Frontiers in Microbiology*. **9**, pp.1–13.

Zhao, Y.H. and Chi, Y.J. 2009. Characterization of collagen from eggshell memrane. *Biotechnology*. **8**(2), pp.254–258.

Zhurauski, P., Arya, S.K., Jolly, P., Tiede, C., Tomlinson, D.C., Ko Ferrigno, P. and Estrela, P. 2018. Sensitive and selective Affimer-functionalised interdigitated electrode-based capacitive biosensor for Her4 protein tumour biomarker detection. *Biosensors and Bioelectronics*. **108**, pp.1–8.

Zimmer & Peacock AS 2020. No Title. [Accessed 9 February 2020]. Available from: https://www.zimmerpeacocktech.com/knowledge-base/faq/electrochemical-polishing-of-zp-electrodes/.

Appendix I

Comparison between the new and old batch Metrohm DropSens CX2220AT (Electrodes 2) to demonstrate faulty electrodes

The images below try to explain the different results obtained with the new batch E:0023829 and the old batch E:0022236.

In order to show the anomalies presented by the new batch, electrodes were first pretreated and polymer-coated. Then, CV analyses were performed and shown.

All the electrodes were pretreated with CV in 0.1 M H_2SO_4 for 5 cycles from 0.0 V to +1.4 V at a scan rate of 50 mV/s. Next, 0.075 mM octopamine was dissolved in 10 mM PB buffer pH 7.2 and electropolymerised through CV from 0.0 V to +1.6 V for 2 cycles at a scan rate of 100 mv/s.

A typical octopamine oxidative peak should appear around +0.45 V to +0.6 V in the electropolymerisation profiles. Next, 10 CV cycles from -0.1 V to +0.5 V under the presence of 10 mM $[Fe(CN_6)]^{3-/4-}$ in 100 mM PBS were conducted to show the flow of current through the electrode surface.

Metrohm DropSens CX2220AT (Electrodes 2) Lot: E0023829 (NEW BATCH)

- 0.075 mM octopamine electropolymerisation

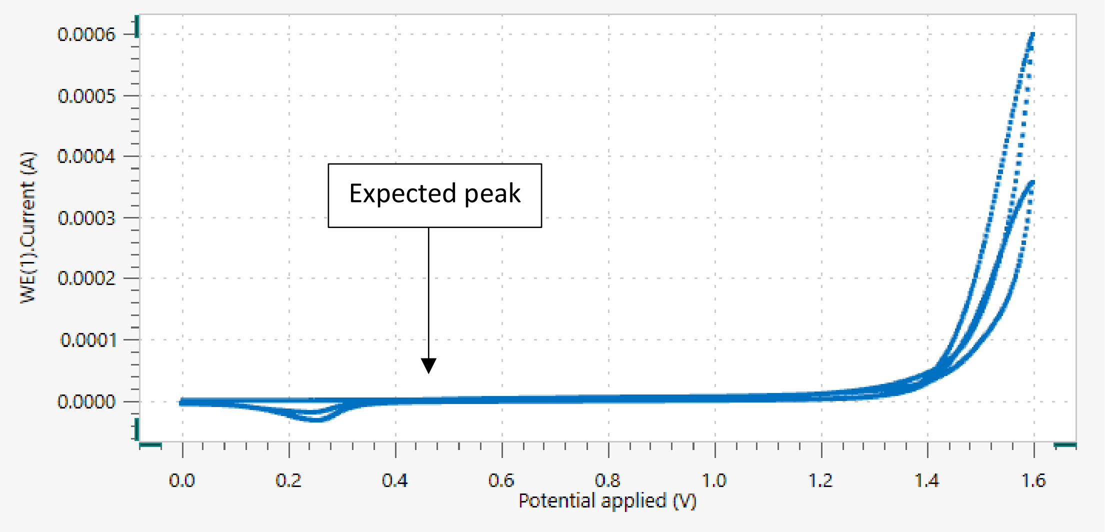

Result: no octopamine oxidative peak was observed through electropolymerisation.

- Zoomed-in insert where octopamine oxidative peak should have taken place during electropolymerisation

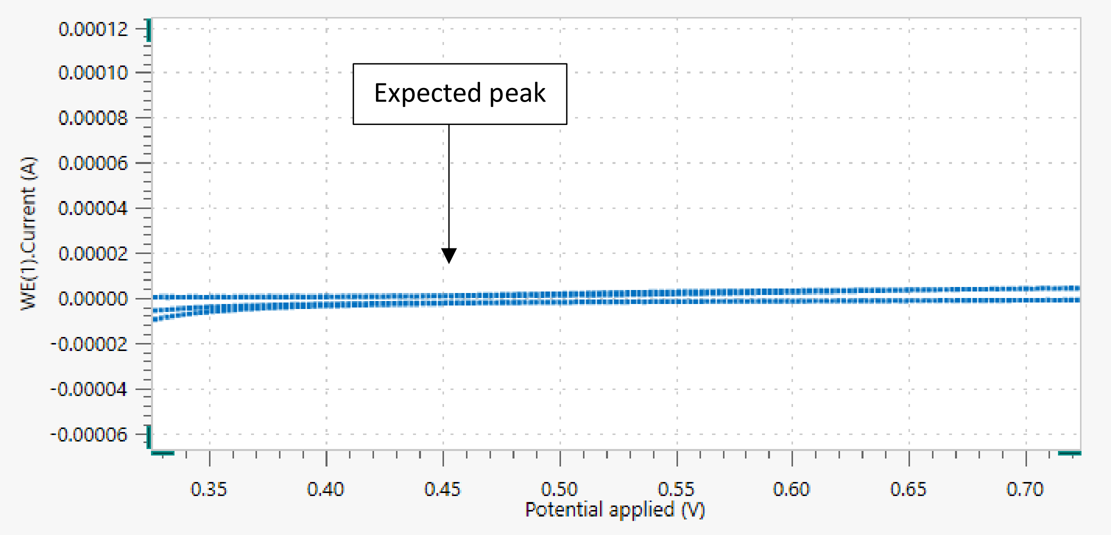

Result: no octopamine oxidative peak was observed through electropolymerisation.

- Ten CV cycles from -0.1 V to +0.5 V in 10 mM $[Fe(CN_6)]^{3-/4-}$ in 100 mM PBS

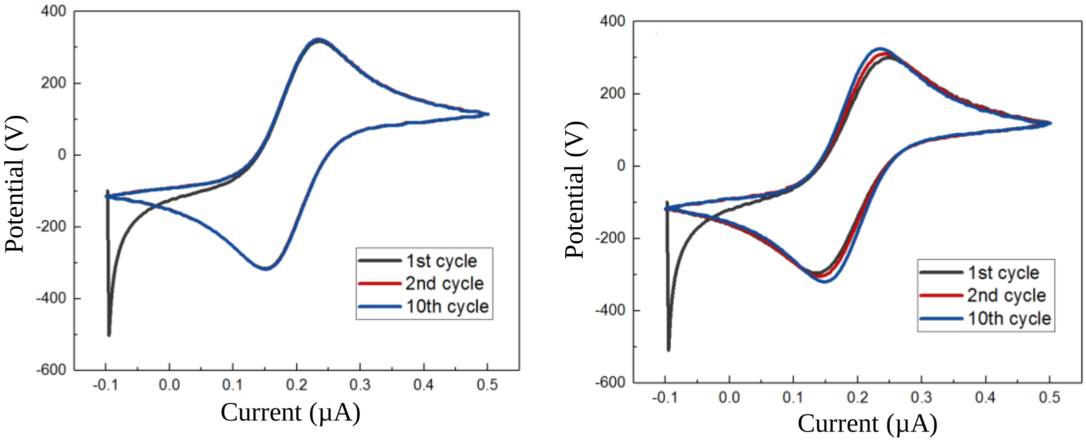

On the left, the CV profile after a theoretical octopamine polymerization. On the right a CV of a bare pretreated electrode. Both profiles show the same electrochemical features in terms of oxidative and reductive potential and intensity.

Result: No difference between the theoretical POc-coated electrode compared to bare electrodes.

Metrohm DropSens CX2220AT (Electrodes 2) Lot: E0022236 (OLD BATCH)

- 0.075 mM octopamine electropolymerisation

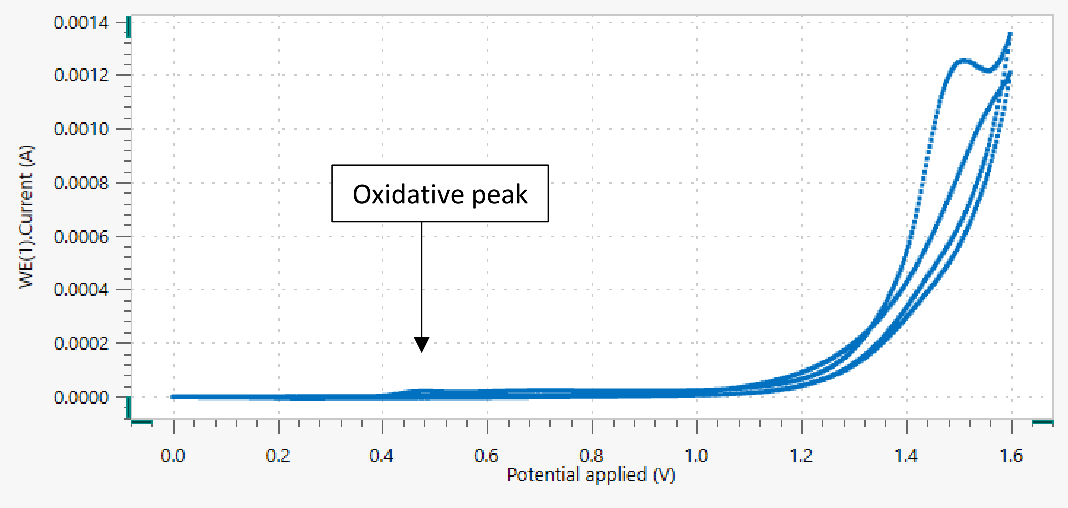

- Zoomed-in insert where electropolymerisation should take place:

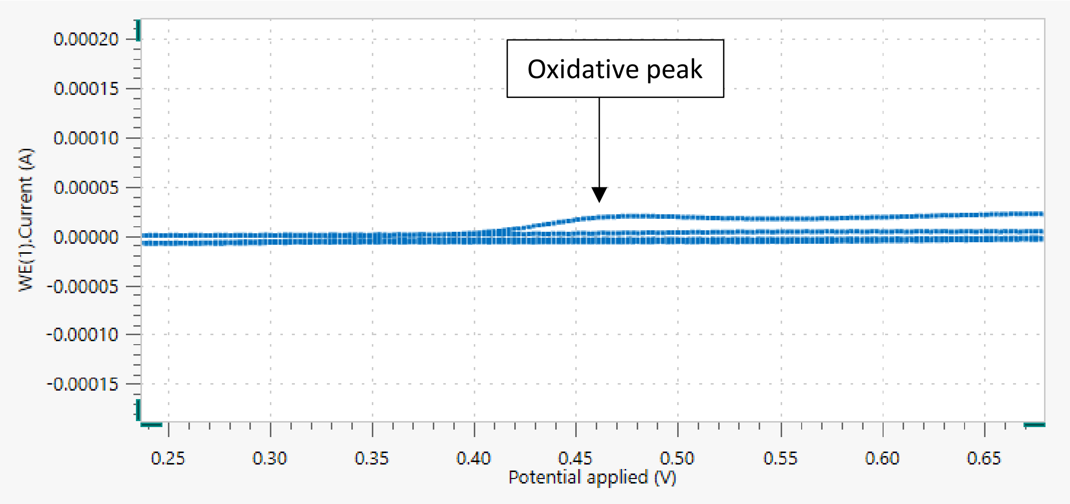

Result: Octopamine oxidative peak can be observed with old batch of the same electrodes.

- Ten CV cycles from -0.1 V to +0.5 V under 10 mM [Fe(CN$_6$)]$^{3-/4-}$ in 100 mM PBS

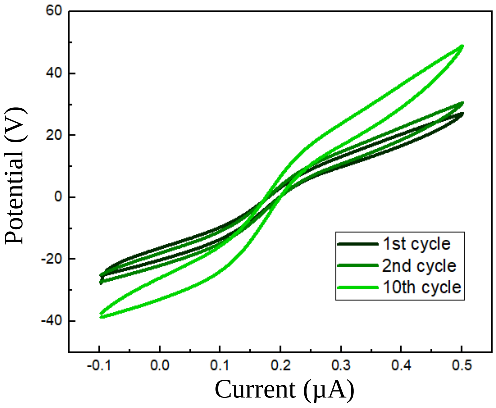

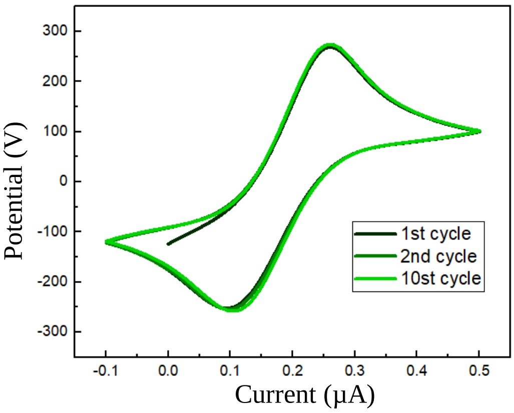

On the left, a typical CV profile of POc-coated. On the right, a typical CV profile with a bare pretreated electrode. A clear difference between both profiles can be observed, thus indicating the surface coating on the octopamine electropolymerised electrodes.

Results: There is clear difference between the POc-coated electrodes compared to bare electrodes.

Conclusion: There is not octopamine electropolymerisation over electrodes from **Lot: E0023829 (NEW BATCH)**. Their CV analysis shows conductive profiles comparable to bare electrodes.

Appendix II

Dot Blot and fluorescence binding assays for purified YadA$_{O:9}$ head domain to heparin carried out by Ina Meuskens.

The following **Figure A$_{II}$1A** shows a dot blot in which purified YadA$_{O:8}$ and YadA$_{O:9}$ head domains were immobilised to detect biotinylated heparin**.** The results appeared to be in line with the previous results for whole bacteria (**Figures 7.2-3**). Next, the purified head domains were immobilised in a 96-well plate and assessed binding for different concentrations for binding quantification (**Figure A$_{II}$1B-C**). It was observed that at a concentration of 450 µg/mL heparin, the binding between the two serotypes was significantly different.

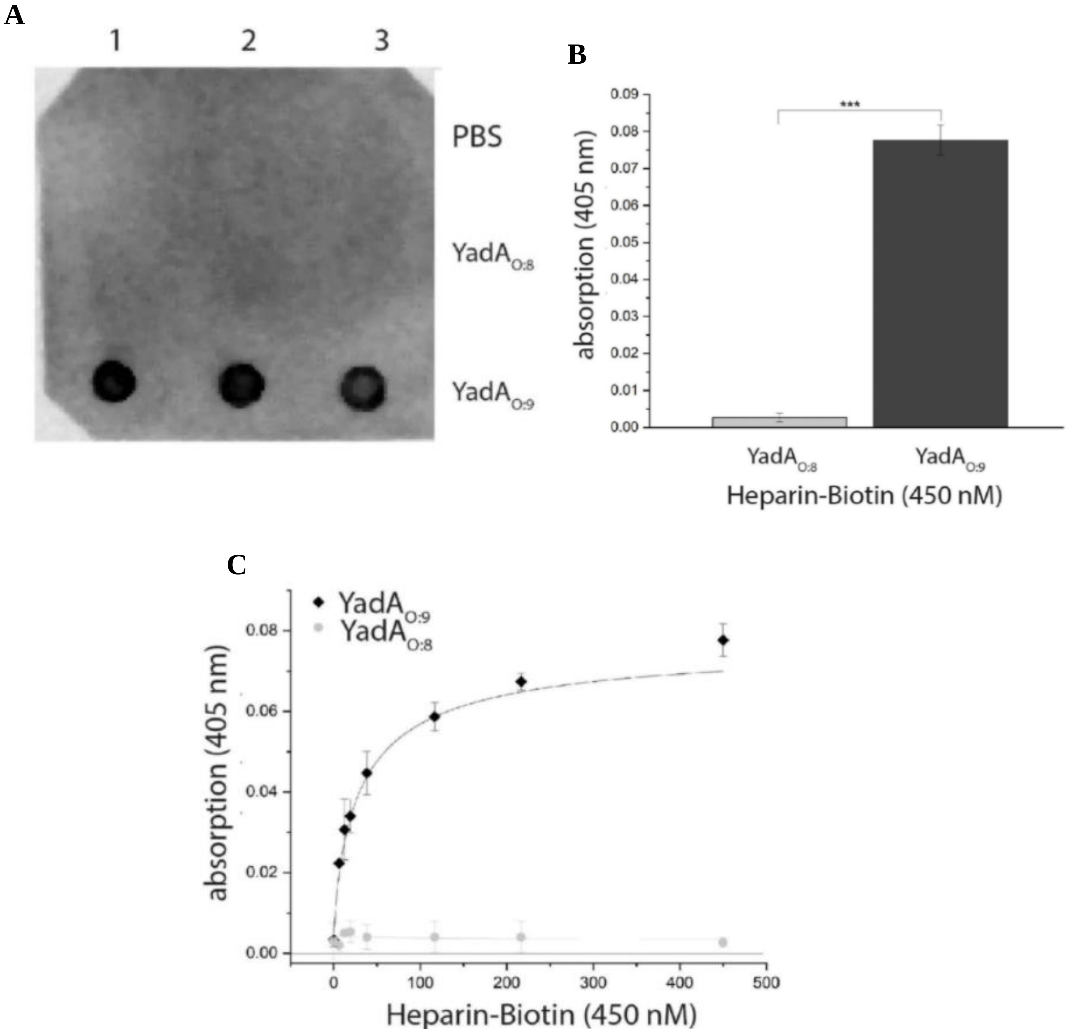

Figure A$_{II}$1. Dot blot and fluorescent assays to test YadA head domains binding to heparin. **A**, Dot blot with immobilised YadA head domains was tested to observe the binding to biotinylated heparin (**Section 2.2.13.3**). **B**, ELISA-like assay employing immobilised YadA head domains to bind biotinylated heparin. **C**, an ELISA-like assay exhibits the interaction between immobilised YadA head domains and biotinylated heparin according to a concentration-dependent manner (**Section 2.2.13.4**). $p < 0.001$ is indicated with ***. Figures reproduced from (Meuskens et al., 2022)